

# **Cosmology with Gravitational Lensing: Measuring Quasar Time Delays and Cosmic Shear**

THÈSE N° 5546 (2013)

PRÉSENTÉE LE 28 FEVRIER 2013  
À LA FACULTÉ DES SCIENCES DE BASE  
LABORATOIRE D'ASTROPHYSIQUE  
PROGRAMME DOCTORAL EN PHYSIQUE

ÉCOLE POLYTECHNIQUE FÉDÉRALE DE LAUSANNE

POUR L'OBTENTION DU GRADE DE DOCTEUR ÈS SCIENCES

PAR

**Malte TEWES**

acceptée sur proposition du jury:

Prof. O. Schneider, président du jury  
Prof. G. Meylan, Dr F. Courbin, directeurs de thèse  
Dr J. Lesgourgues, rapporteur  
Prof. T. Treu, rapporteur  
Prof. J. Wambsganss, rapporteur



ÉCOLE POLYTECHNIQUE  
FÉDÉRALE DE LAUSANNE

Suisse  
2013



Theories crumble, but good observations never fade.  
— Harlow Shapley (1885 – 1972)

To John D. Hunter (1968 – 2012), lead author of matplotlib.



These are the login names of the observers who contributed to the COSMOGRAIL monitoring at the Swiss Euler telescope, up to September 2012. The font size is proportional to the square root of the number of science exposures. In total, more than 26000 images of gravitational lenses were taken by Euler's instruments C2 and ECAM. The above people dutifully scheduled these lens observations at optimal airmass, took focus exposures, and waited for the infamous morning flats. Without them, COSMOGRAIL light curves would not be the same.

Many thanks to you all, including the observers and technicians from the Mercator, Maidanak, HCT, Liverpool and SMARTS-1.3m telescopes !



# Acknowledgements

My thesis director Georges Meylan and codirector Frédéric Courbin have initiated the COSMOGRAIL monitoring campaign in 2004. At this time I was just slowly starting to consider that astronomy might become more than a hobby of mine. COSMOGRAIL constitutes the primary pillar of this thesis, and I feel extremely fortunate that I could contribute to – and benefit from – this fascinating and hands-on observational project. I am profoundly grateful to Georges Meylan and Frédéric Courbin for inviting me to work at LASTRO, and also for their trust, guidance, ideas, availability, and the outstanding science environment offered by this laboratory.

COSMOGRAIL is teamwork, and I thank all my other colleagues from this collaboration, in particular Ildar Asfandiyarov, Eva Eulaers, Pierre Magain, Rathna Kumar Keerthi and Chelliah Subramonian Stalin for their dedication to the monitoring and numerous discussions about both science and software. It is also a great pleasure to thank Christopher Kochanek, Christopher Morgan, and their respective groups for the fruitful collaboration on monitoring and light curve analysis. And I am deeply thankful to Sherry Suyu and all her collaborators for their patience with our delay... measurements of RX J1131–1231, and for turning these into cosmology in such a resounding, convincing, and elegant way. Concerning the second subject of this thesis, I thank Tom Kitching and his challenge coordination team for organizing GREAT10, that got me connected with the thrilling prospects of cosmic shear surveys.

Back to the Observatoire de Sauverny: I thank all my present and past colleagues from EPFL and from the University of Geneva – it is a delight to work here ! I am grateful to my officemate Nicolas Cantale, notably for the fun we had pair-coding MegaLUT a few days before the GREAT10 deadline. To Christel Vuissoz for organizing the monitoring at the Euler telescope until 2008, from which my work profits so much. To all the “lensers” Dominique Sluse, Cécile Faure, Alexander Eigenbrod, Daria Nurbaeva and Marc Gentile for the precious discussions. To the master and summer job students Gianni Cataldi, Denis Vörös, Alexis Arnaudon, François Rérat, Dheeraj Reddy, to name just those who directly worked with me on the COSMOGRAIL or QSO-lens search codes. To LASTRO’s exceptional sysadmins Olivier Genevay and Yves Revaz (module add whatineed), and of course, to the obliging administrative staff, in particular Carol Maury and Nicole Tharin.

The stays at the ESO La Silla Observatory are certainly among the most memorable events of my last 4 years. I thank the entire team of engineers that keep improving the Swiss Euler station, telescope, instruments, and software. You have created an amazingly productive system. I also owe something (a beer ?) to Kristof Smolders, who made me reconsider python *just* in time, in 2008.

I am deeply grateful to the members of the thesis jury, listed on the front cover, for their precious time.

## Acknowledgements

---

Outside of the professional community, I thank my friends from Callista to the Samaritains for all the good moments. And finally, I thank my parents Gisela and Rüdiger for their love and support. Das Glück das ich habe, euer Sohn zu sein, ist ungeheuerlich. Jetzt wird's Zeit zum Spätzlemachen lernen !

*Lausanne, 23 September 2012*

M. T.

# Abstract

Since its first observational evidence in 1919, gravitational lensing – the deflection of light by gravitation – has become an established astrophysical tool. Its physical description, by means of general relativity, is well understood. Observations of the gravitational lensing effect can be employed to probe the distribution of deflecting mass structures and to study magnified astrophysical sources in otherwise unachievable ways. Furthermore, observable differences in light travel time along the multiple optical paths of strong gravitational lens systems probe their absolute scales. This latter effect allows to constrain the Hubble constant  $H_0$  at high redshift, without the need of any secondary distance estimators or complex astrophysics. Such a direct measurement of  $H_0$  features high complementarity to other cosmological probes, and, in particular, is crucial for understanding dark energy.

The first, and primary, part of this thesis is embedded in the COSmological MONitoring of GRAvitational Lenses (COSMOGRAIL) project, and deals with the measurement of the *time delays* between the multiple images of gravitationally lensed quasars. COSMOGRAIL is a monitoring campaign of such lenses, making use of several medium sized optical telescopes. The project was initiated in 2004 by the Laboratory of Astrophysics at EPFL, and has now secured data spanning nearly a decade for some of the targeted lenses. Through a state-of-the-art image processing pipeline, this data yields light curves of the individual quasar images, characterized by an unprecedented combination of length and photometric quality.

To robustly measure the delays as well as the associated uncertainties from these light curves, even in presence of prominent microlensing variations, novel numerical techniques are required. For this purpose, three different techniques have been developed in this thesis, that are all explicitly designed to handle light curves with extrinsic variability. The precision and the accuracy (bias) of the time delay measurements are empirically estimated, using realistic simulated light curves with known time delays that closely mimic the observations. The international COSMOGRAIL collaboration now homogeneously employs both the new photometric pipeline and the delay measurement methods. This will significantly increase the number of robustly measured quasar time delays. Furthermore, our unique light curves have an impact in the field of quasar microlensing studies.

A central result of this thesis is the measurement of the time delays of the quadruply lensed  $z_{\text{QSO}} = 0.658$  quasar RX J1131–1231, from more than 700 monitoring epochs. Several sharp quasar variability features strongly constrain the analysis. While the delays between the 3 close images of this long axis cusp lens are compatible with being 0, the delay of image D is measured to be 91 days, with a fractional uncertainty of 1.5% ( $1\sigma$ ), including systematic errors. At this level of accuracy, the resulting cosmological inference, performed in collaboration with Suyu et al. (2012a), is limited by the residual uncertainty of the lens model. In combination with the Wilkinson Microwave Anisotropy Probe seven-year data (WMAP7), the time delays of this *single* lens already yield  $H_0 = 80.0^{+5.8}_{-5.7} \text{ km s}^{-1} \text{ Mpc}^{-1}$ ,  $\Omega_{\text{de}} = 0.79 \pm 0.03$ , and  $w = -1.25^{+0.17}_{-0.21}$

## Abstract

---

in a flat  $w$ CDM cosmology. The combination with only one other quasar lens (B1608+656) – also performed in Suyu et al. (2012a) – further reduces these uncertainties, as quasar lenses are independent and all known systematic errors are under control.

The second part of this thesis addresses another problem in observational cosmology. It describes a simple and fast method to correct ellipticity measurements of galaxies from the distortion by the instrumental and atmospheric point spread function (PSF), in view of weak lensing *cosmic shear* measurements. Forthcoming surveys such as the ESA Euclid mission will exploit this cosmological probe to yield stringent constraints on the dark universe and its history. Our method performs a classification of galaxies and associated PSFs according to measured shape parameters, and corrects the measured galaxy ellipticities by querying a large lookup table (LUT), built by supervised learning. This method was developed in the scope of the GREAT10 image analysis challenge, and achieves excellent results in terms of the different challenge evaluation metrics. Of particular interest is the efficiency of the method, with a processing time below 3 ms per galaxy on an ordinary CPU.

Finally, the third part of this thesis presents the discovery of the first cases of quasar host galaxies acting as strong lenses on background sources. We have selected four candidates from the spectroscopic database of the Sloan Digital Sky Survey (SDSS). Our follow-up observations with the Hubble Space Telescope show that two of them feature spectacular gravitational arcs, offering a unique way of weighing these quasar host galaxies.

**Keywords:** astrophysics, observational cosmology, gravitational lensing, time delay, quasar, light curve, microlensing, Hubble constant, cosmic shear, galaxy shape measurement, cosmological parameter, deconvolution

# Résumé

Depuis sa première mise en évidence observationnelle en 1919, le phénomène de lentille gravitationnelle – la déflexion de la lumière par la gravitation – est devenu un outil astrophysique établi. Sa description physique, par la relativité générale, est bien comprise. Les observations d'effets de lentille gravitationnelle peuvent être utilisées pour sonder la distribution de matière défléchissant la lumière, mais aussi pour étudier les sources astrophysiques dont l'apparence se trouve agrandie. De plus, la différence mesurable de la durée du parcours de la lumière le long de différents chemins optiques d'un système de lentille gravitationnelle est sensible à la taille physique de ce dernier. Cet effet permet de contraindre la valeur de la constante de Hubble  $H_0$  à décalage vers le rouge élevé, sans aucune calibration par d'autres indicateurs de distance. Une telle mesure directe de  $H_0$  est très complémentaire à d'autres observations cosmologiques, et est notamment essentielle pour comprendre l'énergie sombre.

La première et principale partie de cette thèse s'intègre au projet COSmological MONitoring of GRAvitational Lenses (COSMOGRAIL), et concerne la mesure de *retards temporels* (time delays) entre les images multiples de quasars subissant l'effet de lentille gravitationnelle. COSMOGRAIL est un programme d'observation continue de ces lentilles, et utilise plusieurs télescopes optiques de taille moyenne. Ce projet international a été initié en 2004 au Laboratoire d'astrophysique de l'EPFL, et a maintenant obtenu des données pendant presque une décennie pour certaines de ses cibles. Grâce à un logiciel de traitement d'image à la pointe du savoir-faire, ces données brutes délivrent des courbes de lumière des images individuelles de quasar, caractérisées par une combinaison de longueur et de qualité photométrique unique au monde.

Afin de mesurer les retards temporels ainsi que les incertitudes associées à partir de ces courbes, même en présence de perturbations due à l'effet de microlentille gravitationnelle, de nouvelles techniques d'analyse se sont avérées nécessaires. Pour répondre à ce besoin, trois méthodes différentes ont été développées dans cette thèse. Chacune d'elles est explicitement conçue pour analyser des courbes de lumière avec variabilité extrinsèque. Les dispersions statistiques et erreurs systématiques de nos mesures de retards temporels sont évaluées de façon empirique, en appliquant les méthodes à des courbes de lumière simulées avec retards temporels connus, et qui imitent les données observées. Toute la collaboration COSMOGRAIL utilise maintenant de façon homogène le nouveau logiciel de photométrie ainsi que ces méthodes de mesures de retards temporels. Ceci va significativement augmenter le nombre de retards temporels mesurés de façon robuste. De plus, nos courbes de lumière uniques en leur genre ont un intérêt considérable pour les analyses de microlentilles gravitationnelles.

Un résultat central de cette thèse est la mesure des retards temporels du système de lentille quadruple du quasar RX J1131–1231 à  $z_{\text{QSO}} = 0.658$ , à partir de plus de 700 époques d'observations. Plusieurs structures nettes de variabilité intrinsèque permettent une analyse précise. Alors que les retards entre les 3 images proches de ce système sont compatibles avec zéro, le re-

tard de l'image D est mesuré à 91 jours, avec une incertitude relative de 1.5% ( $1\sigma$ ), comprenant les erreurs systématiques. A ce niveau de précision, les déductions cosmologiques réalisées en collaboration avec Suyu et al. (2012a) sont limitées par l'incertitude résiduelle sur le modèle de masse de la lentille. En combinaison avec les données du Wilkinson Microwave Anisotropy probe (WMAP7), les retards temporels de cette lentille *individuelle* donnent  $H_0 = 80.0^{+5.8}_{-5.7}$  km s<sup>-1</sup> Mpc<sup>-1</sup>,  $\Omega_{de} = 0.79 \pm 0.03$ , et  $w = -1.25^{+0.17}_{-0.21}$  dans le formalisme d'une cosmologie  $w$ CDM à courbure spatiale nulle. La combinaison de cette analyse avec une seule autre lentille de quasar (B1608+656) – aussi réalisée dans Suyu et al. (2012a) – réduit encore ces incertitudes. Les lentilles de quasar sont en effet indépendantes, et toutes les erreurs systématiques connues sont déterminées.

La deuxième partie de cette thèse répond à un autre problème de cosmologie observationnelle. Elle décrit une méthode simple et rapide de corriger une mesure d'ellipticité de galaxie des effets de distorsion occasionnées par la fonction d'étalement du point (PSF) du télescope et de l'atmosphère. Ces mesures d'ellipticité précises sont primordiales pour analyser le signal du *cisaillement cosmologique* (cosmic shear). De futurs relevés, comme celui de la sonde Euclid de l'ESA, vont exploiter cette information cosmologique pour contraindre l'univers sombre et son histoire. Notre méthode classe les galaxies et les étoiles de PSF selon leurs formes mesurées, et corrige les ellipticités des galaxies à l'aide d'une table de correspondance construite par apprentissage automatique supervisé. Cette méthode a été développée dans le cadre du défi d'analyse d'image GREAT10, et obtient des résultats excellents en terme des métriques d'évaluation de ce défi. Un intérêt tout particulier de notre méthode est son efficacité : elle traite une image de galaxie en moins de 3 ms sur un processeur standard.

Finalement, la troisième partie de cette thèse présente la découverte des premiers cas de galaxies hôtes de quasar agissant comme lentilles gravitationnelles produisant des images multiples de sources d'arrière plan. Nous avons sélectionnés quatre candidats dans la base de donnée spectroscopique du Sloan Digital Sky Survey (SDSS). Nos observations de suivi avec le Télescope Spatial Hubble montrent que deux de ces candidats affichent des arcs gravitationnels spectaculaires, offrant une façon unique de déterminer la masse de ces galaxies hôtes de quasar.

**Mots clés :** astrophysique, lentille gravitationnelle, retard temporel, quasar, courbe de lumière, microlentille gravitationnelle, constante de Hubble, cisaillement cosmologique, mesure morphologique de galaxies, paramètre cosmologique, déconvolution.

# Contents

<b>Acknowledgements</b>	<b>v</b>
<b>Abstract (English/Français)</b>	<b>vii</b>
<b>Contents</b>	<b>xi</b>
<b>List of figures</b>	<b>xiii</b>
<b>1 Introduction</b>	<b>1</b>
1.1 Physical cosmology . . . . .	2
1.1.1 Cosmological redshift . . . . .	2
1.1.2 $\Lambda$ CDM: a model for the Universe . . . . .	3
1.1.3 Dark energy . . . . .	3
1.1.4 Dark matter . . . . .	5
1.1.5 Spatial curvature . . . . .	5
1.1.6 Distance measurements probe cosmology . . . . .	6
1.1.7 Why measure $H_0$ ? . . . .	7
1.2 Gravitational lensing . . . . .	9
1.2.1 Strong lensing . . . . .	10
1.2.2 Time delays, and their link to $H_0$ . . . . .	12
1.2.3 Microlensing . . . . .	16
1.2.4 Weak lensing . . . . .	18
<b>2 COSMOGRAIL</b>	<b>21</b>
2.1 Monitoring . . . . .	23
2.2 Photometry . . . . .	24
2.3 Curve shifting . . . . .	24
Paper: COSMOGRAIL curve shifting techniques (Tewes et al. 2012b) . . . . .	29
<b>3 COSMOGRAIL results</b>	<b>43</b>
3.1 Selected light curves . . . . .	43
Paper: time delay measurements of RX J1131–1231 (Tewes et al. 2012c) . . . . .	49
Paper: cosmological inference from RX J1131–1231 (Suyu et al. 2012a) . . . . .	61
Paper: time delays and lens analysis of HE 0435–1223 (Courbin et al. 2011) . . . . .	83
3.2 Microlensing analysis of Q J0158–4325 . . . . .	95

## Contents

---

<b>4</b>	<b>Cosmic shear measurement</b>	<b>97</b>
4.1	Introduction . . . . .	97
4.2	The GREAT10 data analysis challenge . . . . .	100
4.3	MegaLUT applied to GREAT10 . . . . .	102
4.4	Outlook . . . . .	104
	Paper: MegaLUT (Tewes et al. 2012a) . . . . .	107
<b>5</b>	<b>Strong lensing by QSO host galaxies</b>	<b>115</b>
5.1	Introduction . . . . .	115
5.2	The SDSS spectroscopic survey . . . . .	116
5.3	Results . . . . .	119
	Paper: discovery of the first candidate, SDSS J0013+1523 (Courbin et al. 2010) . . . .	123
<b>A</b>	<b>QCgravlens: a didactic simulation</b>	<b>129</b>
	<b>Bibliography</b>	<b>131</b>
	<b>Curriculum vitae &amp; list of publications</b>	<b>135</b>



# List of Figures

1.1	Large scale structure seen by the SDSS galaxy survey . . . . .	4
1.2	WMAP7 constraints on cosmology . . . . .	8
1.3	SH0ES and WMAP7 constraints on dark energy . . . . .	8
1.4	Schema of strong gravitational lensing . . . . .	10
1.5	HST image of RX J1131–1231 . . . . .	12
1.6	Strong lensing time delays . . . . .	14
1.7	Quasar microlensing . . . . .	17
1.8	Weak gravitational lensing . . . . .	19
2.1	Inside Euler’s head . . . . .	23
2.2	Photometry pipeline : PSF visualization . . . . .	25
2.3	Photometry pipeline : deconvolution visualization . . . . .	26
2.4	PyCS website . . . . .	27
3.1	Light curves of RX J1131–1231 . . . . .	44
3.2	Light curves of WFI 2033–4723 . . . . .	45
3.3	Light curves of HE 0047–1756 . . . . .	45
3.4	Light curves of SDSS J0246–0825 . . . . .	46
3.5	Light curves of SDSS J1226–0006 . . . . .	46
3.6	Light curves of HE 2149–274 . . . . .	46
3.7	Light curves of SDSS J1206+4332 . . . . .	47
3.8	Light curves of SDSS J1001+5027 . . . . .	47
3.9	HST image of Q J0158–4325 . . . . .	95
3.10	Light curves of Q J0158–4325 . . . . .	96
3.11	Inference of the size of the quasar J0158–4325 . . . . .	96
4.1	A filament of dark matter detected by weak lensing . . . . .	98
4.2	The weak lensing “forward process” . . . . .	99
4.3	GREAT10 stamps . . . . .	101
4.4	MMD shape measurement . . . . .	102
4.5	Accuracy on dark energy inference versus survey area . . . . .	104
5.1	Schema of strong lensing by QSO host galaxies . . . . .	115
5.2	SDSS “plug-plate”, holding optical fibers . . . . .	117
5.3	SDSS spectrum of J0919+2720 . . . . .	118
5.4	SDSS and HST images of J0919+2720 . . . . .	118
5.5	SDSS spectra of J0827+5224 and J1005+4016 . . . . .	120

## List of Figures

---

5.6	HST/WFC3 images of 3 discovered QSO lenses . . . . .	121
A.1	QCgravlens . . . . .	129

# 1 Introduction

This thesis deals with measurements of particularly tangible observables constraining *cosmology*, the science that studies the evolution of our Universe as a whole. By definition, the Universe englobes all existing matter and space surrounding us. The speculative description and narration of this totality has a history of at least several thousand years. Compared to this, *observational* cosmology, that confronts factual measurements to predictions from physical models, is very young.

Arguably the first observational steps that lead to our current understanding of the Universe happened exactly 100 years ago, when Vesto Slipher measured, from September 1912 on, large Doppler shifts in the spectra of “nebulae” (Slipher 1913, 1915). Most of these observed spectra were shifted towards larger wavelengths, i.e. *redshifted*. The majority of nebulae were thus apparently receding.

A few years later, Harlow Shapley estimated the approximatively correct size of our Galaxy and our location with respect to its center. He achieved this by observing *Cepheid* variable stars in globular clusters of the Milky Way (Shapley 1918). As discovered by Henrietta Leavitt, Cepheid variables follow a tight relation between their pulsation period and intrinsic luminosity : the longer the period, the brighter the star (Leavitt & Pickering 1912). By measuring such pulsation periods, Shapley deduced the distance to globular clusters. However, Leavitt’s relation alone does not yield the *absolute* intrinsic luminosity of Cepheids, which is required to infer the absolute distance of a star from its apparent brightness. To obtain this information, Shapley therefore had to calibrate his distances, using some local cepheids with measured parallaxes.

From 1922 on, Edwin Hubble identified Cepheids in nebulae (Hubble 1925), and it became clear that many of these nebulae are in fact remote galaxies on their own. The measured distances to galaxies lead Georges Lemaître and Hubble to interpret the Doppler shift measurements initiated by Slipher as resulting from an *expanding* Universe (Lemaître 1927; Hubble 1929). The apparent recession velocity  $v$  of a galaxy was observed to be proportional to its distance  $D$ , with a proportionality constant known as the Hubble constant  $H_0$ :  $v = H_0 \cdot D$ . The Hubble constant expresses the present-day rate of expansion of the Universe. The latest estimate of its value from a technique based on Cepheids, thus somehow in the line of the work from Hubble, is  $73.8 \pm 2.4 \text{ km s}^{-1} \text{ Mpc}^{-1}$  (Riess et al. 2011). In this abbreviation, which stands

for kilometers per second per megaparsec, a megaparsec is a unit of length<sup>1</sup> that corresponds approximately to the distance of the Andromeda galaxy.

The accurate determination of  $H_0$  plays a major role in this thesis; it is the primary objective of the COSMOGRAIL project. The Hubble constant is a fundamental parameter in cosmology, and the interest in constraining its value goes beyond measuring distances. The uncertainty of  $H_0$  is directly related to our understanding of *dark energy*, one of the biggest and entirely unsolved problems in all physics, as will be described in just a few pages ahead.

COSMOGRAIL (Chapters 2 and 3) exploits the so-called *time delay technique*, proposed by Refsdal (1964), to constrain  $H_0$ . This technique involves the measurement of light travel time differences between the multiple images of gravitationally lensed quasars. As will be elucidated in simple terms in Section 1.2 these time delays allow to measure the Hubble constant in a direct way. We won't need calibrations such as required, e.g., by the Cepheid method outlined above.

Chapter 4 presents a technique for the measurement of *cosmic shear*, another promising cosmological probe related to gravitational lensing. The development of this numerical technique was driven by the GREAT10 data analysis challenge, which will hence also be summarily described. And finally, chapter Chapter 5 deals with the search – and discovery – of new strong gravitational lenses.

The primary content of my dissertation consists of research publications, which are directly included in between the pages of this document. The following introductions on cosmology and gravitational lensing, as well as the material at the beginning of each chapter, are intended to give the context of these publications. They are rather minimal and qualitative, but hopefully comprehensible also for readers not familiar with observational cosmology. In any case, they are highly biased towards the topics related to my work.

### 1.1 Physical cosmology

The objective of this short primer is to present the main cosmological parameters that are related to the measurements discussed in this thesis. The last part of this section also describes why measuring  $H_0$  to high accuracy (say 1%) is so important in the present cosmological context.

#### 1.1.1 Cosmological redshift

The *redshift* of light, as measured for spectra of galaxies by Slipher, is defined by

$$z := \frac{\lambda_{\text{obs}} - \lambda_{\text{rest}}}{\lambda_{\text{rest}}} \quad (1.1)$$

where  $\lambda_{\text{obs}}$  is the observed wavelength, and  $\lambda_{\text{rest}}$  is the emitted, or “restframe”, wavelength. For nearby sources, such as stars within the Milky Way, redshifts (or blueshifts, if  $z < 0$ )

---

<sup>1</sup>One *parsec* (pc)  $\approx 3 \cdot 10^{16}$  m, roughly the average distance between neighboring stars around our Sun.

result from the relative velocity between the source and the observer, i.e. the Doppler effect. However, for *cosmological* sources, such as remote galaxies, redshifts are interpreted as being predominantly due to the expansion of space itself. The wavelength of a photon directly undergoes this expansion, from emission until absorption. For example, observing a galaxy to be “at” a redshift of  $z = 1$  ( $\lambda_{\text{obs}} = 2 \times \lambda_{\text{rest}}$ ) means that the Universe expanded by a factor 2 since the light that we observe today was emitted. The higher the redshift of a source, the deeper we look into the past.

### 1.1.2 $\Lambda$ CDM: a model for the Universe

A central objective of cosmology is to understand how – and according to which physical principles – this expansion takes place. Most astrophysicists currently agree on a “concordance” cosmological model denoted  $\Lambda$ CDM. So far this model is successfully describing all robust observations, and it remains qualitatively unchanged since more than a decade, despite the availability of better and better data. The last profound evolution in our description of the Universe followed the discovery that its expansion is *accelerating*, by Riess et al. (1998) and Perlmutter et al. (1999).

The concordance model relies on Einstein’s general relativity as theory of gravitation, and on the assumption that the Universe is homogeneous and isotropic (all locations and spatial directions are similar) on large scales. In this context, the expansion is described by the Friedmann equations (Friedmann 1922, 1924), that link the dynamics of the Universe to its contents.

Let us briefly consider the assumption of homogeneity and isotropy. Obviously, our cosmos is not homogeneous on scales of planets, stars and galaxies. And even galaxies gather in groups, clusters, and filaments, tracing the *large scale structure* of the Universe. However, these inhomogeneities smooth out beyond scales on the order of 500 Mpc. Several independent observations of, for example, the Cosmic Microwave Background (CMB) and the three-dimensional distribution of galaxies (Figure 1.1) have confirmed this general hypothesis to be highly plausible.

### 1.1.3 Dark energy

Given the homogeneity on large scales, the content of the Universe can be described by average mass-energy densities of its components, at least for the purpose of investigating expansion. At the present epoch of cosmic evolution, the predominant of these components is referred to as *dark energy*. This term is nothing but a placeholder. We don’t know anything about the nature of dark energy, but we plainly need to invoke its existence in order to explain the observed accelerated expansion at our present cosmic epoch. Gravitational interaction between matter is attractive; something else, with a “repulsive” overall effect, must be driving the acceleration.

To parametrize its behavior, dark energy is described by an equation-of-state parameter  $w = p/\rho$ , where  $p$  is its pressure and  $\rho$  its density. This parameter  $w$  must be negative and inferior to  $-1/3$  for dark energy to act repulsively. The  $\Lambda$  in  $\Lambda$ CDM stands for a simple

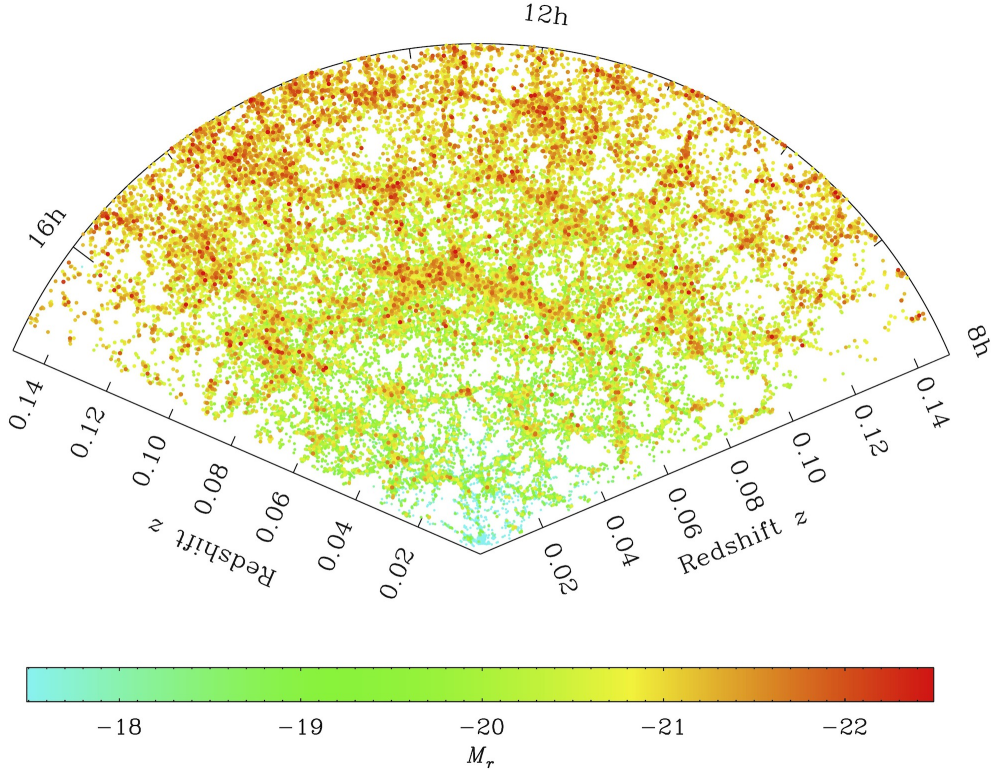


Figure 1.1: Slice through the *SDSS redshift survey*, showing the distribution of galaxies within  $\pm 4$  degrees of the celestial equator, from Zehavi et al. (2011). Each dot is a galaxy, color and dot size encode luminosity. We, the observers, are located at the bottom tip of this diagram (redshift 0), and the radius towards the edge of this plot corresponds to about 500 Mpc. Note that in this 2D representation the foamy structure tends to loose contrast with increasing redshift, due to the projection through progressively larger thickness. Section 5.2 of this thesis further introduces this SDSS survey.

homogeneous and stationary form of dark energy, the so-called cosmological constant.  $\Lambda$  corresponds to the special case  $w = -1$ , and so far this form of dark energy is sufficient to model the observations.

But in all generality,  $w$  can be seen as a free parameter; the resulting extended version of the concordance model is denoted  $w$ CDM. Furthermore, given our ignorance about dark energy, we could expect  $w$  to change with the evolution of the Universe. To explore this possibility,  $w$  is often written as a Taylor expansion, e.g.,

$$w(a) = w_0 + w_a(1 - a) \quad \text{with} \quad a = \frac{1}{1+z}. \quad (1.2)$$

The aim of postulating such an arbitrary but simple form for the time- or redshift-dependence of  $w$  is to predict observable effects (*cosmological probes*) that are sensitive to these new parameters  $w_0$  and  $w_a$ . Finding that  $w$  evolves with time would be an enormous step towards a better understanding of dark energy. It would at least tell us what dark energy is *not*, by

rejecting some of the numerous proposed theories. See for instance (Barger et al. 2006) for a classification of dark energy models in this  $(w_0, w_a)$  plane. Of course, to refute the cosmological constant  $\Lambda$ , measuring  $w$  to be different from -1 would be sufficient.

#### 1.1.4 Dark matter

The other main component of  $\Lambda$ CDM is Cold Dark Matter (CDM). It is called dark, because so far it is only observed through its gravitational interaction. In fact dark matter was invoked precisely to explain several independent gravitational observations. Assuming that general relativity is correct, dark matter is required to account for the observed high orbital speeds of stars and gas in galaxies, and of galaxies in galaxy clusters. It also plays a dominant role in explaining gravitational lensing observations, as will be seen all along this thesis. From the successful theory of primordial nucleosynthesis, which explains the abundance of chemical elements in the Universe, we think to know that dark matter cannot be *baryonic*, i.e., made of atoms. Its nature is currently perfectly unknown, even if we know more about dark matter – or about what it is not – than about dark energy. In particular, the “cold” in CDM refers to the fact that it must clump under the effect of gravitation. If dark matter would be made from “hot” relativistic particles, its distribution would be too smooth. Dark matter is required in the form of halos around galaxies and even satellite galaxies.

#### 1.1.5 Spatial curvature

By fitting the concordance model to relevant cosmological observations (structures in the cosmic microwave background, distribution of galaxies, luminosity of distant supernovae) it was inferred that about 73% of today's total energy density consists of dark energy, 23% is dark matter, and only 4% is ordinary matter (numbers may slightly vary). The energy content of radiation is negligible at the present epoch.

Summing up the densities of these components, one gets a total average density. From the exact value of this density depends the *spatial curvature* of the Universe<sup>2</sup>. Indeed, according to general relativity, which describes gravity in terms of curved spacetime, the geometry of the Universe is not necessarily flat on the largest scales. The total density at the present day can be written as

$$\Omega = \Omega_\Lambda + \Omega_M, \quad (1.3)$$

where  $\Omega_\Lambda$  is a density parameter associated to dark energy in form of  $\Lambda$ , and  $\Omega_M$  represents the total (dark and baryonic) matter density. All terms in this equation are dimensionless. The corresponding physical densities have been normalized by the so-called critical density that would yield a flat universe. In other words,  $\Omega = 1$  corresponds to a flat spatial geometry. Curvature can now be quantified by an associated “curvature density” parameter  $\Omega_k$ ,

$$\Omega_k = 1 - \Omega. \quad (1.4)$$

<sup>2</sup>Note that strictly speaking the minimal  $\Lambda$ CDM model is *flat* – allowing for curvature already consists of an “extension” to the model, like the free equation of state parameter  $w$ .

Experiments have shown so far that  $\Omega_k$  is compatible with being 0, i.e., the total density of the Universe is close to the critical density, which corresponds to about  $2 \cdot 10^{-26} \text{ kg/m}^3$ . As a property of space itself, curvature has fundamental consequences in definitions of distance.

### 1.1.6 Distance measurements probe cosmology

With these very brief descriptions of density parameters in hand, we can proceed to the definition of the *angular diameter distance*. This definition is of perceivable importance to motivate the COSMOGRAIL-part of this thesis (Chapters 2 and 3), as it links the strong lensing time delays to cosmological parameters (Section 1.2.2).

In an expanding universe, the notion of distance is ambiguous and not intuitive. Several definitions, convenient for different calculations, coexist. The angular diameter distance  $D_A$  is constructed so that, for an object of angular size  $\theta$ ,  $D_A \cdot \theta$  corresponds to the proper dimension of this object, perpendicular to the line of sight.

Following the notations of Hogg (1999), this angular diameter distance  $D_A$  measured from us<sup>3</sup> ( $z = 0$ ) to an object at redshift  $z$  is

$$D_A = \frac{D_M}{(1+z)}, \quad (1.5)$$

where the transverse comoving distance  $D_M$  is given by

$$D_M = \begin{cases} \frac{c}{H_0} \frac{1}{\sqrt{|\Omega_k|}} \sin\left(\sqrt{|\Omega_k|} \frac{H_0}{c} \cdot D_C\right) & \text{if } \Omega_k < 0 \text{ (spherical universe)} \\ D_C & \text{if } \Omega_k = 0 \text{ (flat universe)} \\ \frac{c}{H_0} \frac{1}{\sqrt{|\Omega_k|}} \sinh\left(\sqrt{|\Omega_k|} \frac{H_0}{c} \cdot D_C\right) & \text{if } \Omega_k > 0 \text{ (hyperbolic universe)} \end{cases} \quad (1.6)$$

and the line-of-sight comoving distance  $D_C$  is

$$D_C = \frac{c}{H_0} \int_0^z \frac{dz}{\Omega_M(1+z^3) + \Omega_k(1+z)^2 + \Omega_\Lambda}. \quad (1.7)$$

Another common distance, directly related to observations, is the luminosity distance  $D_{\text{lum}}$ . It is to be used when comparing the apparent brightness (flux  $S$ , in units of  $\text{W/m}^2$ ) of a source to its intrinsic luminosity  $L$  through the ordinary relation  $S = L/(4\pi D_{\text{lum}}^2)$ . The luminosity distance is linked to the previous relations by

$$D_{\text{lum}} = (1+z)D_M. \quad (1.8)$$

These formal distance definitions are given here purely to illustrate the connection between distances and cosmological parameters, especially  $H_0$ . Note that for  $z \ll 1$  and a flat universe

---

<sup>3</sup>In the scope of gravitational lensing, angular diameter distances between any two redshifts are to be evaluated. Note that angular diameter distances are not additive functions of redshifts. To avoid detailed descriptions, this general relation is not given here. It can be found, e.g., in Longair (2008).



( $\Omega_k = 0$  and  $\Omega_M + \Omega_\Lambda = 1$ ) we simply have  $D_{\text{lum}} \approx D_A \approx D_M \approx D_C \approx cz/H_0$ . For such small redshifts, which can be interpreted as resulting from the Doppler effect,  $cz$  corresponds to an apparent recession velocity  $v$ . Hence,  $v \approx H_0 \cdot D$  – all the above definitions fall back on “Hubble’s law”. In the local universe, the apparent recession velocities or redshifts of galaxies do not depend on other cosmological parameters than  $H_0$ . For larger redshifts, a dependance on the densities of matter, dark energy, and curvature sets progressively in. But also in this latter regime,  $H_0$  can be constrained in combination with the density parameters by independently measuring the redshift of, and the distance to, a given source. Measuring an angular diameter (luminosity) distance is done by comparing the observed angular size (flux) with the known proper size (luminosity). Sources for which we know this intrinsic size (luminosity) are called standard rulers (standard candles).

### 1.1.7 Why measure $H_0$ ?

$\Lambda$ CDM is a minimal model able to consistently account for cosmological observations. But certainly, our incomprehension of 96% of the total mass energy density is not satisfactory. To test – and eventually refute –  $\Lambda$ CDM and its underlying assumptions, we can constrain its parameters until incompatibilities with observations show up, or we can constrain extended models, such as  $w$ CDM or free curvature.

Over the next decades, a range of ambitious experiments exploiting different cosmological probes will deliver stringent observational constraints. The most imminent results are those from the ESA Planck mission<sup>4</sup>. Planck observed anisotropies in the Cosmic Microwave Background (CMB), with both higher sensitivity and higher resolution than its predecessor, the NASA Wilkinson Microwave Anisotropy Probe (WMAP). The observations are already completed, and Planck’s results are expected to be released in just a few months.

The angular scales of anisotropies in the CMB contain precious information about a wealth of cosmological parameters, notably the density of baryons, the density of dark matter, and the curvature. However, this probe also suffers from *degeneracies*: while it is sensitive to combinations of parameters, it typically cannot pin down their individual values on its own.

By combining probes that are sensitive to different combinations of parameters, these degeneracies can be broken. In the case of CMB data, external measurements of  $H_0$  are particularly helpful, as the CMB itself does not constrain the Hubble constant very well. As a high redshift probe, the CMB can constrain the present-day expansion rate  $H_0$  only when other assumptions, such as flatness or  $w = -1$ , are made. Figures 1.2 and 1.3 illustrate this in the case of the 7-year WMAP data. Clearly, a tight prior of  $H_0$  immensely increases the value of this probe, resulting in actual constraints on parametrized dark energy.

In a similar way,  $H_0$  is also important for obtaining narrow limits on *neutrino masses*. The mass of neutrinos is difficult to study in particle physics experiments: while the latter have shown that neutrinos do have a mass, the scale of this mass is not known. Cosmology probes this absolute mass scale, as massive neutrinos would reduce the amplitude of matter fluctuations on small scales, and contribute to the matter density of the Universe. Combining data from a

<sup>4</sup><http://www.sciops.esa.int/planck/>

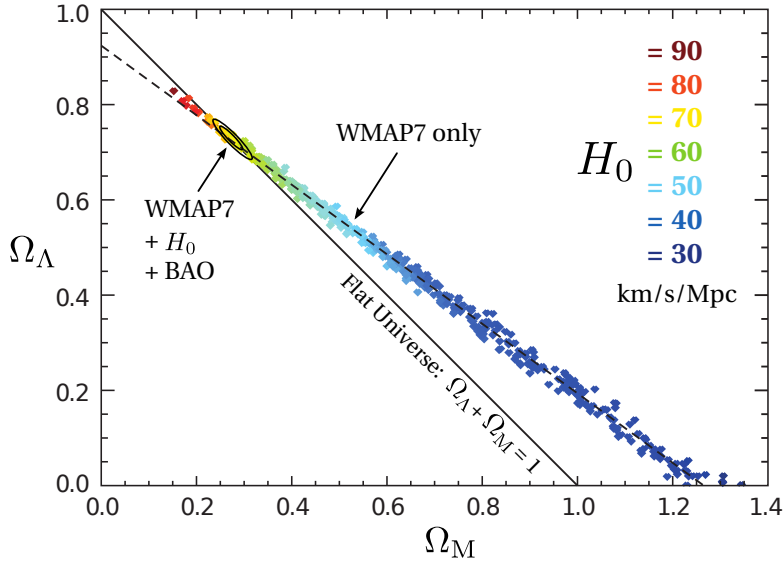


Figure 1.2: WMAP7 constraints on cosmology, from Larson et al. (2011). The colored points sample the posterior probability distribution of a  $\Lambda$ CDM model with curvature, fitted to WMAP7 CMB data *only*. Taken on its own, this dataset is compatible with a wide range of values for  $H_0$ , and does not strongly constrain curvature. However, these degeneracies can be broken when combining the data from several independent cosmological probes. The black  $1\sigma$  and  $2\sigma$  contours were obtained from WMAP7 +  $H_0$  + BAO data (Komatsu et al. 2011). As these contours cross the  $\Omega_k = 0$  line, this combination shows that our universe is roughly flat. Figure from Larson et al. (2011).

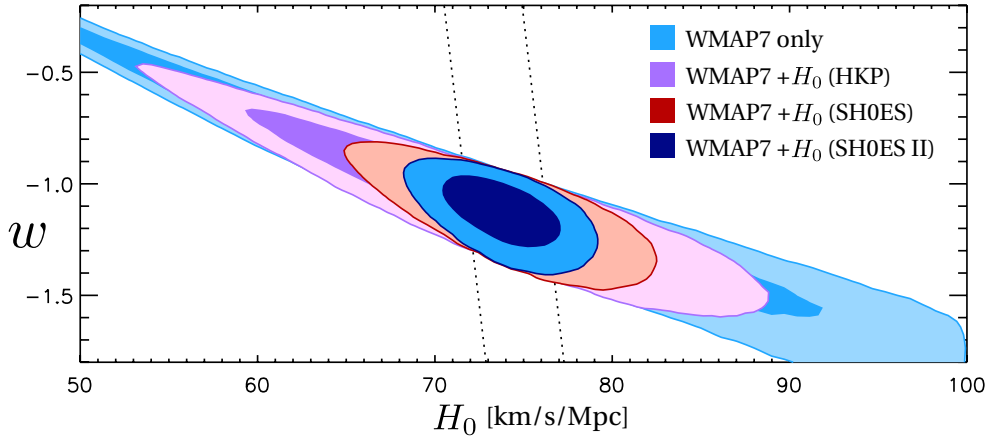


Figure 1.3: Constraints on dark energy from the combination of WMAP7 CMB data and  $H_0$  as measured from Type Ia supernovae observed in the scope of the SH0ES program (Supernovae and H0 for the Equation of State), by Riess et al. (2011).  $1\sigma$  and  $2\sigma$  confidence regions are shown. As in Figure 1.2, it's the combination of WMAP7 with additional constrains on  $H_0$  that breaks degeneracies and constrains in this case the equation-of-state parameter of dark energy,  $w$ , to be close to  $-1$ . Figure from Riess et al. (2011).

galaxy survey, the CMB, baryon acoustic oscillations, supernovae, and a prior on  $H_0$ , Thomas et al. (2010) have determined upper bounds around 0.3 eV for the sum of the neutrino masses. As these authors stress, determining by how much neutrinos affect cosmology is also crucial to avoid biases in the inference of other cosmological parameters.

To conclude, the complementarity of  $H_0$  to other observables, in order to probe dark energy, curvature, neutrino physics, and general relativity, gives a strong motivation to pin down its value. For a review about the Hubble constant, how it can be measured, and the *increasing* importance of the accuracy of its measurement in the light of future surveys, see Freedman & Madore (2010). Suyu et al. (2012b) give an up to date overview on this topic, in form of a short summary of a recent workshop.

## 1.2 Gravitational lensing

This section provides an introduction to the three traditional regimes of gravitational lensing, that happen to all play an important role in this thesis. As for the preceding overview of cosmology, the following synopsis is clearly not comprehensive: it focuses only on the aspects relevant to my work. A detailed account of the vast field of gravitational lensing can be found in the textbook of Schneider, Kochanek, & Wambsganss (2006). For a shorter introduction to the formalism of gravitational lensing, see, e.g., the freely available lecture notes of Narayan & Bartelmann (1996).

The first observed manifestation of light being “bent” by gravitation was made by Arthur Eddington and collaborators in 1919 (Dyson et al. 1920). Their observation consists in small apparent displacements in the angular positions of stars, when these stars are seen close to the limb of the Sun. Einstein’s theory of general relativity (1915) – a theory of gravitation – correctly predicted the amplitude of this bending (*deflection*) of light rays. In the formalism of general relativity, the apparent displacements of background stars result from the local curvature of spacetime induced by the mass of the Sun. The term *gravitational lensing* designates all effects of this curvature on the propagation of light.

A central equation of gravitational lensing connects the small deflection angle  $\hat{\alpha}$  of a light ray in empty space passing next to a point mass  $M$  with a distance of closest approach  $\xi$  :

$$\hat{\alpha} = \frac{4GM}{c^2\xi} = 1.''75 \cdot \frac{(M/M_\odot)}{(\xi/R_\odot)}, \quad (1.9)$$

where  $G$  is the gravitational constant and  $c$  is the speed of light in vacuum. The above equation is an approximation valid only for small deflection angles, but this restriction is easily satisfied by observed situations of gravitational lensing. At the limb of the Sun, i.e., when  $M$  is one solar mass  $M_\odot$  and  $\xi$  is the solar radius  $R_\odot$ , the deflection is of only 1.75 arcsecond, denoted by the double prime<sup>5</sup>. For so small deflections, i.e. when the curvature is relatively weak, the total deflection resulting from a concentrated distribution of mass can be computed by integrating over the deflections from many point masses.

<sup>5</sup>One degree is equivalent to 60′ (arcminute), or 3600″ (arcsecond).

As gravitational lensing is a geometrical consequence of curved space, it does not depend on the wavelength of the light – provided that the medium is a vacuum (see Tsupko & Bisnovatyi-Kogan 2012, for what happens in a plasma). And indeed, the different regimes of gravitational lensing described in the following are successfully explored from X-ray to radio wavelengths. Gravitational lensing has become a veritable astrophysical tool, and only some of its numerous applications will be mentioned in this introduction.

### 1.2.1 Strong lensing

After Eddington’s validation of Equation 1.9 using the Sun as deflector, it took 60 years to discover the first occurrence of gravitational lensing due to another massive object. Walsh et al. (1979) identified that the “two” quasars SBS 0957+561 A and B, both at  $z = 1.41$ , and separated by only  $5''.7$ , are in fact two images of one single source. The light emitted by this quasar gets deflected by a foreground galaxy at  $z = 0.35$  in such a way that it reaches us from several directions, as depicted in Figure 1.4. This regime, in which several images, or highly distorted images of a source are observed, is known as *strong lensing*. Foreground objects responsible for the local curvature are called *lenses* or *deflectors*, and the background objects emitting the light that gets “lensed” are called *sources*, whatever their nature.

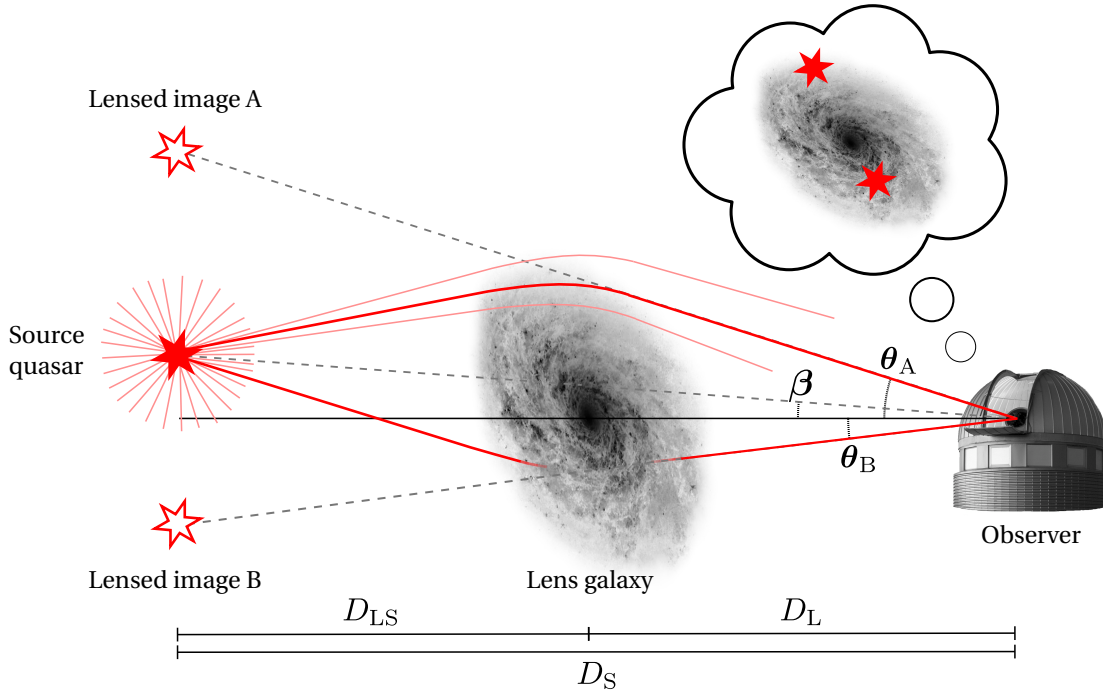


Figure 1.4: Schema of strong gravitational lensing of a distant quasar by a foreground galaxy.  $\beta$  and  $\theta_A$  denote respectively the angular positions of the source and the image A. These angular positions are two dimensional on the plane of the sky. The source is never directly observed:  $\beta$  is an unconstrained parameter that can only be inferred via a lens model reproducing the observed image positions.

This strong lens schema might remind you of the illustration of a common convergent glass

lens. But note that following Equation 1.9, the deflection angle of light rays is larger for rays that come closer to the deflector, as depicted in light red in figure Figure 1.4. Light rays that seem to originate from these lensed images diverge. Hence gravitational lensing does not form a “real” image in the plane of the observer, following the terminology of conventional optics. Instead, we see *virtual* images of the source, at different positions on the sky, when looking through the lens.

If a source is perfectly aligned behind a point mass, or behind a lens whose mass distribution is circularly symmetric with respect to the line of sight, the source will be seen as a ring around the lens. The dimensionless angular radius of this so-called *Einstein ring* is the *Einstein radius*

$$\theta_E = \sqrt{\frac{4GM}{c^2} \frac{D_{LS}}{D_L D_S}}, \quad (1.10)$$

where  $M$  is the mass of the lens enclosed in the cylinder described by the ring, and  $D_{LS}$ ,  $D_L$  and  $D_S$  are the angular diameter distances between the source, the lens, and the observer, as indicated in Figure 1.4. Trough this equation, the mass of the deflector within this cylinder can be precisely determined from the measured Einstein radius, provided that the involved distances are known. In practice, such a perfectly symmetric case is seldom observed. When the source-lens alignment is slightly broken, when the lens is an ellipsoid, or when the system is perturbed by the gravitational influence of additional external masses, the ring splits up into several magnified and stretched images of the source. For an example, see the case of J0919+2720 in Figure 5.6 (page 121, left panel) of this thesis. However, the distance between these multiple images remains about twice the Einstein radius, especially when lensed by the mass density profiles of galaxies. Hence the Einstein radius is a characteristic angle of any given strong lens.

The strong gravitational lens discovered by Walsh et al. (1979) has a *quasar* as source. From the observational point of view, quasars appear *point-like*: they cannot be spatially resolved by telescopes. Quasars follow a broad redshift distribution – typically  $z \approx 0.5$  to 3 – and emit a phenomenal amount of electromagnetic radiation across the spectrum. Different quasar variants can be observed from gamma-ray to radio wavelengths, and they are typically much brighter than entire galaxies. In the optical, quasars are characterized by broad emission lines, facilitating their spectroscopic redshift determination. Furthermore, quasars vary in luminosity over a broad range of temporal scales (e.g., MacLeod et al. 2010), sometimes as fast as a few hours (e.g., Stalin et al. 2005) at optical wavelengths. This is evidence that the light emitting regions must be compact. All these observations led to a widely accepted physical model: quasars result from the accretion of matter on supermassive black holes, located at the center of their *host galaxies*. Quasars are an extremely luminous subcategory of Active Galactic Nuclei (AGN). In the scope of gravitational lensing, their small size has important consequences.

A point-like source is a source whose apparent size on a recorded image is only due to the limited resolution of the telescope, which smears the “point” into a bell-shaped Point Spread Function (PSF). If such a point-like source lies behind a gravitational lens, the magnified and stretched (*sheared*) multiple images of the source will still be very small, and likely remain unresolved. As a consequence, multiple *point-like* images of the source are seen, and only the

brightness of these images relates their magnification. This is precisely the case for quasars. On the order of 100 strongly lensed quasars are known<sup>6</sup>, and by far the most common multiple image configurations are so-called “doubles” (2 observed images) followed by the “quads” (4 observed images) which result from a better source-lens alignment. Figure 1.5 shows the quadruply lensed quasar RX J1131–1231, seen by the Hubble Space Telescope (HST). Note how the 4 images of the quasar, labeled A, B, C and D are round PSFs, while the *host galaxy* of the quasar, an extended source, is stretched into numerous arcs. The object in the middle, marked G, is the lens galaxy. Appendix A briefly presents a simulation software that can be used to reproduce all multiple image configurations of strong lensing, by moving a source “behind” this particular lens galaxy.

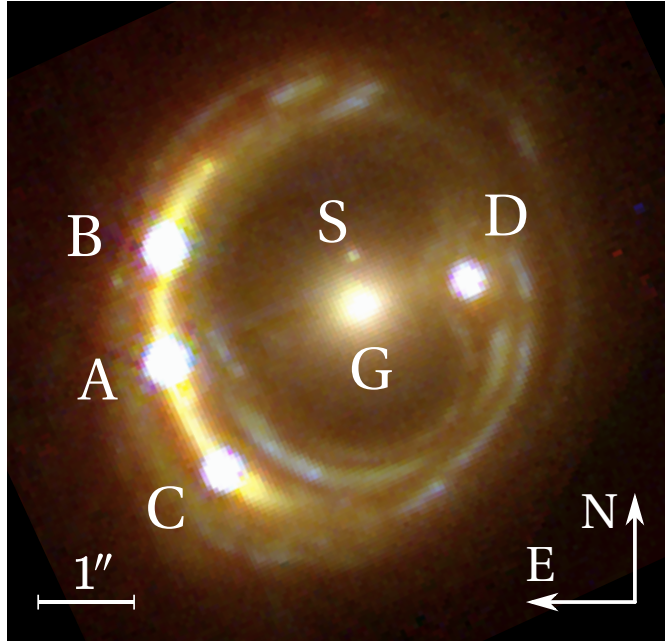


Figure 1.5: HST image of the quadruply lensed quasar RX J1131–1231. The multiple quasar images are labeled A, B, C and D. The letter G indicates the primary lens galaxy. The object marked S is likely a satellite of G (Claeskens et al. 2006). The color combination is made from ACS F555W, ACS F814W and NICMOS2 F160W images. Image courtesy of Dominique Sluse.

### 1.2.2 Time delays, and their link to $H_0$

An astonishing yet trivial property of strong lensing is that the light travel time from the source to the observer is generally not identical for the different images. In other words, we not only see several images of one same object, but we also see this object, in each image, at different moments of its history. Given a physical model of the lens, the light travel time for each image can be computed. Gravitational lensing can in fact be formulated in terms of this light travel time, by associating an effective index of refraction  $n$  to the gravitational potential of the lens, in close analogy to conventional optics.

---

<sup>6</sup>An exhaustive database of strong lenses will soon be available at <http://masterlens.astro.utah.edu/>.

The *excess* light travel time, with respect to the unlensed case, of photons originating from a source at  $\boldsymbol{\beta}$  and reaching the observer from the direction  $\boldsymbol{\theta}$  (see Figure 1.4) is given by

$$t(\boldsymbol{\theta}, \boldsymbol{\beta}) = \frac{D_{\Delta t}}{c} \left[ \frac{(\boldsymbol{\theta} - \boldsymbol{\beta})^2}{2} - \psi(\boldsymbol{\theta}) \right]. \quad (1.11)$$

The expression in brackets has two components. The first term, proportional to  $(\boldsymbol{\theta} - \boldsymbol{\beta})^2$  is called the *geometric delay*, and is due to the increased length of the deflected path, as perceivable in Figure 1.4. The second term, known as *Shapiro delay*, is due to time dilation by the gravitational field of the lens, a direct consequence of general relativity. Photons traveling through a gravitational potential seem delayed. For weak fields this delay is directly proportional to the potential, and indeed,  $\psi(\boldsymbol{\theta})$  corresponds to the *lensing potential*  $\psi$  at the position of the images. This lensing potential is a two-dimensional analog to the gravitational potential : its laplacian is proportional to the surface mass density of the lens. Finally,  $t(\boldsymbol{\theta}, \boldsymbol{\beta})$  is directly proportional to  $D_{\Delta t}$ , the so called *time-delay distance* of the given lens system :

$$D_{\Delta t} := (1 + z_{\text{lens}}) \frac{D_L D_S}{D_{LS}}. \quad (1.12)$$

As for the definition of the Einstein radius, the distances  $D_L$ ,  $D_S$  and  $D_{LS}$  are angular diameter distances (see Section 1.1.6). They depend on the redshifts of the lens and the source, and on cosmological parameters – notably the Hubble constant. The time-delay distance  $D_{\Delta t}$  concentrates this cosmological information into one single scalar, which is, given the combination of three angular diameter distances, inversely proportional to  $H_0$ .

Given that we never directly see the source, the above absolute excess light travel time cannot be compared to any observation. However, we can use it to express the relative light travel time difference between two images – say A and B – of the same source. This difference  $t(\boldsymbol{\theta}_A, \boldsymbol{\beta}) - t(\boldsymbol{\theta}_B, \boldsymbol{\beta})$  is the *time delay* between the images:

$$\Delta t_{AB} = \frac{D_{\Delta t}}{c} \left[ \frac{(\boldsymbol{\theta}_A - \boldsymbol{\beta})^2}{2} - \frac{(\boldsymbol{\theta}_B - \boldsymbol{\beta})^2}{2} + \psi(\boldsymbol{\theta}_B) - \psi(\boldsymbol{\theta}_A) \right] \quad (1.13)$$

The interest in this time delay is visualized in Figure 1.6. The time delay is a directly measurable property of a strong gravitational lens. Furthermore, it has a dimension: it can for instance be expressed in days. This distinguishes the delay from the other lensing observables, such as angular image positions, magnification ratios, and redshifts, which are all dimensionless. Figure 1.6 illustrates that these dimensionless observables are not sensitive to the overall physical scale of a gravitational lens system. If we do not know the Hubble constant, which connects redshifts to distance, the measurement of source and lens redshifts only yields their relative distance. But the time delay *does* depend on the physical distances. Equation 1.13 shows that it is proportional to the overall physical scale, namely to the time-delay distance  $D_{\Delta t}$ . Measured time delays scale a given lens system, and hence the universe in which they are embedded.

Remarkably, using time delay measurements as a probe for  $H_0$  was proposed by Refsdal (1964) no less than 15 years before the discovery of the first extragalactic gravitational lens !

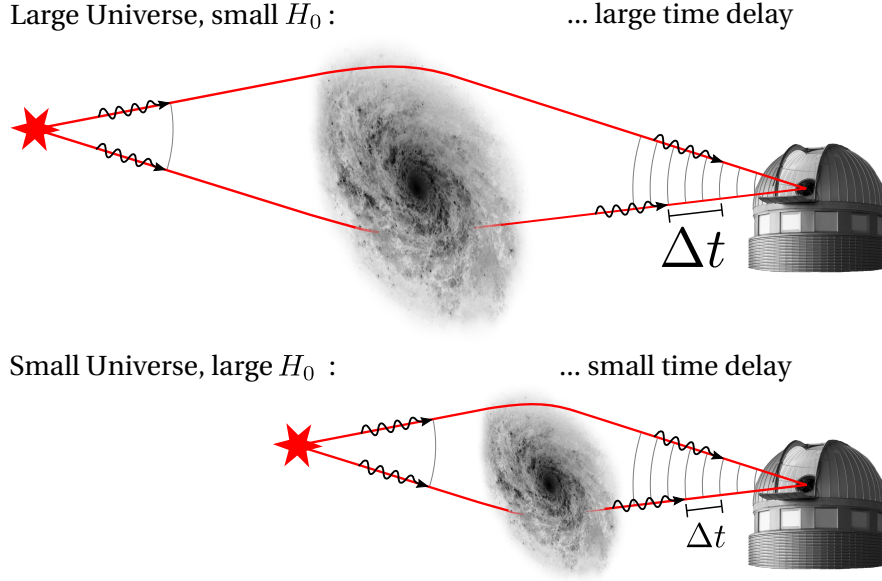


Figure 1.6: Illustration of strong lensing time delays. Disregarding the time delay, the observer cannot tell how large a given lens system is, as the dimensionless observables such as angular image separations do not yield this information. However, the observed time delay is directly proportional to the scale of the system, and inversely proportional to  $H_0$ . Illustration inspired from Narayan & Bartelmann (1996).

Refsdal considered that time delays might be measured for doubly lensed supernovae, whose explosions would be seen twice – once in each image – separated by a couple of months. Multiply imaged supernovae have not yet been observed. But instead, Refsdal’s time-delay method is successfully applied to strongly lensed quasars. Some quasars vary significantly in luminosity on time scales of days. By monitoring the brightness of the lensed quasar images, one obtains *light curves*, i.e., representation of brightness as a function of date (examples are shown at the beginning of Chapter 3). The same quasar luminosity fluctuations may now be seen, shifted in time, in the light curves of the different quasar images. As foreseen by Refsdal, the delays for galaxy-lenses are indeed of the order of a few months.

Let us look in detail at Equation 1.13. Our objective is to measure the time-delay distance  $D_{\Delta t}$ , as it constrains the cosmology ( $H_0$ ) provided that the source and lens redshifts are known. To deduce  $D_{\Delta t}$  from a measured time delay  $\Delta t_{AB}$ , the quantity within brackets must be determined. It contains the source position  $\boldsymbol{\beta}$ , the image positions  $\boldsymbol{\theta}$  (called *astrometry*), and the *difference* in lensing potential  $\psi$  between the image positions. This lensing potential, and the source position  $\boldsymbol{\beta}$ , need to be *modeled* so to reproduce the observed lens. The main difficulties in measuring  $D_{\Delta t}$ , and how to address them, are the following.

- The measurement of time delays  $\Delta t$  between lensed quasar images is not trivial, although in terms of technological effort it is rather cheap when compared to other cosmological probes. These measurements, in order to constrain  $H_0$ , are the foremost objective of the COSMOGRAIL monitoring campaign, subject to Chapters 2 and 3 of this



thesis.

- The difference in lensing potential at the image positions must be well constrained, as any error on this difference directly propagates to  $D_{\Delta t}$ . Galaxy lenses are typically modeled by parametrized elliptical mass density profiles. The radial concentration of such a profile has a direct influence on this lensing potential difference at the position of the images. Unfortunately, while the observed astrometry of the images yields the total mass inside of the Einstein radius, the shape of this radial profile is much harder to constrain: it is subject to degeneracies (see, e.g., Saha 2000; Kochanek & Schechter 2004, for a review). One notable lensing degeneracy is that some amount of the mass responsible for an observed lens may be distributed in form of a homogeneous “mass sheet” across the line of sight. This reduces the lens potential difference between the images, without affecting their astrometry or magnification ratios – that is, without observable consequences at the level of the lensed images. As demonstrated e.g. by Suyu et al. (2012a) and Courbin et al. (2011) (see Chapter 3) and references therein, these problems can however be addressed,
  - using additional information about the mass profile of the lensing galaxy, from stellar dynamics in the this galaxy. Typically, a measured velocity dispersion of the lens probes its mass inside a radius different from the Einstein radius.
  - using the extended arcs and rings formed by the lensed quasar host galaxy to constrain the lens model.
  - using additional information about the mass *external* to the lensing galaxy ( $\kappa_{\text{ext}}$ ) and distributed along the line of sight.
- Finally, a somewhat less severe difficulty is to obtain accurate astrometry  $\theta$  of the images. This can be achieved by deconvolving HST images, resulting in an accuracy of a few milliarcseconds – a task that is also performed in the scope of the COSMOGRAIL collaboration (Sluse et al. 2012; Chantry et al. 2010). Compared to the uncertainties on the time delay measurement and on the lensing potential, the *direct* influence of milliarcsecond astrometric errors on Equation 1.13 is negligible. However such accurate relative astrometry is highly important to constrain the lens model and hence  $\psi(\theta)$ .

Since the discovery of the first lensed quasar SBS 0957+561, time delays for about 20 different lenses have been published. However, the number of *robustly* measured time delays with appropriate error bars is much lower, as can be deduced from the disillusioning reanalysis of 11 light curve sets by Eulaers & Magain (2011). One general reason to be cautious about time delays measured from light curves spanning only 2 or 3 seasons is quasar *microlensing*, presented in the next section.

A recent enumeration of published delay measurements can be found in the article of Paraficz & Hjorth (2010), which presents the latest effort of simultaneously inferring one value for  $H_0$  from all these lenses. Such studies exploit the independence of each different lens to statistically increase the precision of  $H_0$ , instead of performing a detailed study to address the degeneracies at the level of each individual lens. Both (1) this statistical approach applied to a much larger number of lenses, and (2) the meticulous analysis of a smaller number of individual lenses (Suyu et al. 2010; Courbin et al. 2011; Suyu et al. 2012a, Chapter 3 of this

thesis) will allow for percent-level determinations of  $H_0$  (Dobke et al. 2009; Weinberg et al. 2012).

### 1.2.3 Microlensing

The light deflections yielding the multiple strong lensing quasar images as seen on Figure 1.5 result from the *total* gravitational field induced by matter in the lens galaxy. These usually 2 or 4 multiple images of the source will be called "macro-images" in the following paragraphs. As described in the previous section, they are magnified and sheared, but we still perceive them as point-like images given the limited spatial resolution of the observations.

Let us now assume that we could zoom, by a factor  $10^6$  (!), onto one of these macro-images. What would we see ? The narrow bundle of light rays that forms the macro-image has traveled through the outskirts of the lens galaxy, as illustrated in Figure 1.4. On the scale of the width of this bundle, a lens galaxy is not a smooth matter distribution : at least some amount of the mass in this galaxy comes in form of stars. The Einstein radius associated to these individual stars, via Equation 1.10, is of the order of the *microarcsecond* – the angle approximatively subtended by a coin on the Moon. As a consequence, at the assumed phenomenal resolution, we would see the macro-image of the quasar strongly lensed and split into several *micro-images* by the stellar population of the lens galaxy. This view is qualitatively simulated in Figure 1.7, in which a red dot with a diameter of 2 light days and at a redshift of  $z = 0.6$  is seen lensed by stars in a galaxy at  $z = 0.3$ . The overall mass distribution of the lens galaxy magnifies and shears the image (top right panel), while individual stars close to the line of sight act as additional strong lenses and heavily distort this macro-image. This general regime of gravitational lensing, with Einstein radii of microarcsecond scale, is called *microlensing*. When images of a strongly lensed quasar are magnified or demagnified by mass structure in the lens galaxy, as described in this paragraph, one speaks of *quasar microlensing*.

Gravitational lensing has the remarkable intrinsic property that it conserves surface brightness. A camera recording the different scenes of Figure 1.7 would measure the same local intensity of light in all parts of the red areas in *all* four panels. Clearly, there is more red light seen in the bottom right panel than in the top right panel, as the red area got larger due to the distortion. Zooming back at any realistic resolution achievable by telescopes, we do not see these micro-images anymore. All their light is blended into a tiny point-like macro-image. But the *intensity* of this point-like image is affected by microlensing, and this intensity can well be measured even from low resolution observations.

This effect has several fascinating observational consequences. The two main aspects are outlined below.

1. When monitoring the brightness of quasar images over time, the micro-image configurations will change as stars of the lens galaxy move "through" the macro-image. Even if the quasar would be a perfectly stationary and tiny source, microlensing adds perturbations to the light curves as the total magnification changes with time. These perturbations are random and independent for each macro-image of a strongly lensed quasar.
2. Microlensing randomly magnifies different *subregions* of a source in different ways. The

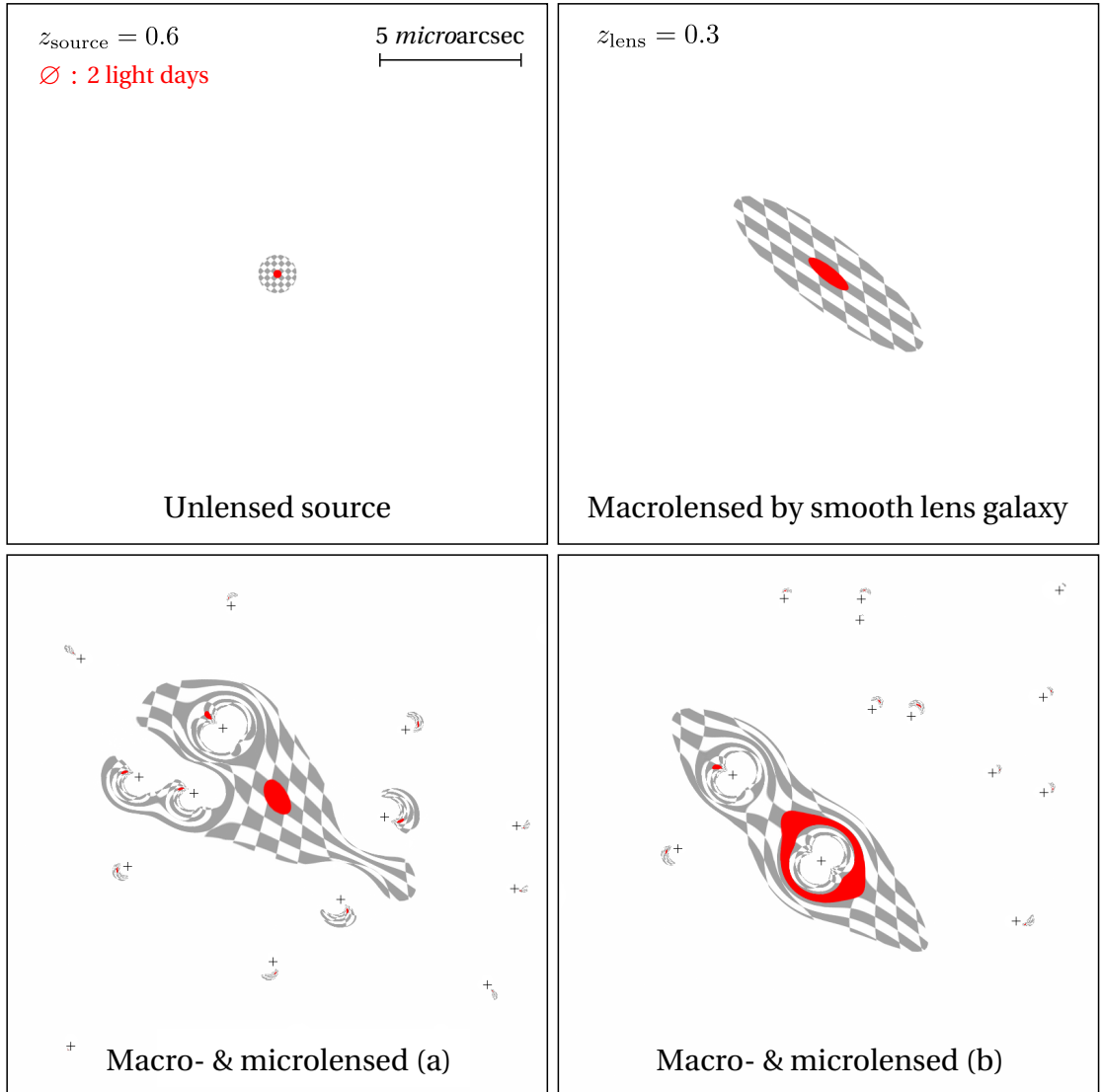


Figure 1.7: Visualization of *quasar microlensing*, that is microlensing of a strongly lensed quasar by stars of the lens galaxy. All four panels share the same exceedingly large scale: we assume here that we can zoom onto one of the two macro-images of Figure 1.4 at a resolution below a *microarcsecond*. In the bottom panels, the image of the source is seen lensed by solar-mass stars (+) of the lens galaxy, instead of a purely smooth potential. Depending on the position of these stars, different parts of the source are magnified by different amounts. While these image configurations are far too small to be spatially resolved by telescopes, we can nevertheless observe fluctuations of the total image brightness, as the stars move through the field.

smaller a given source region, the faster and stronger its magnifications will vary as stars move through the scene. To see why, compare the two bottom panels of Figure 1.7. Between these configurations, there is a large difference in the total magnification of the small, red source, while the total area of the larger checkerboard area is much less affected no matter how the stars are located.

Microlensing perturbations are, at some level, practically omnipresent in observations of gravitationally lensed quasars. From the point of view of time delay measurements, this is a nuisance, as the signal of the intrinsic quasar variability is degraded. The first paper of this thesis, at the end of Chapter 2, addresses this issue by proposing new techniques to accurately measure time delays despite microlensing.

However, quasar microlensing itself is a unique tool to probe both the structure of the source and statistical properties of the mass distribution (stars, dark matter) inside of the lens galaxy. This is a large topic on its own; for a recent review see Schmidt & Wambsganss (2010), and, for example, publications of former LASTRO PhD student Alexander Eigenbrod (Eigenbrod et al. 2008a,b). Section 3.2 of the present thesis briefly presents the inference of the physical size of a quasar, at optical and X-ray wavelengths, obtained through a microlensing analysis.

### 1.2.4 Weak lensing

Weak lensing designates the regime of gravitational lensing in which the images are only *weakly* distorted, and do not form wide arcs or multiple image systems. This happens if the lens mass in front of a source is not concentrated enough to form multiple images. The resulting small distortions cannot be seen on individual sources, as we do not know their unlensed, “intrinsic” shape. However, if an entire population of background sources is available, the distortions can be revealed, either statistically or by local averaging. In practice, galaxies offer such a field of sources, as illustrated in Figure 1.8.

To mathematically describe the weak lensing of a small source in the  $(x, y)$ -plane of the sky, the distortion is locally approximated, at the position of each source, by a linear remapping between the source and the image :

$$\begin{pmatrix} x_{\text{source}} \\ y_{\text{source}} \end{pmatrix} = \begin{pmatrix} 1 - \kappa - \gamma_1 & -\gamma_2 \\ -\gamma_2 & 1 - \kappa - \gamma_1 \end{pmatrix} \begin{pmatrix} x_{\text{image}} \\ y_{\text{image}} \end{pmatrix}. \quad (1.14)$$

The *convergence*  $\kappa$  is the term responsible for the isotropic magnification of the image, and the two components  $\gamma_1$  and  $\gamma_2$  of the *shear* stretch the image anisotropically. Both  $\kappa$  and  $\gamma$  are directly related to the mass distribution responsible for the distortions. Chapter 4 of this thesis presents a method to accurately measure the shape of weakly lensed galaxies in order to reconstruct the shear. As will be discussed in this chapter, weak gravitational lensing affects the entire sky of high redshift sources. For distant quasars and the cosmic microwave background, the average total deflection due to foreground large scale structures is in the order of 2 arcminutes (see e.g. Hanson et al. 2010), that is one fifteenth of the apparent diameter of the Moon !

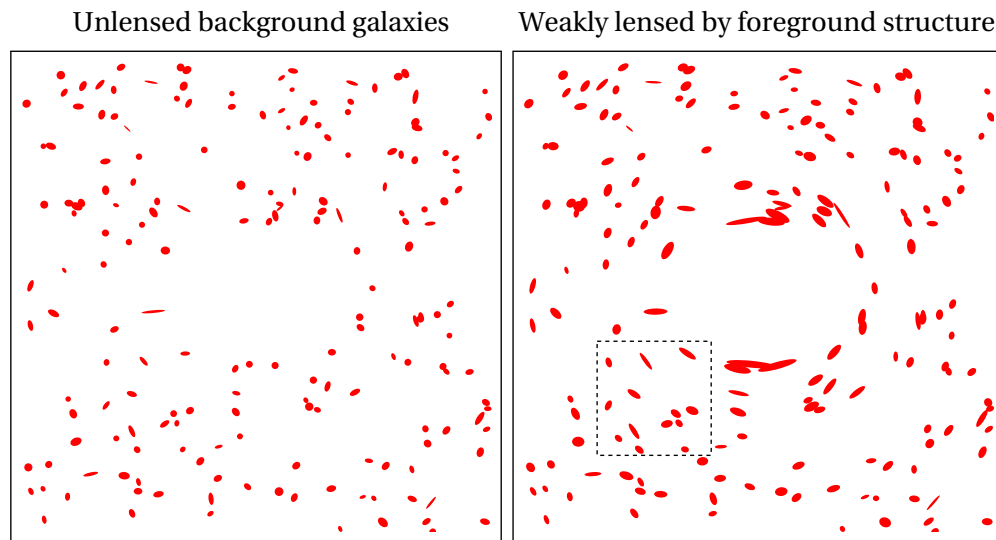


Figure 1.8: Illustration of weak gravitational lensing. The left panel shows an “unlensed” field of randomly oriented background galaxies. In the right panel, gravitational lensing by a foreground mass distorts the images of these galaxies. The lensed galaxies in the dashed square, taken individually, do not disclose that they are weakly lensed. But considered altogether, these galaxies clearly tend to be oriented tangentially to the center of this panel, revealing a foreground mass overdensity at this location. Original illustration by User:TallJimbo / Wikimedia Commons / CC-BY-SA-3.0



## 2 COSMOGRAIL

COSMOGRAIL, the COSmological MONitoring of GRAVItational Lenses<sup>1</sup>, is a monitoring campaign of gravitationally lensed quasars, involving several optical meter-class telescopes. The primary aim of this project is to increase the sample of accurate time delay measurements between the multiple images of these quasars. As elaborated in the introduction to this thesis (Section 1.2.2), time delay measurements constrain the Hubble constant  $H_0$ , and such a standalone inference is highly complementary to other cosmological probes. But several methods to constrain  $H_0$  exist, as reviewed, e.g., in Freedman & Madore (2010). So why use quasar time delays ?

1. The time-delay technique directly probes  $H_0$ . It does not make use of step by step calibrations, such as required to reach the Hubble flow with standard candles.
2. The physics of time delays are well understood, and do not involve any complex astrophysics related for example to dust absorption or metallicities.
3. Considering constraints on the dark energy equation of state, time delays are particularly complementary to other distance measurements. As shown by Linder (2004), the degeneracy between the parameters  $w_0$  and  $w_a$  (see Equation 1.2) from time delays is largely *orthogonal* to the same degeneracy from, e.g., SN Ia. Realistic time delay data from 150 lenses can improve the “equation of state area uncertainty” – a figure of merit for dark energy – of Planck and mid-term supernova surveys by almost a factor 5 (Linder 2011).
4. When compared to the space-based observational efforts to calibrate Cepheids and Type Ia supernovae, measuring quasar time delays is extremely cheap. As COSMOGRAIL shows, measuring accurate time delays can be done from the ground even with meter-class telescopes. Only a relatively modest amount of follow-up observations with large telescopes is required to constrain the lens models.
5. The outlook for this technique is excellent. The cosmological inference from time delays is currently dominated by random errors due to lack of data, not systematics. Measuring more time delay distances will yield better results. At the time of writing, the Dark

---

<sup>1</sup><http://www.cosmograil.org>

Energy Survey (DES)<sup>2</sup> is about to start. According to the predictions by Oguri & Marshall (2010), DES will detect hundreds of new lensed quasars, accessible for monitoring by medium-sized telescopes. Furthermore, the next generation of optical surveys, like the Large Synoptic Survey Telescope<sup>3</sup>, should provide thousands of lenses – including time delay measurements. As stressed by Dobke et al. (2009), these large samples will reduce the importance of lens parameter degeneracies, as the statistical *distributions* of these parameters are better constrained than, e.g., the density profile of a particular lens.

6. The monitoring light curves have high “legacy” value for quasar microlensing studies. They allow to probe the mean stellar mass and the overall stellar mass fraction in the cosmologically distant lens galaxies, and the structure of quasars (Kochanek et al. 2007). Strongly lensed quasars are mandatory for these studies, as the multiple light paths allow to disentangle the microlensing from the intrinsic variability of the quasar.
7. Some redundancy in cosmological probes is needed to check that systematic errors are under control, or, in other words, to allow for unexpected deviations to show up. In this context, it is highly welcome that measurements of  $H_0$  accurate to 1% are now within reach of several methods (Suyu et al. 2012b). Furthermore, time delays are observables that link  $H_0$  to lens models, and this link can be exploited in both directions. As presented by Keeton & Moustakas (2009), time delay *anomalies* would allow to detect dark matter substructure in galaxies.

From the observational point of view, the measurement of time delays by COSMOGRAIL splits into three distinct parts. First, the lenses are *monitored* for several years, by cameras of the involved telescopes. Second, the brightness of each quasar image in each exposure is measured, a process called *photometry* and yielding *light curves*. And third, the time delays between the images are measured from these light curves, using so-called *curve shifting* techniques.

The technical supervision of the monitoring at the Swiss Euler telescope and the development and application of (1) a new COSMOGRAIL photometry pipeline and (2) new curve shifting algorithms constitute my main contribution to these observational aspects of COSMOGRAIL. A description of the monitoring and the photometry is given in Tewes et al. (2012c), which is included in Chapter 3 (page 49) of this thesis. The curve shifting techniques are the subject of a dedicated paper, Tewes et al. (2012b), at the end of this present chapter (page 29).

The next pages give selected additional illustrations of some of these topics, in complement to the research publications.

---

<sup>2</sup><http://www.darkenergysurvey.org/>

<sup>3</sup><http://www.lsst.org/>



## 2.1 Monitoring

The COSMOGRAIL monitoring is an international effort, to which several 1 to 2 meter telescopes are contributing. Lenses in the southern hemisphere are monitored with the 1.2 meter Swiss Euler telescope and the SMARTS 1.3-m telescope, both located in Chile. The monitoring with SMARTS is done by the group of Kochanek et al. (2006), with which COSMOGRAIL has started a productive cooperation, resulting in the largest monitoring campaign of strongly lensed quasars ever conducted.

The Euler telescope (Figure 2.1), completed in 1998, is operated at the ESO La Silla Observatory in close collaboration between the University of Geneva and EPFL. It is mainly dedicated to the discovery and characterization of extrasolar planets. This research is conducted using both the Coralie high-resolution echelle spectrograph and the new EulerCAM imaging instrument, commissioned in September 2010. About one 8th of Euler's observing time goes to the COSMOGRAIL monitoring, in the form of one half-night every 4 days, although this half-night can be spread over several dates. The telescope observes every clear night of the year, and is steered mostly by researchers from the observatoire de Sauverny, who travel to Chile for two-week shifts. The observing instrument, Coralie or EulerCAM, is typically switched several times per night, in a matter of seconds. Our monitoring of gravitationally lensed quasars enormously benefits from this flexibility, and complements very well the time-critical observations of extrasolar planets.



Figure 2.1: The Swiss Euler telescope at the ESO La Silla Observatory in Chile, as revealed by a 75-second exposure taken while the slit of its dome was rotating through the field of view. Image credit: M. Tewes / ESO, with thanks to Amaury Triaud and Vincent Mégevand.

The monitoring in the northern hemisphere is currently conducted by the 2 m Himalayan Chandra Telescope (HCT), and previously involved the 1.2 m Mercator telescope (La Palma, Spain), the 1.5 m telescope of the Maidanak observatory in Uzbekistan, and the 2 m robotic Liverpool telescope, also located at La Palma. Details about these telescopes can be found on the COSMOGRAIL webpage, and in the related publications.

### 2.2 Photometry

The photometric measurement of the quasar images and the reference stars is done following the MCS deconvolution algorithm (Magain, Courbin, & Sohy 1998), which, for this particular purpose, can be seen as a form of “PSF-fitting”. This is a two step process. First, a model of the point spread function (PSF) of each exposure is constructed, by fitting field stars with a hybrid (both parametric and pixelated) model. Second, one single model for the target (lens) is simultaneously fitted to all exposures, convolved with the respective PSFs. This algorithm is specifically designed with highly blended sources in mind. But even in the case of an isolated point source, the resulting photometry is significantly better than what can be achieved by aperture photometry, as the additional information of the PSF of the exposure is exploited.

Figures 2.2 and 2.3 show control visualizations of PSF construction and the deconvolution of the lens, respectively. These images are automatically produced by the COSMOGRAIL photometry pipeline, and allow for a fast and efficient visual inspection of the photometric process, even for thousands of exposures. They were particularly useful in the development phase of the pipeline.

### 2.3 Curve shifting

The three curve shifting techniques of Tewes et al. (2012b), including the associated Monte Carlo uncertainty estimation, are implemented in form of a `python` package. This software is publicly available (Figure 2.4), as its interest goes beyond COSMOGRAIL. The release of this software, together with the light curves, also makes our measurements at least in part easily reproducible.

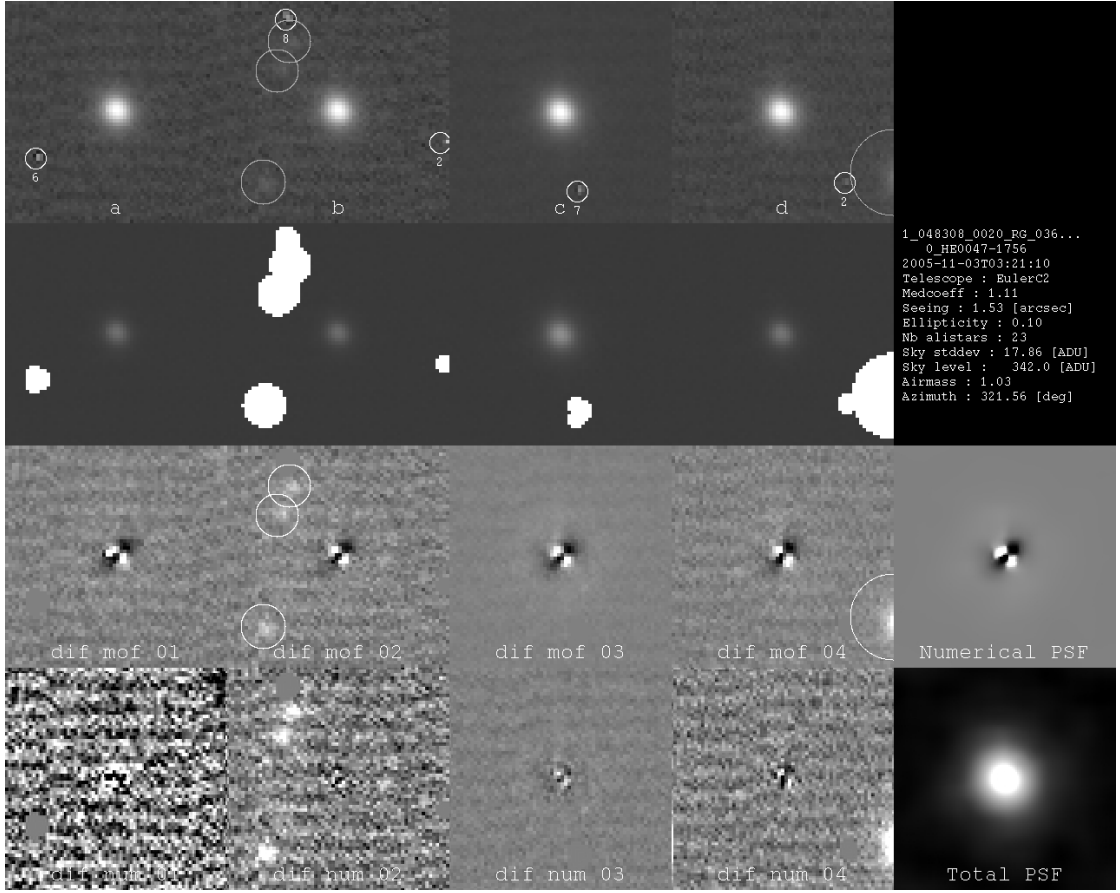


Figure 2.2: Example of a control visualization of the PSF construction, in the case of an Euler C2 image of the lens HE 0047–1756. The top row shows four field stars. Cosmic ray hits are automatically detected in each exposure, and get masked together with manually selected neighboring sources. The second row shows the associated noise maps, and the third row shows the residuals after subtraction of the simply parametrized component of the PSF model. These residuals share a very similar structure, which is modeled by a wavelet-regularized fine pixel grid. Importantly, the final residuals (bottom row) do not share a common structure anymore. They result from noise and from PSF evolution across the field of the telescope. The wavy aspect of the background in this particular example image is due to electronic interferences during the CCD readout, a problem that has been solved since then.

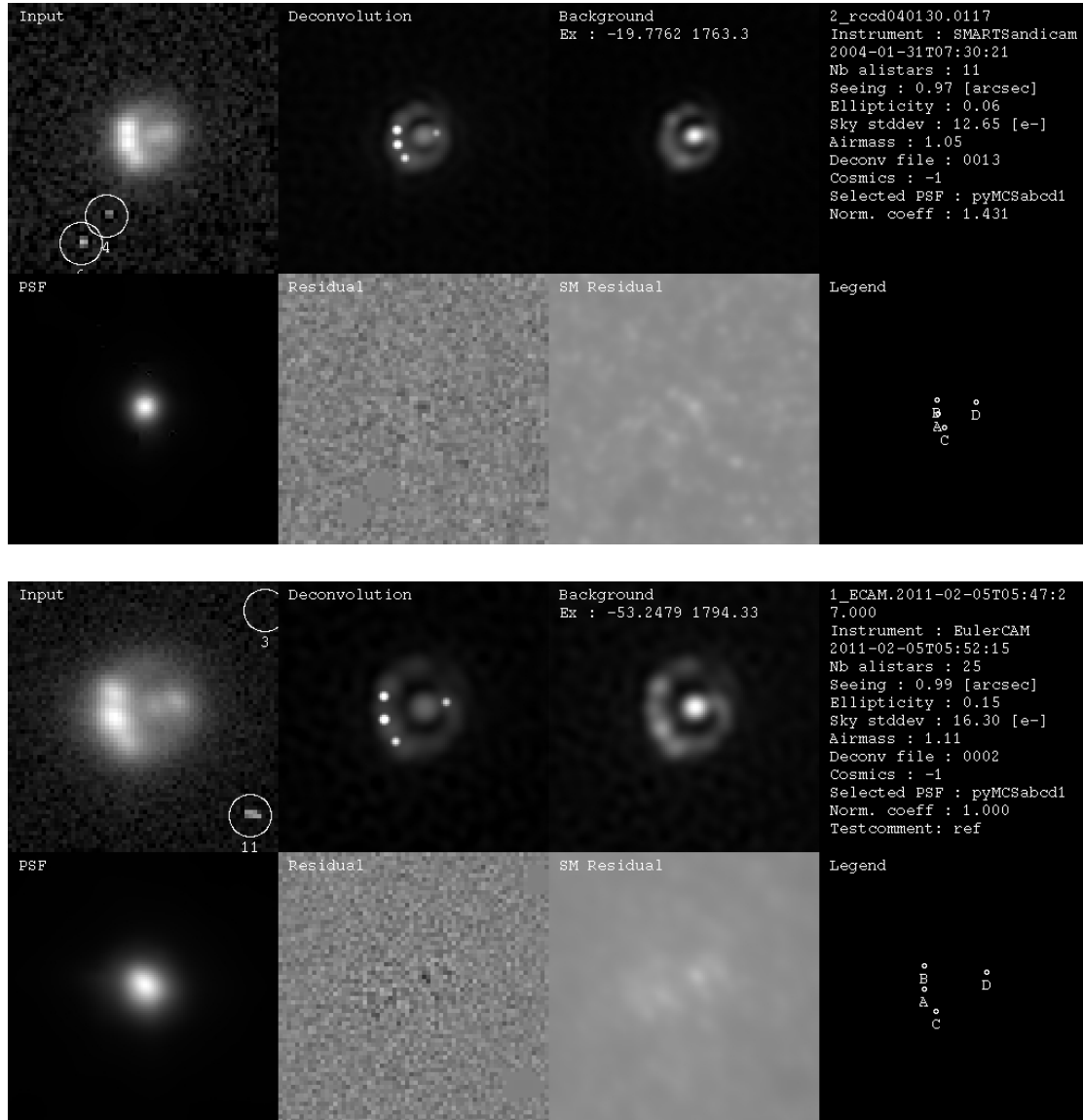


Figure 2.3: Example of deconvolution control visualizations, for two exposures of RX J1131-1231 by the SMARTS 1.3-m ANDICAM (top,  $0''.369$  pixels) and EulerCAM (bottom,  $0''.215$  pixels) instruments. The FWHM of the images is of  $1''$  in both cases. The rightmost panel in the top row shows the pixelated deconvolution component, that represents the lens galaxy and the Einstein ring.

pycs 1.0 documentation »

next | modules | index

## PyCS : Python Curve Shifting

### About

PyCS is a software toolbox to estimate time delays between multiple images of strongly lensed quasars, from resolved light curves such as obtained by the [COSMOGRAIL](#) monitoring program. The methods implemented in PyCS are described in our paper [COSMOGRAIL XI: Techniques for time delay measurement in presence of microlensing](#) (Tewes et al. 2012).

PyCS is not a standalone program; it comes in the form of a python package called `pycs`, and heavily depends on `numpy`, `scipy`, and `matplotlib`. The `pycs` package defines a collection of classes and high level functions, that you can *script* in a flexible way. PyCS makes it easy to compare different point estimators (including your own) without much code integration.

If you have already read our paper, you might want to proceed with [Download & Installation](#), or the [Tutorial](#).

### Questions / Feedback

Don't hesitate to contact us, for instance via email at [malte.tewes at epfl dot ch](mailto:malte.tewes@epfl.ch) !

### Contents

- Download & Installation
  - Dependencies
  - Download
  - Installation
- Tutorial
  - 1. Generalities
  - 2. The lightcurve object
  - 3. Matching telescopes
  - 4. First steps with microlensing
  - 5. Curve shifting, finally
  - 6. Drawing synthetic light curves
  - 7. Shifting synthetic curves & error analysis
  - 8. Demonstration scripts
  - 9. Tips and Tricks, code snippets
- Autogenerated Full API
  - `pycs` Package
  - Subpackages
- Lists of todos
- Building this documentation

pycs 1.0 documentation »

next | modules | index

© Copyright 2012, COSMOGRAIL. Created using [Sphinx](#) 1.1.3.

Figure 2.4: Website of the COSMOGRAIL curve shifting techniques, which provides documentation and a tutorial. The software is available at <http://www.cosmograil.org>.



# COSMOGRAIL: the COSmological MONitoring of GRAVitational Lenses

## XI. Techniques for time delay measurement in presence of microlensing

M. Tewes, F. Courbin, and G. Meylan

Laboratoire d'astrophysique, Ecole Polytechnique Fédérale de Lausanne (EPFL), Observatoire de Sauverny, CH-1290 Versoix, Switzerland  
e-mail: malte.tewes@epfl.ch

Received ; accepted

### ABSTRACT

Measuring time delays between the multiple images of gravitationally lensed quasars is now recognized as a competitive way to constrain the cosmological parameters, well complementary with other cosmological probes. This requires long and well sampled optical light curves of numerous lensed quasars, e.g., as obtained by the COSMOGRAIL collaboration. High-quality data from our monitoring campaign calls for novel numerical techniques to robustly measure the delays as well as the associated random and systematic uncertainties, even in presence of microlensing variations. We propose three different point estimators to measure time delays, that are explicitly designed to handle light curves with extrinsic variability. These methods share a common formalism, which enables them to process data from  $n$ -image lenses. As the estimators rely on significantly contrasting ideas, we expect them to be sensitive to different bias sources. For each method and data set, we empirically estimate both the precision and accuracy (bias) of the time delay measurement using simulated light curves with known time delays that closely mimic the observations. Eventually, we test the self-consistency of our approach, and we demonstrate that our bias estimation is serviceable. These new methods, including the empirical uncertainty estimator, will represent the standard benchmark for the analysis of the COSMOGRAIL light curves.

**Key words.** Methods: data analysis – Gravitational lensing: strong – cosmological parameters

### 1. Introduction

In the era of precision cosmology, in which a concordance model seems to fit independant observations, it is of utmost importance to both confront and combine all possible methods that constrain cosmological parameters. Confronting them yields an invaluable cross-check of the methods and the model. Combining them allows to break the degeneracies inherent to single techniques. Probes including baryonic acoustic oscillations, weak lensing, supernovae, and cosmic microwave background measurements fit exactly in this context.

Also among these probes is the so-called "time-delay method", first proposed by Refsdal (1964) to measure cosmological distances independently of any standard candle. In practice, the method uses strongly lensed quasars with significant photometric variability. Photons emitted by the source quasar propagate towards us along different optical paths, resulting in multiple images. The light travel times associated to these images differ due to (i) the different path lengths, and (ii) the different Shapiro delays induced by the gravitational field of the lensing galaxy. As a consequence, the same quasar variability is seen with distinct time shifts in the light curves of the multiple quasar images. This paper presents methods to infer the relative time delays between the quasar images, from such resolved, i.e. unblended, light curves.

Measured time delays, in combination with deep HST imaging and dynamical information on the lensing galaxy lead to competitive measurement of the Hubble constant  $H_0$  (e.g., Suyu et al. 2009, 2010). The complementarity between quasar time delays and several other cosmological probes has been illustrated

recently by Linder (2011) who points out that the dark energy figure of merit of a combination of Stage III experiments is improved by a factor of 5 if 150 quasar time delays are added. This also holds if the Universe is not assumed to be flat. It is noteworthy that adding this time delay information is very cheap compared to other Stage III or IV projects.

The COSMOGRAIL collaboration has now gathered almost a decade of photometric points for about 30 lensed quasars. With such data, the time delays can in most cases clearly be seen "by eye". The data analysis is not anymore about sorting out which time delay is the best among several plausible yet incompatible possibilities, but rather to perform an accurate measurement of the delay that can be reliably used for cosmology. New *curve shifting techniques* must be devised to extract the delays from such curves, which sometimes include a thousand points and typically display substantial microlensing variability due to stars of the lensing galaxy.

In this paper we present three independent curve shifting algorithms that can deal with extrinsic variability. Our motivation behind the development of *several* techniques is to provide a range of methods that rely on different principles. While the methods might not be free of systematics, we expect them to be biased in different ways, and we devote a large part of this work to the estimation of comprehensive error bars. Comparing the results from different curve shifting techniques will allow us in particular to systematically cross-check our quantification of the biases.

Our paper is structured as follows: Section 2 gives an overview of features to be expected in light curves, most of them

complicating the time delay extraction problem. We then present the point estimation formalism that is common to our curve shifting techniques in Section 3. Sections 4 to 6 describe the three techniques, and we explain how we consistently compute error bars for each time delay and technique in Section 7. We confront our techniques as well as the associated uncertainty estimates in Section 8, using a set of simulated light curves with known time delays. Finally, we present a summary and our conclusions in Section 9.

## 2. Light curves of lensed quasars

The COSMOGRAIL monitoring program obtains decade-long light curves from 1-2 meter class telescopes (e.g., Courbin et al. 2011). This data is reduced in a homogeneous way using deconvolution photometry. In the following we enumerate properties and effects that will or might be observed in light curves from such ground based optical observations.

1. **Sampling and season gaps:** the data have irregular sampling, spaced on average by 3-4 days for typical COSMOGRAIL curves. By construction of the light curves, all quasar images of a lensing system are observed at the same epochs. The sampling can show some amount of periodicity on the scale of one day, as the targets tend to be observed always at optimal airmass. Almost all light curves are also affected by gaps of 2 to 5 months, corresponding to a period of the year where the lens is not observable.
2. **Time delays:** by definition, the time delays produce a time-shifted version of the original variability curve of the source quasar. These delays range from hours to years. Depending on the length of the delays and the non-visibility gaps, the intrinsic light curve of the quasar source may be fully or only partially sampled by the observations. The size of the “overlap” regions, in which several quasar images follow the same intrinsic source variability, strongly varies from one lens to another.
3. **Macrolensing image flux ratios:** the different strong lensing magnifications, as well as possible absorption by the lens galaxy or lensing perturbations by its satellites, yield stationary flux ratios between the lensed quasar images. As the light curves are usually manipulated in magnitude scales, this translates into magnitude shifts between the curves.
4. **Variable microlensing:** stars moving in the lensing galaxy act as secondary lenses that induce independent flickering of the light curve of each image. While this effect is interesting in itself as a tool to zoom on the lensed quasar (e.g., Kochanek et al. 2007; Eigenbrod et al. 2008a,b), it is an important complication in time delay determinations. Microlensing variations can occur on a broad range of time-scales. We will refer to *slow* microlensing when speaking about any extrinsic variability that happens on time scales significantly larger than the intrinsic variability of the quasar. In extreme cases, microlensing can dominate the intrinsic variability of the quasar at all observable scales, preventing us from measuring time delays (e.g., Morgan et al. 2012).
5. **Variable source structure:** the light magnification by microlensing depends on source structure and size, i.e., microcaustics due to stars may occur on spatial scales comparable in size with the quasar. In other words, in each source image, microlensing predominantly magnifies different parts of the source. As the total intrinsic luminosity of the quasar fluctuates, the light emitting region might physically change in shape and size, on the same time scales. This can introduce

mismatch between the light curves, that correlates with the intrinsic variability of the quasar. In particular, intrinsic variability patterns might be seen with different amplitudes in the light curves (see Barkana 1997, also for a curve shifting method that tackles this issue).

6. **Spurious additive flux:** the photometry of the quasar images might suffer from light contamination by the lensing galaxy, or by the lensed images of the quasar host galaxy, resulting in constant additive shifts in *flux* (not in magnitude) in the light curves. If in addition the photometric points are obtained from different telescopes or instruments, i.e., different resolutions, filters and CCDs, these flux shifts might well be different for each setup.
7. **Flux sharing:** this occurs in narrow blends of quasar images. The effect is due to the limited ability of photometric methods in separating the flux of individual images in such blends: while the total flux of the blend is very well measured, one observes random transfer of flux between the components, leading to measurable anticorrelated “noise” in the light curves. This problem is accentuated by bad seeing conditions.
8. **Photometric calibration errors:** positively correlated “noise” between the light curves, due to noise/inaccuracies in the photometric normalization, i.e. magnitude zero point, of each observing epoch. This normalization is carried out using stars in the field of view. Small variability of some of the considered stars, as well as colour terms that are unaccounted for, can contribute to errors in the relative flux calibration of the CCD frames.

None of these effects is anything new. They affect all past and present optical monitoring programs. However, their significance increases with the quality of the data.

When considering only points 1 to 3 of the above, the problem of extracting time delays from noisy light curves is easy to formulate, as it literally corresponds to “curve shifting” along the time and magnitude axes. A large variety of methods have been proposed to tackle the problem, from cross-correlations to simultaneous model fits. Hirv et al. (2011) provide an overview of the different existing approaches, and present an algorithm based on the optimal prediction technique by Press et al. (1992). Recent works focusing on the statistical tools include a bayesian estimation scheme (Harva & Raychaudhury 2008), and a kernel-based approach combined with an evolutionary algorithm (Cuevas-Tello et al. 2010).

Only few of the existing techniques address the problem of extrinsic variability due to microlensing, or at least acknowledge this variability in their time delay uncertainty estimation. This can be attributed to the lack of long light curves of sufficiently high quality to clearly exhibit extrinsic variability. If incorporated, models for microlensing variability were kept very simple (e.g., linear trends). A notable exception is the method of Morgan et al. (2008), which uses a *physical* microlensing model in a bayesian formalism (Kochanek 2004). However, the latter has a high computational cost, prohibitive in the case of decade long curves of quadruply lensed quasars.

The methods presented in the following sections use pragmatic mathematical models to represent extrinsic variability. In this paper we are not interested in any modeling of microlensing but rather want to minimize and estimate its effect on the time delay measurement. Our methods should not be used to evaluate the odds of mutually exclusive time delay measurements, which often result from insufficient data. A noticeable example of such a situation is the decade-long controversy about two compet-



ing value of the time delay of Q 0957+561 (Walsh et al. 1979), measured in the optical ( $\Delta t = 415 \pm 20$  days) by Vanderriest et al. (1989) and in the radio ( $\Delta t = 513 \pm 40$  days) by Lehar et al. (1992). The debate was closed by Kundic et al. (1997) using additional photometric measurements, as opposed to refined methods. A more recent example is the delay measurement of HE 1104-1805 (see, e.g., Gil-Merino et al. 2002; Pelt et al. 2002). In our opinion the reliability of time delay measurement techniques has often been overestimated, especially when insufficient data could not hint at the presence of potential extrinsic variability.

### 3. Curve shifting through point estimators

All three curve shifting techniques presented in this paper are *point estimators*; they can be seen as functions that take  $n$  light curves as input ( $n \geq 2$ , usually 2 or 4) and return  $n$  corresponding *time shifts*  $\tau$ , one for each curve. These optimal time shifts minimize the mismatch between the common intrinsic quasar variability features of all the light curves. Of course, the individual time *shifts* are not informative, but they directly translate into unambiguous time delay estimations between each pair of curves:

$$\Delta t_{XY} = \tau_Y - \tau_X \quad (1)$$

Hence, time shift estimates obtained from  $n$  light curves of a lens system yield  $n(n-1)/2$  dependent – and consistent – time delay estimations. Note that this would naturally generalize to probability distributions instead of point estimates.

By construction, this trivial time shift formalism avoids the selection of any reference curve with respect to which  $n$  independent delays would be expressed. This is crucial as it can well be that, for example, strong extrinsic variability in quasar image A prevents us from measuring the delays  $\Delta t_{AB}$  and  $\Delta t_{AC}$ , while the delay  $\Delta t_{BC}$  can be well determined. Furthermore, methods complying with this formalism shift all four light curves of quad lenses simultaneously. This is a strong advantage especially in presence of extrinsic variability, as using all curves constrains the intrinsic variability much better than a pairwise processing.

Importantly, we will also exploit the common formalism of our point estimators by estimating their variance and bias in exactly the same way (Section 7).

Before describing the three methods, we underline that our point estimators all rely on iterative nonlinear optimization algorithms. As a consequence, they all show a certain amount of dependence upon the choice of initial guesses for the time shifts. For each lens system to be analysed, we systematically evaluate this dependence by running our methods a few hundred times on the exact same observed light curves, starting from initial shifts randomly selected in a range of generally  $\pm 10$  days around a plausible solution. We call the variance of the resulting monomodal distributions of time delays the *intrinsic variance* of a delay estimator applied to the particular set of curves. We will illustrate this in Section 4. In principle this intrinsic variance can be made arbitrarily small, by increasing the robustness and precision of the optimizations. In practice, a compromise with CPU cost has to be found. We have implemented our methods so that their intrinsic variance is significantly smaller than the other sources of error. In any case, the intrinsic variance will be part of the total uncertainty evaluation. Furthermore, we will always use the mean of these distributions as our best time delay estimations between observed light curves.

## 4. Method 1: simultaneous spline fit

Our first method fits a single continuous model to all data points of the light curves, simultaneously adjusting time and magnitude shifts between these curves so to minimize a  $\chi^2$  fitting statistic between the data points and the model. We will designate this common model as *intrinsic*, even when in practice microlensing might prevent us from getting access to the pure intrinsic variability of the source quasar. The idea of fitting such a single model to shifted light curves defines a whole family of existing time delay measurement methods. These techniques differ by the mathematical representation of the intrinsic curve; for instance, Press et al. (1992) use a Gaussian process, Lehar et al. (1992) use Legendre polynomials, Barkana (1997) uses cubic splines with equidistant knots, Burud et al. (2001) use a regularized numerical model, Cuevas-Tello et al. (2006) use a linear combination of Gaussian kernels, and Vakulik et al. (2009) use a linear combination of sinc functions.

In presence of independent “extrinsic” variability such as slow quasar microlensing, light curves will not adequately overlap for any shifts in time and magnitude. It is easy to conceive that mismatch of this type can lead to strongly biased time delay estimations. It is therefore mandatory to explicitly model the extrinsic variability, to the price of an increased number of free parameters. For example, to represent the microlensing in their high quality light curves of the lensed quasar HE 0435-1223, Kochanek et al. (2006) use independent quadratic polynomials for each season.

Models representing the relative extrinsic variability act similarly to high-pass filters on the data. If these models are as flexible as the intrinsic curve, they can compensate for wrong time shifts, and the information of the time delay is lost. This is our main motivation in proposing a new method that tries to *locally* adapt the flexibility of the models to the peculiarities of the curves.

### 4.1. Free knot splines: the principle

We use so-called *free knot* B-splines to represent both the intrinsic and the extrinsic variability of the light curves. A spline is a piecewise polynomial function, and its knots are the locations where the polynomial pieces connect. We will only consider splines of degree 3, i.e., with continuous second derivatives all across the curves. For these free knot regression splines, not only the polynomial coefficients but also the knot positions are seen as free variables to be optimized. These splines yield significantly better fits than uniform splines, for a given number of knots. Furthermore, they do not introduce any arbitrary discrete grid in the model, which is of high importance for our application. Ideally we want our models to be shift-invariant in terms of their ability to fit any given pattern.

In the case of fixed knots, finding the unique least-squares spline approximation to some data points is a linear problem. This property does not hold for free knot splines: optimizing the knot positions to minimize the  $\chi^2$  requires nonlinear parameter estimation. The nonlinear optimization is particularly difficult, as the motion of the knots leads to many local optima and stationary areas in the parameter space.

Molinari et al. (2004) present an efficient algorithm named “Bounded Optimal Knots” (BOK) to optimize the knot locations of least-squares spline approximations. The authors recall that fitting a free knot spline is a problem that can be separated in a linear and a nonlinear part (Golub & Pereyra 1973). For any given knot configuration, the computation of the corresponding

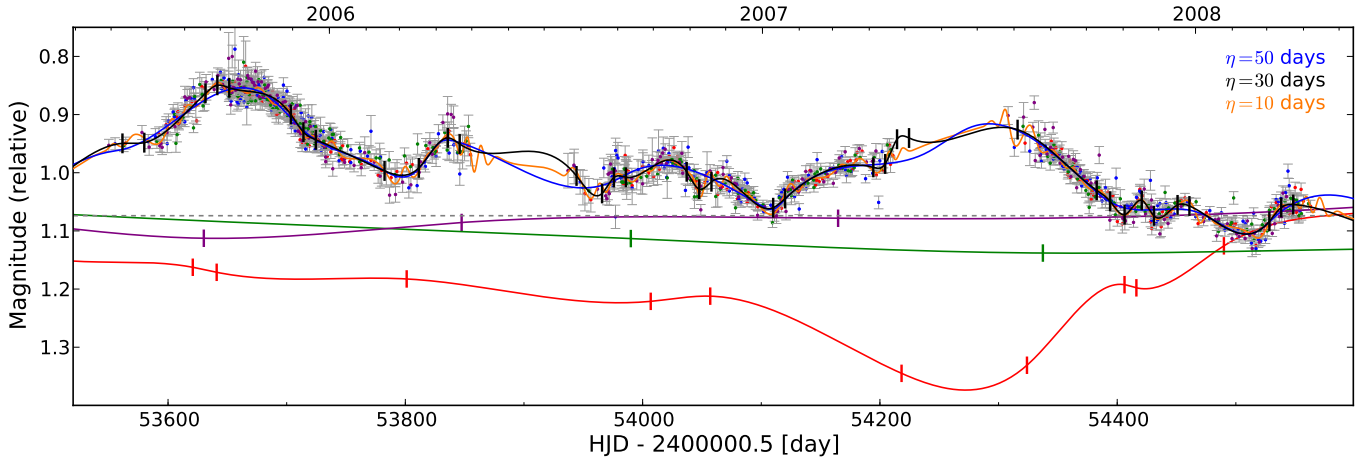


**Fig. 1.** Illustration of the free knot spline technique. The data points are shifted COSMOGRAIL light curves of the quadruply lensed quasar HE 0435-1223, published in Courbin et al. (2011). A reasonable spline representing the intrinsic variability is shown in black (initial knot step  $\eta = 30$ ); knots are shown as vertical ticks. The red, green, and violet splines represent the relative extrinsic variability corrections, applied to the observed light curves A, C and D (respectively), so that they match to the common intrinsic spline. These extrinsic splines are plotted relative to the dashed grey line. The optimization starts with uniformly distributed knots; note how the knots tend to migrate to areas in which they are required by well constrained patterns of the data. The blue and orange curves are alternative intrinsic splines (shown without knots to avoid clutter) with inadequate knot densities of  $\eta = 50$  and 10 (see text).

optimal spline *coefficients* remains linear, and thus fast – in our case using `scipy`’s wrappers around FITPACK (Dierckx 1995). The main idea of BOK is to wrap the linear coefficient computation inside an iterative *bounded* optimization of the knots. The bounded optimization guarantees a well-defined minimal distance between the knots, by keeping them confined into disjoint windows. This scheme avoids the “coalescence” (i.e., superposition) of knots, that would correspond to unwanted discontinuities in the derivatives of the spline. Following an idea of the *Evolutionary BOK* algorithm (also described by Molinari et al. 2004) we update the bounds of the windows once the knot locations have been robustly optimized, and iteratively repeat the process. This mechanism effectively pushes the window bounds to follow their knots, yet always ensuring a minimal knot distance.

Fitting a single spline to fixed data points is only a fragment of the curve shifting problem; our model for the light curves not only consists of a common intrinsic spline, but also of several independent extrinsic splines. In addition, to make our curve shifting technique efficient, we adjust the time shifts between the curves simultaneously with the splines, instead of performing independent fits for different trial delays. In mathematical terms, we aim at finding the global minimum of

$$\chi^2 = \sum_{i=1}^n \sum_{j=1}^{N_i} \frac{[m_{ij} - s(t_{ij} + \tau_i) - \mu_i(t_{ij})]^2}{\sigma_{ij}^2} \quad (2)$$

in which  $n$  is the number of light curves with  $N_i$  photometric points ( $t_{ij}, m_{ij} \pm \sigma_{ij}$ ),  $\tau_i$  are the time shifts,  $s$  is the intrinsic spline and  $\mu_i$  are the extrinsic splines.

We minimize this  $\chi^2$  in an iterative process, in which the splines and the time shifts get optimized one after the other, using custom strategies for each parameter. Several formal difficulties arise as the “footprint” of the mixed data points evolves when the time shifts are modified; we have for instance to stretch the knot locations so that they follow the extent of a spline’s domain. For details of the admittedly intricate but modular optimization procedure, we refer the reader to the source code.

#### 4.2. Free knot splines in practice

In Fig. 1, we show 3 seasons of a spline fit obtained for the light curves of the quadruply lensed quasar HE 0435-1223 (Courbin et al. 2011). The intrinsic spline, going through the shifted data points, is shown in black. The red, green, and purple splines illustrate extrinsic variability for which the data points have been corrected (see caption). Vertical ticks across the splines indicate the knot locations. For a quad lens with 500 points on each curve, 100 knots for the intrinsic spline, and 50 knots (in total) for the extrinsic splines, the fit converges in less than a minute on a single ordinary CPU.

Each spline is parametrized by its knot epochs and associated polynomial coefficients. The curve shifting starts with equidistant knots, and flat splines. Before running the optimization, one has to choose a number of knots for the intrinsic spline (e.g., one knot every 30 days,  $\eta = 30$ ), the number of knots for each extrinsic spline (e.g., one knot every 150 days, depending on the apparent microlensing variability in each individual curve), and the respective minimum knot distances,  $\epsilon$  (e.g. 10 days). These numbers remain unchanged by the fitting; they control the global flexibility of each spline.

How sensitive is the technique to these choices? In Fig. 2 we illustrate the effect of the initial uniform knot step  $\eta$  of the intrinsic spline on the resulting time delay measurements; a smaller step corresponds to a larger number of knots. These time delay histograms are obtained by repeatedly running the optimization on the *same* data, starting from random initial time shifts, uniformly distributed within a range of  $\pm 10$  days around the typical best fitting solutions. We also randomly shuffle the order in which the optimizer processes the microlensing splines, to marginalize over any possible asymmetry introduced by our iterative spline fitting algorithm. For each number of knots, the distributions of measured time delays display a finite scatter. This is the *intrinsic variance* introduced in Section 3. It depends on the robustness of the  $\chi^2$  minimization algorithm, and thus also on the complexity (degeneracies, local minima) of the  $\chi^2$  hypersurface. As we observe, the result of our optimization is by no means global. A visual inspection of the splines reveals that the knots tend to settle in a few different repeating configurations.

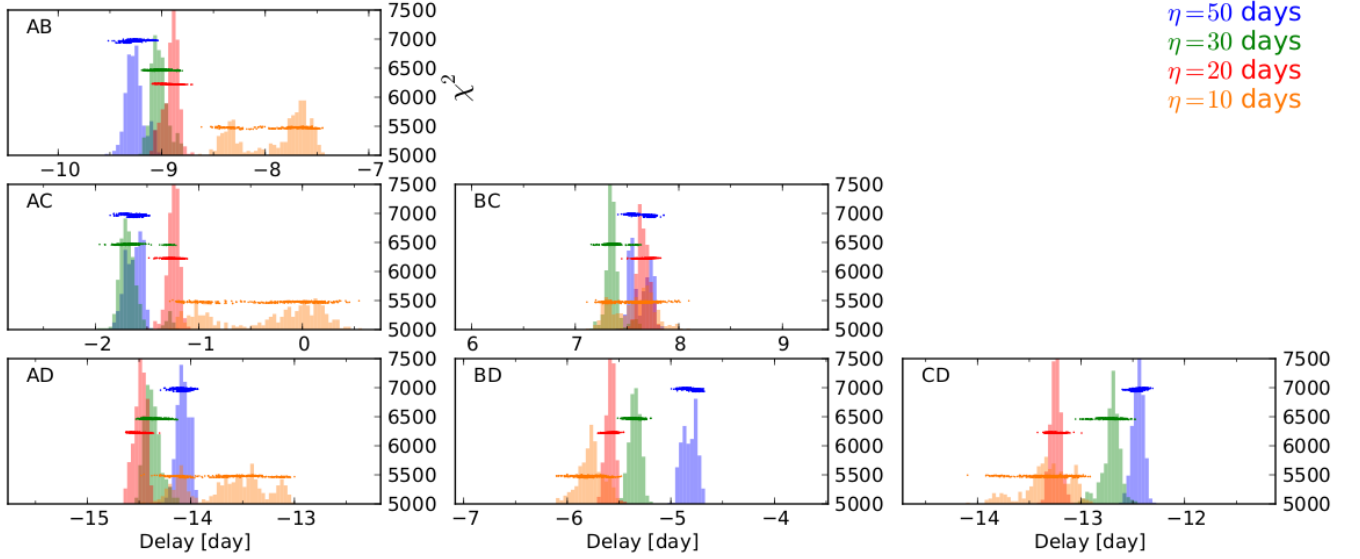


**Fig. 2.** Distributions of time delays obtained by running the free knot spline technique on always the *same* data, starting from randomised initial time shifts. The light curves are from Courbin et al. (2011), an excerpt is shown in Fig. 1. The colours encode the initial knot step  $\eta$  of the intrinsic spline, spanning a large range corresponding to a factor 5 in the number of knots. Superposed to the histograms are scatter plots of the minimal  $\chi^2$  values obtained by the optimization. We stress that the histograms shown here are not to be mistaken for probability density functions of time delay measurements on HE 0435-1223. They only illustrate the intrinsic variance, i.e., the finite precision of the optimization algorithm, as applied to a high quality data set.

This intrinsic variance will naturally contribute to the error bar that we attribute to a time delay measurement.

The influence of the step  $\eta$  on the centroids of the measured delays in Fig. 2 is surprisingly small, considering that the range of tested values covers a factor 5 in the number of knots. Visualizing the intrinsic spline fits (3 examples are shown in Fig 1), an initial step of  $\eta = 50$  days is clearly too large for this particular data set, as the resulting spline is not able to follow obvious intrinsic trends. On the other hand, setting  $\eta = 10$  days yields far too many knots and the spline tends to fit the noise of individual curves. As expected, we observe in Fig. 2 that deliberately selecting a too large number of knots leads to an increase of the intrinsic variance of the method. This behaviour is easily reproduced when changing the knot density of the extrinsic splines. Too few knots bias the measured time delays, too many knots “dilute” them, due to the degeneracies with the intrinsic spline. Note that it is well possible to attribute an extrinsic spline to *each* light curve instead of leaving one curve as a reference; this leads to obvious degeneracies between the extrinsic splines, but it does not systematically increase the intrinsic variance.

Finally, we note that the choice of the minimum knot distance  $\epsilon$  of the intrinsic spline, in a range from 2 to 15 days, has practically no effect at all on the time delay measurements. Only a very low minimal distance ( $\epsilon < 5$ ), combined with a high number of knots ( $\eta < 15$ ) significantly increases the intrinsic variance of the delay measurements, without introducing systematic shifts. In all the following, we will use a minimal knot distance of 10 days.

We postpone to Section 7 the assessment of the total uncertainties of delay measurements, for any (possibly fine-tuned) choices of the number of knots.

## 5. Method 2: variability of regression differences

Our second curve shifting technique consists of a much less parametric approach, and can be summarized as follows:

1. Instead of simultaneously fitting one intrinsic model to all light curves, we start by performing an *independent* regression on each individual curve. We can then easily express numerical *difference curves* between time shifted pairs of these finely sampled regressions. As we work with light curves in magnitudes, these difference curves correspond to flux ratios.
2. The regression curves are shifted along the time axis so to minimize the *variability*, i.e., structures, of the difference curves. In mathematical terms, we propose to measure this variability through the “weighted average variation”, a concept inspired by the *total variation*. This approach minimizes the derivative of the difference curves, as opposed to the difference curves themselves.

This method is illustrated in Fig. 3. Regressions of the light curves of two quasar images are shown in red and blue. If the regressions are shifted in time so to correctly compensate for the delays, any intrinsic variability pattern of the quasar cancels out in the difference light curves (black curve of Fig. 3). In this particular situation, the difference curves contain only the relative extrinsic variability between the curves. If the absolute extrinsic variability is independent for each curve, any statistical property of the relative extrinsic variability between the curves will a priori be independent of the time shifts. In practice this is not entirely the case, due, e.g., to the finite length of the light curves, which is much shorter than the largest time scales of microlensing variability.

In contrast, if the regressions are not shifted by the correct time delays, the intrinsic variability does not cancel out. As a consequence, the difference curves also contain a finite difference of the intrinsic quasar variability. If the latter is fast and strong enough, this corresponds to clear additional irregularities in the difference curves. These can be observed in the brown difference curve of Fig. 3, that was obtained by attributing wrong time shifts to the regressions.

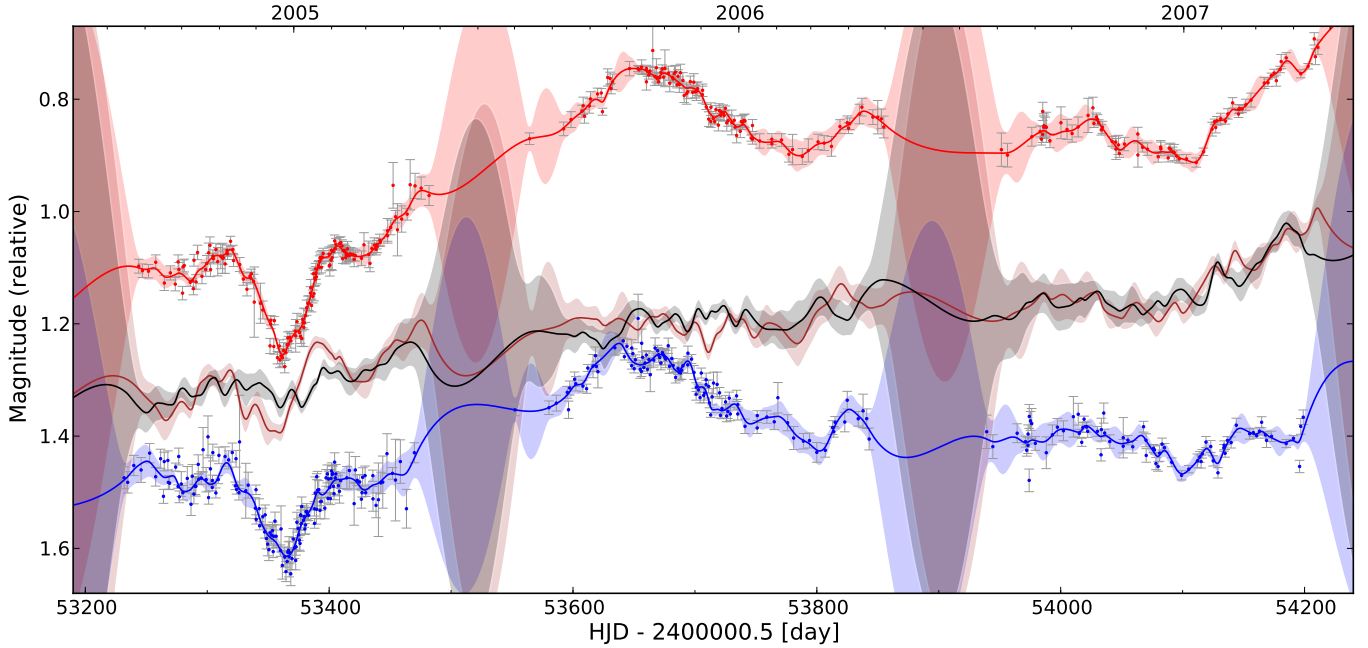


**Fig. 3.** Illustration of the regression difference technique, on light curves of HE 0435-1223 (Courbin et al. 2011). For clarity, only the light curves of images A (red) and B (blue) are shown. The Gaussian Process Regressions are shown as red and blue continuous mean functions and  $1\sigma$  envelopes. Curve B has been shifted in time with respect to A so to minimize the weighted total variation of the  $A - B$  difference curve, shown in black. The brown difference curve was obtained by deliberately shifting B by 15 days with respect to its optimal position. The curves have been arbitrarily offset in magnitudes for display purposes.

### 5.1. Gaussian Process Regression difference curves

The purpose of the regression is to allow the measurement of relative variability between time shifted light curves, despite the highly irregular sampling and season gaps. To adequately weight localized variability according to its uncertainty, we need a regression that expresses not only a most likely value but also a confidence interval for this value at each epoch.

Gaussian Process Regression (GPR) is a powerful formalism whose predictor curve, a Gaussian process, does not follow a predetermined parametrized form. Instead, the regression curve is constrained in its freedom by a covariance function, that describes how correlated two given points of the curve are, depending on their separation along the time axis. Given (i) such a prior covariance function, (ii) a prior for the regression function itself, and (iii) the observed data, the GPR yields a Gaussian distribution (i.e., a mean value and a variance) for the regression value at any interpolation epoch. For a pedagogical introduction to GPR, see e.g. Press et al. (2007).

To implement our curve shifting technique, we make use of the GPR functionality provided by the `pymc`<sup>1</sup> python package (Patil et al. 2010). Before computing a regression, we have to choose priors for both the covariance and a mean function. For the latter, we simply use an uninformative constant function, at the mean magnitude of the curve’s data points. The choice of a prior covariance function is less trivial. Several families of covariance functions are implemented in `pymc`; in all the following we make use of the Matérn family, with an amplitude parameter of 2 magnitudes, a scale of 200 days, and a smoothness degree  $\nu = 1.5$ . By analogy to the knot density of the splines used in our first technique, we do not justify a particular covariance function or its parameters. We consider this choice to be part of

the fine tuning of the curve shifting technique. This fine tuning can be done empirically, to minimize the time delay uncertainty determined in Section 7. When experimenting with covariance functions, it is of particular importance to ensure that the season gaps are interpolated with adequately large variances.

In practice, for each of the  $n$  light curves, we evaluate the GPR every 0.2 days. Given some trial time shifts, we express the  $n(n-1)/2$  difference curves by subtracting linearly interpolated magnitudes of the shifted regression curves. Indeed, each pair of curves has to be considered only once; for the variability analysis, the difference curve  $A - B$  yields the same result as  $B - A$ . In a similar way, the uncertainties at each epoch of the difference curves are obtained by summing the linearly interpolated variances. We proceed by quantifying the variability of the difference curves.

### 5.2. Minimizing the Weighted Average Variation

For a differentiable function  $f : \mathcal{R} \rightarrow \mathcal{R}$ , the *total variation* on an interval  $[a, b]$  is defined by:

$$\text{TV}_{[a,b]}(f) := \int_a^b |f'(x)| dx \quad (3)$$

Note that this total variation is monotonically increasing with the length of the interval  $[a, b]$ . To measure the variability of our difference curves, we replace the above derivative by a finite difference quotient, and the integration by a discrete averaging over the regular 0.2 day sampling epochs. Furthermore, we weight the terms of this averaging by the respective uncertainty of the difference curve, and normalize this weighting so to cancel the influence of the varying size of the overlapping regions. We will refer to this statistic as the *Weighted Average Variation* (WAV).

<sup>1</sup> <http://pypi.python.org/pypi/pymc/>



For a difference curve  $f(t_j)$  with variance  $\sigma^2(t_j)$ , and  $N$  regularly sampled points ( $j = 1, \dots, N$ ), we define:

$$\text{WAV}(f) := \frac{\sum_{j=1}^{N-1} |\hat{f}'(t_j)| \cdot w(j)}{\sum_{j=1}^{N-1} w(j)} \quad (4)$$

where

$$\hat{f}'(t_j) = \frac{f(t_{j+1}) - f(t_j)}{t_{j+1} - t_j} \quad (5)$$

and the weights are given by:

$$w(j) = \frac{2}{\sigma(t_j) + \sigma(t_{j+1})} \quad (6)$$

The time shifts of the regression curves are optimized using a nonlinear technique that minimizes a single scalar objective function obtained by summing the WAV of all pairwise difference curves. Due to the low number of parameters ( $n$  time shifts) compared to the free knot spline technique, this optimization can be made very robust, i.e., leading to a negligible sensitivity to initial conditions. The total computing time for a quad lens with 500 epochs in each curve is of the order of one minute on a single CPU. The GPR takes more than half of this time.

### 6. Method 3: dispersion minimization

Our third curve shifting method is broadly inspired by the dispersion techniques from Pelt et al. (1996). In Courbin et al. (2011), we have already applied this particular time delay estimator to the light curves of HE 0435-1223. It has also been used in Eulaers & Magain (2011). A notable difference to classical dispersion techniques is that we make use of a simple linear interpolation to form pairs of predicted and observed points, instead of considering only pairs of closeby observed points.

The method consists of a nonlinear optimization of the time shift of each light curve so to minimize a single scalar objective function that quantifies the “mismatch”. *Dispersion functions* are such objective functions that do not involve any model for the intrinsic variability, but only use the relative dispersion between the *time-shifted points* of the light curves. As for the free knot spline method (Section 4), it is necessary to explicitly compensate for any slow extrinsic variability before evaluating the dispersion for given trial time shifts. We represent this extrinsic variability by low order polynomials added to either the full curves or to individual seasons (for an illustration, see Fig. 5 of Courbin et al. 2011). These polynomials are optimized simultaneously with the time shifts, so to minimize the same dispersion function.

Remains to define the dispersion function. It should be able to evaluate the mismatch between  $n \geq 2$  time-shifted light curves of a quasar lens, treating all those  $n$  curves equally, i.e., without choice of an arbitrary reference curve. We achieve this by first defining an *elementary* dispersion function that operates on pairs of curves, and then averaging its value over all  $n(n-1)$  permutations of 2 among  $n$  light curves. This elementary dispersion function between two curves  $X$  and  $Y$  is illustrated in Fig. 4. We linearly interpolate (and never extrapolate) the light curve  $X$  at each epoch of  $Y$ , provided that the time interval over which this interpolation is done is smaller than  $\delta = 30$  days. Given the typical sampling of light curves, this means that we do not interpolate across observing season gaps. We then compute a sum of square differences between the interpolated magnitudes  $m_{X,\text{interp}}(t_i)$  and

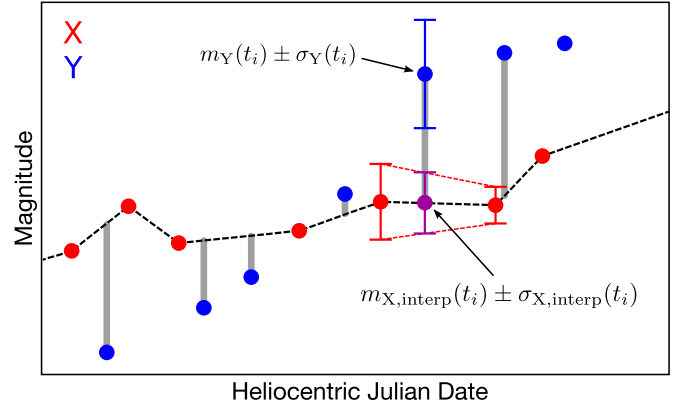


**Fig. 4.** Illustration of the “elementary” dispersion function used in the curve shifting technique described in Section 6. The vertical gray bars represent the terms of the summation of equation 7. Note that the last shown point of  $Y$  would *not* contribute to the dispersion, as it falls into a season gap of  $X$ . This elementary dispersion function is not invariant with respect to swapping the curves  $X$  and  $Y$ . However, our total dispersion estimate is symmetric, as we average these elementary dispersion across all permutations of 2 curves among  $n$ . Not shown in this sketch are the polynomial corrections for extrinsic variability. These corrections are optimized against the same total dispersion.

the corresponding magnitude measurements  $m_Y(t_i)$  of light curve  $Y$ :

$$D^2(X, Y) = \frac{1}{N} \sum_{i=1}^N \frac{(m_{X,\text{interp}}(t_i) - m_Y(t_i))^2}{\sigma_{X,\text{interp}}^2(t_i) + \sigma_Y^2(t_i)}, \quad (7)$$

where the summation goes over the  $N$  epochs of  $Y$  for which the interpolation of  $X$  was performed, given the above criteria. Each term is weighted by a combination of the linearly interpolated uncertainty on  $m_{X,\text{interp}}(t_i)$  and the uncertainty of  $m_Y(t_i)$ .

For a set  $S$  of  $n$  lightcurves, e.g.  $S = \{A, B, C, D\}$ , the average dispersion is computed by:

$$D^2(S) = \frac{1}{n(n-1)} \sum_{\{X,Y\} \subset S, X \neq Y} D^2(X, Y) \quad (8)$$

This dispersion is a function of the time shifts and the extrinsic variability corrections of each light curve. In practice we minimize the average dispersion by using iteratively a simulated annealing optimizer for the time shifts and a Powell optimizer for the extrinsic variability.

Due to the sampling and scatter of the light curves, the dispersion function usually has a very rough structure in time shift space, resulting in a poorly defined minimum. It is tempting to “smooth” this dispersion function. This can be done for instance by using a regression instead of a simple linear interpolation, or by determining the dispersion minimum through a local fit (see e.g. Fig 5. of Vuissoz et al. 2008). Such measures clearly reduce the intrinsic variance (see Section 3) of the estimator by increasing its stability against random initial time shifts. But we also observe that they often introduce additional bias. We therefore prefer to simply use the dispersion function described above, tackling its “noisy” minimum with a robust optimization algorithm.

### 7. Empirical estimation of time delay uncertainties

As described in Section 3, the three curve shifting techniques presented in this paper can be seen as recipes that yield a single

time *shift* estimation  $\tau$  for each light curve of a lensed quasar. In this section, we describe how we proceed to empirically obtain reliable error bars for time *delays* between pairs of curves ( $\Delta\tau_{XY} = \tau_Y - \tau_X$ ), as measured through these point estimations  $\tau$ . This error analysis is done individually for each quasar lens, i.e., for each set of observed light curves.

To compute the time delay uncertainties, we follow a Monte Carlo approach. We apply the curve shifting techniques on a large quantity of synthetic light curves with *known* time delays. This allows us to assess both the variance and the bias of our point estimators, as we relate in Section 7.3. We draw these synthetic light curves from a comprehensive “generative” model, i.e., a mathematical model for randomly generating mock light curves from scratch, while controlling the hidden parameters such as the time delays. For a given lensed quasar, our generative model – whose details are described in the following sections – is composed of:

1. A single intrinsic variability curve, common to all  $n$  quasar images. We use the intrinsic free knot spline obtained by applying our first curve shifting method (Section 4, black spline of Fig. 1) to the observed light curves.
2. A smooth extrinsic variability curve (“slow” microlensing) for each curve of the lens. Again, we directly use the curves obtained by the spline fitting technique on the observed data (red, green, and purple splines of Fig. 1).
3. An independent “fast” extrinsic variability, which can be seen as correlated noise, for each curve. This contribution is randomised, i.e., individually drawn for each realization of the synthetic curves.

We always sample from this generative model at the actual observing epochs of the monitoring. As a result, we obtain synthetic curves that closely imitate the intrinsic and extrinsic variability, sampling, and scatter characteristics of the real data. If the properties of the randomised fast extrinsic variability are well adjusted, these synthetic curves are statistically undistinguishable from the observations. As illustrated in Fig. 5, they could easily be mistaken for the real light curves. Yet, they have known time delays.

Our first objective of this methodology is to obtain synthetic curves that share a very similar “time delay constraining power” with the observations, so that we can assume our delay measurement methods to perform equally well or badly on both. Clearly, this constraining power of a set of light curves increases with the amount of intrinsic variability, and decreases as this variability gets diluted by extrinsic effects such as microlensing, sampling, and noise (Eigenbrod et al. 2005). Furthermore, curve shifting methods might not be able to optimally exploit the information content of the data points. In particular, they are likely to be *biased* even by those peculiarities of the data that can be indubitably determined from the observations, such as the interplay between large scale extrinsic and intrinsic variability, and season gaps. Hence, our second objective in generating synthetic curves that mimic as closely as possible the real data is to reveal these biases. Provided that a rough but unambiguous estimation of time delays can be made, the observed light curves do yield some nearly unmistakable information about the intrinsic and extrinsic variability. We use this information as a deterministic, smooth part of our generative model, and marginalize over the unknown true time delays and short scale extrinsic variability. We proceed by describing the generative model in detail.

### 7.1. Model for the intrinsic and slow extrinsic variability

We directly use the free knot spline fits of our first curve shifting technique as a model for the intrinsic and slow extrinsic variability. While quasars frequently show variability on scales of hours (see e.g. Stalin et al. 2005), we do not add any additional small scale variability to the relatively smooth intrinsic spline, as this could exaggeratedly increase the time delay constraining power of our synthetic curves.

We observe that the shapes, amplitudes, and the slopes of the intrinsic and extrinsic splines are virtually insensitive to any plausible time shifts of the light curves around the estimated time delays. Therefore, we simply use the set of splines from our free knot spline technique as a fixed, deterministic part of our model. We have verified that our results do not significantly change if we perform a time-shift-constrained spline fit on the observed curves for each particular delay that we want to simulate.

### 7.2. Model for the randomised fast extrinsic variability

To add fast extrinsic variability to our synthetic light curves, we randomly generate “power law noise”, i.e., a time series whose Fourier spectrum follows a power law. The characteristics of this noise are adjusted individually for each quasar image. This procedure can be summarized as follows:

1. For each quasar light curve, draw power law noise following Timmer & Koenig (1995), using a fine regular sampling of e.g. 0.2 days.
2. Linearly interpolate these finely sampled signals at the observing epochs of the light curves, to obtain a noise contribution for each data point.
3. Locally rescale the noise, so that its amplitude follows the scatter in the observed curves.
4. Run the free knot spline technique on the synthetic curves, and analyse the residuals.
5. Iteratively repeat the above steps, adjusting the parameters of the power law noise until the residuals obtained at step 4 are statistically compatible with the residuals obtained from the real observations.

Note that we use this model to generate both correlated extrinsic variability and independent shot noise at once. Therefore, the regular sampling used in step 1 should be chosen significantly finer than the minimal distance between observing epochs.

Let us now revisit the steps leading to a well adjusted fast extrinsic variability in more detail, starting with the power law noise. The idea of Timmer & Koenig’s algorithm is to generate random amplitude and phase coefficients in the discrete Fourier space, and then build the real signal by inverse Fourier transform. We limit the generation of random amplitudes to a finite window of the frequency domain, thus avoiding to affect the large scale variability of our extrinsic model curves. The power law noise is controlled by the following parameters:

- $\beta$ : the exponent of the spectrum power law;  $\beta = -2$  corresponds to a random walk,  $\beta = 0$  is white noise).
- $A$ : a scaling factor for the generated noise
- $f_{\text{Min}}$ : low cut-off of the frequency window. We set  $f_{\text{Min}}$  to  $1/500 \text{ day}^{-1}$ , as any lower frequencies are by construction well represented by the extrinsic free knot spline fit.
- $f_{\text{Max}}$ : high cut-off of the frequency window. We take this as the maximum (Nyquist) frequency of the 0.2 day sampling.

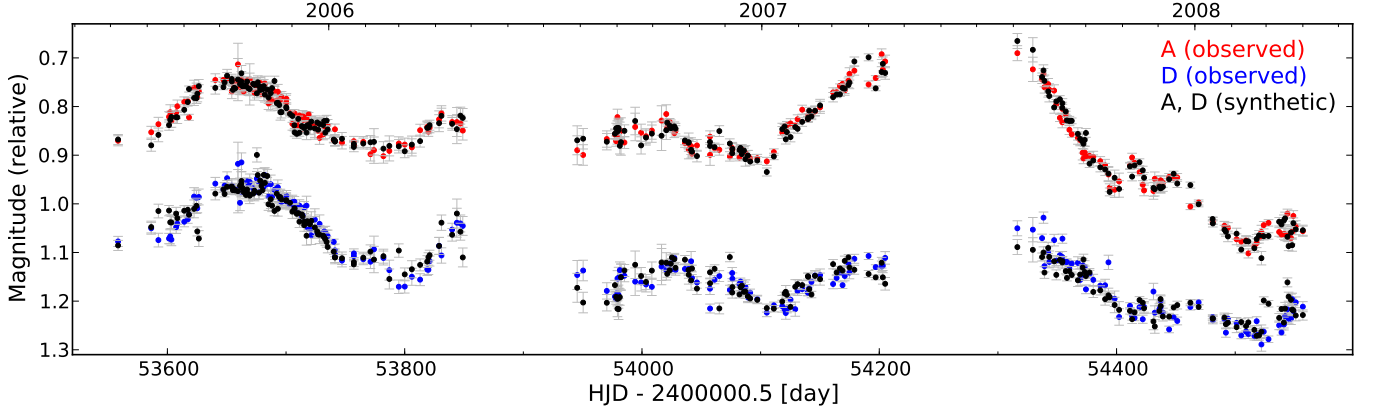


**Fig. 5.** Synthetic curves (black) drawn from a well adjusted generative model (see text), and the corresponding observed data points for the lensed quasar HE 0435-1223. For illustration purposes only 3 seasons of 2 quasar images are shown, arbitrarily offset in magnitude. The purpose of the generative model is to simulate curves with *known* time delays that nevertheless mimic the observations at best. These synthetic curves are used to evaluate the accuracy and precision of our curve shifting algorithms, using a Monte Carlo approach. Note that the strong degeneracies between the extrinsic splines used in the model have no influence on the match between the synthetic and observed light curves; in the scope of our simple generative model we do not need to know if, for instance, a light curve is amplified by microlensing in image A, or demagnified in B. Only relative extrinsic variability is relevant.

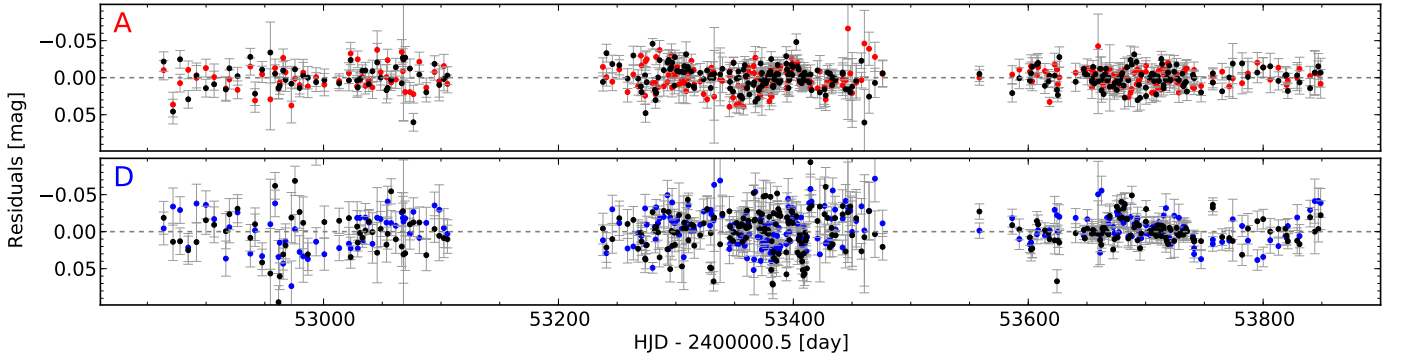


**Fig. 6.** Residuals of the observed (red, blue) and the synthetic (black) light curve of images A and D of HE 0435-1223, as obtained by applying the free knot spline method. The power law noise used for the synthetic curve is adjusted so that these residuals show on average (i) the same standard deviation and (ii) the same number of “runs” as those of the observations. As described in the text, the power law noise has been rescaled to locally match the scatter amplitude of the observed curves, as can be clearly seen in this figure.

The free parameters  $\beta$  and  $A$  have a direct influence on the accuracy and precision that time delay estimators will achieve on the synthetic curves; these are the parameters that will be adjusted for each light curve. We observe that reasonable changes in the parameters  $f_{\text{Min}}$  and  $f_{\text{Max}}$  (i.e., the sampling) have a negligible effect compared to the influence of  $\beta$  and  $A$ .

Interpolating this power law noise at the observing epochs leads to a contribution  $\epsilon_i$  for each data point. The next step is to locally adapt the amplitude of these  $\epsilon_i$  to the observed scatter in the light curves. This is empirically well motivated, as observed light curves often contain subregions that clearly display different smoothness. To perform this local rescaling for a given curve, we use the residuals  $r_{i,\text{obs}}$  obtained by running the free knot spline technique on the observed light curves (red and blue points of Fig. 6). We normalize the absolute values of these noisy residuals to an average of one, and smooth the resulting signal using a median filter with a window of 7 observing epochs:

$$s_i = \text{median} \left( \frac{|r_{j,\text{obs}}|}{\langle |r_{\text{obs}}| \rangle}, j \in \{i-3, \dots, i+3\} \right) \quad (9)$$

where  $\langle |r_{\text{obs}}| \rangle$  denotes the average absolute residual taken over all points of the curve. The rescaled  $\epsilon_i$  that we add to our synthetic light curves are given by:

$$\epsilon_{i,\text{rescale}} = \epsilon_i \cdot s_i \quad (10)$$

This local rescaling does not affect the average amplitude of the synthetic noise, which is still controlled by  $A$ .

We proceed by running the spline fitting technique from scratch on the set of synthetic curves, i.e., disregarding any information from the generative model. This yields residuals, shown as black points in Fig. 6, that can be equitably compared with the residuals of the observations.

To fine-tune  $A$  and  $\beta$ , we quantitatively analyse these residuals. For this, we make use of two simple statistics: their standard deviation  $\sigma$ , and their number of “runs”  $r$ . A *run* is a sequence of adjacent either positive or negative residuals. The total number of positive and negative runs is a statistic that can be used to test the hypothesis that successive residuals are independent (Wall & Jenkins 2003, chap. 5). For large samples of  $N$  truly independent observations with  $N_+$  positive and  $N_-$  negative residuals,

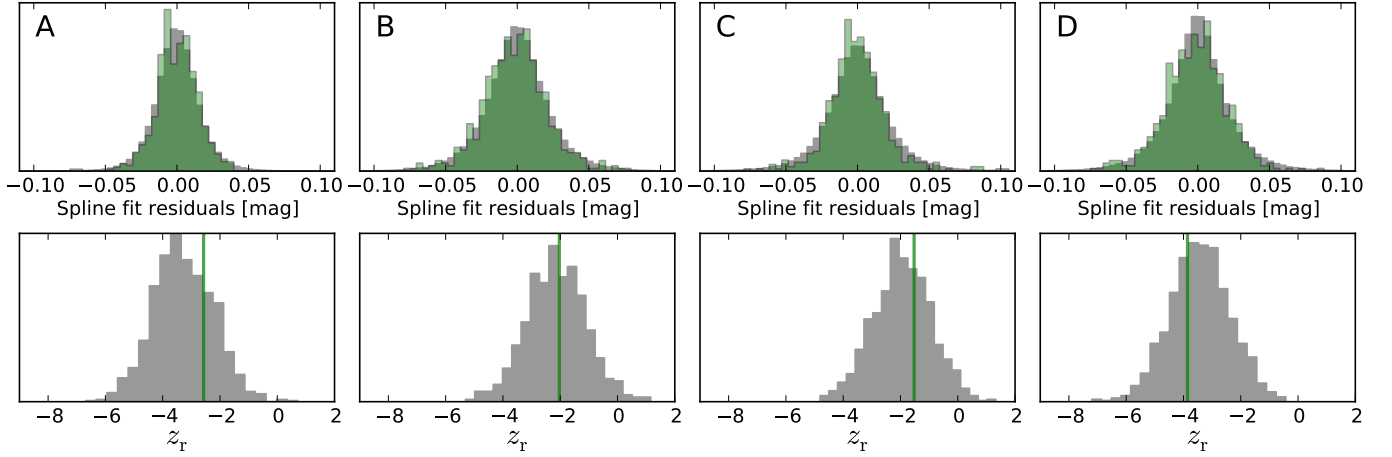


**Fig. 7.** Top: histogram of residuals obtained by running the free knot spline fit technique on the observed light curves of HE 0435-1223 (green), and the corresponding synthetic curves (gray). Bottom: distribution of the  $z_r$  parameter computed from these residuals. Only one set of observed light curves is available, while the distributions related to the synthetic curves are averaged over 1000 realizations. In this example, the parameters of the generative model have already been adequately adjusted; the synthetic curves shown in Fig. 5 and 6 are drawn from this adjusted model.

the number of runs  $r$  is normally distributed with an expectation value and a variance respectively given by

$$\mu_r = \frac{2N_+N_-}{N} + 1 \quad \text{and} \quad \sigma_r^2 = \frac{(\mu_r - 1)(\mu_r - 2)}{N - 1}. \quad (11)$$

In practice we “normalise” a measured number of runs  $r$  to this hypothesis of independent residuals:

$$z_r = \frac{r - \mu_r}{\sigma_r}. \quad (12)$$

Applying the free knot spline technique on COSMOGRAIL light curves, we typically observe a number of runs in the residuals at least about  $2\sigma_r$  lower than  $\mu_r$ , i.e.,  $z_r \approx -2$ , meaning that the residuals are indeed correlated. Fig. 7 shows a comparison in terms of residual distribution and  $z_r$  between the residuals obtained from synthetic curves (gray distributions, averaged over 1000 realizations) and from the observations of HE 0435-1223 (in green). One can now adjust the parameters  $A$  and  $\beta$  of the power law noise so that the average standard deviation and number of runs of the residuals obtained from the synthetic curves match the values measured on the observations. The procedure is straightforward, as the residuals’ number of runs directly relates to  $\beta$ , and their standard deviation to  $A$ , without much crosstalk. Hence a good match such as shown in Fig. 7 is obtained after just a few trial and error iterations, simultaneously modifying  $A$  and  $\beta$  of each quasar image.

Finally, we attribute to all our synthetic light curves the photometric error bars of the observed data. We stress that nowhere else in our generative model we made use of these photometric error bars. Photometric error bars only describe the experimental measurement uncertainty, which is not necessarily the only source of short scale “mismatch” between multiple light curves. Furthermore, for all methods presented in this paper, the photometric error bars essentially only act as *relative weights* between the data points. As a consequence, our time delay measurements – including their uncertainty estimates – are not directly influenced by a potential systematic under- or over-estimation of the photometric errors. We see this as a very desirable feature.

### 7.3. Quantifying variance and bias of our time delay estimators

With the well adjusted generative model in hand, we proceed by drawing typically 1000 synthetic curve sets, choosing model time shifts in a range of several days around the point estimates obtained from the observations. We run the curve shifting technique on these synthetic curves, using the same parameters as for the estimation performed on the real observations. We always start the techniques from random initial time shifts, to take into account the potential intrinsic variance of the curve shifting technique described in Section 3. We then compute the resulting errors between the estimated and the true time delays.

To analyse these errors, we bin the synthetic curve sets according to their true time delays, individually for each quasar image pair. This allows us to check if the uncertainties that we will derive do not strongly depend on the true time delays. Fig. 10 illustrates the procedure in the case of a quad lens. In each bin, we estimate the *variance* and the *bias* of our time delay estimators, by computing the sample variance ( $\sigma_{\text{ran}}^2$ ) and the average ( $\sigma_{\text{sys}}$ ) of the delay measurement errors, respectively.

By construction, the main practical origin of the bias has to be related to those properties of light curves that are kept constant in the Monte Carlo simulations, such as the interplay between intrinsic and slow extrinsic variability, season gaps and sampling. This bias quantifies the accuracy of a time delay estimation. Note that such a characterization of accuracy has often been neglected in past time delay measurements; it cannot be obtained through resampling techniques that don’t involve a generative model, such as jackknifing or bootstrapping.

On the other hand, the variance of our time delay estimators mainly results from their sensitivity to the fast extrinsic variability and noise, which we randomise in our synthetic curves. This variance describes the precision of the time delay measurements. It is often possible to increase the precision of a curve shifting technique, by somehow smoothing either the input light curves or the cost function to be optimized. Using the approach described in this paper, we can verify if such an increase in precision is not obliterated by an even higher decrease in accuracy.

Lastly, we obtain a comprehensive 1-sigma error bar  $\sigma_{\text{tot}}$  for the time delay measurement between each quasar image pair by



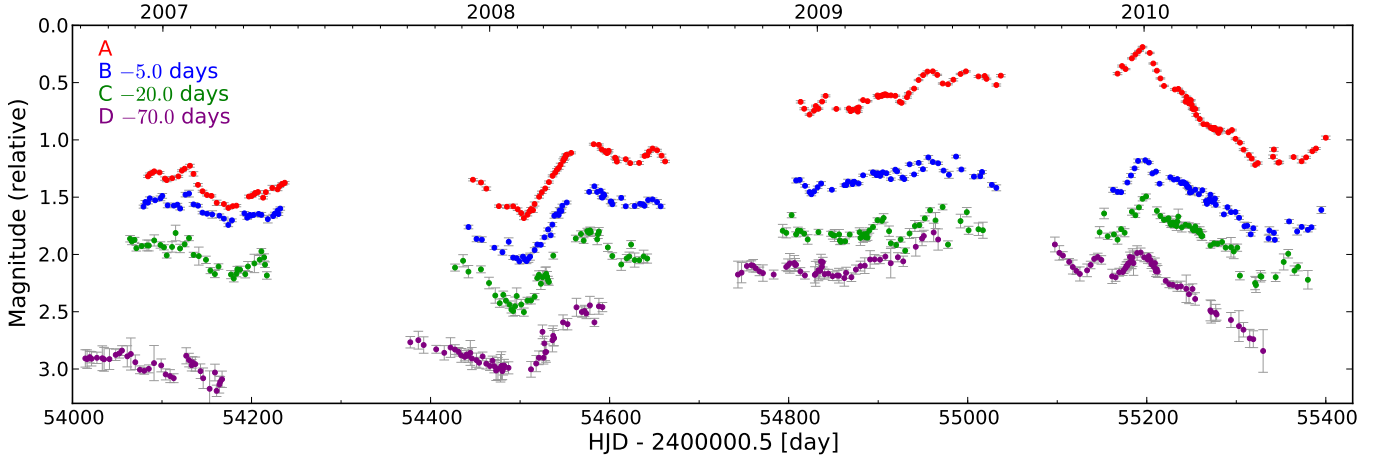


**Fig. 8.** The “trial curves”, i.e., a set of artificial 4 season long lightcurves of a quad lens, used in place of real observations for the self-consistency check performed in Section 8. These curves are drawn from a generative model that closely mimics COSMOGRAIL observations. Note the prominent microlensing on large time scales, but also the presence of obviously extrinsic variability on scales of weeks (e.g., middle of third season of curve C). The true time delays are  $\Delta t_{AB} = -5.0$ ,  $\Delta t_{AC} = -20.0$  and  $\Delta t_{AD} = -70.0$  days. In this figure the curves are shifted according to these delays.

combining the maximal bias and the maximal variance observed in the bins of true time delays:

$$\sigma_{\text{tot}} = \sqrt{\max_{\Delta t_{\text{true}}} \sigma_{\text{ran}}^2 + \max_{\Delta t_{\text{true}}} \sigma_{\text{sys}}^2} \quad (13)$$

In situations where bias and variance do not significantly depend on the true time delays,  $\sigma_{\text{tot}}^2$  simply corresponds the mean squared error (MSE) of our time delay estimators. Fig. 10 corresponds about to such a situation.

As will become evident in the next section, it appears very tempting to empirically *correct* each time delay estimation for its bias, instead of simply combining the bias and the variance into the total error budget. To avoid any circular argumentation, we do not perform such a correction in this paper. The circularity would arise as we have to assume time delays for the observed data in order to *build* the generative model of the synthetic curves. If these initial guesses for time delays are significantly biased, the generative model will contain erroneous intrinsic and extrinsic variability patterns, yet still mimic the observed curves. Hence, running the curve shifting techniques on the synthetic curves would yield measured delays close to their true delays, and thus not fully reveal the initial errors.

We prefer to simply use the amplitude of the bias, gauged through the above procedure, as a quality criterion of each method.

## 8. Application to trial curves, discussion

In this section, we apply our three curve shifting techniques, as well as the error bar computation procedure of Section 7, to a set of artificial curves with known time delays. This allows us to check the consistency of the error bar computation, and to illustrate some general observations about the latter.

### 8.1. The trial curves

We use the scheme described in Section 7 to generate a single set of 4-season long light curves, that mimic the data of one of the quadruply imaged quasars monitored by the COSMOGRAIL collaboration. In the following, we refer to these artificial curves

as the “trial curves”; they are shown in Fig. 8. The trial curves include realistic intrinsic variability and sampling, as well as obvious long- and short-scale microlensing. We choose time delays of  $\Delta t_{AB} = -5.0$ ,  $\Delta t_{AC} = -20.0$  and  $\Delta t_{AD} = -70.0$  days.

### 8.2. Analysis

From here on we process the trial curves as if they would be real observations. We use our time delay estimators on them, disregarding any prior information about the true delays and intrinsic or extrinsic variations. For the spline method, we choose an average knot step of 20 days for the intrinsic spline, and of 150 days for the four extrinsic splines. The dispersion-like method is allowed to correct for extrinsic variability using independent linear trends on each of the 16 seasons. All other parameters of the curve shifting techniques are fixed to the default values presented earlier.

As described in Section 3, we systematically run the curve shifting methods several hundreds of times on the same light curves, starting from randomised initial time shifts, and we use the mean of the resulting time delay distributions as our best estimation. This leads to the centroids of the time delay estimates, presented in Fig. 9. The dashed vertical lines indicate the true time delays of the trial curves analysed in this section.

Finally, we compute error bars for these time delay measurements following the procedure of Section 7. In doing so, the curves used for the Monte Carlo runs are drawn from a *new generative model built from scratch* from the trial curves. Note that despite this precaution, the same kind of recipes were used to build the trial curves and the synthetic curves used in the Monte Carlo procedure. The analysis performed in this section should therefore be seen as a self-consistency check of our time delay uncertainty estimation procedure.

We present this error analysis in Fig. 10. For each bin of true delay used in the Monte Carlo simulations, we show the mean  $\sigma_{\text{sys}}$  and standard deviation  $\sigma_{\text{ran}}$  of the measurement errors as a shaded rod and as an associated error bar, respectively. From this figure, we directly obtain the total uncertainty  $\sigma_{\text{tot}}$  following Eq. 13, for each technique and pair of quasar images. These  $\sigma_{\text{tot}}$  are used as error bars in Fig. 9.

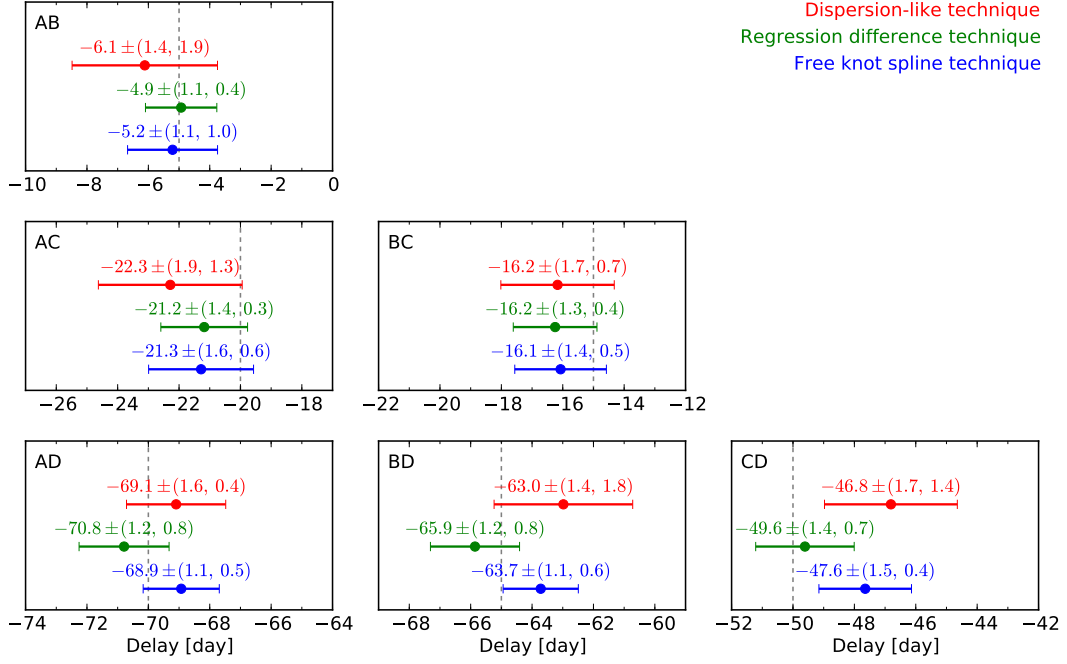


**Fig. 9.** Time delay estimations and associated uncertainties obtained by each of the three curve shifting techniques from the trial curves in Fig. 8. For each delay measurement, the random error bar,  $\sigma_{\text{ran}}$  and the bias,  $\sigma_{\text{sys}}$ , are given in parentheses. The drawn error bars depict the total error,  $\sigma_{\text{tot}}$ , as obtained from equation 13. The dashed vertical lines show the true delays of the trial curves analysed in this section.

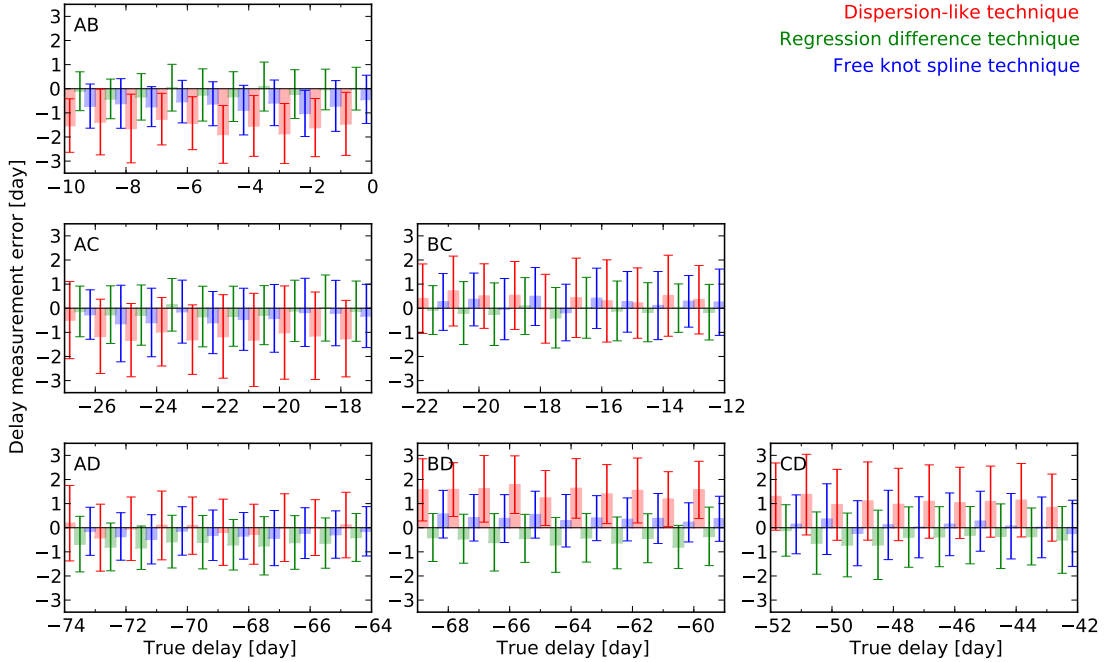


**Fig. 10.** Error analysis for the trial curves shown in Fig. 8. For each curve shifting technique, the estimates of the time delay uncertainties are obtained by analyzing delay measurement errors on 1000 synthetic curves with known time delays. In each panel, the delay measurement errors (vertical axis) are represented against the true input delays of these synthetic curves (horizontal axis). Instead of showing a scatter plot, the averaged measurement error (i.e., the bias  $\sigma_{\text{sys}}$ ) in each bin of the true delay is shown by the shaded rod, while the error bars represent the standard deviation  $\sigma_{\text{ran}}$ . For increased clarity, the rods are drawn three times narrower than the actual bin width. To give an example, we can observe on this figure that the dispersion-like technique systematically underestimates the delay  $\Delta t_{\text{AB}}$  by about 1.5 days, no matter the true delay used in the synthetic curves. For this specific curve shifting technique and pair of curves, the bias is larger than the standard deviation of the measurement errors, hence underlining the importance of evaluating the bias. Recall that the Monte Carlo procedure described in Section 7 allows us to perform the analysis summarized in this figure for any set of observed light curves. The knowledge of the true delays, as available for the artificial curves examined in this section, is not used at any step here.

### 8.3. Discussion

Several important observations can be made from Figs. 9 & 10. We recall that the analysis leading to these figures did not use any knowledge of the true time delays between the trial curves at any time, except for plotting the dashed vertical lines in Fig. 9.

1. We observe in Fig. 9 that, on average, the total  $1\sigma$  error bars computed by our Monte Carlo approach compare well with the actual errors made by our point estimators on the trial curves. In particular, this holds for the dispersion-like technique, that suffers in this example from the largest biases. The self-consistency check of our uncertainty estimation procedure is successful.
2. Fig. 10 clearly shows that, in the case of these trial curves, our estimates of both the bias and the variance of each curve shifting method does not depend much on the true time delays of the Monte Carlo simulations. This optimal situation is often not observed for shorter or lower quality curves, motivating our conservative decision to combine the maximum bias and variance to get the total error bar following equation 13.
3. We can make an additional observation about the *direction and magnitude* of the bias. Lets consider for example the time delay  $\Delta t_{BD}$ . From Fig. 9 we see that the lowest estimate of the delay is obtained by the regression difference technique (green), followed by the spline technique (blue) and then by the dispersion-like technique (red). Independently, Fig. 10 shows that on our Monte Carlo simulations, the regression difference technique tends to underestimate this delay, the spline technique tends to slightly overestimates it, while the dispersion-like technique overestimates it on average by  $\sim 1.5$  days. Hence the “order” of the biases as estimated from the Monte Carlo simulations is consistent with the sequence of time delays measured on the trial curves. A similar statement holds for nearly all pairs of quasar images, which is remarkable. We conclude that our uncertainty estimation procedure of Section 7 is at least in part successful in separating the bias due to flaws of the methods from the random error that genuinely originates from the data. Note that this aspect can be analysed for real data, as it does not involve the knowledge of the true time delays between the trial curves.

### 8.4. Investigating error correlations between pairs of quasar images

The error bars computed for a given delay with our a method marginalize over the other delays of the same lens. However, the delay measurements are not independent in their very nature. For example,  $\Delta t_{AC} = \Delta t_{AB} + \Delta t_{BC}$ , hence any estimation of  $\Delta t_{AC}$  correlates positively with both  $\Delta t_{AB}$  and  $\Delta t_{BC}$ . The formalism presented in this paper does not fully exploit this joint information.

We can nevertheless use the measurements obtained from the Monte Carlo simulations to explore correlations between delay estimation errors of different pairs of quasar images. In Fig. 11, we show this correlation for pairs of curves, marginalizing over the true delays used in the Monte Carlo simulations.

Displacements of these distributions with respect to the zero-error crosshairs indicate bias, while the width of the distributions indicates the variance of the time delay estimators. As expected, we observe positive and negative correlations, that is ellipsoids

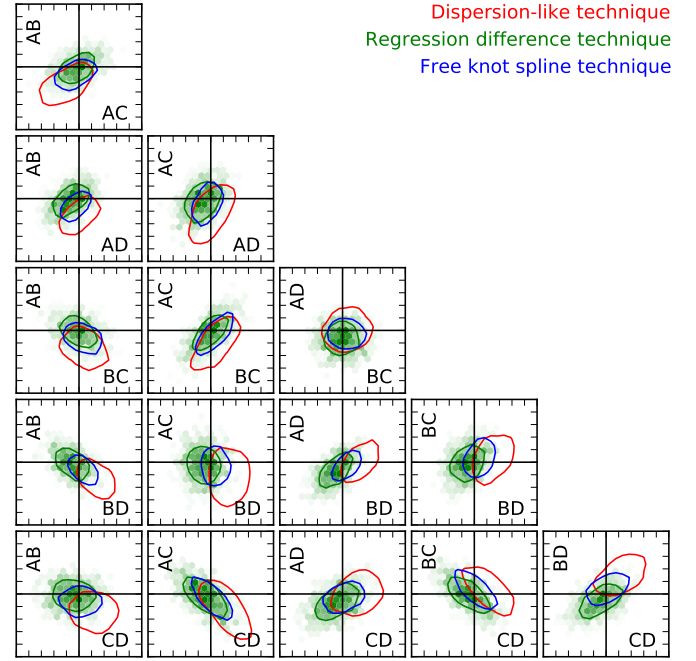


**Fig. 11.** Correlations of delay measurement errors for the quad lens analysed in Section 8. The distribution of delay measurement errors on 1000 synthetic curves is shown for each quasar image pair against each other pair, marginalizing over the true delays of the synthetic curves. The central crosshair of each panel indicates zero error and the ticks are days, i.e., each axis shows errors from  $-5$  to  $+5$  days. Displacements of the distributions with respect to the crosshairs indicates bias, while the width of the distributions indicates variance of the time delay estimators. For clarity, only single contours at half of the maximum density are shown for two of the techniques. The measurement errors shown in this figure are exactly the same as used in Fig. 10.

with oblique orientations, for pairs of delays that involve a common quasar image. Very importantly, at least for the specific set of light curves used in this work, we do *not* observe correlations between the 3 “disjoint” pairs of delays AB/CD, AC/BD, and AD/BC, located along the short diagonal of Fig. 11.

This analysis is to be made for the light curves of every specific quadruply imaged quasar, as the sensitivity of the curve shifting algorithms certainly depends on the details of the features in real quasar light curves. If the results are qualitatively similar to those shown in Fig. 11, we deem as appropriate to present our time delay measurements in the form of independent estimates, marginalizing over all correlations. Note that in practice a joint probability distribution is only really interesting for quadruply imaged quasars in which several delays are well measurable.

### 8.5. Getting a single answer

It remains to be decided how to “combine” the delay measurements obtained from our different techniques. We cannot combine the measurements as if they were independent, for instance by multiplying associated probability density functions. Indeed, no matter how different the *methods* are, they all use the one and only realization of the observations. In particular, it can well happen that the time delay error bars, as derived by our approach for each method, are significantly larger than the apparent spread of the delay point estimates obtained from the different methods (see e.g. panel BC of Fig. 9). The spread of different estimates

is clearly not an indication of the degree of knowledge of a time delay.

Hence, when analysing real observations, we propose to simply select, individually for each lens, the method that tends to display the smallest total error bar. One can directly use its point estimates and the associated  $1\sigma$  error bars as favored answer.

Average delays between competitive methods could also be used, but in any case the size of the uncertainties are not to be divided by the square root of the number of methods contributing to these averages.

## 9. Conclusions

In this paper, we describe 3 independent “curve shifting techniques” to measure time delays between resolved light curves of gravitationally lensed quasars. All these methods address the presence of variable microlensing in the light curves and can be applied to lens systems with any number of images.

1. **The free knot spline technique** simultaneously fits one common *intrinsic* spline, and independent smoother *extrinsic* splines to the light curves. The curves are shifted in time so to optimize this fit.
2. **The regression difference technique** shifts regressions of the curves so to minimize the *variability* of the differences between them. It is nearly parameter free, and does not require an explicit model for the microlensing variability.
3. **The dispersion-like technique** shifts the curves so to minimize a measure of the *dispersion* between the overlapping data points. This method has no explicit model for the common intrinsic variability of the quasar, but it involves polynomial models for the extrinsic variability. It has previously been applied in Courbin et al. (2011).

A common point of the methods is that they yield point estimates (i.e., single values) for the time delays in a self-consistent way by sharing the formalism of time *shifts* described in Section 3.

In addition, we present a Monte Carlo approach to estimate a comprehensive error bar for each time delay measurement. This procedure is based on synthetic curves that try to mimic as much information about the intrinsic and extrinsic variability as the observations unmistakably reveal. Provided that we accept the generative model of the synthetic curves, the curve shifting techniques themselves are reduced to “recipes”. Given a set of light curves, we can select methods based solely upon their empirical performance. This effectively shifts the requirement of formal justification from the curve shifting techniques to the synthetic curves on which these techniques are evaluated. As a consequence, the recipes can even be fine tuned for each data set.

Finally, we have verified the self-consistency of our time delay uncertainty estimation using a trial set of artificial light curves. Importantly, the availability of 3 different curve shifting techniques allows to perform consistency checks of our *bias* determination when analysing real observations, i.e., data without known time delays. In other words, we acknowledge that any curve shifting technique may display residual biases, due for example to particular patterns of slow microlensing variability, but we provide a mean to credibly quantify this bias, whatever be its origin.

The methods described in this paper will be used as standard benchmark to obtain time delay estimations from the light curves of the COSMOGRAIL monitoring program. We have implemented the curve shifting techniques, the error bar estimation,

and the generation of all the figures of this paper in form of a modular `python` toolbox. This package, called `PyCS`, as well as a tutorial including the trial curves of Section 8 are available from the COSMOGRAIL website<sup>2</sup>.

**Acknowledgements.** This work is supported by the Swiss National Science Foundation (SNSF). We acknowledge support from the International Space Science Institute where this research was initiated, and thank Eva Eulaers and Pierre Magain for helpful discussions. It is also a pleasure to acknowledge heavy use of the `scipy` (Oliphant 2007) and `matplotlib` (Hunter 2007) projects, which are both community efforts.

## References

- Barkana, R. 1997, *ApJ*, 489, 21
- Burud, I., Magain, P., Sohy, S., & Hjorth, J. 2001, *A&A*, 380, 805
- Courbin, F., Chantry, V., Revaz, Y., et al. 2011, *A&A*, 536, A53
- Cuevas-Tello, J. C., Tino, P., & Raychaudhury, S. 2006, *Lecture Notes in Computer Science*, 4212, 614
- Cuevas-Tello, J. C., Tino, P., Raychaudhury, S., Yao, X., & Harva, M. 2010, *Pattern Recognition*, 43, 1165
- Dierckx, P. 1995, *Curve and Surface Fitting With Splines*, Monographs on Numerical Analysis (Clarendon Press)
- Eigenbrod, A., Courbin, F., Meylan, G., et al. 2008a, *A&A*, 490, 933
- Eigenbrod, A., Courbin, F., Sluse, D., Meylan, G., & Agol, E. 2008b, *A&A*, 480, 647
- Eigenbrod, A., Courbin, F., Vuissoz, C., et al. 2005, *A&A*, 436, 25
- Eulaers, E. & Magain, P. 2011, *A&A*, 536, A44
- Gil-Merino, R., Wisotzki, L., & Wambsganss, J. 2002, *A&A*, 381, 428
- Golub, G. & Pereyra, V. 1973, *SIAM Journal on numerical analysis*, 413
- Harva, M. & Raychaudhury, S. 2008, *Neurocomputing*, 72, 32
- Hirv, A., Olsper, N., & Pelt, J. 2011, *Baltic Astronomy*, 20, 125
- Hunter, J. D. 2007, *Computing in Science & Engineering*, 9, 90
- Kochanek, C. S. 2004, *ApJ*, 605, 58
- Kochanek, C. S., Dai, X., Morgan, C., Morgan, N., & Poindexter, S. C. G. 2007, *Statistical Challenges in Modern Astronomy IV ASP Conference Series*, Vol. 371, proceedings of the conference held 12-15 June 2006 at Pennsylvania State University, in University Park, Pennsylvania, USA. Edited by G. Jogesh Babu and Eric D. Feigelson., p.43
- Kochanek, C. S., Morgan, N. D., Falco, E. E., et al. 2006, *ApJ*, 640, 47
- Kundic, T., Turner, E. L., Colley, W. N., et al. 1997, *ApJ*, 482, 75
- Lehar, J., Hewitt, J. N., Burke, B. F., & Roberts, D. H. 1992, *ApJ*, 384, 453
- Linder, E. V. 2011, *Physical Review D*, 84, 123529
- Molinari, N., Durand, J., & Sabatier, R. 2004, *Computational statistics & data analysis*, 45, 159
- Morgan, C. W., Eyler, M. E., Kochanek, C. S., et al. 2008, *ApJ*, 676, 80
- Morgan, C. W., Hainline, L. J., Chen, B., et al. 2012, *arXiv*
- Oliphant, T. 2007, *Computing in Science & Engineering*, 9, 10
- Patil, A., Huard, D., & Fonnesbeck, C. 2010, *Journal of statistical software*, 35, 1
- Pelt, J., Kayser, R., Refsdal, S., & Schramm, T. 1996, *A&A*, 305, 97
- Pelt, J., Refsdal, S., & Stabell, R. 2002, *A&A*, 389, L57
- Press, W. H., Rybicki, G. B., & Hewitt, J. N. 1992, *ApJ*, 385, 404
- Press, W. H., Teukolsky, S. A., Vetterling, W. T., & Flannery, B. P. 2007, *Numerical Recipes Third Edition* (Cambridge University Press)
- Refsdal, S. 1964, *MNRAS*, 128, 307
- Stalin, C. S., Gupta, A. C., Gopal-Krishna, Wiita, P. J., & Sagar, R. 2005, *MNRAS*, 356, 607
- Suyu, S. H., Marshall, P. J., Auger, M. W., et al. 2010, *ApJ*, 711, 201
- Suyu, S. H., Marshall, P. J., Blandford, R. D., et al. 2009, *ApJ*, 691, 277
- Timmer, J. & Koenig, M. 1995, *A&A*, 300, 707
- Vakulik, V. G., Shulga, V. M., Schild, R. E., et al. 2009, *Monthly Notices of the Royal Astronomical Society: Letters*, 400, L90
- Vanderriest, C., Schneider, J., Herpe, G., et al. 1989, *A&A*, 215, 1
- Vuissoz, C., Courbin, F., Sluse, D., et al. 2008, *A&A*, 488, 481
- Wall, J. & Jenkins, C. 2003, *Practical Statistics for Astronomers*, Cambridge Observing Handbooks for Research Astronomers (Cambridge University Press)
- Walsh, D., Carswell, R. F., & Weymann, R. J. 1979, *Nature*, 279, 381

<sup>2</sup> <http://www.cosmograil.org>

## 3 COSMOGRAIL results

This chapter is structured as follows:

**Section 3.1** rapidly presents a selection of COSMOGRAIL light curves that will be published, together with time delay measurements, over the next months.

**Tewes et al. (2012c)** presents the time delays and 9-yr optical monitoring of the quadruply lensed quasar RX J1131–1231. This paper also describes the monitoring and the photometry as outlined in Chapter 2 of this thesis.

**Suyu et al. (2012a)** presents the implications for cosmology of the time delay measurements of RX J1131–1231, also in combination with WMAP7 and the lens B1608+656, from state-of-the-art lens modeling.

**Courbin et al. (2011)** presents time delays, lens dynamics and baryonic fraction in the quad lens HE 0435–1223. Both the photometry and the time delay measurements presented in this paper were obtained in 2010 with *preliminary* versions of the techniques presented in this thesis. However, these results are robust against a reanalysis with the finalized techniques.

**Section 3.2** summarizes the results of the microlensing analysis of Q J0158–4325 by Morgan et al. (2012).

### 3.1 Selected light curves

The next pages show a selection of COSMOGRAIL *R*-band light curves of gravitationally lensed quasars, mostly from the southern hemisphere. Some of these light curves are still preliminary, but they have all been homogeneously obtained using our photometric pipeline. Once published, they will naturally be available in machine-readable form from the COSMOGRAIL website.

COSMOGRAIL currently monitors about 20 quasar lenses, either “doubles” (2 quasar images) or “quads” (4 quasar images). While doubles have longer time delays (see, e.g., Saha 2004), which is good for delay measurements with low fractional uncertainty, two quasar images

yield less constraints on a lens mass model than four. As a consequence, the lens model is highly degenerate, and the time-delay distance of doubles is harder to constrain. However, as shown by Suyu (2012), the radial mass profile of a lens can be accurately constrained from *double* images of the source galaxy with measurable arc thickness. Provided that deep and sharp imaging – revealing these extended arcs – is available, the time-delay distance of these lenses can also be recovered to a few percent. This is valuable also in future, as only about 15% of the quasar lenses expected to be discovered in the next generation of surveys are quads (Oguri & Marshall 2010).

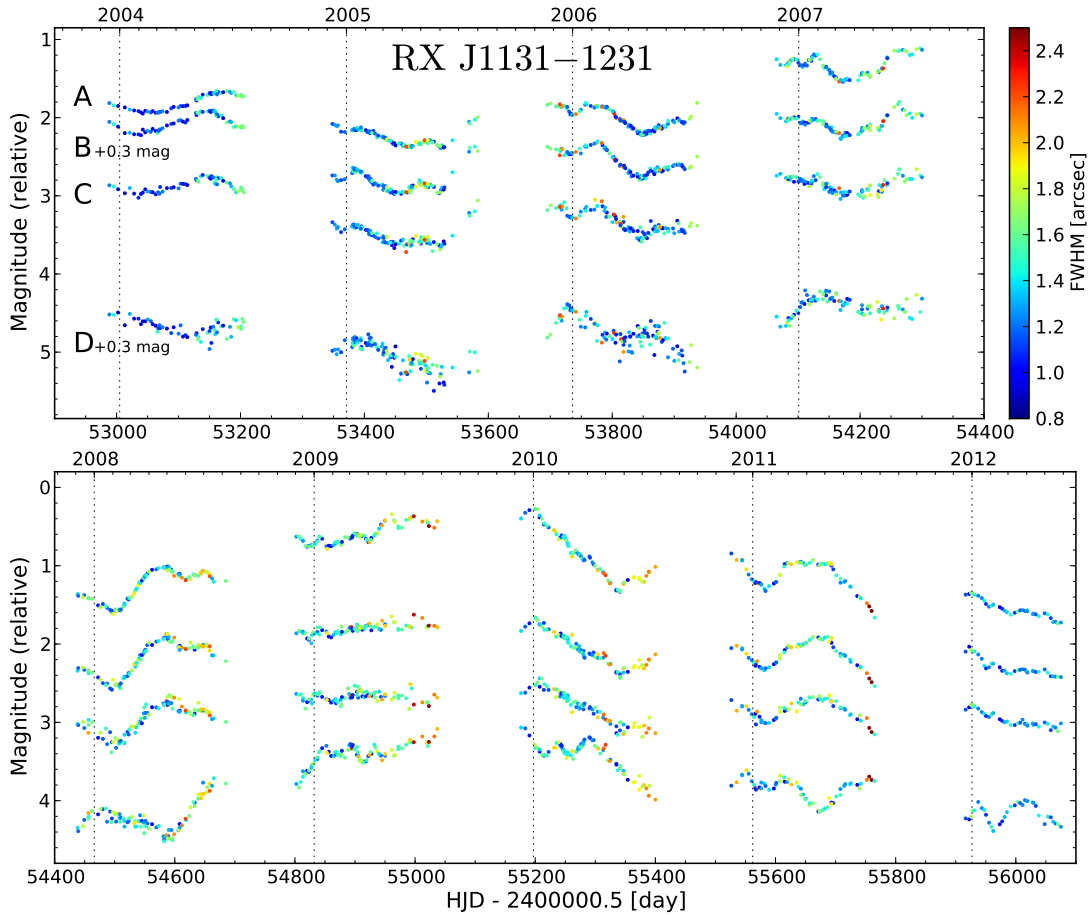


Figure 3.1: The light curves of RX J1131–1231 ( $z_{\text{lens}} = 0.295$ ,  $z_{\text{QSO}} = 0.658$ ). These are the same data points as shown in Fig. 4 of Tewes et al. (2012c), but color-coded according to the spatial resolution of the exposures. For this relatively large and bright lens, our photometric pipeline is able to recover good measurements even from images beyond  $2''.0$  of Full Width at Half Maximum (FWHM) of the point spread function.

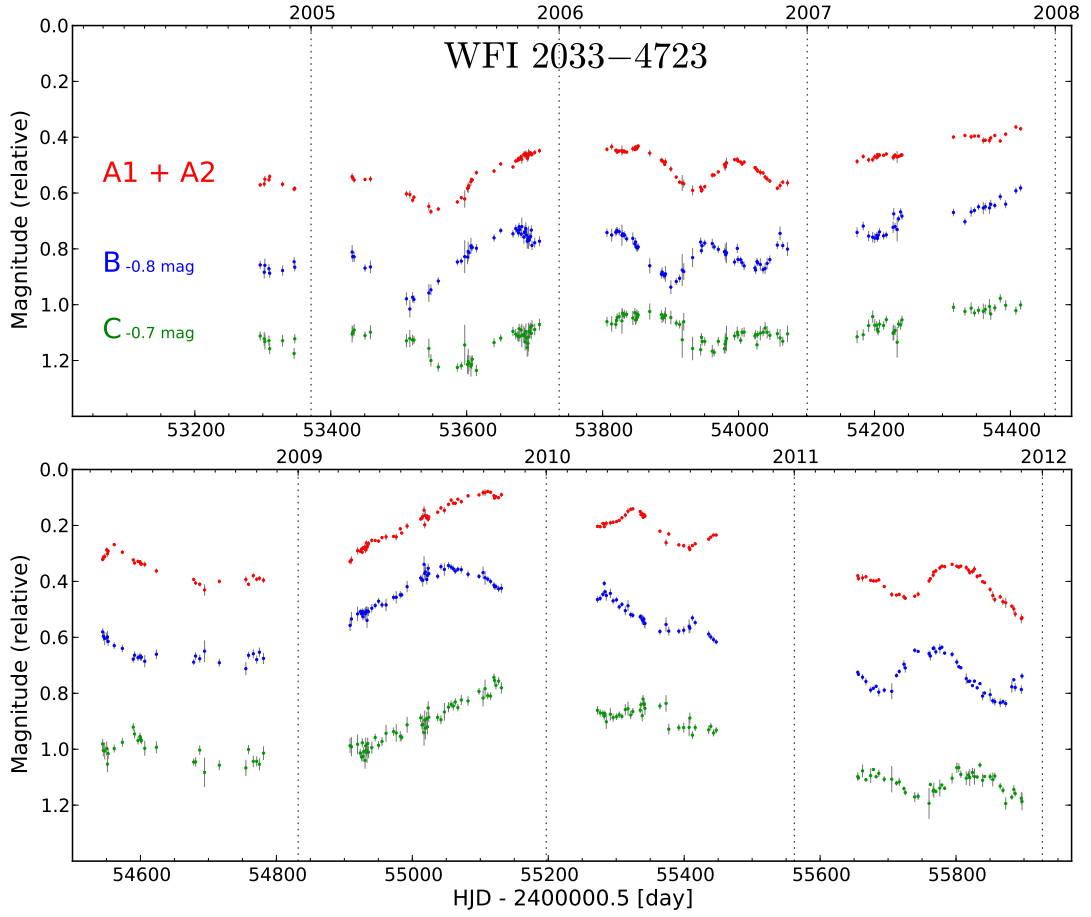


Figure 3.2: The light curves of WFI 2033–4723 ( $z_{\text{lens}} = 0.661$ ,  $z_{\text{QSO}} = 1.66$ ), from the Euler telescope. WFI 2033–4723 is a quadruply lensed quasar in “fold” configuration. The quasar images A1 and A2 are separated by only  $0.7''$  and should have very small time delays (Vuissoz et al. 2008). Therefore, for the purpose of time delay measurements with respect to B and C, their fluxes are shown here summed into one single light curve.

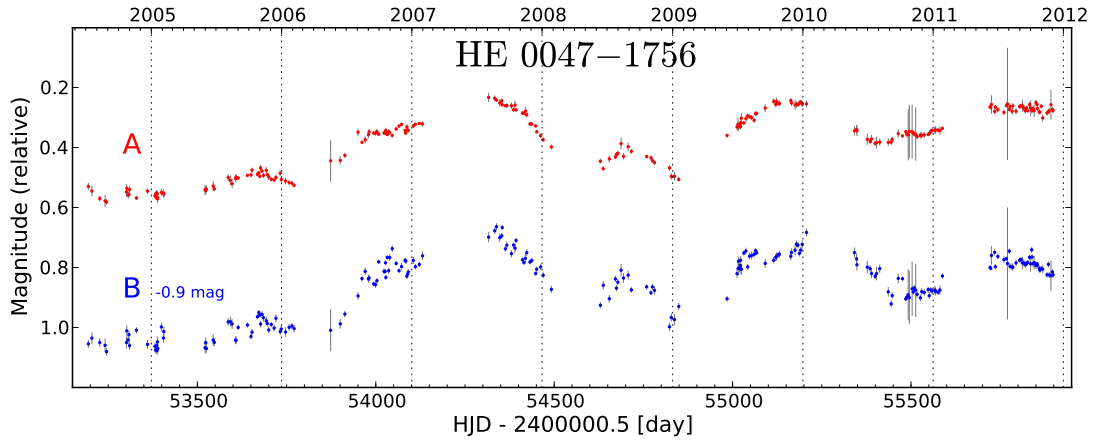


Figure 3.3: The double HE 0047–1756 ( $z_{\text{lens}} = 0.407$ ,  $z_{\text{QSO}} = 1.67$ ), from the Euler telescope.



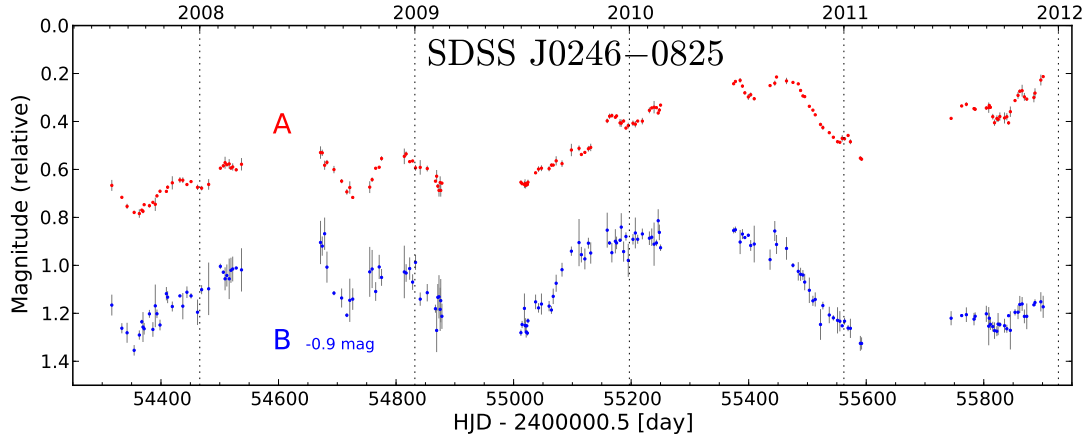


Figure 3.4: The light curves of the double SDSS J0246-0825 ( $z_{\text{lens}} = 0.723$ ,  $z_{\text{QSO}} = 1.68$ ), from the Euler telescope.

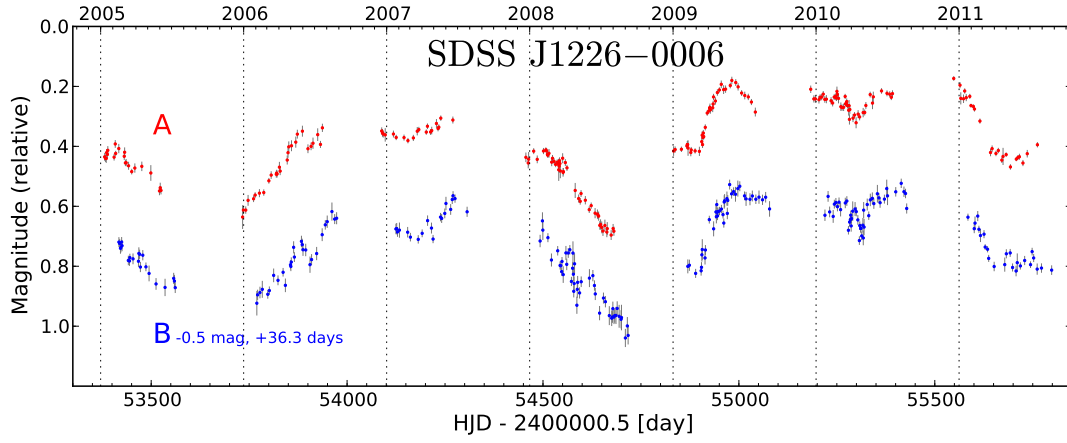


Figure 3.5: The light curves of the double SDSS J1226-0006 ( $z_{\text{lens}} = 0.517$ ,  $z_{\text{QSO}} = 1.125$ ), from the Euler telescope. The B curve is shifted by a plausible time delay. Note the sharp intrinsic variability feature in the 2009 season.

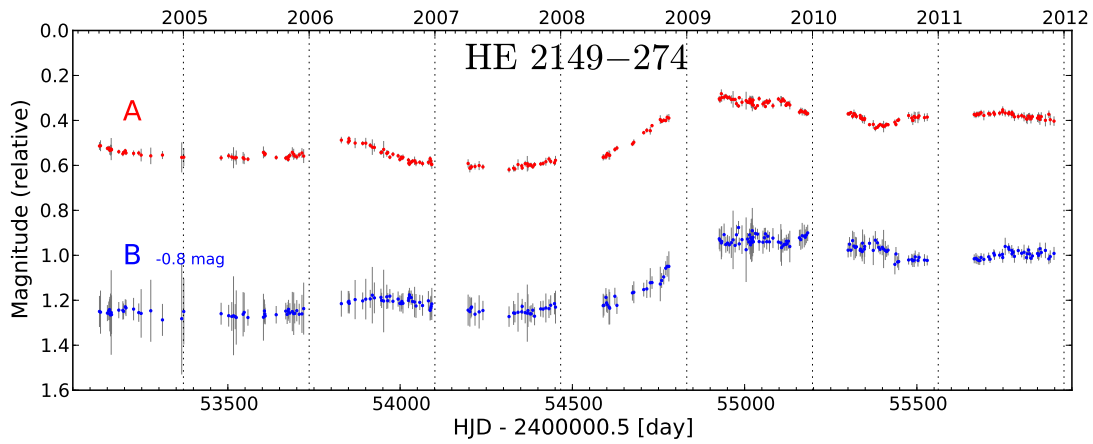


Figure 3.6: The light curves of the double HE 2149-274 ( $z_{\text{lens}} = 0.603$ ,  $z_{\text{QSO}} = 2.03$ ), from Euler.



### 3.1. Selected light curves

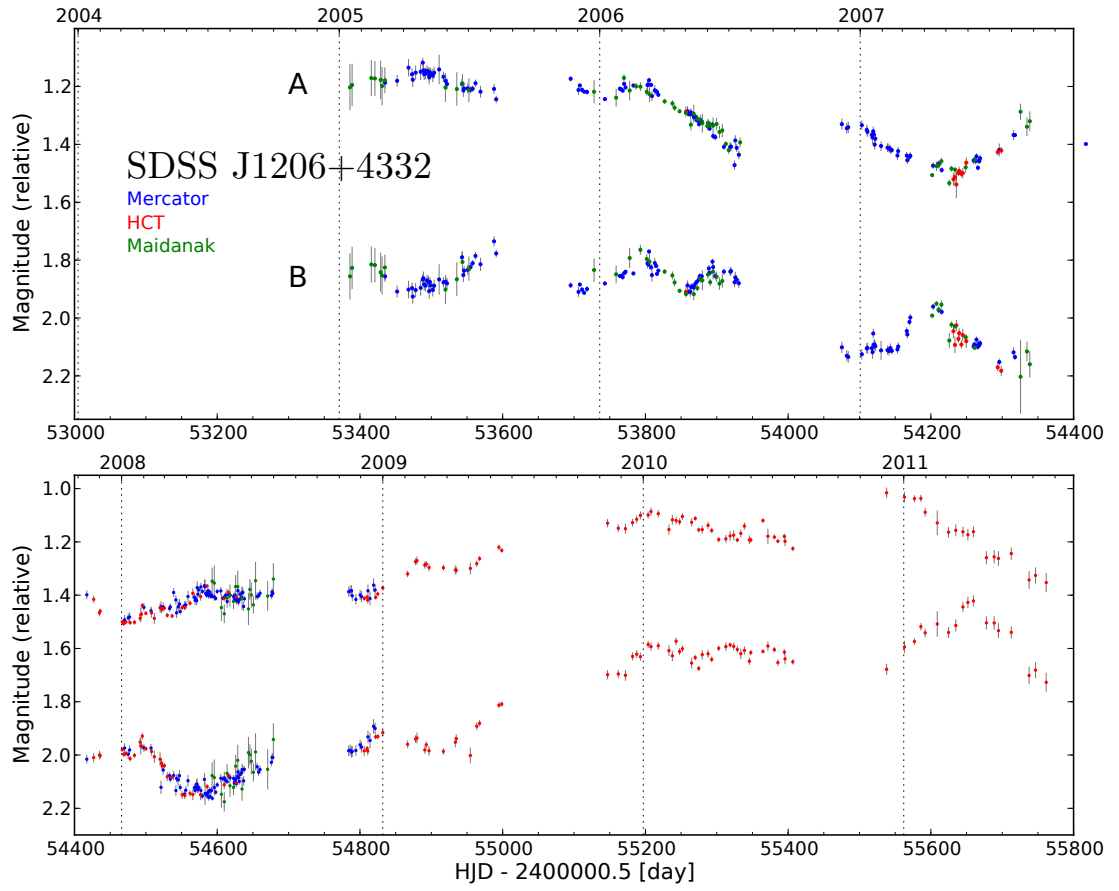


Figure 3.7: The light curves of the northern double SDSS J1206+4332 ( $z_{\text{lens}} \approx 0.75$ ,  $z_{\text{QSO}} = 1.79$ ). E. Eulaers, M. Tewes et al. (2012, in prep).

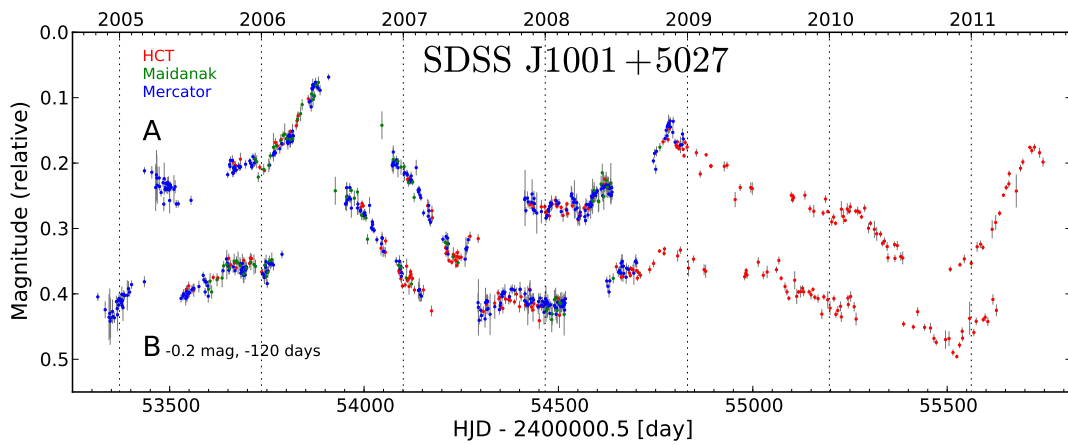


Figure 3.8: The light curves of the northern double SDSS J1001+5027 ( $z_{\text{QSO}} = 1.839$ ). The curve B is shown shifted by 120 days. R. K. S. Keerthi, M. Tewes et al. (2012, in prep).



# COSMOGRAIL: the COSmological Monitoring of GRAvitational Lenses<sup>★,★★</sup>

## XII. Time delays and 9-yr optical monitoring of the lensed quasar RX J1131–1231

M. Tewes<sup>1</sup>, F. Courbin<sup>1</sup>, G. Meylan<sup>1</sup>, C. S. Kochanek<sup>2,3</sup>, E. Eulaers<sup>4</sup>, N. Cantale<sup>1</sup>, A. M. Mosquera<sup>2,3</sup>, P. Magain<sup>4</sup>, H. Van Winckel<sup>5</sup>, D. Sluse<sup>6</sup>, G. Cataldi<sup>1</sup>, D. Vörös<sup>1</sup>, and S. Dye<sup>7,8</sup>

<sup>1</sup> Laboratoire d’astrophysique, Ecole Polytechnique Fédérale de Lausanne (EPFL), Observatoire de Sauverny, 1290 Versoix, Switzerland, e-mail: malte.tewes@epfl.ch

<sup>2</sup> Department of Astronomy, The Ohio State University, 140 West 18th Av., Columbus, OH 43210, USA

<sup>3</sup> Center for Cosmology and Astroparticle Physics, The Ohio State University, 191 West Woodruff Av., Columbus, OH 43210, USA

<sup>4</sup> Institut d’Astrophysique et de Géophysique, Université de Liège, Allée du 6 Août, 17, 4000 Sart Tilman, Liège 1, Belgium

<sup>5</sup> Instituut voor Sterrenkunde, Katholieke Universiteit Leuven, Celestijnenlaan 200B, 3001 Heverlee, Belgium

<sup>6</sup> Argelander-Institut für Astronomie, Auf dem Hügel 71, 53121, Bonn, Germany

<sup>7</sup> School of Physics and Astronomy, University of Nottingham, University Park, Nottingham NG7 2RD, UK

<sup>8</sup> Cardiff University, School of Physics and Astronomy, Queens Buildings, The Parade, Cardiff, CF24 3AA, UK

Received ; accepted

### ABSTRACT

We present the results from 9 years of optically monitoring the gravitationally lensed  $z_{QSO} = 0.658$  quasar RX J1131–1231. The R band light curves of the 4 individual images of the quasar are obtained using deconvolution photometry, for a total of 707 epochs. Several sharp quasar variability features strongly constrain the time delays between the quasar images. Using three different numerical techniques, we measure these delays for all possible pairs of curves, while always processing the 4 curves simultaneously. For all three methods, the delays between the 3 close images A, B and C are compatible with being 0, while we measure the delay of image D to be 91 days, with a fractional uncertainty of 1.5% ( $1\sigma$ ), including systematic errors. Our analysis of random and systematic errors accounts in a realistic way for the observed quasar variability, fluctuating microlensing magnification over a broad range of temporal scales, noise properties, and seasonal gaps. Finally, we find that our time delay measurement methods yield compatible results when applied to subsets of the data.

**Key words.** Gravitational lensing: strong – cosmological parameters

### 1. Introduction

Using the time delays between strong lensing images to measure cosmological distances (Refsdal 1964) has a number of advantages: there is no need for any primary or secondary calibrator, and there are no effects from the intergalactic or interstellar medium. The method, originally proposed for gravitationally lensed supernovae, has so far exclusively been applied to quasars lensed in most cases by individual massive galaxies. Exceptions are SDSS J1004+4112 and J1029+2623, two quasars lensed by galaxy clusters, with long time delays (Fohlmeister et al. 2008, 2012). The quasar lens time delay method is now recognized as a tool that complements other cosmological probes, in particular to constrain  $H_0$  as well as the dark energy equation of state parameter,  $w$  (e.g., Suyu et al. 2012b; Linder 2011; Moustakas et al.

2009). In spite of its advantages, the method has long faced two severe limitations to its effectiveness in constraining cosmology.

First, time delays between the gravitationally lensed images of a quasar are hard to measure. The first time delay measurements were quite controversial (Vanderriest et al. 1989; Press et al. 1992; Schild & Thomson 1997; Kundic et al. 1997). Understandably, early light curves tended to be short and sparse, often too short to clearly demonstrate that *microlensing* variability was not interfering with their analysis. Microlensing is seen as an uncorrelated extrinsic variability in the quasar images, which results from the time-variable magnification created by stars in the lensing galaxy (e.g., Chang & Refsdal 1979; Schmidt & Wambsganss 2010). In the best cases, light curves spanned a few years (see, e.g., Wyrzykowski et al. 2003; Hjorth et al. 2002; Burud et al. 2002a,b). One consequence is that the numerical methods used to measure time delays from these light curves were exceedingly “optimistic” in their assumptions about extrinsic variability. Later measurements with better data frequently yielded delays inconsistent with the error estimates of the earlier measurements.

Second, given measured time delays, and lens and quasar image astrometry, there is a famed degeneracy between the *time delay distance*, which is a scale parameter inversely proportional to  $H_0$ , and the spatial distribution of mass responsible for the

<sup>★</sup> Based on observations made with the 1.2-m Swiss Euler telescope (La Silla, Chile), the 1.3-m SMARTS telescope (Las Campanas, Chile), and the 1.2-m Mercator Telescope. Mercator is operated on the island of La Palma by the Flemish Community, at the Spanish Observatorio del Roque de los Muchachos of the Instituto de Astrofísica de Canarias.

<sup>★★</sup> Light curves will be available at the CDS via anonymous ftp to cdsarc.u-strasbg.fr (130.79.128.5) or via <http://cdsarc.u-strasbg.fr/viz-bin/qcat?J/A+A/???>, and on <http://www.cosmograil.org>.

strong lensing phenomenon. The delays constrain only a combination of this time delay distance and the surface density of the lens near the images (Kochanek 2002). This can be overcome given independent constraints on the structure of the lens. Suyu et al. (2009, 2010) convincingly show that it is possible to control the effects of model degeneracies in the case of B1608+656, a quadruply imaged quasar with accurate radio time delays (Fassnacht et al. 2002). To do this, the authors combine (1) detailed HST images of the lensed quasar host galaxy, (2) a velocity-dispersion measurement of the lens galaxy, and (3) information about the contribution of intervening galaxies along the line of sight, from galaxy number counts calibrated with numerical simulations.

In parallel to the advances in lens modeling, the observational situation has drastically evolved as well. Two observational groups, COSMOGRAIL and Kochanek et al. (2006), have been intensely monitoring  $\approx 20$  lenses for roughly 10 years. In 2010, our 2 groups decided to merge their observational efforts, with the COSMOGRAIL group focusing on the analysis of time delays and the Kochanek et al. group focusing on the analysis of microlensing. While preliminary results have been published both before and after this merger (Kochanek et al. 2006; Vuissoz et al. 2007, 2008; Morgan et al. 2008a,b), exquisite data spanning almost a decade of continuous observation are now being released, such as for the quadruply imaged quasar HE 0435-1223 (Courbin et al. 2011; Blackburne et al. 2011).

In this paper, we present 9 years of optical monitoring of the quadruply imaged quasar RX J1131–1231 (Sluse et al. 2003), and measure its time delays with the techniques of Tewes et al. (2012). RX J1131–1231 is one of the most spectacular lenses of our sample. The redshift of the lensing galaxy is  $z_{\text{lens}} = 0.295$ , while the quasar is at  $z_{\text{QSO}} = 0.658$ . This low quasar redshift means (1) that the photometric variations are fast, numerous and *strong* because it is a lower luminosity quasar (see, e.g., MacLeod et al. 2010), and (2) that the host galaxy of the lensed quasar is seen as a full Einstein ring with many spatially resolved structures in HST images. Similarly, the lensing galaxy is sufficiently bright to allow a precise measurement of its velocity dispersion and possibly of its velocity dispersion profile. These characteristics ease both the time delay measurement and the lens modeling. The latter, with state-of-the-art inferences of cosmological constraints based on our time delay measurements of RX J1131–1231, are presented in Suyu et al. (2012a).

The COSMOGRAIL and SMARTS observations of RX J1131–1231 and their reduction are described in Sections 2 & 3, while the light curves are presented in Section 4. In Section 5, we apply three different curve shifting techniques to the light curves and we infer our best measurements of the delays along with realistic random and systematic error bars. Our results are summarized in Section 6.

## 2. Observations

We have been monitoring the quadruply lensed quasar RX J1131–1231 (J2000:  $11^{\text{h}}31^{\text{m}}52^{\text{s}}$ ,  $-12^{\circ}31'59''$ ) since December 2003 with 3 different telescopes in the R band ( $\sim 600 - 720$  nm). Table 1 summarizes the observational strategy and instrumental characteristics. The light curves presented in this paper cover 9 observing seasons (2004 - 2012, see Fig. 4), with 707 monitoring epochs in total. The average sampling within the seasons is 2.9 days, and the median sampling is 2.0 days. The mean seasonal gap in the combined light curves is of 132 days, with a standard deviation of 2 weeks.

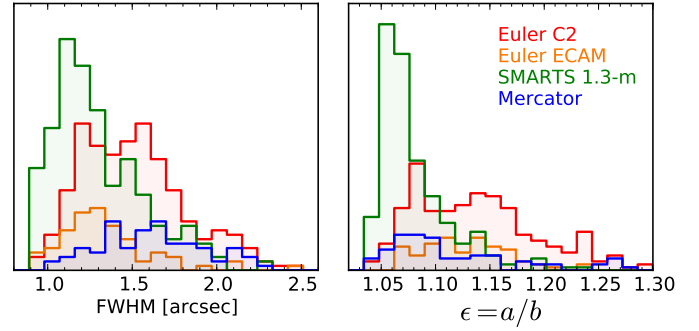


**Fig. 1.** Distributions of stellar FWHM and elongation  $\epsilon$  of all images contributing to the light curves, by telescope.

The majority of the measurements for this southern target came from the Swiss 1.2-m Euler telescope and the SMARTS 1.3-m telescope, both located in Chile under equally good atmospheric conditions. Fig. 1 shows the distributions of stellar Full Width at Half Maximum (FWHM) and elongation  $\epsilon$  of the each observing epoch, as measured by SExtractor (Bertin & Arnouts 2010) using field stars. The SMARTS 1.3-m telescope is guided, in contrast to Euler and Mercator, which are solely tracking. This accounts in part for the broad elongation distribution of the Euler and Mercator images.

The imaging instrument C2 of the Euler telescope was replaced in September 2010 by *EulerCAM*, a liquid nitrogen cooled  $4\text{k} \times 4\text{k}$  e2v 231-84 CCD yielding a pixel scale of  $0''.215$ . At the same time the focusing procedure has been improved. Fig. 1 shows that after two years of observations, images from *EulerCAM* tend to be statistically sharper than C2 images, and more comparable to SMARTS 1.3-m data in terms of FWHM. All images from the SMARTS 1.3-m telescope were obtained through the optical channel of the ANDICAM<sup>1</sup> camera (DePoy et al. 2003). See Kochanek et al. (2006) for details about the SMARTS data.

Fig. 2 shows the central part of a deep combination of Euler monitoring images, totaling 2.5 days of exposure. In the best individual exposures the 4 quasar images are well resolved; images A and B have the smallest separation of  $1''.2$ .

## 3. Image reduction

In this section we describe the reduction procedure leading to the light curves of the multiple quasar images of RX J1131–1231. This same procedure will homogeneously be applied to other lenses monitored by COSMOGRAIL and SMARTS, hence we also focus on general aspects in our description.

All exposures are corrected for bias/readout effects and flat fielded using standard methods. This prereduction is done individually for each telescope and instrument. For Euler and Mercator we have developed custom python pipelines that enable efficient human inspection and validation of each step. Particular attention is given to a semi-automated selection and combination of sky-flats, which is controlled through a simple graphical interface highlighting the temporal evolution of instrumental contaminations such as dust. Using difference images we check that all sources in the flatfield exposures are adequately masked and that the contamination does not evolve significantly within sets of flatfields that are stacked as master-flats. The period over which we stack flatfields can be from single days to

<sup>1</sup> <http://www.astronomy.ohio-state.edu/ANDICAM/>

**Table 1.** Overview of our optical monitoring of RX J1131–1231

Telescope	Location	Instrument	Pixel scale	Field	Exp. time	Epochs	Sampling
Euler 1.2 m	ESO La Silla, Chile	C2	0.344''	11' × 11'	5 × 360s	265	5.0 (4.0)
Euler 1.2 m	ESO La Silla, Chile	EulerCAM	0.215''	14' × 14'	5 × 360s	76	5.4 (4.1)
SMARTS 1.3 m	CTIO, Chile	ANDICAM	0.369''	6.1' × 6.1'	3 × 300s	288	6.1 (5.1)
Mercator 1.2 m	La Palma, Canary Islands, Spain	MEROPE	0.193''	6.5' × 6.5'	5 × 360s	78	8.9 (4.5)

**Notes.** The column “Exp. time” indicates the number of dithered exposures *per epoch* and their individual exposure times. One epoch corresponds to one data point in each light curve. The temporal sampling of the observations is given as the average (median) number of days between consecutive epochs, excluding the seasonal gaps.

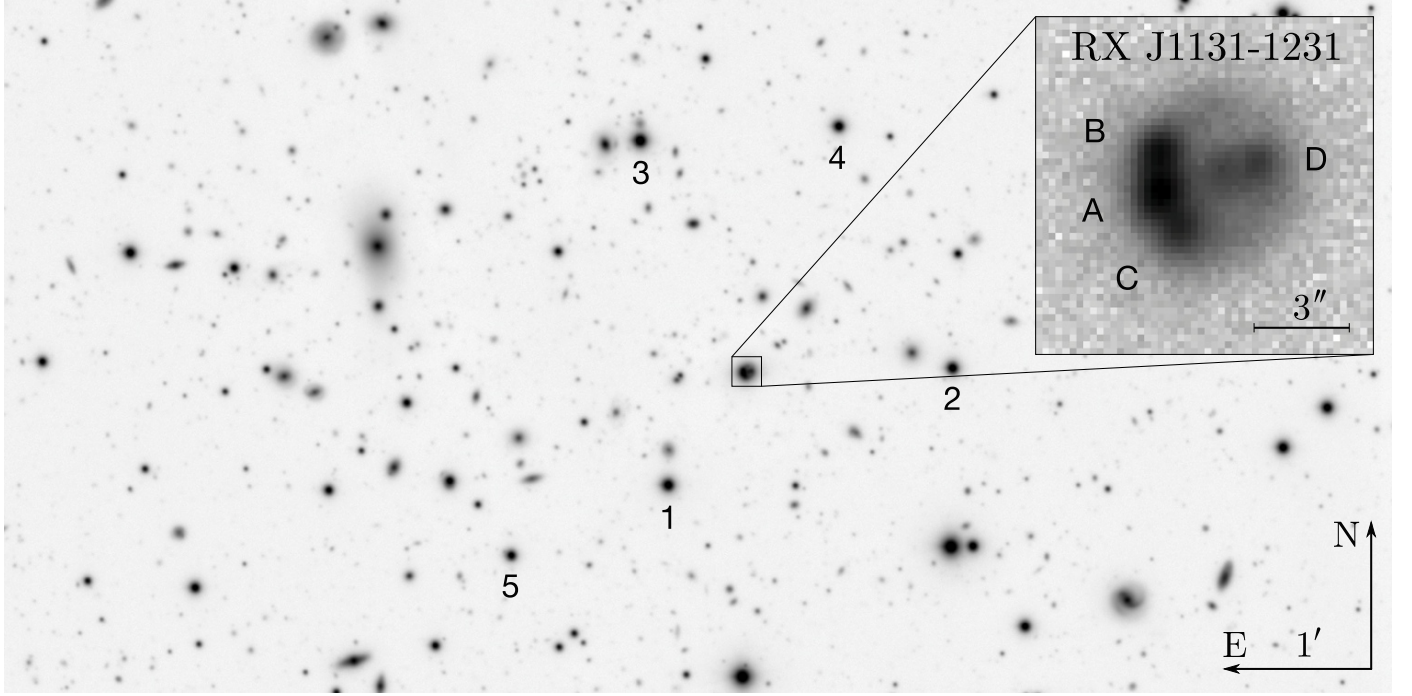


**Fig. 2.** Part of the field of view of the Swiss 1.2-m Euler telescope around RX J1131–1231. The wide-field image is a combination of 600 exposures of 360s each, corresponding to a total exposure time of 2.5 days. The inset shows a single 360s exposure of the *EulerCAM* instrument under good conditions (FWHM~1'',  $\epsilon = 0.1$ , no Moon). All images are taken in the R band. We mainly use the stars labeled 1 to 4 to build a PSF model for each exposure. Stars 1 to 5 are used for the photometric calibration.

several weeks. Some exposures of the Mercator telescope are prereduced using “superflats”, combinations of masked science exposures obtained in a single night. We have developed variants of these pipelines adapted to the particularities of other COSMOGRAIL telescopes.

From here on, all images are processed by a single deconvolution photometry software package. The principle ideas for this reduction procedure are the same as employed for previously published COSMOGRAIL light curves (Vuissoz et al. 2007, 2008; Courbin et al. 2011). Over the years we have reworked the steps, and implemented the procedure in the form of a *python* pipeline linked to a relational database, containing one “row” per exposure.

### 3.1. PSF construction

We first build a conservatively smooth sky model, obtained using SExtractor, for each exposure. This sky model is not critical, as the subsequent photometry procedure will fit for any residual sky level around all sources of interest.

We then align the images, separately for each instrument, and individually estimate the Point Spread Function (PSF) of each exposure. This is done by fitting several field stars using a common model, composed of (i) a simply parametrized profile and (ii) a regularized fine pixel array. The details of this procedure, which is part of a general purpose deconvolution package, are described in Cantale et al. (in prep). For most of the exposures of RX J1131–1231, we use the stars labeled 1 - 4 in Fig. 2 to build the PSF model. The pipeline allows us to easily explore and compare different choices of PSF-stars. The final choice of stars is empirically selected so as to yield the least scatter in the final quasar light curves. In the case of RX J1131–1231 the situation is close to optimal, since (1) the stars 1 - 4 are bright but still in the linear regime of the CCDs, (2) they surround the lens at modest angular distances, and (3) all stellar companions or background objects can be identified and masked, yielding clean fitting residuals. Cosmic ray hits and CCD artifacts are automatically masked using a variant of the L.A. Cosmic algorithm (van Dokkum 2001). We visually supervise the PSF construction and manually adapt the selection of PSF-stars for problematic frames. The construction of the PSF models is the predominant technical issue affecting the final quality of the light curves.

### 3.2. Photometric normalization of the exposures

We next compute a multiplicative normalization coefficient for each exposure, based on photometry of field stars. These coefficients will constitute the reference for the differential photometry of the quasar images.

In a first step, this computation is done separately for each instrument. We measure the instrumental fluxes  $N_{\star ij}$  (in photons) of star  $i$  in each exposure  $j$ , by fitting the PSF $_j$  of this exposure to each star, leaving only the fluxes, astrometric shifts, and background levels of each star as free parameters. For each star and exposure, we then compute an individual coefficient

$$c'_{ij} = \frac{\text{med}_j(N_{\star ij})}{N_{\star ij}}, \quad (1)$$

where  $\text{med}_j$  denotes the median over all exposures of this instrument. Then, for each exposure  $j$ , we obtain the normalization coefficient through

$$c_j = \text{med}_i(c'_{ij}). \quad (2)$$

The advantages of this simple and fast method is that it does not select a single exposure as the “reference” for all stars. For each instrument, the distribution of these coefficients  $c_j$  is highly unimodal, as the exposure time is kept constant.

To select the normalization stars we first inspect the normalized stellar light curves for any anomalies or variability on scales of months or years, and, if required, we iteratively repeat the coefficient computation with a refined selection of stars. In terms of the smoothness of the final quasar light curves, the best results are generally obtained by computing these coefficients from a few well exposed stars with a comparable and high signal-to-noise ratio, as opposed to using larger numbers of noisier stars. Furthermore, the ideal normalization stars should be of similar color to the quasar. This minimizes potential differential effects due to varying atmospheric conditions given the relatively broad R band filters used for the monitoring.

In a second step, we rescale the coefficients of each instrument so that a star whose color is closest to the quasar gets the same normalized median flux across all instruments. Residual adjustments to this normalization between instruments will be performed later, using the quasar light curves in the regions where the data from different telescopes overlap.

### 3.3. Photometry of the quasar images

We obtain deblended light curves of the quasar images by *MCS deconvolution photometry*, following Magain et al. (1998). This algorithm fits a single model consisting of (1) some number of point sources and (2) a fine pixel array (hereafter the *pixel channel*) simultaneously to all exposures. In the case of RX J1131–1231, 4 point sources depict the quasar images, while the pixel channel represents both the lensing galaxy and the Einstein ring. This model is scaled by the normalization coefficients, and convolved by the specific PSFs, before being fit to the corresponding exposures. By construction, the relative astrometry of the 4 point sources and the pixel channel are common to all exposures. Only the fluxes of the point sources, the absolute astrometric shift, and a flat residual sky level around the lens are free to vary between exposures. Iteratively, all these parameters are optimized, together with the structure of the regularized pixel channel, so as to minimize a single global  $\chi^2$ . This algorithm has been successfully applied already in the discovery paper of RX J1131–1231 (Sluse et al. 2003), as well as in

past COSMOGRAIL publications (e.g., Eigenbrod et al. 2007; Vuissoz et al. 2008; Courbin et al. 2011; Sluse et al. 2012) or for similar monitoring data (Burud et al. 2002a; Hjorth et al. 2002; Jakobsson et al. 2005; Morgan et al. 2012). The light curves of the quasar images are a direct output of this procedure.

Errors in the astrometry or the structure of the pixel channel might degrade or bias the photometry of the quasar images. We observe that the influence of the astrometry on the light curves is small. Even for bright quasar images, alterations of the relative position of the point sources by as much as  $0''.05$  do not significantly modify the light curves. Larger errors tend first to smoothly bias the magnitude measurements, before introducing additional scatter. To obtain light curves for gravitational lenses with image separations on the order of the resolution of the best monitoring data, we find no difference between using the tight astrometric constraints from HST images (Chantry et al. 2010) or letting the deconvolution algorithm freely optimize the astrometry of the model.

We reach similar conclusions about the impact of the pixel channel, and its mandatory regularization. Simple numerical experiments show that to first order, the effect of different plausible solutions is similar to very small additive shifts to the flux of the light curves, with only marginally perceptible effects even for faint quasar images. In practice we systematically constrain this pixel channel as well as the point source astrometry using only a subset of images with the best resolution.

### 3.4. Photometric error estimation

In this section we describe how we compute a rather formal “best case” error estimate for the photometry of each quasar image in each exposure. The normalized flux of a quasar image in a given exposure can be written  $f_\star = N_\star \cdot c$ , where  $N_\star$  is the measured number of photons, and  $c$  is the normalization coefficient from Equation 2. We assume that the random error on  $f_\star$  has two independent sources: (i) the shot noise  $\sigma_{N_\star}$  of the quasar image itself, and (ii) the noise  $\sigma_c$  of the normalization coefficient as computed in Section 3.2.

We compute  $\sigma_{N_\star}$  following the standard “CCD equation” (see e.g. Howell 2006, chap. 4.4)

$$\sigma_{N_\star} = \sqrt{N_\star + n_{\text{pix}} \cdot (S + R^2)} \quad (3)$$

where  $S$  is the sky level,  $R$  is the CCD read noise (both in photons per pixel), and  $n_{\text{pix}}$  is the number of (equivalent) pixels of the software aperture. The dark current is negligible in our images. MCS deconvolution of point sources corresponds to PSF fitting, and following Heyer & Biretta (2004, section 6.5.1) we use for  $n_{\text{pix}}$  the reciprocal of the PSF *sharpness*,

$$\frac{1}{n_{\text{pix}}} = \sum_{l,m} (\text{PSF}_{lm})^2, \quad (4)$$

where  $\text{PSF}_{lm}$  is the fraction of light in the total PSF at pixel  $lm$ . In this simple “best case” computation, we assume that the PSF is perfectly known, and that the sky level is well determined by the fitting procedure. We do not take into account the flux of the lensing galaxy, which is generally negligible with respect to the sky level. Furthermore we do not compute noise terms due to the blending with other point sources.

As a sanity check, we have tested our deconvolution photometry algorithm on simulated point source images created with *SkyMaker* (Bertin 2009), for various realistic signal-to-noise ratios, elongations, and seeing conditions. Using 2 or more well-exposed stars to build the PSF, the statistical scatter obtained by



our photometry is only marginally larger than the best-case shot noise computed through the above procedure. Using similar synthetic images, we have also verified that deconvolving two partially blended sources of different fluxes does not significantly bias their measured flux difference in any direction.

To estimate the random uncertainty of the normalization coefficient, we use the standard error of the mean (SEM) of the individual coefficients obtained from the  $n$  normalization stars in the exposure (see Equation 1)

$$\sigma_c = \frac{s}{\sqrt{n}} \quad \text{where} \quad s^2 = \frac{1}{n-1} \sum_{i=1}^n (c'_i - \bar{c})^2. \quad (5)$$

Finally we obtain the error estimated  $\sigma_{f_\star \text{ CCD}}$  on the normalized flux through

$$\frac{\sigma_{f_\star \text{ CCD}}^2}{f_\star^2} = \frac{\sigma_{N_\star}^2}{N_\star^2} + \frac{\sigma_c^2}{c^2}. \quad (6)$$

Note that for our COSMOGRAIL and SMARTS monitoring data, the shot noise term from the CCD equation dominates this error budget. The contribution from  $\sigma_c$  is typically  $\ll 3\%$  of  $\sigma_{f_\star \text{ CCD}}$ . Such small calibration errors are particularly important when measuring very short delays, as they would introduce positively correlated noise into the curves.

### 3.5. Combination of points per night

In each monitoring night, we observe the lenses  $m$  times in a row ( $m = 3$  or  $5$ ), over  $\approx 30$  minutes, yielding flux measurements  $f_{\star k}$ , with  $k = 1, \dots, m$  for each quasar image. To reduce the CPU cost and to reject outliers, we bin these measurements by epochs, separately for each instrument and telescope, before measuring the time delays. We attribute to each epoch the *medians* of the photometric measurements  $f_{\star k}$  within that night, and the mean of the Heliocentric Julian Dates (HJD).

This approach also allows us to obtain an empirical photometric error estimate for each quasar image, using a measure of the spread of the image's  $f_{\star k}$ . For increased robustness against outliers, we quantify this spread using the Median Absolute Deviation from the median, or *MAD* (Hoaglin et al. 1983),

$$\text{MAD}(f_{\star k}) = \text{med}(|f_{\star k} - \text{med}(f_{\star k})|). \quad (7)$$

To estimate the usual  $\sigma$  of an (assumed) Gaussian distribution, the MAD is rescaled as

$$\sigma_{f_\star \text{ MAD}} = 1.4826 \cdot \text{MAD}(f_{\star k}). \quad (8)$$

These procedures give us two different error estimates for each epoch and for each quasar image: (1) the median of the errors estimated individually for each exposure  $\text{med}(\sigma_{f_\star \text{ CCD}})$ , and (2) the more empirical  $\sigma_{f_\star \text{ MAD}}$ . We observe, as expected, that both error estimations are highly correlated, but also that the empirical  $\sigma_{f_\star \text{ MAD}}$  is typically twice as big.

The uncertainty we finally assign to each epoch and quasar image uses the larger of  $\text{med}(\sigma_{f_\star \text{ CCD}})$  and  $\sigma_{f_\star \text{ MAD}}$ . Indeed a realistic error estimate cannot be smaller than either of them. We divide this estimate by the square root of the number of exposures  $m$  of the epoch, so that the final error estimate for the median photometric measurement is

$$\sigma_{\text{med}(f_\star)} = \frac{\max[\text{med}(\sigma_{f_\star \text{ CCD}}), \sigma_{f_\star \text{ MAD}}]}{\sqrt{m}}. \quad (9)$$

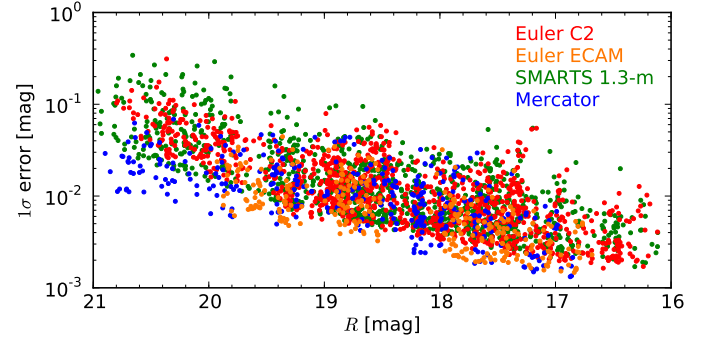


**Fig. 3.** Photometric  $1\sigma$  error estimates of each observing epoch as a function of approximate R band magnitude. These errors are estimated following Equation 9.

Fig. 3 displays the distribution of the resulting error estimates as a function of R band magnitude and instrument. The data points from all 4 quasar images of RX J1131–1231 are shown, yielding a broad spread in magnitudes.

### 3.6. Combination of telescopes

The lens galaxy and the lensed images of the quasar host galaxy differ in color from the quasar itself. As a consequence, the different R filters and CCD response functions of the monitoring instruments might “see” these contaminating sources with slightly different amplitudes even with a perfect calibration of the quasar fluxes. This can result in small mismatches between the light curves obtained using different combinations of telescopes and instruments.

We correct our light curves for such small effects ( $\lesssim 10\%$  of the flux of faint quasar images) in this final step. We typically select the instrument that yields the longest or the highest quality curve as a reference. For each of the other instruments, we optimize additive magnitude and flux shifts (i.e., multiplicative and additive flux corrections) so to minimize a *dispersion measure* between each instrument’s light curve and the reference light curve. We compute this dispersion following the curve shifting technique presented in Tewes et al. (2012), but evaluate it between the light curves of different *instruments*, instead of different quasar images. Provided that the colors of the quasar images are not differentially reddened by absorption in the lens galaxy, we optimize a single common magnitude shift per instrument, and individual flux shifts for each quasar image and instrument. This is adequate for RX J1131–1231, as previously suggested by Sluse et al. (2007) and Chartas et al. (2009).

## 4. The light curves of RX J1131–1231

All these steps were applied to the COSMOGRAIL and SMARTS data for RX J1131–1231. Fig. 4 shows the final 9-year long light curves of the 4 quasar images. The light curves are dominated by intrinsic quasar variability, with some features on scales as fast as a few weeks. It can be readily seen in the 2008 season for instance, that the delays between A, B and C must be very small, while D is delayed by a bit less than 100 days. Intriguingly, looking only at the first season of A, B and C, one might guess that A is significantly delayed with respect to B and C. We attribute this discrepancy to microlensing variability, which manifestly changes the magnitude difference between the A and B images from the first to the second season. We discuss this “event” further in Section 5.3. Prominent microlensing

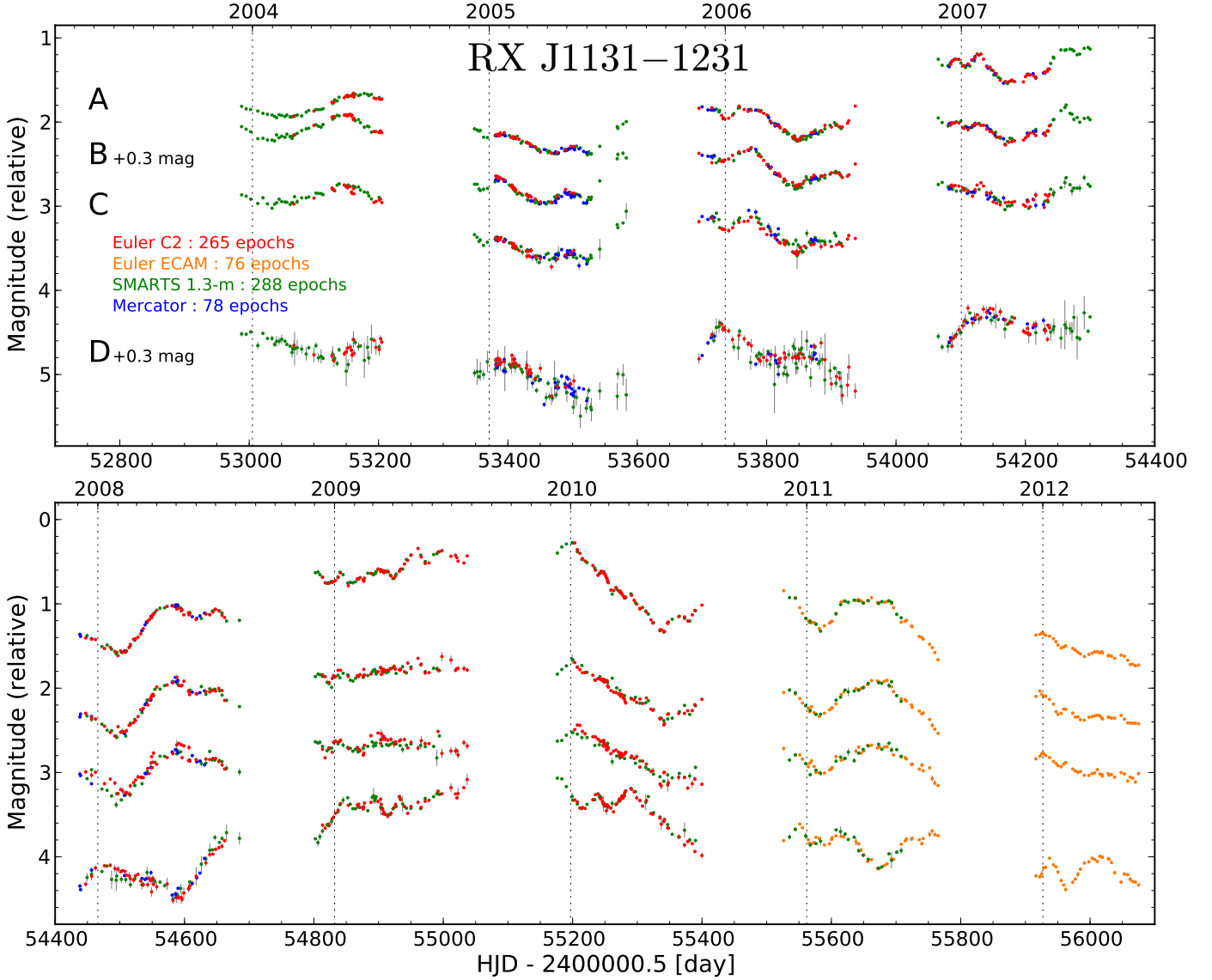


**Fig. 4.** Optical monitoring of RX J1131–1231, as obtained from deconvolution photometry. From top to bottom are shown the R band light curves for the quasar images A, B, C, D along with the  $1\sigma$  photometric error bars. Colors encode the contributing instruments. Curves B and D have been shifted by +0.3 magnitudes for display purposes. The light curves are available in tabular form from the CDS and the COSMOGRAIL website.

variability on large time scales is omnipresent, as the flux ratios between the quasar images evolve by as much as a magnitude. These microlensing effects in RX J1131–1231 have been analyzed in Morgan et al. (2010) and Dai et al. (2010).

Lastly, we observe that the photometric error estimates, obtained from equation 9, match the observed scatter well in the smooth sections of curves from the individual telescopes. They are certainly not conservatively large, but we stress that the scale of these error estimates has *no* direct influence on the uncertainties that we will compute for the time delay measurements in the next Section. Our results are robust against a deliberate increase of these error estimates by up to a factor of 5.

## 5. Time delay estimation

In this section we infer the time delays of RX J1131–1231 from our light curves of Fig. 4, closely following the curve shifting and uncertainty evaluation procedures described in Tewes et al. (2012). We summarize the principal ideas below. A major dif-

ficulty, and potential source of bias, for curve shifting methods is the presence of “extrinsic” variability in the light curves, on top of the “intrinsic” quasar variability common to all 4 images. The main source of the extrinsic signal is variable microlensing magnification due to the motions of the stars in the lens galaxy. As shown by Mosquera & Kochanek (2011), microlensing can affect light curves over a broad range of time scales. For RX J1131–1231, Mosquera & Kochanek (2011) estimate a time scale of  $\approx 11$  years for the crossing of a stellar Einstein radius, and  $\approx 3$  months for the source radius to cross a caustic.

The curve shifting methods of Tewes et al. (2012) try to minimize the bias due to such extrinsic variability in different ways. They all rely on iterative optimizations of time shifts of the 4 light curves, and yield self-consistent point estimates of the time delays between all 6 image pairs :

1. **The free knot spline technique** simultaneously fits one common *intrinsic* spline for the quasar variability, and independent, smoother *extrinsic* splines for the microlensing to the light curves. The curves are shifted in time to optimize



this fit. This method is similar to the polynomial method of Kochanek et al. (2006).

2. **The regression difference technique** shifts continuous regressions of the curves in time, to minimize the *variability* of the differences between them. This novel method does not involve an explicit model for the microlensing variability.
3. **The dispersion-like technique**, inspired by Pelt et al. (1996), shifts the curves so to minimize a measure of the *dispersion* between the overlapping data points. This method has no explicit model for the common intrinsic variability of the quasar, but it includes polynomial models for the extrinsic variability.

Using several independent algorithms allows us to cross-check our estimates for technique-dependent biases. Indeed, as important as the time delay point estimates themselves is the reliable estimation of their uncertainties. For this we follow a Monte Carlo approach, by applying the curve shifting techniques to a large number of synthetic light curves with *known* time delays. These curves are drawn from a light curve model that mimics both the observed intrinsic and extrinsic variability of the real observations, randomizing only the unrecoverable short scale extrinsic variability. This latter “correlated noise” locally adapts its amplitude to the scatter of the observed data points. As a result, the synthetic curves are virtually indistinguishable from the real ones (see Figs. 5 and 6 of Tewes et al. 2012, for an illustration).

### 5.1. Application to RX J1131–1231

We begin by evaluating the robustness of the time shift optimization of each method given the data. For this we repeatedly run the delay point estimators on the observed light curves. Each time, we start the optimizations from random initial conditions, using time shifts uniformly drawn  $\pm 10$  days around plausible solutions. The resulting distributions of point estimates are shown in Fig. 5, characterizing what we call the *intrinsic variance* of the estimates.

These tests are essential to check the reliability of the non-linear optimization algorithms for a given data set and model parameters. We stress that this procedure should not be interpreted as importance sampling of any posteriors. Generally speaking, overly flexible models dilute the time delay information and yield higher intrinsic variances. For the free knot spline technique we have chosen an average knot step of 20 days for the quasar variability spline, and 150 days for the extrinsic splines. For the dispersion-like method we model the extrinsic variability by independent linear trends on each season. If the light curves sufficiently constrain the time delays, the free knot spline and regression difference techniques can easily be adjusted to display small intrinsic variance and roughly unimodal distributions, as in Fig. 5. The dispersion-like technique is inherently more sensitive to initial conditions, due to a much higher roughness of the scalar objective function that it minimizes. As discussed in Tewes et al. (2012), it is important to note that smoothing the objective function does not necessarily lead to a more accurate time delay estimation. For each technique, we use the mean values of the distributions in Fig. 5 as our best time delay estimates. They correspond to the points in Fig. 6, which summarizes our results for RX J1131–1231.

The remaining part of the analysis is solely about estimating realistic error bars for these point estimates. For this we proceed by blindly running the exact same curve shifting techniques on 1000 sets of fully synthetic light curves with true time delays randomly chosen around the measured ones. Again, we start the

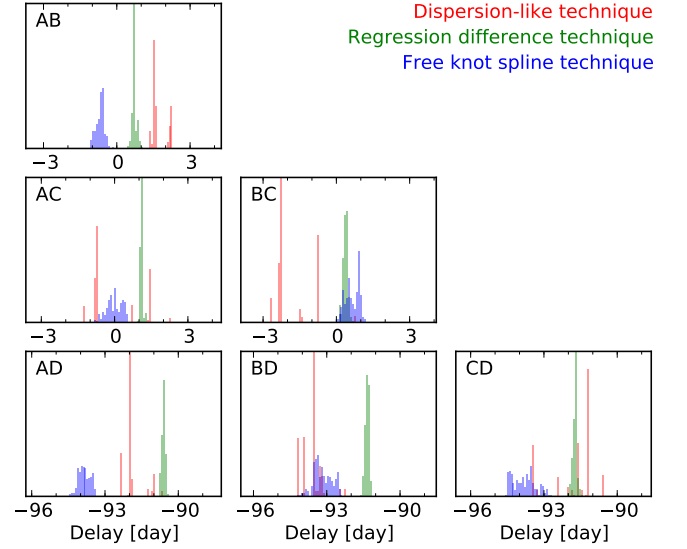


**Fig. 5.** Analysis of the “intrinsic variance” of the time delay point estimators, found by running the three curve shifting techniques 200 times on the light curves shown in Fig. 4, starting the optimizations from random initial time shifts. The *widths* of these distributions reflect the failure of the methods to converge to a single optimal solution given the data. We stress that these distributions do *not* represent probability density functions the time delays, and that a small intrinsic variance does *not* imply that a time delay estimation is precise or accurate, only that the error surface is relatively smooth.

methods from random initial shifts. Statistics of the resulting time delay measurement errors (i.e., measurement – truth), are shown in Fig. 7 as a function of the true delays of the synthetic curves. In this figure, the shaded rods show the mean measurement error, which we call systematic error or bias, while the error bars indicate the standard deviation of the measurement errors, representing the random errors. The total errors for our delay measurements, as shown as error bars in Fig. 6, are computed by adding the maximum bias and the maximum random error of each panel in quadrature. Note that we run the curve shifting techniques only once on each random synthetic curve set, so this error analysis takes into account the intrinsic variance. This is rather conservative, given that we use the mean result of several time shift optimizations as our best estimates for the observed data. However, the additional contribution to the uncertainty estimates is negligible for methods with low intrinsic variance. Before discussing these results, we show in Fig. 8 the same measurement errors as in Fig. 7, but plotted for each delay against each other, in order to explore potential abnormal correlations.

### 5.2. Discussion

In terms of simple lens model considerations, RX J1131–1231 is a “long axis cusp lens”, with the source is located inside a cusp of the tangential caustic curve on the long axis of the potential (Sluse et al. 2003). Images A and D are the saddle points of the arrival time surface, while B and C are minima (Blandford & Narayan 1986). Fig. 14 of Saha et al. (2006) gives an illustration of this particular lens. Hence the delays  $\Delta t_{AB}$  and  $\Delta t_{AC}$  are predicted to be small but positive, while  $\Delta t_{AD}$  is negative and large; the possible arrival time orders are BCAD or CBAD.

Our measured delays, as shown in Fig. 6, are consistent with these predictions, although the delays between A, B and C are

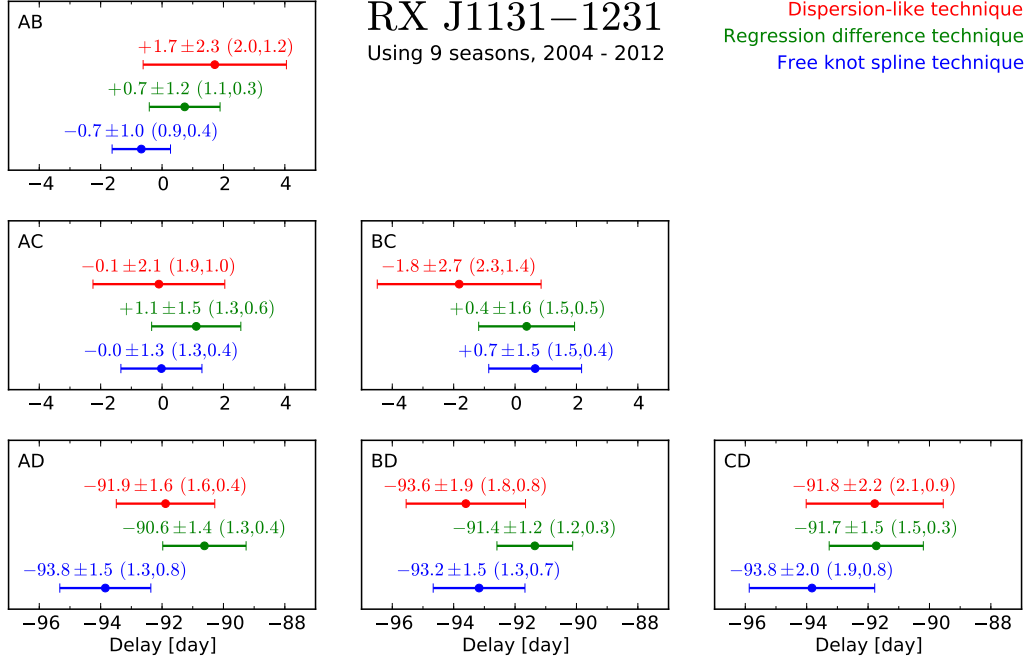


**Fig. 6.** Time delay measurements along with the  $1\sigma$  errors for RX J1131–1231, obtained by the 3 techniques from the full 9-season long light curves shown in Fig 4. The random and systematic error contributions are given in parentheses for each delay. The error bars represent the random plus systematic errors summed in quadrature. A positive AB-delay  $\Delta t_{AB}$  means that image B leads image A. We consider the measurements from the *regression difference technique*, which display the smallest bias and variance in our error analysis, as the delays that should be used to constrain cosmology and/or lens models.

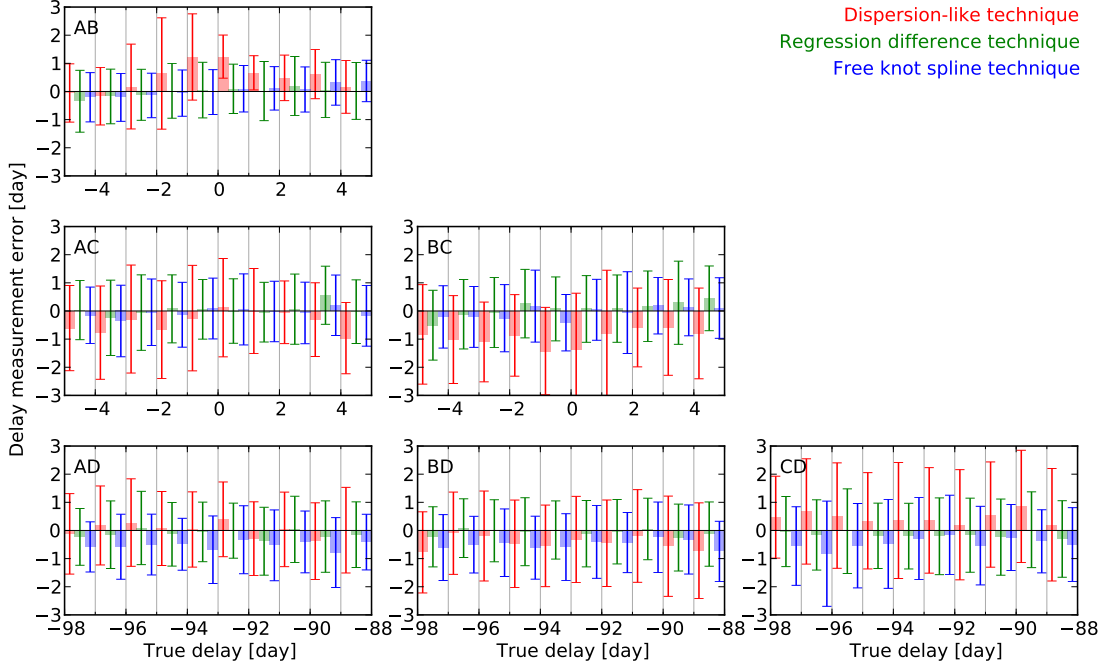


**Fig. 7.** Results of the Monte Carlo analysis leading to the error estimates for our time delay measurements shown in Fig. 6. We obtain our uncertainty estimates by applying the curve shifting techniques to 1000 synthetic light curve sets that closely mimic the observed data but have known “true” time delays. The vertical axes show the delay measurement error, against the true delays used to generate the synthetic curves (horizontal axes). Separately for each panel, the outcomes are binned according to the true time delays. The bin intervals are shown as light vertical lines. Within each bin, the shaded rods and error bars show the systematic and random errors, respectively, of the delay measurements for each technique.

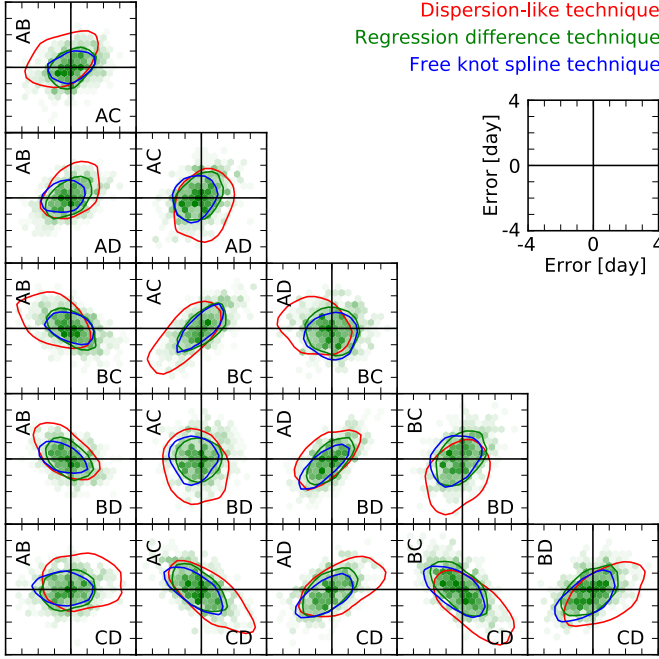


**Fig. 8.** Correlations of delay measurement errors for synthetic light curves mimicking RX J1131–1231; the measurement errors are the same as shown in Fig. 7, but this time marginalizing over the true delays. Crosshairs indicate zero error, and ticks are in days, i.e., each axis displays measurement errors from  $-4$  to  $+4$  days. For clarity, only single contours at half of the maximum density are shown for two of the techniques. We observe no correlations, i.e., oblique contours, for the unrelated delay measurements along the short diagonal of this figure.

compatible with being zero given the  $1\sigma$  errors. It is reassuring to observe that the three methods yield consistent results for all delays despite the very different methodologies, which we see as a success of our error estimation procedure. Keep in mind however that the delay measurements are not independent, because they all use the same single set of observed light curves.

Let us look in more detail at the measurement error analysis shown in Fig. 7, which is based solely on synthetic curves. Overall, we do not observe any strong dependence of a method’s bias or random error on the true time delays used in the simulations. For most image pairs and methods, the random errors are more important than the almost negligible bias. Exceptions are the two results from the dispersion-like technique, which is observed to overpredict  $\Delta t_{AB}$ , and underpredict  $\Delta t_{BC}$ , by about one day. Remarkably, this same technique also measured the highest (lowest) delay  $\Delta t_{AB}$  ( $\Delta t_{BC}$ ) for the observed curves (Fig. 6), when compared to the other methods. We see this as a further indication that the bias estimates are reliable. Finally, Fig. 8 shows no sign of abnormal correlations between measurement errors of quasar image pairs, whether they share a common quasar image or not. By construction our time delay uncertainty estimates for each image pair marginalize over all other pairs.

Which delay measurement method performs best on RX J1131–1231? Given that the regression difference technique yields both the smallest biases and the smallest random errors, we simply conclude that its measurements are the most informative ones. We will use the delays from the regression difference technique, expressed with respect to quasar image B, to measure the time-delay distance towards RX J1131–1231. Details and results of lens modeling, as ap-

plied to RX J1131–1231, are described in detail in Suyu et al. (2012a).

### 5.3. Delay measurement on subsets of the light curves

Our long light curves, featuring several delay-constraining intrinsic variability patterns, suggest to independently measure time delays from subsets of the observing seasons. This analysis represents an invaluable check of the consistency of the time delay estimation procedure of Tewes et al. (2012), and hence for the results from the full light curves.

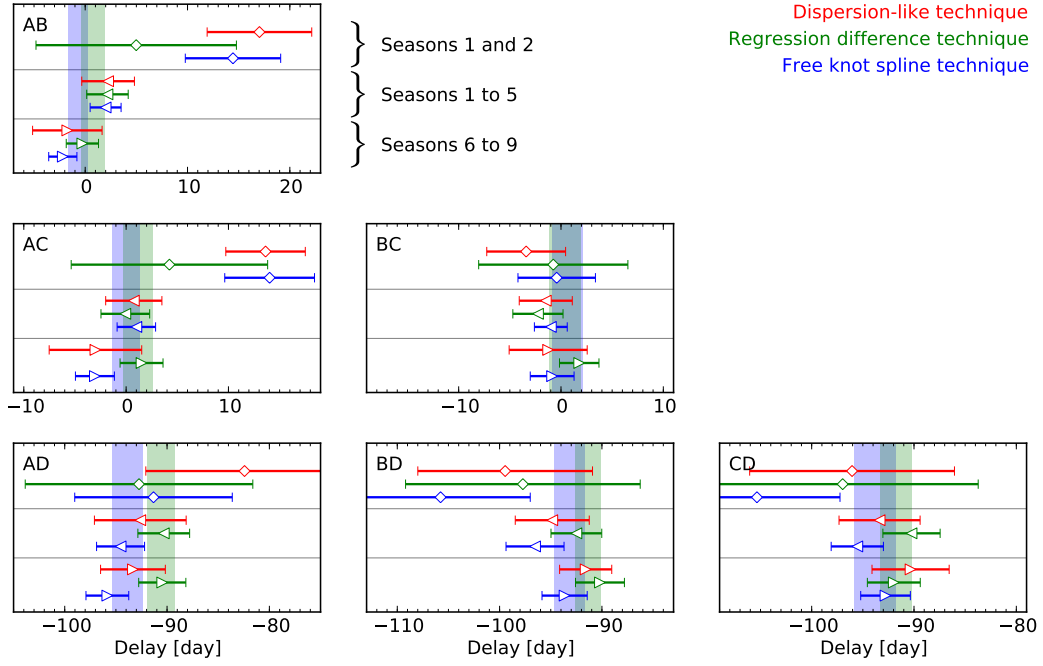
We analyze 3 subsets of the available data : (1) the first two seasons, (2) the first 5 seasons, and (3) the remaining last 4 seasons. Case (1) is chosen for comparison with Morgan et al. (2006). We perform the analyses *from scratch*, without using any knowledge about the delay estimates from the full curves. In particular, for each case, we build a new model for the synthetic light curves, independently adjusted so that they best resemble the observations based on the statistical criteria presented in Tewes et al. (2012, Section 7). We do not alter any parameters of the curve-shifting techniques.

Fig. 9 presents the resulting delay measurements. The data points and error bars depict the individual point estimates and the corresponding  $1\sigma$  total errors obtained by each technique for the 3 cases. The shaded regions show the  $1\sigma$  intervals from the full 9 seasons taken from Fig. 6. We observe :

1. Using only the first 2 seasons, our three methods are systematically biased towards large values of  $\Delta t_{AB}$  and  $\Delta t_{AC}$ . Our interpretation is that some microlensing variability in image A conspiratorially imitates a time shift, particularly around mid 2004. The estimates from the dispersion-like and spline technique roughly reproduce the results obtained from the same two seasons by Morgan et al. (2006,  $\Delta t_{AB} = 12.0 \pm 1.5$ ,  $\Delta t_{AB} = 9.6 \pm 1.9$  and  $\Delta t_{AD} = -87 \pm 8$ ), but with significantly wider, yet still too small, error bars. This demonstrates the need of long monitoring programs to measure accurate time delays and minimize the influence of unfortunately placed microlensing events.
2. For these same two seasons, the regression difference method yields far better estimates for these delays – including adequately sized error bars that encompass the delays estimated from the full light curves. Note that the regression difference technique is the only one that does not involve an explicit *model* for the microlensing.
3. For the other 2 divisions of the data, namely seasons 1-5 and 6-9, which are disjoint and hence independent, our methods give consistent results. As would be expected, both cases show larger error bars than the combined analysis of all seasons.

## 6. Conclusions

The first part of this paper describes the COSMOGRAIL data reduction procedure, which will be used to reduce all the data gathered by our monitoring campaign of gravitationally lensed quasars. In the second part we apply this pipeline to our COSMOGRAIL and SMARTS observations of the quad lens RX J1131–1231, leading to an unprecedented set of 9 year long light curves of high photometric quality. Several strong and fast intrinsic quasar variability patterns constrain the time delays between the multiple images. Microlensing-related “extrinsic” variability is clearly present, as pointed out and analyzed in previous studies (Sluse et al. 2006, 2007; Morgan et al. 2010; Dai



**Fig. 9.** Application of the curve shifting techniques to subsections of the full light curves. The square diamonds (top) show measurements using only the 2 first seasons, the leftward triangles (middle) use the first 5 seasons, and the rightward triangles (bottom) use the last 4 seasons. All error bars depict *total* errors, as in Fig. 6. The blue and green shaded regions correspond to the interval covered by the total error bars using the full 9 seasons, by the spline and regression difference techniques, respectively.

et al. 2010; Chartas et al. 2012). However, this distorting signal does not prevent us from measuring accurate time delays, using the three independent algorithms of Tewes et al. (2012).

The best time delay estimates of RX J1131–1231 are provided by the regression difference technique. It measures the 91-day delays between D and the other quasar images to a fractional  $1\sigma$  uncertainty of 1.5%. This error estimate is obtained by applying the techniques to synthetic curves with known time delays, which contain extrinsic variability features similar to the observed ones. We demonstrate the consistency of our error estimates by independently measuring time delays – including error bars – from subsets of the observed light curves of RX J1131–1231. This experiment also reveals that long multi-year monitoring is essential to reliably measure time delays, despite progress on the methods.

The results from this paper are used to constrain the time delay distance towards RX J1131–1231, and deduce stringent implications for cosmology in Suyu et al. (2012a). We note that the uncertainty of this time delay distance – and hence of  $H_0$  – is not dominated by the error on the time delays, given the achieved precision of our measurements.

**Acknowledgements.** We are deeply grateful to the numerous observers who contributed to the data acquisition at the Swiss Euler telescope, the SMARTS 1.3-m telescope, and the Flemish-Belgian Mercator telescope. We wish to thank Sherry Suyu and Tommaso Treu for precious discussions and comments. COSMOGRAIL is financially supported by the Swiss National Science Foundation (SNSF). We also acknowledge support from the International Space Science Institute in Bern, where some of this research has been discussed. CSK and AMM are supported by NSF grant AST-1009756. EE was partially supported by ESA and the Belgian Federal Science Policy (BELSPO) in the framework of the PRODEX Experiment Arrangement C-90312. DS acknowledges support from the Deutsche Forschungsgemeinschaft, reference SL172/1-1.

## References

Bertin, E. 2009, *Memorie della Società Astronomica Italiana*, 80, 422

- Bertin, E. & Arnouts, S. 2010, *Astrophysics Source Code Library*, record ascl:1010.064
- Blackburne, J. A., Kochanek, C. S., Chen, B., Dai, X., & Chartas, G. 2011, arXiv, 1112.0027
- Blandford, R. & Narayan, R. 1986, *ApJ*, 310, 568
- Burud, I., Courbin, F., Magain, P., et al. 2002a, *A&A*, 383, 71
- Burud, I., Hjorth, J., Courbin, F., et al. 2002b, *A&A*, 391, 481
- Chang, K. & Refsdal, S. 1979, *Nature*, 282, 561
- Chantry, V., Sluse, D., & Magain, P. 2010, *A&A*, 522, 95
- Chartas, G., Kochanek, C. S., Dai, X., et al. 2012, arXiv, 1204.4480
- Chartas, G., Kochanek, C. S., Dai, X., Poindexter, S., & Garmire, G. 2009, *ApJ*, 693, 174
- Courbin, F., Chantry, V., Revaz, Y., et al. 2011, *A&A*, 536, A53
- Dai, X., Kochanek, C. S., Chartas, G., et al. 2010, *ApJ*, 709, 278
- DePoy, D. L., Atwood, B., Belville, S. R., et al. 2003, in *Proceedings of SPIE (SPIE)*, 827–838
- Eigenbrod, A., Courbin, F., & Meylan, G. 2007, *A&A*, 465, 51
- Fassnacht, C. D., Xanthopoulos, E., Koopmans, L., & Rusin, D. 2002, *ApJ*, 581, 823
- Fohlmeister, J., Kochanek, C. S., Falco, E. E., Morgan, C. W., & Wambsganss, J. 2008, *ApJ*, 676, 761
- Fohlmeister, J., Kochanek, C. S., Falco, E. E., et al. 2012, arXiv, 1207.5776
- Heyer & Biretta. 2004, *WFPC2 Instrument Handbook*, STScI, Baltimore
- Hjorth, J., Burud, I., Jaunsen, A. O., et al. 2002, *ApJ*, 572, L11
- Hoaglin, D. C., Mosteller, F., & Tukey, J. W., eds. 1983, *Understanding Robust and Exploratory Data Analysis* (Wiley)
- Howell, S. B. 2006, *Handbook of CCD Astronomy*, 2nd edn. (Cambridge University Press)
- Jakobsson, P., Hjorth, J., Burud, I., et al. 2005, *A&A*, 431, 103
- Kochanek, C. S. 2002, *ApJ*, 578, 25
- Kochanek, C. S., Morgan, N. D., Falco, E. E., et al. 2006, *ApJ*, 640, 47
- Kundic, T., Turner, E. L., Colley, W. N., et al. 1997, *ApJ*, 482, 75
- Linder, E. V. 2011, *Physical Review D*, 84, 123529
- MacLeod, C. L., Ivezić, Z., Kochanek, C. S., et al. 2010, *ApJ*, 721, 1014
- Magain, P., Courbin, F., & Sohy, S. 1998, *ApJ*, 494, 472
- Morgan, C. W., Eyler, M. E., Kochanek, C. S., et al. 2008a, *ApJ*, 676, 80
- Morgan, C. W., Hainline, L. J., Chen, B., et al. 2012, *ApJ*, 756, 52
- Morgan, C. W., Kochanek, C. S., Dai, X., Morgan, N. D., & Falco, E. E. 2008b, *ApJ*, 689, 755
- Morgan, C. W., Kochanek, C. S., Morgan, N. D., & Falco, E. E. 2010, *ApJ*, 712, 1129

- Morgan, N. D., Kochanek, C. S., Falco, E. E., & Dai, X. 2006, arXiv, astro-ph/0605321
- Mosquera, A. M. & Kochanek, C. S. 2011, *ApJ*, 738, 96
- Moustakas, L. A., Abazajian, K., Benson, A., et al. 2009, *Astro2010: The Astronomy and Astrophysics Decadal Survey Science White Papers*
- Pelt, J., Kayser, R., Refsdal, S., & Schramm, T. 1996, *A&A*, 305, 97
- Press, W. H., Rybicki, G. B., & Hewitt, J. N. 1992, *ApJ*, 385, 404
- Refsdal, S. 1964, *MNRAS*, 128, 307
- Saha, P., Courbin, F., Sluse, D., Dye, S., & Meylan, G. 2006, *A&A*, 450, 461
- Schild, R. & Thomson, D. J. 1997, *Astronomical Journal*, 113, 130
- Schmidt, R. W. & Wambsganss, J. 2010, *General Relativity and Gravitation*, 42, 2127
- Sluse, D., Chantry, V., Magain, P., Courbin, F., & Meylan, G. 2012, *A&A*, 538, A99
- Sluse, D., Claeskens, J.-F., Altieri, B., et al. 2006, *A&A*, 449, 539
- Sluse, D., Claeskens, J.-F., Hutsemekers, D., & Surdej, J. 2007, *A&A*, 468, 885
- Sluse, D., Surdej, J., Claeskens, J.-F., et al. 2003, *A&A*, 406, L43
- Suyu, S. H., Auger, M. W., Hilbert, S., et al. 2012a, *ApJ*, submitted
- Suyu, S. H., Marshall, P. J., Auger, M. W., et al. 2010, *ApJ*, 711, 201
- Suyu, S. H., Marshall, P. J., Blandford, R. D., et al. 2009, *ApJ*, 691, 277
- Suyu, S. H., Treu, T., Blandford, R. D., et al. 2012b, arXiv, 1202.4459
- Tewes, M., Courbin, F., & Meylan, G. 2012, arXiv, 1208.5598
- van Dokkum, P. G. 2001, *PASP*, 113, 1420
- Vanderriest, C., Schneider, J., Herpe, G., et al. 1989, *A&A*, 215, 1
- Vuissoz, C., Courbin, F., Sluse, D., et al. 2008, *A&A*, 488, 481
- Vuissoz, C., Courbin, F., Sluse, D., et al. 2007, *A&A*, 464, 845
- Wyrzykowski, L., Udalski, A., Schechter, P. L., et al. 2003, *Acta Astronomica*, 53, 229





## TWO ACCURATE TIME-DELAY DISTANCES FROM STRONG LENSING: IMPLICATIONS FOR COSMOLOGY

S. H. SUYU<sup>1,2</sup>, M. W. AUGER<sup>3</sup>, S. HILBERT<sup>2</sup>, P. J. MARSHALL<sup>4</sup>, M. TEWES<sup>5</sup>, T. TREU<sup>1,\*</sup>, C. D. FASSNACHT<sup>6</sup>,  
 L. V. E. KOOPMANS<sup>7</sup>, D. SLUSE<sup>8</sup>, R. D. BLANDFORD<sup>2</sup>, F. COURBIN<sup>5</sup>, G. MEYLAN<sup>5</sup>

*Draft version August 28, 2012*

### ABSTRACT

Strong gravitational lenses with measured time delays between the multiple images and models of the lens mass distribution allow a one-step determination of the time-delay distance, and thus a measure of cosmological parameters. We present a blind analysis of the gravitational lens RXJ1131–1231 incorporating (1) the newly measured time delays from COSMOGRAIL, the COSmological MONitoring of GRAvItational Lenses, (2) archival *Hubble Space Telescope* imaging of the lens system, (3) a new velocity-dispersion measurement of the lens galaxy of  $323 \pm 20 \text{ km s}^{-1}$  based on Keck spectroscopy, and (4) a characterization of the line-of-sight structures via observations of the lens' environment and ray tracing through the Millennium Simulation. Our blind analysis is designed to prevent experimenter bias. The joint analysis of the data sets allows a time-delay distance measurement to 6% precision that takes into account all known systematic uncertainties. In combination with the *Wilkinson Microwave Anisotropy Probe* seven-year (WMAP7) data set in flat  $w$ CDM cosmology, our unblinded cosmological constraints for RXJ1131–1231 are:  $H_0 = 80.0_{-5.7}^{+5.8} \text{ km s}^{-1} \text{ Mpc}^{-1}$ ,  $\Omega_{\text{de}} = 0.79 \pm 0.03$ ,  $w = -1.25_{-0.21}^{+0.17}$ . We find the results to be statistically consistent with those from the analysis of the gravitational lens B1608+656, permitting us to combine the inferences from these two lenses. The joint constraints from the two lenses and WMAP7 are  $H_0 = 75.2_{-4.2}^{+4.4} \text{ km s}^{-1} \text{ Mpc}^{-1}$ ,  $\Omega_{\text{de}} = 0.76_{-0.03}^{+0.02}$  and  $w = -1.14_{-0.20}^{+0.17}$  in flat  $w$ CDM, and  $H_0 = 73.1_{-3.6}^{+2.4} \text{ km s}^{-1} \text{ Mpc}^{-1}$ ,  $\Omega_{\Lambda} = 0.75_{-0.02}^{+0.01}$  and  $\Omega_{\text{k}} = 0.003_{-0.006}^{+0.005}$  in open  $\Lambda$ CDM. Time-delay lenses constrain especially tightly the Hubble constant  $H_0$  (5.7% and 4.0% respectively in  $w$ CDM and open  $\Lambda$ CDM) and curvature of the universe. The overall information content is similar to that of Baryon Acoustic Oscillation experiments. Thus, they complement well other cosmological probes, and provide an independent check of unknown systematics. Our measurement of the Hubble constant is completely independent of those based on the local distance ladder method, providing an important consistency check of the standard cosmological model and of general relativity.

*Subject headings:* galaxies: individual (RXJ1131–1231) — gravitational lensing: strong — methods: data analysis — distance scale

### 1. INTRODUCTION

In the past century precise astrophysical measurements of the geometry and content of the universe (hereafter cosmography) have led to some of the most remarkable discoveries in all of physics. These include the expansion and acceleration of the Universe, its large scale structure, and the existence of non-baryonic dark matter (see review by Freedman & Turner 2003). These observations form the empirical foundations of the standard cosmo-

logical model, which is based on general relativity and the standard model of particle physics but requires additional non-standard features such as non-baryonic dark matter and dark energy.

Even in the present era of so-called precision cosmography, many profound questions about the Universe remain unanswered. What is the nature of dark energy? What are the properties of the dark matter particle? How many families of relativistic particles are there? What are the masses of the neutrinos? Is general relativity the correct theory of gravity? Did the Universe undergo an inflationary phase in its early stages?

From an empirical point of view, the way to address these questions is to increase the accuracy and precision of cosmographic experiments. For example, clues about the nature of dark energy can be gathered by measuring the expansion history of the Universe to very high precision, and modeling the expansion as being due to a dark energy component having an equation of state parametrized by  $w$  that evolves with cosmic time (e.g., Frieman et al. 2008, and references therein). Likewise, competing inflationary models can be tested by measuring the curvature of the Universe to very high precision. Given the high stakes involved, it is essential to develop multiple independent methods as a way to control for known systematic uncertainties, uncover new ones, and

suyu@physics.ucsb.edu

<sup>1</sup> Department of Physics, University of California, Santa Barbara, CA 93106, USA

<sup>2</sup> Kavli Institute for Particle Astrophysics and Cosmology, Stanford University, 452 Lomita Mall, Stanford, CA 94035, USA

<sup>3</sup> Institute of Astronomy, University of Cambridge, Madingley Rd, Cambridge, CB3 0HA, UK

<sup>4</sup> Department of Physics, University of Oxford, Keble Road, Oxford, OX1 3RH, UK

<sup>5</sup> Laboratoire d'Astrophysique, Ecole Polytechnique Fédérale de Lausanne (EPFL), Observatoire de Sauverny, CH-1290 Versoix, Switzerland

<sup>6</sup> Department of Physics, University of California, Davis, CA 95616, USA

<sup>7</sup> Kapteyn Astronomical Institute, University of Groningen, P.O.Box 800, 9700 AV Groningen, The Netherlands

<sup>8</sup> Argelander-Institut für Astronomie, Auf dem Hügel 71, 53121 Bonn, Germany

\* Packard Research Fellow

ultimately discover discrepancies that may reveal new fundamental physics. For example, a proven inconsistency between inferences at high redshift from the study of the cosmic microwave background, with inferences at lower redshift from galaxy redshift surveys would challenge the standard description of the evolution of the Universe over this redshift interval, and possibly lead to revisions of either our theory of gravity or of our assumptions about the nature of dark matter and dark energy.

In this paper we present new results from an observational program aimed at precision cosmography using gravitational lens time delays. The idea of doing cosmography with time-delay lenses goes back fifty years and it is a simple one (Refsdal 1964). When a source is observed through a strong gravitational lens, multiple images form at the extrema of the time-delay surface, according to Fermat's principle (e.g., Schneider et al. 1992; Falco 2005; Schneider et al. 2006). If the source is variable, the time delays between the images can be measured by careful monitoring of the image light curves (see, e.g., Courbin 2003). With an accurate model of the gravitational lens, the absolute time delays can be used to convert angles on the sky into an absolute distance, the so-called time-delay distance, which can be compared with predictions from the cosmological model given the lens and source redshifts (e.g., Blandford & Narayan 1992; Jackson 2007; Treu 2010, and references therein). This distance is a combination of three angular diameter distances, and so is primarily sensitive to the Hubble constant, with some higher order dependence on the other cosmological parameters (Coe & Moustakas 2009; Linder 2011). Gravitational time delays are a one-step cosmological method to determine the Hubble constant that is completely independent of the local cosmic distance ladder (Freedman et al. 2001; Riess et al. 2011; Freedman et al. 2012; Reid et al. 2012). Knowledge of the Hubble constant is currently the key limiting factor in measuring parameters like the dark energy equation of state, curvature, or neutrino mass, in combination with other probes like the cosmic microwave background (Freedman & Madore 2010; Riess et al. 2011; Freedman et al. 2012; Weinberg et al. 2012; Suyu et al. 2012). These features make strong gravitational time delays a very attractive probe of cosmology.

Like most high-precision measurements, however, a good idea is only the starting point. A substantial amount of effort and observational resources needs to be invested to control the systematic errors. In the case of gravitational time delays, this has required several observational and modeling breakthroughs. Accurate, long duration, and well-sampled light curves are necessary to obtain accurate time delays in the presence of microlensing. Modern light curves have much higher photometric precision, sampling and duration (Fassnacht et al. 2002; Courbin et al. 2011) compared to the early pioneering light curves (e.g., Lehar et al. 1992). High resolution images of extended features in the source, and stellar kinematics of the main deflector, provide hundreds to thousands of data points to constrain the mass model of the main deflector, thus reducing the degeneracy between the distance and the gravitational potential of the lens that affected previous models constrained only by the positions of the lensed quasars (e.g., Schechter et al. 1997). Finally, cosmological numerical simulations can now be

used to characterize the distribution of mass along the line of sight (LOS) (Hilbert et al. 2009), which was usually neglected in early studies that were not aiming for precisions of a few percent. The advances in the use of gravitational time delays as a cosmographic probe are summarized in the analysis of the gravitational lens system B1608+656 by Suyu et al. (2010). In that paper, we demonstrated that, with sufficient ancillary data, a single gravitational lens can yield a time-delay distance measured to 5% precision, and the Hubble constant to 7% precision. In combination with the *Wilkinson Microwave Anisotropy Probe* 5-year (WMAP5) results, the B1608+656 time-delay distance constrained  $w$  to 18% precision and the curvature parameter to  $\pm 0.02$  precision, comparable to contemporary Baryon Acoustic Oscillation experiments (Percival et al. 2007) and observations of the growth of massive galaxy clusters (on  $w$  constraints; Mantz et al. 2010).

Building on these recent developments in the analysis, and on the state-of-the-art monitoring campaigns carried out by the COSMOGRAIL (COSmological MONitoring of GRAvitational Lenses; e.g., Vuissoz et al. 2008; Courbin et al. 2011; Tewes et al. 2012b) and Kochanek et al. (2006) teams, it is now possible to take gravitational time delay lens cosmography to the next level and achieve precision comparable to current measurements of the Hubble constant, flatness,  $w$  and other cosmological parameters (Riess et al. 2011; Freedman et al. 2012; Komatsu et al. 2011). To this end we have recently initiated a program to obtain data and model four additional gravitational lens systems with the same quality as that of B1608+656.

We present here the results for the first of these systems, RXJ1131–1231, based on new time delays measured by the COSMOGRAIL collaboration (Tewes et al. 2012b), new spectroscopic data from the Keck Telescope, a new analysis of archival *Hubble Space Telescope* (*HST*) images, and a characterization of the LOS effects through numerical simulations, the observed galaxy number counts in the field, and the modeled external shear. We carry out a self-consistent modeling of all the available data sets in a Bayesian framework, and infer (1) a likelihood function for the time-delay distance that can be combined with any other independent probe of cosmology, and (2) in combination with our previous measurement of B1608+656 and the WMAP 7-year (WMAP7) results, the posterior probability density function (PDF) for the Hubble constant, curvature density parameter and dark energy equation-of-state parameter  $w$ .

Three additional lens systems are scheduled to be observed with *HST* in cycle 20 (GO 12889; PI Suyu) and will be published in forthcoming papers. An integral part of this program is the use of blind analysis, to uncover unknown systematic errors and to avoid unconscious experimenter bias. Only when each system's analysis has been judged to be complete and final by its authors, are the implications for cosmology revealed. These results are then published without any further modification. In this way, we can assess whether the results are mutually consistent within the estimated errors or whether unknown systematics are adding significantly to the total error budget.

This paper is organized as follows. After a brief re-



cap of the theory behind time-delay lens cosmography in Section 2, we summarize our strategy in Section 3 and describe our observational data in Section 4. In Section 5, we write out the probability theory used in the data modeling and describe the procedure for carrying out the blind analysis. The lensing and time-delay analysis are presented in Section 6, and a description of our treatment of the LOS mass structure in the RXJ1131–1231 field is in Section 7. We present measurements of the time-delay distance, and discuss the sources of uncertainties in Section 8. We show our unblinded cosmological parameter inferences in Section 9, which includes joint analysis with our previous lens data set and with WMAP7. Finally, we conclude in Section 10. Throughout this paper, each quoted parameter estimate is the median of the appropriate one-dimensional marginalized posterior PDF, with the quoted uncertainties showing, unless otherwise stated, the 16<sup>th</sup> and 84<sup>th</sup> percentiles (that is, the bounds of a 68% credible interval).

## 2. COSMOGRAPHY FROM GRAVITATIONAL LENS TIME DELAYS

In this section, we give a brief overview of the use of gravitational lens time delays to study cosmology. More details on the subject can be found in, e.g., Schneider et al. (2006), Jackson (2007), Treu (2010) and Suyu et al. (2010). Readers familiar with time-delay lenses may wish to proceed directly to Section 3.

In a gravitational lens system, the time it takes the light from the source to reach us depends on both the path of the light ray and also the gravitational potential of the lens. The excess time delay of an image at angular position  $\theta = (\theta_1, \theta_2)$  with corresponding source position  $\beta = (\beta_1, \beta_2)$  relative to the case of no lensing is

$$t(\theta, \beta) = \frac{D_{\Delta t}}{c} \left[ \frac{(\theta - \beta)^2}{2} - \psi(\theta) \right], \quad (1)$$

where  $D_{\Delta t}$  is the so-called time-delay distance,  $c$  is the speed of light, and  $\psi(\theta)$  is the lens potential. The time-delay distance is a combination of the angular diameter distance to the lens (or deflector) ( $D_d$ ) at redshift  $z_d$ , to the source ( $D_s$ ), and between the lens and the source ( $D_{ds}$ ):

$$D_{\Delta t} \equiv (1 + z_d) \frac{D_d D_s}{D_{ds}}. \quad (2)$$

The lens potential  $\psi(\theta)$  is related to the dimensionless surface mass density of the lens,  $\kappa(\theta)$ , via

$$\nabla^2 \psi(\theta) = 2\kappa(\theta), \quad (3)$$

where

$$\kappa(\theta) = \frac{\Sigma(D_d \theta)}{\Sigma_{\text{crit}}}, \quad (4)$$

$\Sigma(D_d \theta)$  is the surface mass density of the lens (the projection of the three dimensional density  $\rho$  along the LOS),  $\Sigma_{\text{crit}}$  is the critical surface mass density defined by

$$\Sigma_{\text{crit}} = \frac{c^2}{4\pi G} \frac{D_s}{D_d D_{ds}}, \quad (5)$$

and  $G$  is the gravitational constant.

For lens systems whose sources vary in time (as do active galactic nuclei, AGNs), one can monitor the brightnesses of the lensed images over time and hence measure

the time delay,  $\Delta t_{ij}$ , between the images at positions  $\theta_i$  and  $\theta_j$ :

$$\begin{aligned} \Delta t_{ij} &\equiv t(\theta_i, \beta) - t(\theta_j, \beta) \\ &= \frac{D_{\Delta t}}{c} \left[ \frac{(\theta_i - \beta)^2}{2} - \psi(\theta_i) - \frac{(\theta_j - \beta)^2}{2} + \psi(\theta_j) \right] \end{aligned} \quad (6)$$

By using the image configuration and morphology, one can model the mass distribution of the lens to determine the lens potential  $\psi(\theta)$  and the unlensed source position  $\beta$ . Lens systems with time delays can therefore be used to measure  $D_{\Delta t}$  via Equation (6), and constrain cosmological models via the distance-redshift test (e.g., Refsdal 1964, 1966; Fadelly et al. 2010; Suyu et al. 2010). Having dimensions of distance,  $D_{\Delta t}$  is inversely proportional to  $H_0$ , and being a combination of three angular diameter distances, it depends weakly on the other cosmological parameters as well.

The radial slope of the lens mass distribution and the time-delay distance both have direct influence on the observables: for a given time delay, a galaxy with a steep radial profile leads to a lower  $D_{\Delta t}$  than that of a galaxy with a shallow profile (e.g., Witt et al. 2000; Wucknitz 2002; Kochanek 2002). Therefore, to measure  $D_{\Delta t}$ , it is necessary to determine the radial slope of the lens galaxy. Several authors have shown that the spatially extended sources (such as the host galaxy of the AGN in time-delay lenses) can be used to measure the radial slope at the image positions, where it matters (e.g., Dye & Warren 2005; Dye et al. 2008; Suyu et al. 2010; Vegetti et al. 2010; Suyu 2012).

In addition to the mass distribution associated with the lens galaxy, structures along the LOS also affect the observed time delays. The external masses and voids cause additional focussing and defocussing of the light rays respectively, and therefore affect the time delays and  $D_{\Delta t}$  inferences. We follow Keeton (2003), Suyu et al. (2010) and many others and suppose that the effect of the LOS structures can be characterized by a single parameter, the external convergence  $\kappa_{\text{ext}}$ , with positive values associated with overdense LOS and negative values with underdense LOS. Except for galaxies very nearby to the strong lens system, the  $\kappa_{\text{ext}}$  contribution of the LOS structures to the lens is effectively constant across the scale of the lens system.

Given the measured delays between the images of a strong lens, a mass model that does not account for the external convergence leads to an under/overprediction of  $D_{\Delta t}$  for over/underdense LOS. In particular, the true  $D_{\Delta t}$  is related to the modeled one by

$$D_{\Delta t} = \frac{D_{\Delta t}^{\text{model}}}{1 - \kappa_{\text{ext}}}. \quad (7)$$

Two practical approaches to overcome this degeneracy are (1) to use the stellar kinematics of the lens galaxy (e.g., Treu & Koopmans 2002; Koopmans & Treu 2003; Treu & Koopmans 2004; Barnabè et al. 2009; Auger et al. 2010; Suyu et al. 2010; Sonnenfeld et al. 2012) to make an independent estimate of the lens mass and (2) to study the environment of the lens system (e.g., Keeton & Zabludoff 2004; Fassnacht et al. 2006; Momcheva et al. 2006; Suyu et al. 2010; Wong et al. 2011; Fassnacht et al. 2011) in order to estimate  $\kappa_{\text{ext}}$  directly. In Section 7, we combine both approaches to infer  $\kappa_{\text{ext}}$ .

### 3. ACCURATE AND PRECISE DISTANCE MEASUREMENTS

We summarize our strategy for accurate and precise cosmography with all known sources of systematic uncertainty taken into account. We assemble the following key ingredients for obtaining  $D_{\Delta t}$  via Equation (6)

- observed time delays: dedicated and long-duration monitoring, particularly from COSMOGRAIL, yields delays with uncertainties of only a few percent (Tewes et al. 2012a,b).
- lens mass model: deep and high-resolution images of the lensed arcs, together with our flexible modeling techniques that use as data the thousands of surface brightness pixels of the lensed source, allow constraints of the potential difference between the lensed images (in Equation (6)) at the few percent level (e.g., Suyu et al. 2010).
- external convergence: the stellar velocity dispersion of the lens galaxy provides constraints on both the lens mass distribution and external convergence. We further calibrate observations of galaxy counts in the fields of lenses (Fassnacht et al. 2011) with ray tracing through numerical simulations of large-scale structure (e.g., Hilbert et al. 2007) to constrain directly and statistically  $\kappa_{\text{ext}}$  at the  $\sim 5\%$  level (Suyu et al. 2010).

With all these data sets for the time-delay lenses, we can measure  $D_{\Delta t}$  for each lens with  $\sim 5 - 8\%$  precision (including all sources of known uncertainty). A comparison of a sample of lenses will allow us to test for residual systematic effects, if they are present. With systematics under control, we can combine the individual distance measurements to infer global properties of cosmology since the gravitational lenses are independent of one another.

### 4. OBSERVATIONS OF RXJ1131–1231

The gravitational lens RXJ1131–1231 was discovered by Sluse et al. (2003) during polarimetric imaging of a sample of radio quasars. The spectroscopic redshifts of the lens and the quasar source are  $z_d = 0.295$  and  $z_s = 0.658$ , respectively. We present the archival *HST* images in Section 4.1, the time delays from COSMOGRAIL in Section 4.2, the lens velocity dispersion in Section 4.3 and information on the lens environment in Section 4.4.

#### 4.1. Archival *HST* imaging

*HST* Advanced Camera for Surveys (ACS) images were obtained for RXJ1131–1231 in two filters, F814W and F555W (ID 9744; PI Kochanek). In each filter, five exposures were taken with a total exposure time of 1980s. We show in Figure 1 the F814W image of the lens system. The background quasar source is lensed into four images denoted by A, B, C, and D, and the spectacular features surrounding the quasar images are the lensed images of the quasar host that is a spiral galaxy (Claeskens et al. 2006). The primary lens galaxy is marked by G, and the object marked by S is most likely a satellite of G (Claeskens et al. 2006). Henceforth, we refer to S as the satellite.

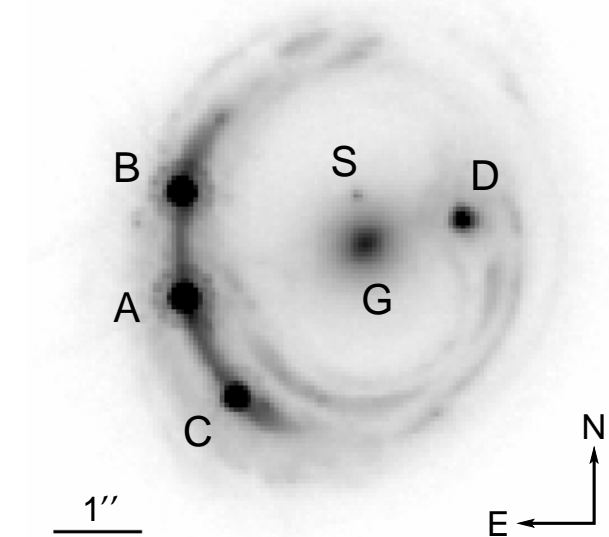


FIG. 1.— *HST* ACS F814W image of the gravitational lens RXJ1131–1231. The lensed AGN images of the spiral source galaxy are marked by A, B, C and D, and the star forming regions of the spiral galaxy form the spectacular lensed structures. The primary lens galaxy and the satellite lens galaxy are indicated by G and S, respectively.

We reduce the images using MULTIDRIZZLE<sup>10</sup> with charge transfer inefficiency taken into account (e.g., Anderson & Bedin 2010; Massey et al. 2010). The images are drizzled to a final pixel scale of  $0''.05 \text{ pix}^{-1}$  and the uncertainty on the flux in each pixel is estimated from the science and the weight image by adding in quadrature the Poisson noise from the source and the background noise due to the sky and detector readout. We note that in some of the exposures the central regions of the two brightest AGN images are slightly saturated and are masked during the drizzling process.

To model the lens system using the spatially extended Einstein ring of the host galaxy, we focus on the F814W image since the contrast between the ring and the AGN is more favorable in F814W. In particular, the bright AGNs in F555W have diffraction spikes extending into the Einstein ring that are difficult to model and are thus prone to systematics effects. The detailed modeling of the F814W image is in Section 6.

#### 4.2. Time delays

We use the new time-delay measurements of RXJ1131–1231 presented in Tewes et al. (2012b). The COSMOGRAIL and Kochanek et al. teams have monitored RXJ1131–1231 since December 2003 using several optical 1–1.5m telescopes. Resolved light curves of the four AGN images are extracted from these observations by “deconvolution photometry”, following Magain et al. (1998). These curves presently span 9 years with over 700 epochs, and display a typical sampling of 2–3 days within the observation seasons. The time delays are measured through several new and independent techniques (detailed in Tewes et al. 2012a), all specifically devel-

<sup>10</sup> MULTIDRIZZLE is a product of the Space Telescope Science Institute, which is operated by AURA for NASA.

oped to handle microlensing variability due to stars in the lens galaxy. All these techniques yield consistent results, attributed to both the long light curves and the comprehensive uncertainty estimation. For our analysis we select the time-delay measurements from the *regression difference technique*, which displays the smallest systematic error when applied to synthetic curves mimicking the microlensing variability in RXJ1131–1231. In particular we use the time delays relative to image B, namely:  $\Delta t_{AB} = 0.7 \pm 1.4$  days,  $\Delta t_{CB} = -0.4 \pm 2.0$  days, and  $\Delta t_{DB} = 91.4 \pm 1.5$  days, where the uncertainties are conservative and direct sums of the estimated statistical and systematic contributions from Tewes et al. (2012b).

#### 4.3. Lens velocity dispersion

We observed RXJ1131–1231 with the Low-Resolution Imaging Spectrometer (LRIS; Oke et al. 1995) on Keck 1 on 4–5 January 2011. The data were obtained from the red side of the spectrograph using the 600/7500 grating with the D500 dichroic in place. A slit mask was employed to obtain simultaneously spectra for galaxies near the lens system. The night was clear with a nominal seeing of  $0''.7$ , and we use 4 exposures of 1200s for a total exposure time of 4800s.

We follow Auger et al. (2008) to reduce each exposure by performing a single resampling of the spectra onto a constant wavelength grid. We use the same wavelength grid for all exposures to avoid resampling the spectra when combining them. An output pixel scale of  $0.8 \text{ \AA pix}^{-1}$  was used to match the dispersion of the 600/7500 grating. Individual spectra are extracted from an aperture  $0''.81$  wide (corresponding to 4 pixels on the LRIS red side) centered on the lens galaxy. The size of the aperture was chosen to avoid contamination from the spectrum of the lensed AGNs. We combine the extracted spectra by clipping the extreme points at each wavelength and taking the variance-weighted sum of the remaining data points. We repeat the same extraction and coaddition scheme for a sky aperture to determine the resolution of the output co-added spectrum:  $R = 2300$ , corresponding to  $\sigma_{\text{obs}} = 56 \text{ km s}^{-1}$ . The typical signal-to-noise ratio per pixel of the final spectrum is  $\sim 20$ .

The stellar velocity dispersion is determined in the same manner as Suyu et al. (2010). Briefly, we use a suite of stellar templates of K and G giants, augmented with one A and one F star template, from the INDO-US library (Valdes et al. 2004) to fit directly to the observed spectrum, after convolving each template with a kernel to bring them to the same spectral resolution as the data. First and second velocity moments are proposed by a Markov chain Monte Carlo (MCMC) simulation and the templates are shifted and broadened to these moments. We then fit the model templates to the data in a linear least squares sense, including a fifth order polynomial to account for any emission from the background source (e.g., Suyu et al. 2010). The observed and modeled spectra are shown in Figure 2. Our estimate for the central line-of-sight velocity dispersion from this inference is  $\sigma = 323 \pm 20 \text{ km s}^{-1}$ , including systematics from changing the polynomial order and choosing different fitting regions.

#### 4.4. Galaxy counts in the field

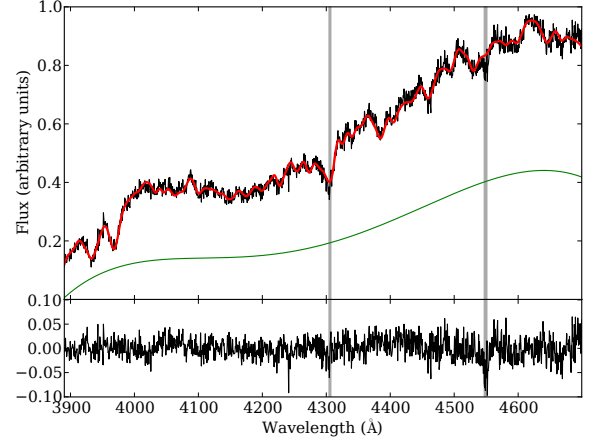


FIG. 2.— Top panel: The LRIS spectrum of RXJ1131–1231 (black line) with a model generated from 9 INDO-US templates and a 5<sup>th</sup> order continuum overplotted (red line, with green showing the continuum). The gray shaded areas were not included in the fit. Bottom panel: the residuals of the model fit. From the spectrum and model, we measure a central velocity dispersion of  $\sigma = 323 \pm 20 \text{ km s}^{-1}$ , including systematic uncertainties.

Fassnacht et al. (2011) counted the number of galaxies with F814W magnitudes between 18.5 and 24.5 that lie within  $45''$  from the lens system. Compared to the aperture counts in random lines of sight in pure-parallel fields, RXJ1131–1231 has 1.4 times the average number of galaxy counts. We use this relative galaxy count in Section 7.2 to estimate statistically the external convergence.

### 5. PROBABILITY THEORY FOR COMBINING MULTIPLE DATA SETS

We now present the mathematical framework for the inference of cosmological parameters from the combination of the data sets described in the previous section. In order to test for the presence of any unknown systematic uncertainty, we describe a procedure for blinding the results during the analysis phase in Section 5.2. This procedure is designed to ensure against unconscious experimenter bias towards “acceptable” results.

#### 5.1. Joint analysis

The analysis performed here is similar to the one presented in Suyu et al. (2010), with a few improvements. We briefly describe the procedure below.

The data sets are denoted by  $\mathbf{d}_{\text{ACS}}$  for the ACS image (packaged into a vector of  $160^2$  surface brightness values),  $\Delta \mathbf{t}$  for the delays between the images,  $\sigma$  for the lens velocity dispersion, and  $\mathbf{d}_{\text{env}}$  for properties of the lens environment such as the relative galaxy count  $n_r = n_{\text{gal}} / \langle n_{\text{gal}} \rangle$ . We are interested in obtaining the posterior PDF of the model parameters  $\xi$  given all available data,

$$P(\xi | \mathbf{d}_{\text{ACS}}, \Delta \mathbf{t}, \sigma, \mathbf{d}_{\text{env}}) \propto P(\mathbf{d}_{\text{ACS}}, \Delta \mathbf{t}, \sigma, \mathbf{d}_{\text{env}} | \xi) P(\xi) \quad (8)$$

where the proportionality follows from Bayes’ Theorem. The first term is known as the likelihood, and the second is the prior PDF. Since the data sets are independent, the likelihood is separable,

$$P(\mathbf{d}_{\text{ACS}}, \Delta \mathbf{t}, \sigma, \mathbf{d}_{\text{env}} | \xi) = P(\mathbf{d}_{\text{ACS}} | \xi) P(\Delta \mathbf{t} | \xi) P(\sigma | \xi) P(\mathbf{d}_{\text{env}} | \xi). \quad (9)$$



Some of the parameters influence all the predicted data sets, while other parameters affect the fitting of particular data sets only. Specifically,  $\xi = \{\pi, \gamma', \theta_E, \gamma_{\text{ext}}, \eta, r_{\text{ani}}, \kappa_{\text{ext}}\}$ , where  $\pi$  are the cosmological parameters (e.g.,  $H_0$ ,  $w$ ,  $\Omega_{\text{de}}$ ),  $\gamma'$  is the radial profile slope of the main lens galaxy (where  $\rho \propto r^{-\gamma'}$ ),  $\theta_E$  is the Einstein radius of the main lens (that characterizes the normalization of the lens mass profile),  $\gamma_{\text{ext}}$  is the external shear strength at the lens,  $\eta$  denotes the remaining lens model parameters for the ACS data,<sup>11</sup>  $r_{\text{ani}}$  is the anisotropy radius for the stellar orbits of the lens galaxy, and  $\kappa_{\text{ext}}$  is the external convergence. For the lensing and time delays, we subsume the cosmological dependence into the time-delay distance  $D_{\Delta t} = D_{\Delta t}(\pi)$ . Keeping only the direct dependencies in each of the likelihoods, we obtain

$$P(\xi | d_{\text{ACS}}, \Delta t, \sigma, d_{\text{env}}) \propto P(d_{\text{ACS}}, \Delta t | D_{\Delta t}, \gamma', \theta_E, \gamma_{\text{ext}}, \eta, \kappa_{\text{ext}}) P(\sigma | \pi, \gamma', \theta_E, r_{\text{ani}}, \kappa_{\text{ext}}) P(d_{\text{env}} | \kappa_{\text{ext}}, \gamma_{\text{ext}}) P(\pi) P(\gamma') P(\theta_E) P(\gamma_{\text{ext}}) P(\eta) P(r_{\text{ani}}) P(\kappa_{\text{ext}}). \quad (10)$$

For cosmography, we are interested in the cosmological parameters  $\pi$  after marginalizing over all other parameters

$$P(\pi | d_{\text{ACS}}, \Delta t, \sigma, d_{\text{env}}) = \int d\gamma' d\theta_E d\gamma_{\text{ext}} d\eta dr_{\text{ani}} d\kappa_{\text{ext}} P(\xi | d_{\text{ACS}}, \Delta t, \sigma, d_{\text{env}}) \quad (11)$$

We describe the forms of the partially marginalized lensing and time-delay likelihood in Section 6, the kinematics likelihood in Section 7.1 and the external convergence likelihood in Section 7.2. For marginalizing the parameters that are common to the data sets, we importance sample the priors following Lewis & Bridle (2002) and Suyu et al. (2010) (a procedure sometimes referred to as “simple Monte Carlo”).

### 5.2. Blind analysis

We blind the analysis to avoid experimenter bias, allowing us to test for the presence of residual systematics in our analysis technique by comparing the final unblinded results from RXJ1131–1231 with the constraints from the previous analysis of B1608+656. As described by Conley et al. (2006), the blinding is not meant to hide all information from the experimenter; rather, we blind only the parameters that concern the cosmological inference.

We define two analysis phases. During the initial “blind” phase, we compute likelihoods and priors, and sample the posterior PDF, as given above, taking care to only make parameter-space plots using one plotting code. This piece of software adds offsets to the cosmological parameters ( $D_{\Delta t}$  and the components of  $\pi$ ) before displaying the PDFs, such that we always see the marginalized distributions with centroids at exactly zero. We can therefore still see, and measure, the *precision* of the blinded parameters, and visualize the correlations between these parameters, but without being able to see if we have “the right answer.” Both the parameter uncertainties and degeneracies serve as useful checks during this blind phase: the plotting routine can overlay the

constraints from different models to investigate sources of statistical and systematic uncertainties.

During the blind phase we performed a number of tests on the modeling to quantify the sources of uncertainties, and to check the robustness of the results. These are described in Sections 4–8. At the end of the tests, the collaboration convened a telecon to unblind the results. The authors SHS, MWA, SH, PJM, MT, TT, CDF, LVEK, DS, and FC discussed in detail the analysis and the blinded results, over a summary website. After all agreeing that the blind analysis was complete, and that we would publish without modification the results once unblinded, a script was run to update automatically the same website with plots and tables containing cosmological constraints no longer offset to zero. These are the results presented in Sections 8 and 9.1.

## 6. LENS MODELING

In this section, we simultaneously model the ACS images and the time delays to measure the lens model parameters, particularly  $D_{\Delta t}$ ,  $\gamma'$ ,  $\theta_E$ , and  $\gamma_{\text{ext}}$ .

### 6.1. A comprehensive mass and light model

The ACS image in Figure 1 shows the light from the source as lensed by the galaxies G and S. To predict the surface brightness of the pixels on the image, we need a model for the lens mass distribution (that deflects the light of the source), the lens light distribution, the source light distribution and the point spread function (PSF) of the telescope.

#### 6.1.1. Lens mass profiles

We use elliptically-symmetric distributions with power-law profiles to model the dimensionless surface mass density of the lens galaxies,

$$\kappa_{\text{pl}}(\theta_1, \theta_2) = \frac{3 - \gamma'}{2} \left( \frac{\theta_E}{\sqrt{q\theta_1^2 + \theta_2^2/q}} \right)^{\gamma' - 1}, \quad (12)$$

where  $\gamma'$  is the radial power-law slope (with  $\gamma' = 2$  corresponding to isothermal),  $\theta_E$  is the Einstein radius, and  $q$  is the axis ratio of the elliptical isodensity contours. Various studies have shown that the power-law profile provides accurate descriptions of lens galaxies (e.g., Gavazzi et al. 2007; Humphrey & Buote 2010; Koopmans et al. 2009; Auger et al. 2010; Barnabè et al. 2011). In particular, Suyu et al. (2009) found that the grid-based lens potential corrections from power-law models were only  $\sim 2\%$  for B1608+656 with interacting lens galaxies, thus validating the use of the simple power-law models even for complicated lenses. We note that the surface brightness of the main deflector in RXJ1131–1231 shows no signs of interaction (Section 6.1.2) and it is therefore much simpler than the case of B1608+656, further justifying the use of a simple power-law model to describe the mass distribution within the multiple images.

The Einstein radius in Equation (12) corresponds to the geometric radius of the critical curve,<sup>12</sup> and the mass

<sup>11</sup> excluding the source surface brightness parameters  $s$  that can be marginalized analytically

<sup>12</sup> The critical curve of  $\kappa_{\text{pl}}$  in Equation (12) is symmetric about  $\theta_1$  and  $\theta_2$ , and the geometric radius is  $\sqrt{\theta_{\text{long}}\theta_{\text{short}}}$ , where  $\theta_{\text{long}}$  ( $\theta_{\text{short}}$ ) is the distance of the furthest (closest) point on the critical curve from the origin.

enclosed within the isodensity contour with the geometric Einstein radius is

$$M_E = \pi \theta_E^2 D_d^2 \Sigma_{\text{crit}} \quad (13)$$

that depends only on  $\theta_E$ , a robust quantity in lensing.

The deflection angle and lens potential of the power-law profile are computed following Barkana (1998). For each lens galaxy, the distribution is suitably translated to the position of the lens galaxy and rotated by the position angle  $\phi$  of the lens galaxy (where  $\phi$  is a free parameter, measured counterclockwise from  $\theta_2$ ). Since the satellite galaxy is small in extent, we approximate its mass distribution as a spherical isothermal mass distribution with  $\gamma'_S = 2$  and  $q_S = 1$  in Equation (12). The (very small) impact of the satellite on cosmographic inferences is discussed in Section 8.5.

Our coordinate system is defined such that  $\theta_1$  and  $\theta_2$  point to the west and north, respectively. The origin of the coordinates is at the bottom-left corner of the ACS image containing  $160 \times 160$  pixels.

In addition to the lens galaxies, we include a constant external shear of the following form in polar coordinates  $\theta$  and  $\varphi$ :

$$\psi_{\text{ext}}(\theta, \varphi) = \frac{1}{2} \gamma_{\text{ext}} \theta^2 \cos 2(\varphi - \phi_{\text{ext}}), \quad (14)$$

where  $\gamma_{\text{ext}}$  is the shear strength and  $\phi_{\text{ext}}$  is the shear angle. The shear position angle of  $\phi_{\text{ext}} = 0^\circ$  corresponds to a shearing along the  $\theta_1$  direction whereas  $\phi_{\text{ext}} = 90^\circ$  corresponds to a shearing in the  $\theta_2$  direction.

We do not include the external convergence  $\kappa_{\text{ext}}$  at this stage, since this parameter is completely degenerate with  $D_{\Delta t}$  in the ACS and time-delay modeling. Rather, we use  $D_{\Delta t}^{\text{model}} \equiv (1 - \kappa_{\text{ext}}) D_{\Delta t}$  for the lensing and time-delay data, and information on  $\kappa_{\text{ext}}$  will come from kinematics and lens environment in Section 7 to allow us to infer  $D_{\Delta t}$ .

#### 6.1.2. Lens light

For the light distribution of the lens galaxies, we use elliptical Sérsic profiles,

$$I(\theta_1, \theta_2) = A \exp \left[ -k \left( \left( \frac{\sqrt{\theta_1^2 + \theta_2^2 / q_L^2}}{R_{\text{eff}}} \right)^{1/n_{\text{Sersic}}} - 1 \right) \right], \quad (15)$$

where  $A$  is the amplitude,  $k$  is a constant such that  $R_{\text{eff}}$  is the effective (half-light) radius,  $q_L$  is the axis ratio, and  $n_{\text{Sersic}}$  is the Sérsic index (Sérsic 1968). The distribution is suitably rotated by positions angle  $\phi_L$  and translated to the galaxy positions  $(\theta_{1,L}, \theta_{2,L})$ . We find that a single Sérsic profile for the primary lens galaxy leads to significant residuals, as was found by Claeskens et al. (2006). Instead, we use two Sérsic profiles with common centroids and position angles to describe the lens galaxy G. For the small satellite galaxy that illuminates only a few pixels, we use a circular Sérsic profile with  $n_{\text{Sersic}} = 1$ . This simplifying assumption has no effect on the mass modeling since the light of the satellite is central and compact, and thus does not affect the light or mass of the other components.

#### 6.1.3. Source light

To describe the surface brightness distribution of the lensed source, we follow Suyu (2012) and use a hybrid model comprised of (1) point images for the lensed AGNs on the image plane, and (2) a regular grid of source surface brightness pixels for the spatially extended AGN host galaxy. Modeling the AGN point images independently accommodates variations in the fluxes arising from microlensing, time delays and substructures. Each AGN image therefore has three parameters: a position in  $\theta_1$  and  $\theta_2$  and an amplitude. We collectively denote these AGN parameters as  $\nu$ . The extended source on a grid is modeled following Suyu et al. (2006), with curvature regularization.

#### 6.1.4. PSF

A PSF is needed to model the light of the lens galaxies and the lensed source. We use stars in the field to approximate the PSF, which has been shown to work sufficiently well in modeling galaxy-scale strong lenses (e.g., Marshall et al. 2007; Suyu et al. 2009; Suyu 2012). In particular, we adopt the star that is located at  $2.4$  northwest of the lens system as the model of the PSF.

#### 6.1.5. Image pixel uncertainties

The comprehensive mass and light model described above captures the large-scale features of the data very well. However, small-scale features in the image might cause misfits which, if not taken into account, may lead to an underestimation of parameter uncertainties and biased parameter estimates. Suyu (2012) found that by boosting the pixel uncertainty of the image surface brightness, the lens model parameters can be faithfully recovered with realistic estimation of uncertainties.

Following this study, we introduce two terms to describe the variance of the intensity at pixel  $i$  of the ACS image  $\mathbf{d}_{\text{ACS}}$ ,

$$\sigma_{\text{pix},i}^2 = \sigma_{\text{bkgd}}^2 + f d_{\text{ACS},i}, \quad (16)$$

where  $\sigma_{\text{bkgd}}$  is the background uncertainty,  $f$  is a scaling factor, and  $d_{\text{ACS},i}$  is the image intensity. The second term,  $f d_{\text{ACS},i}$ , corresponds to a scaled version of Poisson noise for the astrophysical sources. We measure  $\sigma_{\text{bkgd}}$  from a blank region in the image without astrophysical sources. We set the value of  $f$  such that the reduced  $\chi^2$  is  $\sim 1$  for the lensed image reconstruction (see, e.g., Suyu et al. 2006, for details on the computation of the reduced  $\chi^2$  that takes into account the regularization on the source pixels). Equation (16) by design downweights regions of high intensities where the residuals are typically most prominent. This allows the lens model to fit to the overall structure of the data instead of reducing high residuals at a few locations at the expense of poorer fits to the large-scale lensing features. The residuals near the AGN image positions are particularly high due to the high intensities and slight saturations in some of the images. Therefore, we set the uncertainty on the inner pixels of the AGN images to a very large number that effectively leads to these pixels being discarded. We discard only a small region in fitting the AGN light, and increase the region to minimize AGN residuals when using the extended source features to constrain the lens mass parameters.

## 6.2. Likelihoods

The model-predicted image pixel surface brightness can be written as a vector

$$\mathbf{d}_{\text{ACS}}^{\text{P}} = \mathbf{B}\mathbf{g} + \mathbf{B}\mathbf{L}\mathbf{s} + \sum_{i=1}^{N_{\text{AGN}}} \mathbf{a}_i(\boldsymbol{\nu}), \quad (17)$$

where  $\mathbf{B}$  is a blurring operator that accounts for the PSF convolution,  $\mathbf{g}$  is a vector of image pixel intensities of the Sérsic profiles for the lens galaxy light,  $\mathbf{L}$  is the lensing operator that maps source intensity to the image plane based on the deflection angles computed from the parameters of the lens mass distributions (such as  $\gamma'$ ,  $\theta_{\text{E}}$ ,  $\gamma_{\text{ext}}$ ),  $\mathbf{s}$  is a vector of source-plane pixel intensities,  $N_{\text{AGN}} (= 4)$  is the number of AGN images, and  $\mathbf{a}_i(\boldsymbol{\nu})$  is the vector of image pixel intensities for PSF-convolved image  $i$  of the AGN.

The likelihood of the ACS data with  $N_{\text{d}}$  image pixels is

$$P(\mathbf{d}_{\text{ACS}}|\gamma', \theta_{\text{E}}, \gamma_{\text{ext}}, \boldsymbol{\eta}) = \int d\mathbf{s} P(\mathbf{d}_{\text{ACS}}|\gamma', \theta_{\text{E}}, \gamma_{\text{ext}}, \boldsymbol{\eta}, \mathbf{s}) P(\mathbf{s}), \quad (18)$$

where

$$P(\mathbf{d}_{\text{ACS}}|\gamma', \theta_{\text{E}}, \gamma_{\text{ext}}, \boldsymbol{\eta}, \mathbf{s}) = \frac{1}{Z_{\text{d}}} \exp \sum_{i=1}^{N_{\text{d}}} \left[ -\frac{(d_{\text{ACS},i} - d_{\text{ACS},i}^{\text{P}})^2}{2\sigma_{\text{pix},i}^2} \right] \cdot \prod_i^{N_{\text{AGN}}} \frac{1}{\sqrt{2\pi}\sigma_i} \exp \left[ -\frac{|\boldsymbol{\theta}_i - \boldsymbol{\theta}_i^{\text{P}}|^2}{2\sigma_i^2} \right]. \quad (19)$$

In the first term of this likelihood function,  $Z_{\text{d}}$  is just the normalization

$$Z_{\text{d}} = (2\pi)^{N_{\text{d}}/2} \prod_{i=1}^{N_{\text{d}}} \sigma_{\text{pix},i}, \quad (20)$$

$d_{\text{ACS},i}$  is the surface brightness of pixel  $i$ ,  $d_{\text{ACS},i}^{\text{P}}(\gamma', \theta_{\text{E}}, \gamma_{\text{ext}}, \boldsymbol{\eta}, \mathbf{s})$  is the corresponding predicted value given by Equation (17) (recall that  $\boldsymbol{\eta}$  are the remaining lens model parameters to which the ACS data are sensitive), and  $\sigma_{\text{pix},i}^2$  is the pixel uncertainty given by Equation (16). The second term in the likelihood accounts for the positions of the AGN images, modeled as independent points (i.e. non-pixelated sources) in the image. In this term,  $\boldsymbol{\theta}_i$  is the measured image position (listed in Table 1),  $\sigma_i$  is the estimated positional uncertainty of  $0.005''$ , and  $\boldsymbol{\theta}_i^{\text{P}}(\gamma', \theta_{\text{E}}, \gamma_{\text{ext}}, \boldsymbol{\eta})$  is the predicted image position given the lens parameters. (Notice that this second term does not contribute to the marginalization integral of Equation (18).) The form of  $P(\mathbf{s})$  for the source intensity pixels and the resulting analytic expression for the marginalization in Equation (18) are detailed in Suyu et al. (2006).

The likelihood for the time delays is given by

$$P(\Delta t | D_{\Delta t}^{\text{model}}, \gamma', \theta_{\text{E}}, \gamma_{\text{ext}}, \boldsymbol{\eta}) = \prod_i \left( \frac{1}{\sqrt{2\pi}\sigma_{\Delta t,i}} \exp \left[ -\frac{(\Delta t_i - \Delta t_i^{\text{P}})^2}{2\sigma_{\Delta t,i}^2} \right] \right), \quad (21)$$

TABLE 1  
LENS MODEL PARAMETERS

Description	Parameter	Marginalized or optimized constraints
Time-delay distance (Mpc)	$D_{\Delta t}^{\text{model}}$	$1883^{+89}_{-85}$
Lens mass distribution		
Centroid of G in $\theta_1$ (arcsec)	$\theta_{1,\text{G}}$	$4.420^{+0.003}_{-0.002}$
Centroid of G in $\theta_2$ (arcsec)	$\theta_{2,\text{G}}$	$3.932^{+0.004}_{-0.003}$
Axis ratio of G	$q_{\text{G}}$	$0.763^{+0.005}_{-0.008}$
Position angle of G ( $^\circ$ )	$\phi_{\text{G}}$	$115.8^{+0.5}_{-0.5}$
Einstein radius of G (arcsec)	$\theta_{\text{E}}$	$1.64^{+0.01}_{-0.02}$
Radial slope of G	$\gamma'$	$1.95^{+0.05}_{-0.04}$
Centroid of S in $\theta_1$ (arcsec)	$\theta_{1,\text{S}}$	4.323
Centroid of S in $\theta_2$ (arcsec)	$\theta_{2,\text{S}}$	4.546
Einstein radius of S (arcsec)	$\theta_{\text{E},\text{S}}$	$0.20^{+0.01}_{-0.01}$
External shear strength	$\gamma_{\text{ext}}$	$0.089^{+0.006}_{-0.006}$
External shear angle ( $^\circ$ )	$\phi_{\text{ext}}$	$92^{+1}_{-2}$
Lens light as Sérsic profiles		
Centroid of G in $\theta_1$ (arcsec)	$\theta_{1,\text{GL}}$	$4.411^{+0.001}_{-0.001}$
Centroid of G in $\theta_2$ (arcsec)	$\theta_{2,\text{GL}}$	$4.011^{+0.001}_{-0.001}$
Position angle of G ( $^\circ$ )	$\phi_{\text{GL}}$	$121.6^{+0.5}_{-0.5}$
Axis ratio of G1	$q_{\text{GL1}}$	$0.878^{+0.004}_{-0.003}$
Amplitude of G1	$A_{\text{GL1}}$	$0.091^{+0.001}_{-0.001}$
Effective radius G1 (arcsec)	$R_{\text{eff,GL1}}$	$2.49^{+0.01}_{-0.01}$
Index of G1	$n_{\text{seraic,GL1}}$	$0.93^{+0.03}_{-0.03}$
Axis ratio of G2	$q_{\text{GL2}}$	$0.849^{+0.004}_{-0.004}$
Amplitude of G2	$A_{\text{GL2}}$	$0.89^{+0.03}_{-0.03}$
Effective radius of G2 (arcsec)	$R_{\text{eff,GL2}}$	$0.362^{+0.009}_{-0.009}$
Index of G2	$n_{\text{seraic,GL2}}$	$1.59^{+0.03}_{-0.03}$
Centroid of S in $\theta_1$ (arcsec)	$\theta_{1,\text{SL}}$	4.323
Centroid of S in $\theta_2$ (arcsec)	$\theta_{2,\text{SL}}$	4.546
Axis ratio of S	$q_{\text{SL}}$	$\equiv 1$
Amplitude of S	$A_{\text{SL}}$	34.11
Effective radius of S (arcsec)	$R_{\text{eff,SL}}$	0.01
Index of S	$n_{\text{seraic,SL}}$	$\equiv 1$
Lensed AGN light		
Position of image A in $\theta_1$ (arcsec)	$\theta_{1,\text{A}}$	2.383
Position of image A in $\theta_2$ (arcsec)	$\theta_{2,\text{A}}$	3.412
Amplitude of image A	$a_{\text{A}}$	1466
Position of image B in $\theta_1$ (arcsec)	$\theta_{1,\text{B}}$	2.344
Position of image B in $\theta_2$ (arcsec)	$\theta_{2,\text{B}}$	4.594
Amplitude of image B	$a_{\text{B}}$	1220
Position of image C in $\theta_1$ (arcsec)	$\theta_{1,\text{C}}$	2.960
Position of image C in $\theta_2$ (arcsec)	$\theta_{2,\text{C}}$	2.300
Amplitude of image C	$a_{\text{C}}$	502
Position of image D in $\theta_1$ (arcsec)	$\theta_{1,\text{D}}$	5.494
Position of image D in $\theta_2$ (arcsec)	$\theta_{2,\text{D}}$	4.288
Amplitude of image D	$a_{\text{D}}$	129

Notes. There are a total of 39 parameters that are optimized or sampled. Parameters that are optimized are held fixed in the sampling of the full parameter space and have no uncertainties tabulated. Changes in these optimized parameters have little effect on the key parameters for cosmology (such as  $D_{\Delta t}^{\text{model}}$ ). The tabulated values for the sampled parameters are the marginalized constraints with uncertainties given by the 16<sup>th</sup> and 84<sup>th</sup> percentiles (to indicate the 68% credible interval). For the lens light, two Sérsic profiles with common centroid and position angle are used to describe the primary lens galaxy G. They are denoted as G1 and G2 above. The position angles are measured counterclockwise from positive  $\theta_2$  (north). The source surface brightness of the AGN host is modeled on a grid of pixels; these pixel parameters ( $\mathbf{s}$ ) are analytically marginalized and are thus not listed.



where  $\Delta t_i$  is the measured time delay with uncertainty  $\sigma_{\Delta t,i}$  for image pair  $i=AB, CB, \text{ or } DB$ , and  $\Delta t_i^P(D_{\Delta t}^{\text{model}}, \gamma', \theta_E, \gamma_{\text{ext}}, \boldsymbol{\eta})$  is the corresponding predicted time delay computed via Equation (6) given the lens mass model parameters.

The joint likelihood for the ACS and time delay data that appears in Equation (10),  $P(\mathbf{d}_{\text{ACS}}, \Delta \mathbf{t} | D_{\Delta t}, \gamma', \theta_E, \gamma_{\text{ext}}, \boldsymbol{\eta}, \kappa_{\text{ext}})$ , is just the product of the likelihoods in Equations (18) and (21).

We assign uniform priors over reasonable ranges for all the lens parameters:  $D_{\Delta t}^{\text{model}}, \gamma', \theta_E, \gamma_{\text{ext}}$  and  $\boldsymbol{\eta}$ .

### 6.3. MCMC sampling

We model the ACS image and time delays with GLEE<sup>13</sup>. The ACS image has  $160 \times 160$  surface brightness pixels as constraints. There are a total of 39 lens model parameters that are summarized in Table 1. This is the most comprehensive lens model of RXJ1131–1231 to date. The list of parameters excludes the source surface brightness pixel parameters,  $\mathbf{s}$ , which are analytically marginalized in computing the likelihood (see, e.g., Suyu & Halkola 2010, for details). With such a large parameter space, we sequentially sample individual parts of the parameter space first to get good starting positions near the peak of the PDF before sampling the full parameter space. The aim is to obtain a robust PDF for the key lens parameters for cosmography:  $D_{\Delta t}^{\text{model}}, \gamma', \theta_E$ , and  $\gamma_{\text{ext}}$ .

For an initial model of the lens light, we create an annular mask for the lensed arc and use the image pixels outside the annular mask to optimize the lens Sérsic profiles. The parameters for the light of the satellite is fixed to these optimized values for the remainder of the analysis since the satellite light has negligible effect on  $D_{\Delta t}^{\text{model}}$  and other lens parameters. Furthermore, we fix the centroid of the satellite’s mass distribution to its observed light centroid. We obtain an initial mass model for the lenses using the image positions of the multiple knots in the source that are identified following Brewer & Lewis (2008). Specifically, we optimize for the parameters that minimize the separation between the identified image positions and the predicted image positions from the mass model. We then optimize the AGN light together with the light of the extended source while keeping the lens light and lens mass model fixed. The AGN light parameters are then held fixed to these optimized values. Having obtained initial values for all the lens model parameters to describe the ACS data, we then proceed to sample the lens parameters listed in Table 1 using a MCMC method. In particular, we simultaneously vary the following parameters: all mass parameters of G, the Einstein radius of S, external shear, the extended source intensity distribution, the lens light profile of G. GLEE employs several of the methods of Dunkley et al. (2005) for efficient MCMC sampling and for assessing chain convergence.

### 6.4. Constraints on the lens model parameters

We explore various parameter values for the AGN light and the satellite Sérsic light, try different PSF models, and consider different masks for the lensed arcs and

the AGNs (which are fixed in the MCMC sampling). These variations have negligible effect on the sampling of the other lens parameters. The only attribute that changes the PDF of the parameters significantly is the number of source pixels, or equivalently, the source pixel size. We try a series of source resolution from coarse to fine, and the parameter constraints stabilize starting at  $\sim 50 \times 50$  source pixels, corresponding to source pixel sizes of  $\sim 0''.05$ . Nonetheless, the parameter constraints for different source resolutions are shifted significantly from one another. Different source pixelizations minimize the image residuals in different manners, and predict different relative thickness of the arcs that provides information on the lens profile slope  $\gamma'$  (e.g., Suyu 2012). To quantify this systematic uncertainty, we consider the following set of source resolutions:  $50 \times 50$ ,  $52 \times 52$ ,  $54 \times 54$ ,  $56 \times 56$ ,  $58 \times 58$ ,  $60 \times 60$ , and  $64 \times 64$ . The likelihood  $P(\mathbf{d}_{\text{ACS}}, \Delta \mathbf{t} | D_{\Delta t}^{\text{model}}, \gamma', \theta_E, \gamma_{\text{ext}})$ , which is proportional to the marginalized posterior of these parameters  $P(D_{\Delta t}^{\text{model}}, \gamma', \theta_E, \gamma_{\text{ext}} | \mathbf{d}_{\text{ACS}}, \Delta \mathbf{t})$  since the priors are uniform, is plotted in Figure 3 for each of these source resolutions. The scatter in constraints among the various source resolutions allows us to quantify the systematic uncertainty. In particular, we weight each choice of the source resolution equally, and combine the Markov chains together. In Table 1, we list the marginalized parameters from the combined samples.

We show the most probable image and source reconstruction for the  $64 \times 64$  resolution in Figure 4. Only the image intensity pixels within the annular mask shown in the top-middle panel are used to reconstruct the source that is shown in the bottom-right panel. A comparison of the top-left and bottom-left panels shows that our lens model reproduces the global features of the ACS image. The time delays are also reproduced by the model: for the various source resolutions, the  $\chi^2$  is  $\sim 2$  for the three delays relative to image B. There are some small residual features in the bottom-middle panel of Figure 4, and these cause the shifts in the parameter constraints seen in Figure 3 for different source pixel sizes. The reconstructed host galaxy of the AGN in the bottom-right panel shows a compact central peak, which is probably the bulge of the spiral source galaxy, embedded in a more diffuse patch of light (the disk) with knots/spiral features.

### 6.5. Understanding the external shear

The inferred external shear is  $\gamma_{\text{ext}} = 0.089 \pm 0.006$  (marginalizing over all other model parameters) from modeling the ACS image and the time delays. The external shear may provide information on the amount of external convergence, since they originate from the same external structures. However, the high  $\gamma_{\text{ext}}$  found in our model could potentially be attributed to deviations of the primary lens from its elliptical power-law description; if this were the case, some of  $\gamma_{\text{ext}}$  would in fact be internal shear. To gauge whether the modeled shear is truly external, we also considered a model that includes a constant external convergence gradient. This introduces two additional parameters:  $\kappa'$  (gradient) and  $\phi_\kappa$  (the position angle of the gradient, where  $\phi_\kappa = 0$  corresponds to positive  $\kappa$  gradient along the positive  $\theta_2$  direction, i.e., north). The ACS data allow us to con-

<sup>13</sup> a lens modeling software developed by S. H. Suyu and A. Halkola (Suyu & Halkola 2010) based on Suyu et al. (2006) and Halkola et al. (2008)

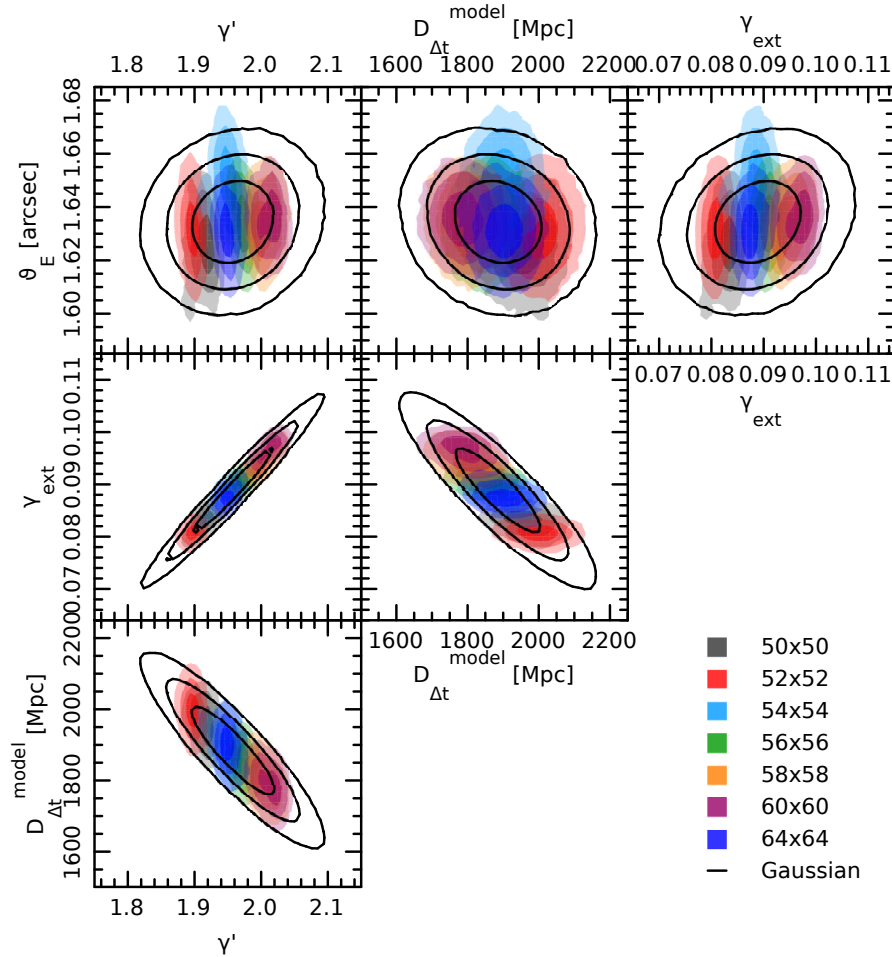


FIG. 3.— Posterior of the key lens model parameters for the lensing and time-delay data. Each color represents a particular source resolution that is the dominant source of systematic uncertainty in the modeling of the ACS data. The solid curves are a Gaussian fit to the PDF by weighting each source resolution chain equally. The contours/shades mark the 68.3%, 95.4%, 99.7% credible regions.

strain  $\kappa' = (5.1^{+0.4}_{-0.3}) \times 10^{-3} \text{ arcsec}^{-1}$  and  $\phi_\kappa = 87 \pm 2^\circ$ . The convergence gradient is aligned along the same direction as the external shear within  $5^\circ$  and has a sensible magnitude, suggesting that the shear is in fact truly external, and is likely due to mass structures to the east of the lens.

To investigate the origin of the external shear, we construct a wide-field R-band image from the COSMOS-GRAB monitoring images that is shown in Figure 5. The lens system is indicated by the box, and the galaxies (stars) in the field are marked by solid (dashed) circles, identified using SExtractor (Bertin & Arnouts 1996). Overlaid on the image within the dashed box are the X-ray contours from Chartas et al. (2009), showing the presence of a galaxy cluster at  $z = 0.1$  that is located at  $158''$  northeast of the lens (Morgan et al. 2006; Chartas et al. 2009). Using the measured X-ray luminosity in Chartas et al. (2009), we estimate that the contribution of the cluster to the external shear at the lens is only a few percent. Nonetheless, large-scale structures associated with the cluster and the plethora of mass structures to the east of the lens could generate additional shear. The fact that our modeled external shear and convergence gradients both point toward mass structures in the east that are visible in Figure 5 is a further indication that the modeled shear is indeed external. We

will use this external shear in Section 7.2 to constrain the external convergence.

### 6.6. Propagating the lens model forward

To facilitate the sampling and marginalization of the posterior of the *cosmological* parameters in Equations (10) and (11), we approximate the overall likelihood of  $\mathbf{d}_{\text{ACS}}$  and  $\Delta t$  from the multiple source resolutions in Figure 3 with a multivariate Gaussian distribution for the interesting parameters  $\gamma', \theta_E, \gamma_{\text{ext}}$  and  $D_{\Delta t}^{\text{model}}$ , marginalizing over the nuisance parameters  $\eta$ . This approximation allows the value of  $P(\mathbf{d}_{\text{ACS}}, \Delta t | \gamma', \theta_E, \gamma_{\text{ext}}, D_{\Delta t}^{\text{model}})$  to be computed at any position in this 4-dimensional parameter space. Note that in contrast to the other parameters, the Einstein radius of the primary,  $\theta_E$ , is well determined, with minimal degeneracy with other parameters. This robust quantity is used in the dynamics modeling of the lens galaxy. The approximated Gaussian likelihood provides an easy way to combine with the stellar kinematics and lens environment information for measuring  $D_{\Delta t}$ .

## 7. CONSTRAINING $\kappa_{\text{ext}}$

In this section, we fold in additional information on the lens galaxy stellar kinematics and density environment to constrain the nuisance parameter  $\kappa_{\text{ext}}$ .



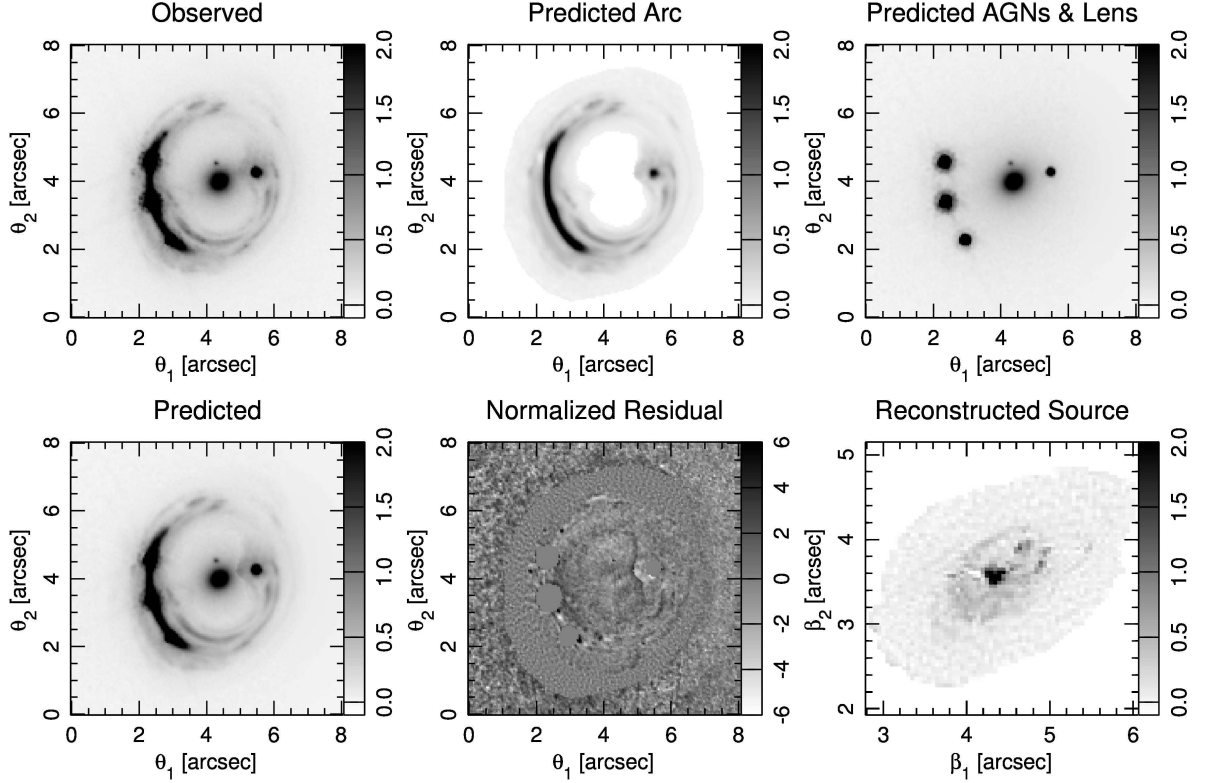


FIG. 4.— ACS image reconstruction of the most probable model with a source grid of  $64 \times 64$  pixels. Top left: observed ACS F814W image. Top middle: predicted lensed image of the background AGN host galaxy. Top right: predicted light of the lensed AGNs and the lens galaxies. Bottom left: predicted image from all components, which is a sum of the top-middle and top-right panels. Bottom middle: image residual, normalized by the estimated  $1\sigma$  uncertainty of each pixel. Bottom right: the reconstructed source. Our lens model reproduces the global features of the data.

### 7.1. Stellar kinematics

We follow Suyu et al. (2010) and model the velocity dispersion of the stars in the primary lens galaxy G, highlighting the main steps. The three-dimensional mass density distribution of the lens galaxy can be expressed as

$$\rho_G(r) = (\kappa_{\text{ext}} - 1) \Sigma_{\text{crit}} \theta_E^{\gamma' - 1} D_d^{\gamma' - 1} \frac{\Gamma(\frac{\gamma'}{2})}{\pi^{1/2} \Gamma(\frac{\gamma' - 3}{2})} \frac{1}{r^{\gamma'}}. \quad (22)$$

Note that the projected mass of the lens galaxy enclosed within  $\theta_E$  is  $(1 - \kappa_{\text{ext}})M_E$ , while the projected mass associated with the external convergence is  $\kappa_{\text{ext}}M_E$ ; the sum of the two is the Einstein mass  $M_E$  that was given in Equation (13). We employ spherical Jean's modeling to infer the line-of-sight velocity dispersion,  $\sigma^P(\pi, \gamma', \theta_E, r_{\text{ani}}, \kappa_{\text{ext}})$ , from  $\rho_G$  by assuming the Hernquist profile (Hernquist 1990) for the stellar distribution (e.g., Binney & Tremaine 1987; Suyu et al. 2010).<sup>14</sup> An anisotropy radius of  $r_{\text{ani}} = 0$  corresponds to pure radial stellar orbits, while  $r_{\text{ani}} \rightarrow \infty$  corresponds to isotropic orbits with equal radial and tangential velocity dispersions. We note that  $\sigma^P$  is independent of  $H_0$ , but is dependent on the other cosmological parameters (e.g.,  $w$  and  $\Omega_{\text{de}}$ ) through  $\Sigma_{\text{crit}}$  and the physical scale radius of

the stellar distribution.

The likelihood for the velocity dispersion is

$$P(\sigma | \pi, \gamma', \theta_E, r_{\text{ani}}, \kappa_{\text{ext}}) = \frac{1}{\sqrt{2\pi\sigma_\sigma^2}} \exp \left[ -\frac{(\sigma - \sigma^P(\pi, \gamma', \theta_E, r_{\text{ani}}, \kappa_{\text{ext}}))^2}{2\sigma_\sigma^2} \right] \quad (23)$$

where  $\sigma = 323 \text{ km s}^{-1}$  and  $\sigma_\sigma = 20 \text{ km s}^{-1}$  from Section 4.3. Recall that the priors on  $\gamma'$  and  $\theta_E$  were assigned to be uniform in the lens modeling. We also impose a uniform prior on  $r_{\text{ani}}$  in the range of  $[0.5, 5]R_{\text{eff}}$  for the kinematics modeling, where the effective radius based on the two-component Sérsic profiles in Table 1 is  $1''.85$  from the photometry.<sup>15</sup> The uncertainty in  $R_{\text{eff}}$  has negligible impact on the predicted velocity dispersion. The prior PDF for  $\pi$  is discussed in Section 8.1, while the PDF for  $\kappa_{\text{ext}}$  is described in the next section.

### 7.2. Lens environment

We combine the relative galaxy counts from Section 4.4, the measured external shear in Section 6.4, and the Millennium Simulation (MS; Springel et al. 2005) to obtain an estimate of  $P(\kappa_{\text{ext}} | \mathbf{d}_{\text{env}}, \gamma_{\text{ext}}, \text{MS})$ . This builds on the approach presented in Suyu et al. (2010) that used only the relative galaxy counts.

<sup>14</sup> Suyu et al. (2010) found that Hernquist (1990) and Jaffe (1983) stellar distribution functions led to nearly identical cosmological constraints.

<sup>15</sup> Before unblinding, we used an effective radius of  $3''.2$  based on a single Sérsic fit. The larger  $R_{\text{eff}}$  changes the inference of  $D_{\Delta t}$  at the  $< 0.5\%$  level.

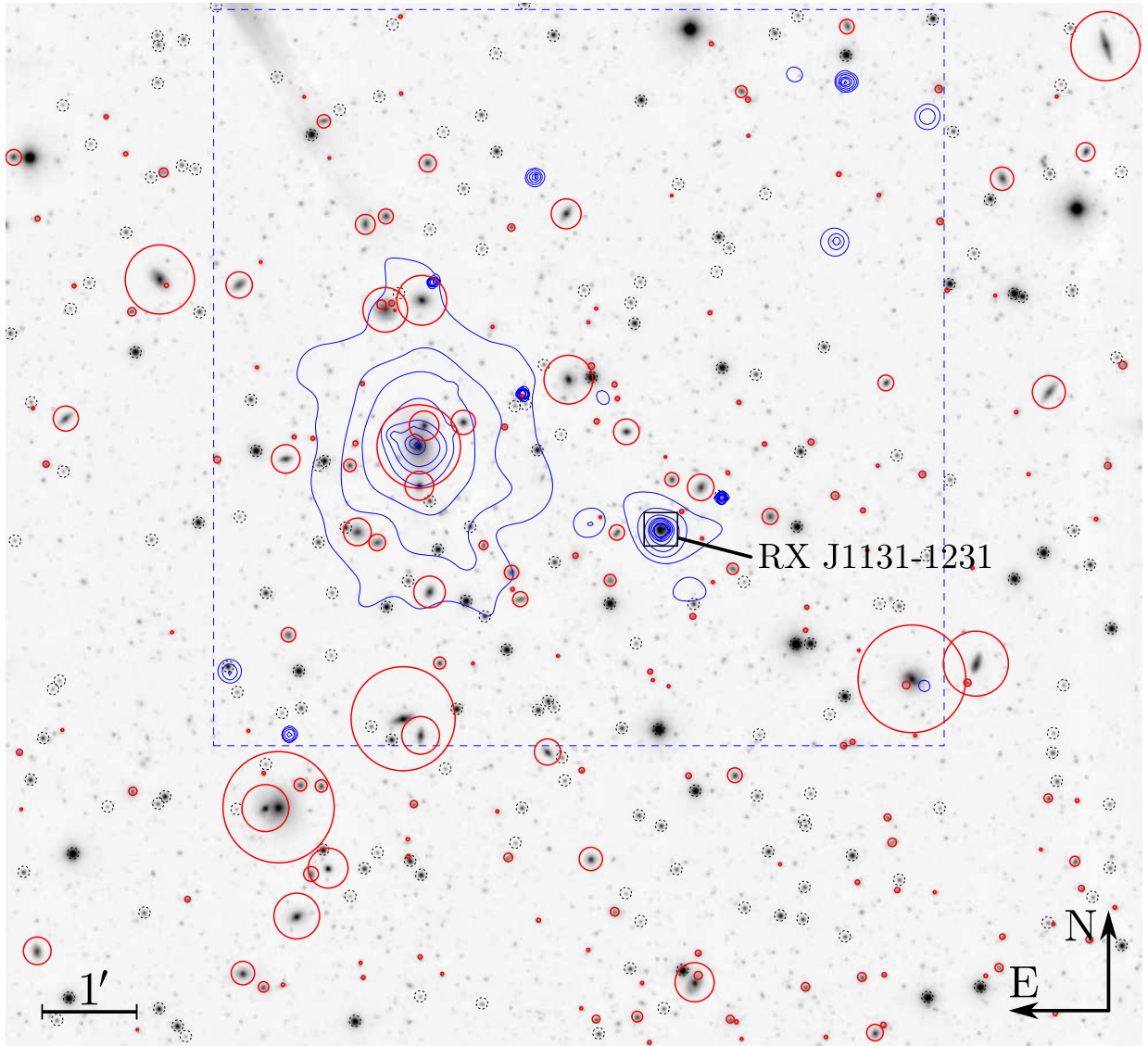


FIG. 5.—  $11.5' \times 10.5'$  R-band image obtained from stacking 60 hours of the best-quality images in the COSMOGRAIL monitoring. The lens system is marked by the box near the center. Galaxies (stars) in the field are indicated by solid (dashed) circles. The radius of the solid circle is proportional to the flux of the galaxy. X-ray map from Chartas et al. (2009) are overlaid on the image within the dashed box. The concentrations of mass structures to the east of the lens are consistent with the modeled external shear and convergence gradient directions.

Tracing rays through the Millennium Simulation (see Hilbert et al. 2009, for details of the method), we create 64 simulated survey fields, each of solid angle  $4 \times 4 \text{ deg}^2$ . In each field we map the convergence and shear to the source redshift  $z_s$ , and catalog the galaxy content, which we derive from the galaxy model by Guo et al. (2010). For each line of sight in each simulated field, we record the convergence, shear, and relative galaxy counts in a  $45''$  aperture having I-band magnitudes between 18.5 and 24.5. These provide samples for the PDF  $P(\kappa_{\text{ext}}, \gamma_{\text{ext}}, \mathbf{d}_{\text{env}} | \text{MS})$ . We assume that the constructed PDF is applicable to strong-lens lines of sight, following Suyu et al. (2010) who showed that the distribution of  $\kappa_{\text{ext}}$  for strong lens lines of sight are very similar to that for all lines of sight.

Structures in front of the lens distort the time delays and the images of the lens/source, while structures behind the lens further affect the time delays and images of

the source. However, to model simultaneously the mass distributions of the strong lens galaxies and all structures along the line of sight is well beyond the current state of the art. In practice, the modeling of the strong lens galaxies is performed separately from the description of line-of-sight structures, and we approximate the effects of the lines-of-sight structures into the single correction term  $\kappa_{\text{ext}}$ , whose statistical properties we estimate from the Millennium Simulation.

By selecting the lines of sight in the Millennium Simulation that match the properties of RXJ1131–1231, we can obtain  $P(\mathbf{d}_{\text{env}} | \kappa_{\text{ext}}, \gamma_{\text{ext}}, \text{MS}) P(\kappa_{\text{ext}})$  and simultaneously marginalize over  $\gamma_{\text{ext}}$  in Equation (10). We assumed a uniform prior for  $\gamma_{\text{ext}}$  in the lensing analysis, such that  $P(\gamma_{\text{ext}})$  is a constant. The lensing likelihood is the only other term that depends on  $\gamma_{\text{ext}}$ , and from Section 6.4, the lensing likelihood provides a tight constraint on  $\gamma_{\text{ext}}$  that is approximately Gaussian:  $0.089 \pm 0.006$ .

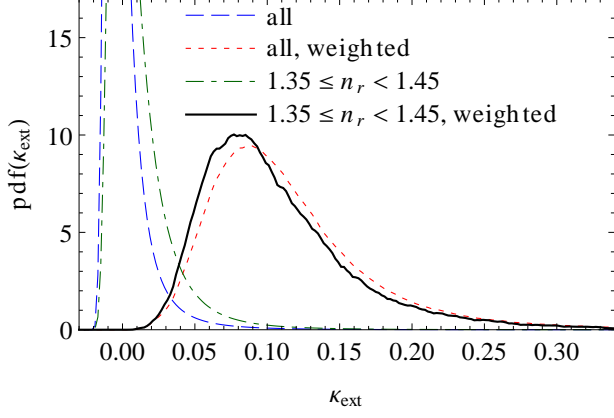


FIG. 6.— The effective prior probability distribution for the external convergence  $\kappa_{\text{ext}}$  from combining ray tracing through the Millennium Simulation with the relative galaxy counts of 1.4 and the modeled external shear of  $0.089 \pm 0.006$ . Dashed line: the convergence distribution for all lines of sight; Dot-dashed line: the convergence distribution for lines of sight with relative galaxy count  $n_r = 1.4 \pm 0.05$ ; Dotted line: the convergence distribution for all lines of sight weighted by the likelihood for  $\gamma_{\text{ext}}$  from the lens model; Solid line: the  $\gamma_{\text{ext}}$ -weighted convergence distribution for lines of sight with  $n_r = 1.4 \pm 0.05$ . The effective prior for  $\kappa_{\text{ext}}$  used in the final cosmological parameter inference is described by this, most informative, distribution.

We can therefore simplify part of Equation (10) to

$$\begin{aligned} \int d\gamma_{\text{ext}} P(\mathbf{d}_{\text{ACS}}, \Delta\mathbf{t} | D_{\Delta t}, \gamma', \theta_E, \gamma_{\text{ext}}, \kappa_{\text{ext}}) \\ \cdot P(\mathbf{d}_{\text{env}} | \kappa_{\text{ext}}, \gamma_{\text{ext}}, \text{MS}) \\ \simeq P(\mathbf{d}_{\text{ACS}}, \Delta\mathbf{t} | D_{\Delta t}, \gamma', \theta_E, \kappa_{\text{ext}}) \\ \cdot P(\mathbf{d}_{\text{env}} | \kappa_{\text{ext}}, \gamma_{\text{ext}} = 0.089 \pm 0.006, \text{MS}), \quad (24) \end{aligned}$$

where the above approximation, i.e., neglecting the covariance between  $\gamma_{\text{ext}}$  and the other parameters in the lensing likelihood and then marginalizing  $\gamma_{\text{ext}}$  separately, is conservative since we would gain in precision by including the covariances with other parameters. Furthermore, by Bayes' rule,

$$\begin{aligned} P(\mathbf{d}_{\text{env}} | \kappa_{\text{ext}}, \gamma_{\text{ext}} = 0.089 \pm 0.006, \text{MS}) P(\kappa_{\text{ext}}) \\ \propto P(\kappa_{\text{ext}} | \mathbf{d}_{\text{env}}, \gamma_{\text{ext}} = 0.089 \pm 0.006, \text{MS}), \quad (25) \end{aligned}$$

which is precisely the PDF of  $\kappa_{\text{ext}}$  by selecting the samples in  $P(\kappa_{\text{ext}}, \gamma_{\text{ext}}, \mathbf{d}_{\text{env}} | \text{MS})$  that satisfies  $\mathbf{d}_{\text{env}}$  with a relative galaxy count within  $1.4 \pm 0.05$ , and subsequently weighting these samples by the Gaussian likelihood for  $\gamma_{\text{ext}}$ . This effective prior PDF for  $\kappa_{\text{ext}}$  that is constructed from the weighted samples,  $P(\kappa_{\text{ext}} | \mathbf{d}_{\text{env}}, \gamma_{\text{ext}} = 0.089 \pm 0.006, \text{MS})$ , is shown by the solid line in Figure 6.

## 8. TIME-DELAY DISTANCE OF RXJ1131–1231

We combine all the PDFs obtained in the previous sections to infer the time-delay distance  $D_{\Delta t}$ .

### 8.1. Cosmological priors

As written above, we *could* infer the time delay distance  $D_{\Delta t}$  directly, given a uniform prior. However, we are primarily interested in the cosmological information contained in such a distance measurement, so prefer to infer these directly. The posterior probability distribution on  $D_{\Delta t}$  can then be obtained by first calculating the posterior PDF of the cosmological parameters  $\pi$  through the marginalizations in Equations (11) and (10), and

then changing variables to  $D_{\Delta t}$ . Such transformations are of course straightforward when working with sampled PDFs.

In Table 2, we consider the following five cosmological world models, each with its own prior PDF  $P(\pi)$ :

- **UH<sub>0</sub>**: Uniform prior PDF for  $H_0$  between 0 and  $150 \text{ km s}^{-1} \text{ Mpc}^{-1}$  in a  $\Lambda$ CDM cosmology with  $\Omega_\Lambda = 1 - \Omega_m = 0.73$ . This is similar to the typical priors that were assumed in most of the early lensing studies, which sought to constrain  $H_0$  at fixed cosmology.
- **UwCDM**: Uniform priors on the parameters  $\{H_0, \Omega_{\text{de}}, w\}$  in a flat  $w$ CDM cosmology, where  $w$  is time-independent and  $\Omega_m = 1 - \Omega_{\text{de}}$ .
- **WMAP7wCDM**: The prior PDF for the parameters  $\{H_0, \Omega_{\text{de}}, w\}$  is taken to be the posterior PDF from the WMAP 7-year data set (Komatsu et al. 2011), assuming a flat  $w$ CDM cosmology, where  $w$  is time-independent and  $\Omega_m = 1 - \Omega_{\text{de}}$ .
- **WMAP7o $\Lambda$ CDM**: The prior PDF for the parameters  $\{H_0, \Omega_\Lambda, \Omega_k\}$  is taken to be the posterior PDF from the WMAP 7-year data set, assuming an open (or rather, non-flat) cosmology, with dark energy described by  $\Lambda$  and  $\Omega_k = 1 - \Omega_\Lambda - \Omega_m$  as the curvature parameter.
- **WMAP7owCDM**: The prior PDF for the parameters  $\{H_0, \Omega_{\text{de}}, w, \Omega_k\}$  is taken to be the posterior PDF from the WMAP 7-year data set, assuming an open  $w$ CDM cosmology, where  $w$  is time-independent and  $\Omega_k = 1 - \Omega_{\text{de}} - \Omega_m$  is the curvature parameter.

### 8.2. Posterior sampling

We sample the posterior PDF by weighting samples drawn from the prior PDF with the joint likelihood function evaluated at those points (Suyu et al. 2010). We generate samples of the cosmological parameters  $\pi$  from the priors listed in Table 2. We then join these to samples of  $\kappa_{\text{ext}}$  drawn from  $P(\kappa_{\text{ext}})$  from Section 7.2 and shown in Figure 6, and to uniformly distributed samples of  $\gamma'$  within  $[1.5, 2.5]$  and  $r_{\text{ani}}$  within  $[0.5, 5] R_{\text{eff}}$ . Rather than generating samples of  $\theta_E$  from the uniform prior, we obtain samples of  $\theta_E$  directly from the Gaussian approximation to the lensing and time-delay likelihood since  $\theta_E$  is quite independent of other model parameters (as shown in Figure 3). This boosts sampling efficiency, and the  $\theta_E$  samples are only used to evaluate the kinematics likelihood.

For each sample of  $\{\pi, \kappa_{\text{ext}}, \gamma', r_{\text{ani}}, \theta_E\}$ , we obtain the weight (or importance) as follows: (1) we determine  $D_{\Delta t}$  from  $\pi$  via Equation (2), (2) we calculate  $D_{\Delta t}^{\text{model}}$  via Equation (7), (3) we evaluate  $P(\mathbf{d}_{\text{ACS}}, \Delta\mathbf{t} | D_{\Delta t}^{\text{model}}, \gamma')$  based on the Gaussian approximation shown in Figure 3 for  $D_{\Delta t}^{\text{model}}$  and  $\gamma'$ , (4) we compute  $P(\sigma | \pi, \gamma', \kappa_{\text{ext}}, \theta_E, r_{\text{ani}})$  via Equation (23), and (5) we weight the sample by the product of  $P(\mathbf{d}_{\text{ACS}}, \Delta\mathbf{t} | D_{\Delta t}^{\text{model}}, \gamma')$  and  $P(\sigma | \pi, \gamma', \kappa_{\text{ext}}, \theta_E, r_{\text{ani}})$  from the previous two steps. The projection of these weighted samples onto  $\pi$  or  $D_{\Delta t}$  effectively marginalizes over the other parameters.



TABLE 2  
PRIORS ON COSMOLOGICAL PARAMETERS

Prior	Description
$UH_0$	uniform $H_0$ in $[0, 150] \text{ km s}^{-1} \text{ Mpc}^{-1}$ , $\Omega_m = 0.27$ , $\Omega_\Lambda = 0.73$ , $w = -1$
$Uw\text{CDM}$	uniform $H_0$ in $[0, 150] \text{ km s}^{-1} \text{ Mpc}^{-1}$ , uniform $\Omega_{de} = 1 - \Omega_m$ in $[0, 1]$ , uniform $w$ in $[-2.5, 0.5]$
$\text{WMAP7}w\text{CDM}$	WMAP7 for $\{H_0, \Omega_{de}, w\}$ with flatness and time-independent $w$
$\text{WMAP7}\Lambda\text{CDM}$	WMAP7 for $\{H_0, \Omega_\Lambda, \Omega_m\}$ with $w = -1$ in open $\Lambda\text{CDM}$
$\text{WMAP7}ow\text{CDM}$	WMAP7 for $\{H_0, \Omega_{de}, w, \Omega_k\}$ with time- independent $w$ and curvature $\Omega_k$

### 8.3. Blind analysis in action

As a brief illustration of our blind analysis approach, we show in the left panel of Figure 7 the blinded plot of the time-delay distance measurement. For all cosmological parameters such as  $D_{\Delta t}$ ,  $D_{\Delta t}^{\text{model}}$ ,  $H_0$ ,  $w$ ,  $\Omega_m$ , etc., we always plotted their probability distribution with respect to the median during the blind analysis. Therefore, we could use the shape of the PDFs to check our analysis without introducing experimenter bias by blinding the absolute parameter values. When we marginalized the parameters during the blind phase, our analysis code also returned the constraints with respect to the median. For example, the blinded time-delay distance for the  $\text{WMAP7}w\text{CDM}$  cosmology would be  $0_{-120}^{+130} \text{ Mpc}$ . We used this particular cosmology as our fiducial world model during the blind analysis. In the remainder of the paper, we show the unblinded results of RXJ1131–1231. The comparison with the gravitational lens B1608+656 and other cosmological probes was performed after we unblinded the analysis of RXJ1131–1231; otherwise, the blind analysis would be spoiled by such a comparison since the results of these previous studies were already known.

### 8.4. Posterior PDF for $D_{\Delta t}$

We show in the right-hand panel of Figure 7 the unblinded probability distribution of the time-delay distance for the first three cosmological models in Table 2. The priors, shown in dotted lines, are broad and rather uninformative. When including information from  $\mathbf{d}_{\text{ACS}}$ ,  $\Delta t$ ,  $\sigma$ , and  $\kappa_{\text{ext}}$ , we obtain posterior PDFs of  $D_{\Delta t}$  for RXJ1131–1231 that are nearly independent of the prior, demonstrating that time-delay lenses provide robust measurements of  $D_{\Delta t}$ . We find that the data constrain the  $D_{\Delta t}$  to RXJ1131–1231 with  $\sim 6\%$  precision.

We can compress these results by approximating the posterior PDF for  $D_{\Delta t}$  as a shifted log normal distribution:

$$P(D_{\Delta t}|H_0, \Omega_{de}, w, \Omega_m) \simeq \frac{1}{\sqrt{2\pi}(x - \lambda_D)\sigma_D} \exp\left[-\frac{(\log(x - \lambda_D) - \mu_D)^2}{2\sigma_D^2}\right], \quad (26)$$

where  $x = D_{\Delta t}/(1 \text{ Mpc})$ ,  $\lambda_D = 1425.6$ ,  $\mu_D = 6.4993$  and  $\sigma_D = 0.19377$ . This approximation accurately reproduces the cosmological inference, in that  $H_0$  is recovered within  $< 1\%$  in terms of its median, 16<sup>th</sup> and 84<sup>th</sup>

percentile values for the WMAP7 cosmologies we have considered. The robust constraint on  $D_{\Delta t}$  serves as the basis for cosmological inferences in Section 9.

### 8.5. Sources of uncertainty

Our  $D_{\Delta t}$  measurement accounts for all known sources of uncertainty that we have summarized in Table 3. The dominant sources are the first three items. The precision for the time delay is the  $1\sigma$  uncertainty as a fraction of the measured value for the longest delay,  $\Delta t_{\text{DB}}$ . For the lens mass model and line-of-sight contributions, we define the precision as half the difference between the 16<sup>th</sup> and 84<sup>th</sup> percentiles of the PDF for  $D_{\Delta t}^{\text{model}}$  from Section 6.4 in fractions of its median value and for  $\kappa_{\text{ext}}$  from Section 7.2 in fractions of 1, respectively. The remaining sources of uncertainty are collectively denoted by “other sources”, and the two main contributors to this category are the peculiar velocity of the lens and the impact of the satellite.

Spectroscopic studies of the field of RXJ1131–1231 indicate that the lens is in a galaxy group with a velocity dispersion of  $429_{-93}^{+119} \text{ km s}^{-1}$  (Wong et al. 2011). RXJ1131–1231 is the brightest red sequence galaxy in this group, and is thus likely to be near the center of mass of the group halo with a small peculiar velocity relative to the group (Zabludoff & Mulchaey 1998; Williams et al. 2006; George et al. 2012). However, the group could be moving relative to the Hubble flow due to nearby large-scale structures. The one-dimensional rms galaxy peculiar velocity is typically  $\lesssim 300 \text{ km s}^{-1}$  (e.g., Mosquera & Kochanek 2011; Peebles 1993). A peculiar velocity of  $300 \text{ km s}^{-1}$  for RXJ1131–1231 would cause  $D_{\Delta t}$  to change by  $0.8\%$ .<sup>16</sup> A similar peculiar velocity for the lensed source has a much smaller impact on  $D_{\Delta t}$ , changing it by only  $0.2\%$ . We note that the peculiar velocities of lenses are stochastic, and this source of uncertainty should average out in a sample of lenses.

We have explicitly included the satellite in our lens mass model in Section 6. However, there is some degeneracy in apportioning the mass between the satellite and the primary lens galaxy since lensing is mostly sensitive to the total mass enclosed within the lensing critical curves (approximately traced by the arcs). The more massive the satellite, the less massive the primary lens galaxy. Owing to its central location and the degeneracy with the mass of the main deflector, we expect the impact of the satellite on the difference in gravitational potential between the multiple images to be very small.

To assess the effect of the mass of the satellite on our  $D_{\Delta t}$  inference, we consider an extreme model where the satellite has zero mass. In this case, we require a more massive primary lens galaxy with higher  $\theta_E$  to fit the lensing features, as expected. The resulting  $D_{\Delta t}^{\text{model}}$  and  $\gamma'$  from this model are consistent with that of the original model, but with larger parameter uncertainties due to poorer fits without the satellite. Even if we use the overestimated  $\theta_E$  of the primary lens from this extreme model for the kinematics, we find that the effect on the inferred  $D_{\Delta t}$  is at the  $< 1\%$  level.

In Table 3, we list the total uncertainty of  $6.7\%$  based on a simple Gaussian approximation where we add up the

<sup>16</sup> The change in redshift due to peculiar velocities is described in, e.g., Harrison (1974).

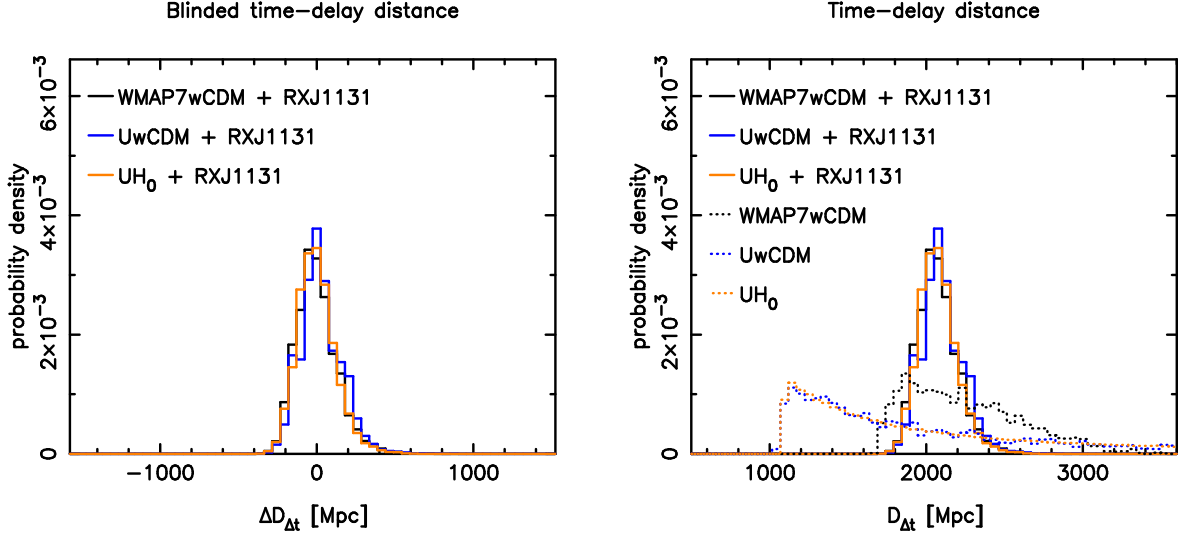


FIG. 7.— Blinded (left) and unblinded (right) PDFs for  $D_{\Delta t}$ , showing the RXJ1131–1231 posterior constraints on  $D_{\Delta t}$  (solid) given assorted priors for the cosmological parameters (dotted, labeled). See the text and Table 2 for a full description of the various priors. RXJ1131–1231 provides tight constraints on  $D_{\Delta t}$ , which translates into information about  $\Omega_m$ ,  $\Omega_{de}$ ,  $w$  and particularly  $H_0$ .

TABLE 3  
ERROR BUDGET ON TIME-DELAY DISTANCE OF RXJ1131–1231

Description	uncertainty
time delays	1.6%
lens mass model	4.6%
line-of-sight contribution	4.6%
other sources	<1%
Total (Gaussian approximation)	6.7%
Total (full sampling)	6.0%

Notes. The other sources of uncertainty that contribute at the <1% include the peculiar velocity of the lens and the impact of the satellite. Details are in Section 8.5. The Gaussian approximation simply adds the uncertainties in quadrature, providing a crude estimate for the total uncertainty based on the full sampling of the non-Gaussian PDFs.

uncertainties of each contribution in quadrature. This is close to the more accurate 6.0% based on proper sampling that takes into account the non-Gaussian distribution (e.g., of  $\kappa_{ext}$ ) and the inclusion of the stellar velocity dispersion. We note that the sampling does not include explicitly the other sources that contribute at the <1% level; however, they are practically insignificant in the overall error budget. Most of the uncertainty in  $D_{\Delta t}$  comes from the lens mass model and the line-of-sight contribution. To reduce the uncertainty on RXJ1131–1231’s  $D_{\Delta t}$  would require a better model of the source intensity distribution that depends less sensitively on the source pixel size (possibly via an adaptive source pixelization scheme (e.g., Vegetti & Koopmans 2009)), and a better characterization of  $\kappa_{ext}$  by using more observational information from the field. Investigations are in progress to improve  $\kappa_{ext}$  constraints (Greene et al. in preparation, Collett et al. in preparation).

## 9. COSMOLOGICAL INFERENCE

We now present our inference on the parameters of the expanding Universe and compare our results to other cos-

mographic probes. Specifically, our  $D_{\Delta t}$  measurement for RXJ1131–1231 provides information on cosmology that is illustrated in Section 9.1. We compare the results to that of B1608+656 to check for consistency in Section 9.2, before combining the two lenses together in Section 9.3. We then compare the constraints from the two time-delay lenses to a few other cosmological probes in Section 9.4.

### 9.1. Constraints from RXJ1131–1231

We have seen that the RXJ1131–1231  $D_{\Delta t}$  measurement is nearly independent of assumptions about the background cosmology. While  $D_{\Delta t}$  is primarily sensitive to  $H_0$ , information from  $D_{\Delta t}$  must be shared with other cosmological parameters via the combination of angular diameter distances. Therefore, cosmological parameter constraints will depend somewhat on our assumptions for the background cosmology. In this section we consider the first three cosmologies listed in Table 2:  $UH_0$ ,  $U\Lambda CDM$ , and  $WMAP7\Lambda CDM$ .

With all other parameters fixed in the  $UH_0$  cosmology except for  $H_0$ , all our knowledge of  $D_{\Delta t}$  is converted to information on  $H_0$ . We therefore obtain a precise measurement of  $H_0 = 78.7^{+4.3}_{-4.5} \text{ km s}^{-1} \text{ Mpc}^{-1}$  for RXJ1131–1231 with a 5.5% uncertainty.

Next, we relax our assumptions on  $\Omega_{de}$ ,  $\Omega_m$  and  $w$ , and consider the  $U\Lambda CDM$  and  $WMAP7\Lambda CDM$  cosmologies in a flat Universe. Figure 8 shows the resulting constraints. The contours for the  $U\Lambda CDM$  cosmology with vertical bands in the  $H_0$  panels illustrates that the time-delay distance is mostly sensitive to  $H_0$ . The constraint on  $H_0$  breaks the parameter degeneracies in the WMAP7 data set, and we obtain the following joint parameter constraints for RXJ1131–1231 in combination with WMAP7:  $H_0 = 80.0^{+5.8}_{-5.7} \text{ km s}^{-1} \text{ Mpc}^{-1}$ ,  $\Omega_{de} = 0.79 \pm 0.03$ , and  $w = -1.25^{+0.17}_{-0.21}$ .

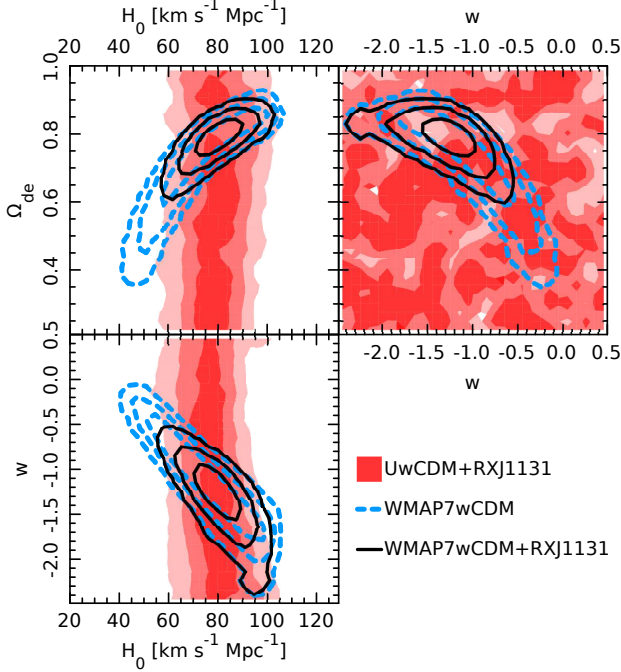


FIG. 8.— RXJ1131–1231 marginalized posterior PDF for  $H_0$ ,  $\Omega_{\text{de}}$  and  $w$  in flat  $w$ CDM cosmological models. Contours/shades mark the 68.3%, 95.4%, 99.7% credible regions. The three sets of contours/shades correspond to three different prior/data set combinations. Shaded red: RXJ1131–1231 constraints given by the  $Uw$ CDM prior; dashed blue: the prior provided by the WMAP seven-year data set alone; solid black: the joint constraints from combining WMAP and RXJ1131–1231.

### 9.2. Comparison between RXJ1131–1231 and B1608+656

How do the results of RXJ1131–1231 compare with that of B1608+656? We show in Figure 9 the overlay of the cosmological constraints of RXJ1131–1231 and B1608+656 in  $UH_0$  (top panel) and  $Uw$ CDM (bottom panel). To investigate the consistency of the two data sets, we need to consider their likelihood functions in the multi-dimensional cosmological parameter space: inconsistency is defined by insufficient overlap between the two likelihoods. We follow Marshall et al. (2006), and compute the Bayes Factor  $F$  in favor of a single set of cosmological parameters and a simultaneous fit:

$$F = \frac{\langle L^R L^B \rangle}{\langle L^R \rangle \langle L^B \rangle}, \quad (27)$$

where  $L^R$  and  $L^B$  are the likelihoods of the RXJ1131–1231 and B1608+656 data respectively, computed at each prior sample point. See the Appendix for the derivation of this result.

For the cosmology  $UH_0$ , the Bayes Factor is 3.2; for  $Uw$ CDM, it takes the value 3.8. For comparison, with two one-dimensional Gaussian PDFs,  $F$  takes the value of 1 when the two distributions overlap at their  $2\sigma$  points, and is about 3.6 when they overlap at their  $1\sigma$  point. From this we conclude that the results from RXJ1131–1231 and B1608+656 are consistent with each other. We do not detect any significant residual systematics given the current uncertainties in our measurements.

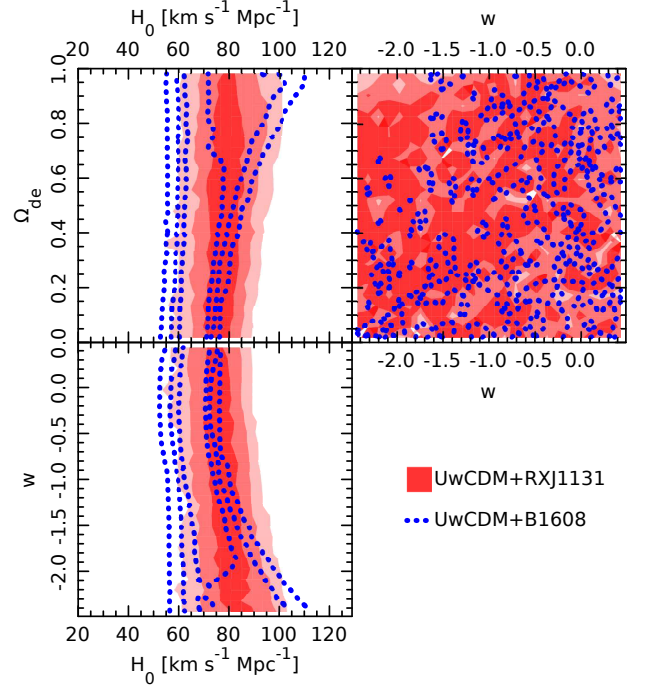
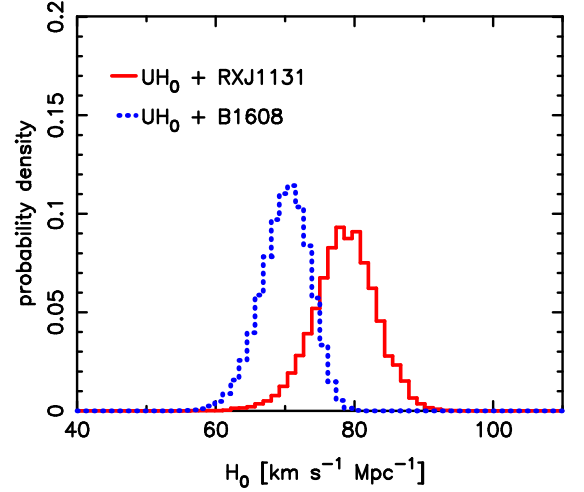


FIG. 9.— Comparison of RXJ1131–1231 (solid red) with B1608+656 (dotted blue) in  $UH_0$  (top) and  $Uw$ CDM (bottom) cosmologies. The two distributions overlap within  $2\sigma$ . The cosmological constraints from the two lenses are statistically consistent with each other: the ratio of the probability that the two lenses share global cosmological parameters to the probability that the lenses require independent cosmologies is 3.2 in  $UH_0$  and 3.8 in  $Uw$ CDM.

### 9.3. RXJ1131–1231 and B1608+656 in unison

Having shown that RXJ1131–1231 and B1608+656 are consistent with each other, we proceed to combine the results from these two lenses for cosmological inferences. In particular, we consider the constraints in the WMAP7 $w$ CDM and WMAP7 $\Lambda$ CDM cosmologies in Table 2.

We show in Figure 10 the cosmological constraints from individual lenses in combination with WMAP7, and the combination of both lenses and WMAP7. By combining

TABLE 4  
COSMOLOGICAL CONSTRAINTS FROM RXJ1131–1231 AND  
B1608+656 IN COMBINATION WITH WMAP7

Cosmology	Parameter	Marginalized Value (68% CI)	Precision
$w$ CDM	$H_0$	$75.2^{+4.4}_{-4.2}$	5.7%
	$\Omega_{de}$	$0.76^{+0.02}_{-0.03}$	2.5%
	$w$	$-1.14^{+0.17}_{-0.20}$	18%
$\Lambda$ CDM	$H_0$	$73.1^{+2.4}_{-3.6}$	4.0%
	$\Omega_\Lambda$	$0.75^{+0.01}_{-0.02}$	1.9%
	$\Omega_k$	$0.003^{+0.005}_{-0.006}$	0.6%

Notes. The  $H_0$  values are in units of  $\text{km s}^{-1} \text{Mpc}^{-1}$ . The “precision” in the fourth column is defined as half the 68% confidence interval, as a percentage of 75 for  $H_0$ , 1 for  $\Omega_{de}$ ,  $\Omega_\Lambda$ , and  $\Omega_k$ , and  $-1.0$  for  $w$ .

the two lenses, we tighten the constraints on  $H_0$ ,  $\Omega_{de}$  and  $\Omega_k$ . The precision on  $w$  does not improve appreciably. With its low lens redshift, RXJ1131–1231 provide very little information to  $w$  in addition to that obtained from B1608+656. In Table 4, we summarize the constraints from the two lenses.

#### 9.4. Comparison of lenses and other cosmographic probes

How do the robust time-delay distances from the strong lenses compare to the distance measures of other probes? We show in Figure 11 a comparison of the cosmological constraints of the two lenses, Baryon Acoustic Oscillations (BAO; e.g., Percival et al. 2010; Blake et al. 2011; Mehta et al. 2012), and supernovae (SN; e.g., Hicken et al. 2009; Suzuki et al. 2012), when each is combined with WMAP7 in the  $ow$ CDM cosmology. The figures are qualitative since the samples for WMAP7 chain in the  $ow$ CDM cosmology are sparse and we have smoothed the contours after importance sampling. Nonetheless, we see that the sizes of the contours are comparable, suggesting that even a small sample of time-delay lenses is a powerful probe of cosmology. Both the lenses and BAO are strong in constraining the curvature of the Universe, while SN provides more information on the dark energy equation of state. Lenses are thus highly complementary to other cosmographic probes, particularly the CMB and SN (see also, e.g., Linder 2011; Das & Linder 2012). Each probe is consistent with flat  $\Lambda$ CDM:  $\Omega_k = 0$  and  $w = -1$  are within the 95% credible regions.

In Figure 12, we compare the precisions on  $\Omega_k$  and  $w$  in  $ow$ CDM from the following cosmological probes in combination with WMAP: the Cepheids distance ladder (Riess et al. 2011)<sup>17</sup>, BAO from the Sloan Digital Sky Survey (SDSS) (Percival et al. 2010), SN from the Union 2.1 sample (Suzuki et al. 2012), reconstructed BAO using the SDSS galaxies (Mehta et al. 2012) and our two time-delay lenses. We note that the precisions on the Cepheids and the time-delay lenses are only approximates since the samples of WMAP7 are sparse in  $ow$ CDM due to the

<sup>17</sup> To derive the constraints on  $\Omega_k$  and  $w$  from the combination of Cepheids and WMAP7, we importance sample the WMAP7 chain by a Gaussian likelihood centered on  $H_0 = 73.8 - 1.475(w + 1) \text{ km s}^{-1} \text{Mpc}^{-1}$  with a width of  $2.4 \text{ km s}^{-1} \text{Mpc}^{-1}$  (Riess et al. 2011). The  $-1.475(w + 1)$  corresponds to the tilt in the  $H_0$ - $w$  plane shown in Figure 10 of Riess et al. (2011).

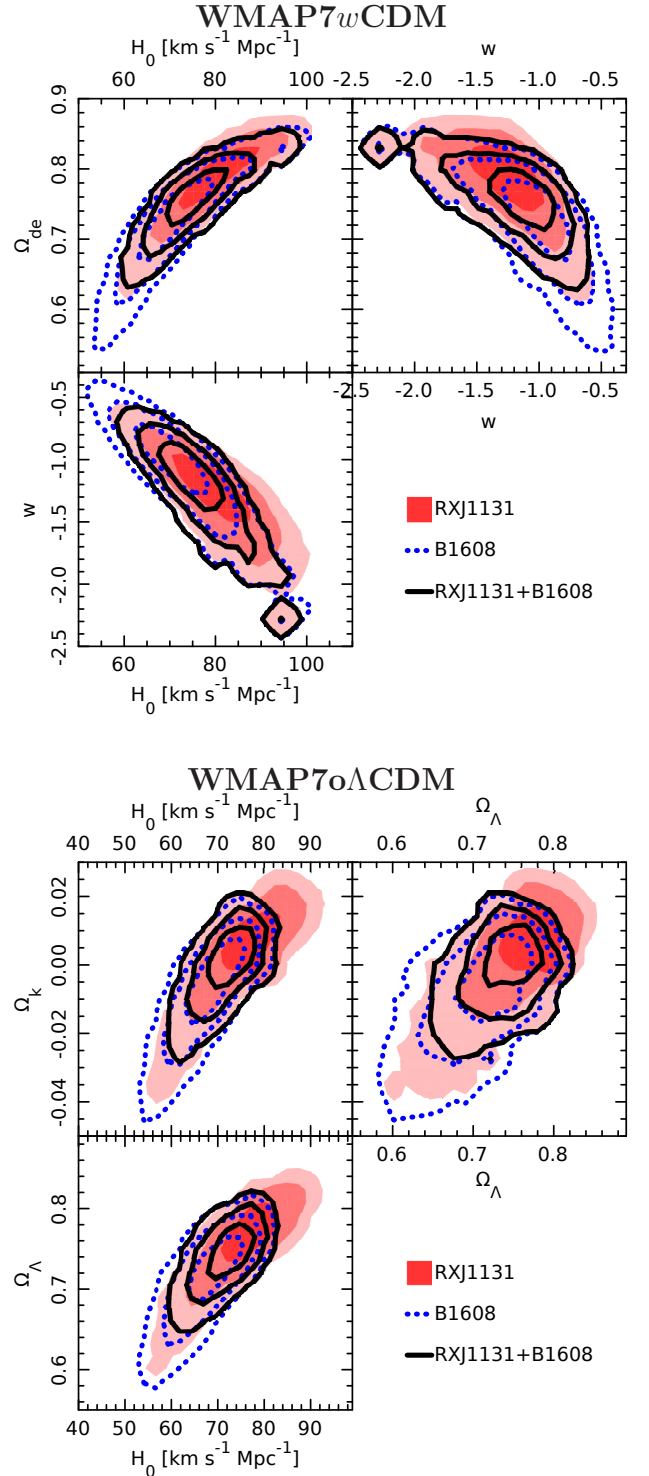


FIG. 10.— Cosmological constraints from the combination of RXJ1131–1231 and B1608+656 assuming WMAP7wCDM (top) and WMAP7o $\Lambda$ CDM (bottom) cosmologies. The combined posterior PDF is shown by the solid contours, the PDF for RXJ1131–1231 in combination with WMAP7 is the shaded contours, and the PDF for B1608+656 in combination with WMAP7 is the dotted contours. Contours/shades mark the 68.3%, 95.4%, 99.7% credible regions.



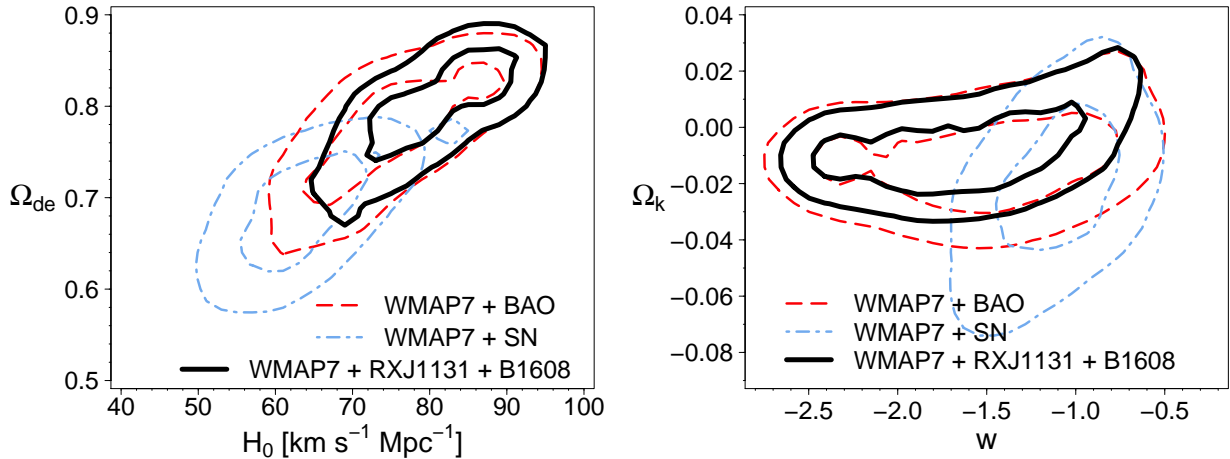


FIG. 11.— Posterior PDF of  $H_0$ ,  $\Omega_{de}$ ,  $w$  and  $\Omega_k$  for BAO (blue dot-dashed; Percival et al. (2010)), SN (red dashed; Hicken et al. (2009)), time-delay lenses (black solid; this work) when each is combined with WMAP7 in an  $\Lambda$ CDM cosmology. Contours mark the 68%, and 95% credible regions. Time-delay lenses are highly complementary to other probes, particularly CMB and SN.

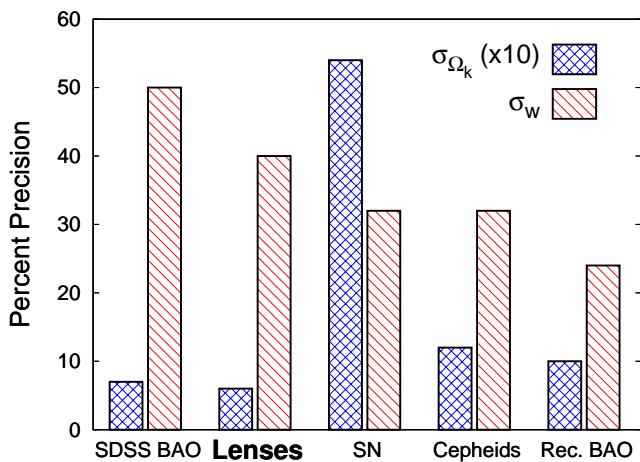


FIG. 12.— Precision of cosmological constraints on  $\Omega_k$  and  $w$  for five probes each in combination with WMAP7 in an  $\Lambda$ CDM cosmology: SDSS BAO (Percival et al. 2010), the two time-delay lenses RXJ1131–1231 and B1608+656 (this work), SN (Suzuki et al. 2012), Cepheids (Riess et al. 2011), and reconstructed BAO (Mehta et al. 2012). Precision for  $\Omega_k$  and  $w$  is defined as half the 68% CI as a percentage of 1.

large parameter space. Nonetheless, the histogram plot shows that time-delay lenses are a valuable probe, especially in constraining the spatial curvature of the Universe.

## 10. SUMMARY

We have performed a blind analysis of the time-delay lens RXJ1131–1231, modeling its high precision time delays from the COSMOGRAIL collaboration, deep *HST* imaging, newly measured lens velocity dispersion, and mass contribution from line-of-sight structures. The data sets were combined probabilistically in a joint analysis, via a comprehensive model of the lens system consisting of the light of the source AGN and its host galaxy, the light and mass of the lens galaxies, and structures along the line of sight characterized by external convergence and shear parameters. The resulting time-delay distance measurement for the lens allows us to infer cosmological constraints. From this study, we draw the following conclusions:

1. Our comprehensive lens model reproduces the global features of the *HST* image and the time delays. We quantify the uncertainty due to the deflector gravitational potential on the time-delay distance to be at the 4.6% level.
2. Based on the external shear strength from the lens model and the overdensity of galaxy count around the lens, we obtained a PDF for the external convergence by ray tracing through the Millennium Simulation. This  $\kappa_{\text{ext}}$  PDF contributes to the uncertainty on  $D_{\Delta t}$  also at the 4.6% level.
3. Our robust time-delay distance measurement of 6% takes into account all sources of known statistical and systematic uncertainty. We provide a fitting formula to describe the PDF of the time-delay distance that can be used to combine with any other independent cosmological probe.
4. The time-delay distance of RXJ1131–1231 is mostly sensitive to  $H_0$ , especially given the low redshift of the lens.
5. Assuming a flat  $\Lambda$ CDM with fixed  $\Omega_{\Lambda} = 0.73$  and uniform prior on  $H_0$ , our unblinded  $H_0$  measurement from RXJ1131–1231 is  $78.7^{+4.3}_{-4.5} \text{ km s}^{-1} \text{ Mpc}^{-1}$ .
6. The constraint on  $H_0$  helps break parameter degeneracies in the CMB data. In combination with WMAP7 in  $w$ CDM, we find  $H_0 = 80.0^{+5.8}_{-5.7} \text{ km s}^{-1} \text{ Mpc}^{-1}$ ,  $\Omega_{de} = 0.79 \pm 0.03$ , and  $w = -1.25^{+0.17}_{-0.21}$ . These are statistically consistent with the results from the gravitational lens B1608+656. There are no significant residual systematics detected in our method based on this combined analysis of the two systems.
7. By combining RXJ1131–1231, B1608+656 and WMAP7, we derive the following constraints:  $H_0 = 75.2^{+4.4}_{-4.2} \text{ km s}^{-1} \text{ Mpc}^{-1}$ ,  $\Omega_{de} = 0.76^{+0.02}_{-0.03}$  and  $w = -1.14^{+0.17}_{-0.20}$  in flat  $w$ CDM, and  $H_0 =$



$73.1^{+2.4}_{-3.6} \text{ km s}^{-1} \text{ Mpc}^{-1}$ ,  $\Omega_{\Lambda} = 0.75^{+0.01}_{-0.02}$  and  $\Omega_k = 0.003^{+0.005}_{-0.006}$  in open  $\Lambda$ CDM.

8. Our measurement of the Hubble constant is completely independent of those based on the local distance ladder method (e.g., Riess et al. 2011; Freedman et al. 2012), providing an important consistency check of the standard cosmological model and of general relativity.
9. A comparison of the lenses and other cosmological probes that are each combined with WMAP7 shows that the constraints from the lenses are comparable in precision to various state-of-the-art probes. Lenses are particularly powerful in measuring the spatial curvature of the universe, and are complementary to other cosmological probes.

Thanks to the dedicated monitoring by the COSMOGRAIL (e.g., Vuissoz et al. 2008; Courbin et al. 2011; Tewes et al. 2012b,a) and Kochanek et al. (2006) collaborations, the number of lenses with accurate and precise time delays are increasing. Deep *HST* imaging for three of these lenses will be obtained in cycle 20 to allow accurate lens mass modeling that turns the delays into distances. Current and upcoming telescopes and surveys including the Panoramic Survey Telescope & Rapid Response System, Hyper-Suprime Camera on the Subaru Telescope, and Dark Energy Survey expect to detect hundreds of AGN lenses with dozens of delays measured (Oguri & Marshall 2010). Ultimately, the Large Synoptic Survey Telescope will discover thousands of time-delay lenses, painting a bright future for cosmography with gravitational lens time delays.

#### ACKNOWLEDGMENTS

We thank B. Brewer, C. Faure and E. Linder for useful discussions. We are grateful to E. Komatsu for provid-

ing us the code to compute the likelihoods of the BAO and SN data that were used in the WMAP 7-year analysis. S.H.S. and T.T. gratefully acknowledge support from the Packard Foundation in the form of a Packard Research Fellowship to T.T.. S.H. and R.D.B. acknowledge support by the National Science Foundation (NSF) grant number AST-0807458. P.J.M. acknowledges support from the Royal Society in the form of a research fellowship, and is grateful to the Kavli Institute for Particle Astrophysics and Cosmology for hosting him as a visitor during part of the period of this investigation. M.T., F.C., and G.M. acknowledge support from the Swiss National Science Foundation (SNSF). C.D.F. acknowledges support from NSF-AST-0909119. L.V.E.K. is supported in part by an NWO-VIDI program subsidy (project No. 639.042.505). D.S. acknowledges support from the Deutsche Forschungsgemeinschaft, reference SL172/1-1. This paper is based in part on observations made with the NASA/ESA *Hubble Space Telescope*, obtained at the Space Telescope Science Institute, which is operated by the Association of Universities for Research in Astronomy, Inc., under NASA contract NAS 5-26555. These observations are associated with program #GO-9744. Some of the data presented in this paper were obtained at the W.M. Keck Observatory, which is operated as a scientific partnership among the California Institute of Technology, the University of California and the National Aeronautics and Space Administration. The Observatory was made possible by the generous financial support of the W.M. Keck Foundation. The authors wish to recognize and acknowledge the very significant cultural role and reverence that the summit of Mauna Kea has always had within the indigenous Hawaiian community. We are most fortunate to have the opportunity to conduct observations from this mountain.

#### REFERENCES

- Anderson, J., & Bedin, L. R. 2010, *PASP*, 122, 1035  
 Auger, M. W., Fassnacht, C. D., Wong, K. C., et al. 2008, *ApJ*, 673, 778  
 Auger, M. W., Treu, T., Bolton, A. S., et al. 2010, *ApJ*, 724, 511  
 Barnabè, M., Czoske, O., Koopmans, L. V. E., Treu, T., & Bolton, A. S. 2011, *MNRAS*, 415, 2215  
 Barnabè, M., Czoske, O., Koopmans, L. V. E., et al. 2009, *MNRAS*, 399, 21  
 Bertin, E., & Arnouts, S. 1996, *A&AS*, 117, 393  
 Binney, J., & Tremaine, S. 1987, *Galactic dynamics* (Princeton, NJ, Princeton University Press, 1987, 747 p.)  
 Blake, C., Davis, T., Poole, G. B., et al. 2011, *MNRAS*, 415, 2892  
 Blandford, R. D., & Narayan, R. 1992, *ARA&A*, 30, 311  
 Brewer, B. J., & Lewis, G. F. 2008, *MNRAS*, 390, 39  
 Chartas, G., Kochanek, C. S., Dai, X., Poindexter, S., & Garmire, G. 2009, *ApJ*, 693, 174  
 Claeskens, J.-F., Sluse, D., Riaud, P., & Surdej, J. 2006, *A&A*, 451, 865  
 Coe, D., & Moustakas, L. A. 2009, *ApJ*, 706, 45  
 Conley, A., Goldhaber, G., Wang, L., et al. 2006, *ApJ*, 644, 1  
 Courbin, F. 2003, e-prints (astro-ph/0304497)  
 Courbin, F., Chantry, V., Revaz, Y., et al. 2011, *A&A*, 536, A53  
 Das, S., & Linder, E. V. 2012, *ArXiv e-prints* (1207.1105)  
 Dunkley, J., Bucher, M., Ferreira, P. G., Moodley, K., & Skordis, C. 2005, *MNRAS*, 356, 925  
 Dye, S., Evans, N. W., Belokurov, V., Warren, S. J., & Hewett, P. 2008, *MNRAS*, 388, 384  
 Dye, S., & Warren, S. J. 2005, *ApJ*, 623, 31  
 Fadely, R., Keeton, C. R., Nakajima, R., & Bernstein, G. M. 2010, *ApJ*, 711, 246  
 Falco, E. E. 2005, *New Journal of Physics*, 7, 200  
 Fassnacht, C. D., Gal, R. R., Lubin, L. M., et al. 2006, *ApJ*, 642, 30  
 Fassnacht, C. D., Koopmans, L. V. E., & Wong, K. C. 2011, *MNRAS*, 410, 2167  
 Fassnacht, C. D., Xanthopoulos, E., Koopmans, L. V. E., & Rusin, D. 2002, *ApJ*, 581, 823  
 Freedman, W. L., & Madore, B. F. 2010, *ARA&A*, 48, 673  
 Freedman, W. L., Madore, B. F., Scowcroft, V., et al. 2012, *ArXiv e-prints* (1208.3281)  
 Freedman, W. L., & Turner, M. S. 2003, *Reviews of Modern Physics*, 75, 1433  
 Freedman, W. L., Madore, B. F., Gibson, B. K., et al. 2001, *ApJ*, 553, 47  
 Frieman, J. A., Turner, M. S., & Huterer, D. 2008, *ARA&A*, 46, 385  
 Gavazzi, R., Treu, T., Rhodes, J. D., et al. 2007, *ApJ*, 667, 176  
 George, M. R., Leauthaud, A., Bundy, K., et al. 2012, *ArXiv e-prints* (1205.4262)  
 Guo, Q., White, S., Li, C., & Boylan-Kolchin, M. 2010, *MNRAS*, 404, 1111  
 Halkola, A., Hildebrandt, H., Schrabback, T., et al. 2008, *A&A*, 481, 65  
 Harrison, E. R. 1974, *ApJ*, 191, L51  
 Hernquist, L. 1990, *ApJ*, 356, 359

- Hicken, M., Wood-Vasey, W. M., Blondin, S., et al. 2009, *ApJ*, 700, 1097
- Hilbert, S., Hartlap, J., White, S. D. M., & Schneider, P. 2009, *A&A*, 499, 31
- Hilbert, S., White, S. D. M., Hartlap, J., & Schneider, P. 2007, *MNRAS*, 382, 121
- Humphrey, P. J., & Buote, D. A. 2010, *MNRAS*, 403, 2143
- Jackson, N. 2007, *Living Reviews in Relativity*, 10, 4
- Jaffe, W. 1983, *MNRAS*, 202, 995
- Keeton, C. R. 2003, *ApJ*, 584, 664
- Keeton, C. R., & Zabludoff, A. I. 2004, *ApJ*, 612, 660
- Kochanek, C. S. 2002, *ApJ*, 578, 25
- Kochanek, C. S., Morgan, N. D., Falco, E. E., et al. 2006, *ApJ*, 640, 47
- Komatsu, E., Smith, K. M., Dunkley, J., et al. 2011, *ApJS*, 192, 18
- Koopmans, L. V. E., & Treu, T. 2003, *ApJ*, 583, 606
- Koopmans, L. V. E., Bolton, A., Treu, T., et al. 2009, *ApJ*, 703, L51
- Lehar, J., Hewitt, J. N., Burke, B. F., & Roberts, D. H. 1992, *ApJ*, 384, 453
- Lewis, A., & Bridle, S. 2002, *Phys. Rev. D*, 66, 103511
- Linder, E. V. 2011, *Phys. Rev. D*, 84, 123529
- Magain, P., Courbin, F., & Sohy, S. 1998, *ApJ*, 494, 472
- Mantz, A., Allen, S. W., Rapetti, D., & Ebeling, H. 2010, *MNRAS*, 406, 1759
- Marshall, P., Rajguru, N., & Slosar, A. 2006, *Phys. Rev. D*, 73, 067302
- Marshall, P. J., Treu, T., Melbourne, J., et al. 2007, *ApJ*, 671, 1196
- Massey, R., Stoughton, C., Leauthaud, A., et al. 2010, *MNRAS*, 401, 371
- Mehta, K. T., Cuesta, A. J., Xu, X., Eisenstein, D. J., & Padmanabhan, N. 2012, *ArXiv e-prints* (1202.0092)
- Momcheva, I., Williams, K., Keeton, C., & Zabludoff, A. 2006, *ApJ*, 641, 169
- Morgan, C. W., Kochanek, C. S., Morgan, N. D., & Falco, E. E. 2006, *ApJ*, 647, 874
- Mosquera, A. M., & Kochanek, C. S. 2011, *ApJ*, 738, 96
- Oguri, M., & Marshall, P. J. 2010, *MNRAS*, 405, 2579
- Oke, J. B., Cohen, J. G., Carr, M., et al. 1995, *PASP*, 107, 375
- Peebles, P. J. E. 1993, *Principles of Physical Cosmology*
- Percival, W. J., Cole, S., Eisenstein, D. J., et al. 2007, *MNRAS*, 381, 1053
- Percival, W. J., Reid, B. A., Eisenstein, D. J., et al. 2010, *MNRAS*, 401, 2148
- Refsdal, S. 1964, *MNRAS*, 128, 307
- . 1966, *MNRAS*, 132, 101
- Reid, M. J., Braatz, J. A., Condon, J. J., et al. 2012, *ArXiv e-prints* (1207.7292)
- Riess, A. G., Macri, L., Casertano, S., et al. 2011, *ApJ*, 730, 119
- Schechter, P. L., Bailyn, C. D., Barr, R., et al. 1997, *ApJ*, 475, L85
- Schneider, P., Ehlers, J., & Falco, E. E. 1992, *Gravitational Lenses*, XIV, 560 pp. 112 figs.. Springer-Verlag Berlin Heidelberg New York.
- Schneider, P., Kochanek, C. S., & Wambsganss, J. 2006, *Gravitational Lensing: Strong, Weak and Micro* (Springer)
- Sérsic, J. L. 1968, *Atlas de galaxias australes* (Cordoba, Argentina: Observatorio Astronomico, 1968)
- Sluse, D., Surdej, J., Claeskens, J.-F., et al. 2003, *A&A*, 406, L43
- Sonnenfeld, A., Treu, T., Gavazzi, R., et al. 2012, *ApJ*, 752, 163
- Springel, V., White, S. D. M., Jenkins, A., et al. 2005, *Nature*, 435, 629
- Suyu, S. H. 2012, *ArXiv e-prints* (1202.0287)
- Suyu, S. H., & Halkola, A. 2010, *A&A*, 524, A94
- Suyu, S. H., Marshall, P. J., Auger, M. W., et al. 2010, *ApJ*, 711, 201
- Suyu, S. H., Marshall, P. J., Blandford, R. D., et al. 2009, *ApJ*, 691, 277
- Suyu, S. H., Marshall, P. J., Hobson, M. P., & Blandford, R. D. 2006, *MNRAS*, 371, 983
- Suyu, S. H., Treu, T., Blandford, R. D., et al. 2012, *ArXiv e-prints* (1202.4459)
- Suzuki, N., Rubin, D., Lidman, C., et al. 2012, *ApJ*, 746, 85
- Tewes, M., Courbin, F., & Meylan, G. 2012a, *A&A*, submitted
- Tewes, M., Courbin, F., Meylan, G., et al. 2012b, *A&A*, submitted
- Treu, T. 2010, *ARA&A*, 48, 87
- Treu, T., & Koopmans, L. V. E. 2002, *MNRAS*, 337, L6
- . 2004, *ApJ*, 611, 739
- Valdes, F., Gupta, R., Rose, J. A., Singh, H. P., & Bell, D. J. 2004, *ApJS*, 152, 251
- Vegetti, S., & Koopmans, L. V. E. 2009, *MNRAS*, 392, 945
- Vegetti, S., Koopmans, L. V. E., Bolton, A., Treu, T., & Gavazzi, R. 2010, *MNRAS*, 408, 1969
- Vuissoz, C., Courbin, F., Sluse, D., et al. 2008, *A&A*, 488, 481
- Weinberg, D. H., Mortonson, M. J., Eisenstein, D. J., et al. 2012, *ArXiv e-prints* (1201.2434)
- Williams, K. A., Momcheva, I., Keeton, C. R., Zabludoff, A. I., & Lehar, J. 2006, *ApJ*, 646, 85
- Witt, H. J., Mao, S., & Keeton, C. R. 2000, *ApJ*, 544, 98
- Wong, K. C., Keeton, C. R., Williams, K. A., Momcheva, I. G., & Zabludoff, A. I. 2011, *ApJ*, 726, 84
- Wucknitz, O. 2002, *MNRAS*, 332, 951
- Zabludoff, A. I., & Mulchaey, J. S. 1998, *ApJ*, 496, 39

## APPENDIX

QUANTIFYING DATA SET CONSISTENCY VIA THE BAYES FACTOR  $B$ 

Marshall et al. (2006) invite us to consider the following two hypotheses: (1)  $H^{\text{global}}$ , in which the two lenses share a common set of cosmological parameters  $\pi = \{H_0, \Omega_{\text{de}}, w\}$ , and (2)  $H^{\text{ind}}$ , in which each of the two lenses is provided with its own independent set of cosmological parameters,  $\pi^{\text{R}} = \{H_0^{\text{R}}, \Omega_{\text{de}}^{\text{R}}, w^{\text{R}}\}$  and  $\pi^{\text{B}} = \{H_0^{\text{B}}, \Omega_{\text{de}}^{\text{B}}, w^{\text{B}}\}$ , with which to fit the data. Each set of parameters covers the same prior volume as in  $H^{\text{global}}$ . If the two data sets are highly inconsistent, only  $H^{\text{ind}}$  will provide a good fit to both data sets in a joint analysis. The question is, do the data require  $H^{\text{ind}}$ , or is  $H^{\text{global}}$  sufficient?

We quantify the answer to this question with the evidence ratio, or Bayes Factor, in favor of  $H^{\text{global}}$ :

$$F = \frac{P(\mathbf{d}^{\text{R}}, \mathbf{d}^{\text{B}} | H^{\text{global}})}{P(\mathbf{d}^{\text{R}} | H^{\text{ind}}) P(\mathbf{d}^{\text{B}} | H^{\text{ind}})}. \quad (\text{A1})$$

where we have collectively denoted all the data sets of RXJ1131–1231 as  $\mathbf{d}^{\text{R}}$  and of B1608+656 as  $\mathbf{d}^{\text{B}}$ . Each of the terms on the right-hand side of the above equation can be written in terms of a multi-dimensional integral over the cosmological parameters. For example, we have (starting with the simpler terms in the denominators)

$$P(\mathbf{d}^{\text{R}} | H^{\text{ind}}) = \int d^3\pi^{\text{R}} P(\mathbf{d}^{\text{R}} | \pi^{\text{R}}, H^{\text{ind}}) P(\pi^{\text{R}} | H^{\text{ind}}), \quad (\text{A2})$$

where  $P(\mathbf{d}^{\text{R}} | \pi^{\text{R}}, H^{\text{ind}})$  is the likelihood of the RXJ1131–1231 data sets (the weights for the cosmological samples) that

we denote by  $L^R$ . Equation (A2) is then just the ensemble average of the samples' likelihood values,

$$P(\mathbf{d}^R | \mathbf{H}^{\text{ind}}) = \langle L^R \rangle. \quad (\text{A3})$$

For  $P(\mathbf{d}^B | \mathbf{H}^{\text{ind}})$ , we can rewrite the likelihood  $P(\mathbf{d}^B | \boldsymbol{\pi}^B, \mathbf{H}^{\text{ind}})$  in terms of  $D_{\Delta t}^B$  to make use of  $P(D_{\Delta t}^B | \mathbf{d}^B, \mathbf{H}^{\text{ind}})$  given by Equation (35) of Suyu et al. (2010):

$$P(\mathbf{d}^B | \boldsymbol{\pi}^B, \mathbf{H}^{\text{ind}}) = \frac{P(D_{\Delta t}^B(\boldsymbol{\pi}^B) | \mathbf{d}^B, \mathbf{H}^{\text{ind}}) P(\mathbf{d}^B | \mathbf{H}^{\text{ind}})}{P(D_{\Delta t}^B | \mathbf{H}^{\text{ind}})}. \quad (\text{A4})$$

The ratio  $Z^B = P(\mathbf{d}^B | \mathbf{H}^{\text{ind}}) / P(D_{\Delta t}^B | \mathbf{H}^{\text{ind}})$  is a constant factor since the prior on  $D_{\Delta t}^B$  is uniform; thus, we obtain

$$P(\mathbf{d}^B | \mathbf{H}^{\text{ind}}) = Z^B \langle L^B \rangle, \quad (\text{A5})$$

where  $L^B$  is given by the likelihood of the time-delay distance  $P(D_{\Delta t}^B(\boldsymbol{\pi}^B) | \mathbf{d}^B, \mathbf{H}^{\text{ind}})$ .

Finally, for the numerator in Equation (A1), we have

$$\begin{aligned} P(\mathbf{d}^R, \mathbf{d}^B | \mathbf{H}^{\text{global}}) &= \int d^3\boldsymbol{\pi} P(\mathbf{d}^R | \boldsymbol{\pi}, \mathbf{H}^{\text{global}}) P(\mathbf{d}^B | \boldsymbol{\pi}, \mathbf{H}^{\text{global}}) P(\boldsymbol{\pi} | \mathbf{H}^{\text{global}}) \\ &= Z^B \langle L^R L^B \rangle, \end{aligned} \quad (\text{A6})$$

where the constant  $Z^B$  is the same as that in  $P(\mathbf{d}^B | \mathbf{H}^{\text{ind}})$  since the parameterization of the cosmology for each independent lens is identical to that of the global cosmology (i.e.,  $\boldsymbol{\pi}^B$  and  $\boldsymbol{\pi}$  are the same cosmological parameterization). Substituting Equations (A3), (A5), and (A6) into Equation (A1), we obtain

$$F = \frac{\langle L^R L^B \rangle}{\langle L^R \rangle \langle L^B \rangle}, \quad (\text{A7})$$

which can be readily computed given the values of  $L^R$  and  $L^B$  (the weights) that we have for each cosmological sample.



# COSMOGRAIL: the COSmological MONitoring of GRAVitational Lenses<sup>★,★★</sup>

## IX. Time delays, lens dynamics and baryonic fraction in HE 0435-1223

F. Courbin<sup>1</sup>, V. Chantry<sup>2,\*\*\*</sup>, Y. Revaz<sup>1</sup>, D. Sluse<sup>3,\*\*\*\*</sup>, C. Faure<sup>1</sup>, M. Tewes<sup>1</sup>, E. Eulaers<sup>2</sup>, M. Koleva<sup>4,5,6</sup>,  
 I. Asfandiyarov<sup>7</sup>, S. Dye<sup>8</sup>, P. Magain<sup>2</sup>, H. van Winckel<sup>9</sup>, J. Coles<sup>10</sup>, P. Saha<sup>10</sup>, M. Ibrahimov<sup>7</sup>, and G. Meylan<sup>1</sup>

<sup>1</sup> Laboratoire d'Astrophysique, École Polytechnique Fédérale de Lausanne (EPFL), Observatoire de Sauverny, 1290 Versoix, Switzerland  
 e-mail: [cecile.faure@epfl.ch](mailto:cecile.faure@epfl.ch)

<sup>2</sup> Institut d'Astrophysique et de Géophysique, Université de Liège, Allée du 6 Août, 17, 4000 Sart Tilman (Bat. B5C), Liège 1, Belgium

<sup>3</sup> Astronomisches Rechen-Institut am Zentrum für Astronomie der Universität Heidelberg, Mönchhofstrasse 12–14, 69120 Heidelberg, Germany

<sup>4</sup> Université Lyon 1, 69622 Villeurbanne; CRAL, Observatoire de Lyon, 69561 St Genis Laval; CNRS, UMR 5574, France

<sup>5</sup> Instituto de Astrofísica de Canarias, La Laguna, 38200 Tenerife, Spain

<sup>6</sup> Departamento de Astrofísica, Universidad de La Laguna, 38205 La Laguna, Tenerife, Spain

<sup>7</sup> Ulugh Beg Astronomical Institute, Academy of Sciences, Tashkent, Uzbekistan

<sup>8</sup> Cardiff University, School of Physics and Astronomy, Queens Buildings, The Parade, Cardiff, CF24 3AA, UK

<sup>9</sup> Instituut voor Sterrenkunde, Katholieke Universiteit Leuven, Celestijnenlaan 200B, 3001 Heverlee, Belgium

<sup>10</sup> Institute of Theoretical Physics, University of Zürich, Winterthurerstrasse 190, 8057 Zürich, Switzerland

Received 7 September 2010 / Accepted 10 October 2011

### ABSTRACT

We present accurate time delays for the quadruply imaged quasar HE 0435-1223. The delays were measured from 575 independent photometric points obtained in the *R*-band between January 2004 and March 2010. With seven years of data, we clearly show that quasar image A is affected by strong microlensing variations and that the time delays are best expressed relative to quasar image B. We measured  $\Delta t_{BC} = 7.8 \pm 0.8$  days,  $\Delta t_{BD} = -6.5 \pm 0.7$  days and  $\Delta t_{CD} = -14.3 \pm 0.8$  days. We spacially deconvolved HST NICMOS2 F160W images to derive accurate astrometry of the quasar images and to infer the light profile of the lensing galaxy. We combined these images with a stellar population fitting of a deep VLT spectrum of the lensing galaxy to estimate the baryonic fraction,  $f_b$ , in the Einstein radius. We measured  $f_b = 0.65^{+0.13}_{-0.10}$  if the lensing galaxy has a Salpeter IMF and  $f_b = 0.45^{+0.04}_{-0.07}$  if it has a Kroupa IMF. The spectrum also allowed us to estimate the velocity dispersion of the lensing galaxy,  $\sigma_{ap} = 222 \pm 34$  km s<sup>-1</sup>. We used  $f_b$  and  $\sigma_{ap}$  to constrain an analytical model of the lensing galaxy composed of an Hernquist plus generalized NFW profile. We solved the Jeans equations numerically for the model and explored the parameter space under the additional requirement that the model must predict the correct astrometry for the quasar images. Given the current error bars on  $f_b$  and  $\sigma_{ap}$ , we did not constrain  $H_0$  yet with high accuracy, i.e., we found a broad range of models with  $\chi^2 < 1$ . However, narrowing this range is possible, provided a better velocity dispersion measurement becomes available. In addition, increasing the depth of the current HST imaging data of HE 0435-1223 will allow us to combine our constraints with lens reconstruction techniques that make use of the full Einstein ring that is visible in this object.

**Key words.** cosmological parameters – gravitational lensing: strong

## 1. Introduction

To determine the expansion rate of the Universe,  $H_0$ , accurately, it is important to scale the extragalactic distance ladder and to measure  $w(z)$ , the redshift evolution of the dark energy equation of state parameter (e.g., [Frieman et al. 2008](#)).

Some of the most popular methods in use to measure  $H_0$  have recently been reviewed ([Freedman & Madore 2010](#)). The huge observational and theoretical efforts invested in these measurements have led to random errors between 3% and 10%, depending on the methods. However, all these methods rely at some level on each other and are in the end all based on the same local standard candles. In addition, the accuracy required on  $H_0$  to measure  $w(z)$  and  $H(z)$  is of the order of 1% ([Hu 2005](#); [Riess et al. 2009, 2011](#)). It is therefore of interest (i) to explore methods that are fully independent of any standard candle and (ii) to combine the different methods to further reduce the current error bar on  $H_0$ .

\* Based on observations made with the 1.2 m Euler Swiss Telescope, the 1.5 m telescope of Maidanak Observatory in Uzbekistan, and with the 1.2 m Mercator Telescope, operated on the island of La Palma by the Flemish Community, at the Spanish Observatorio del Roque de los Muchachos of the Instituto de Astrofísica de Canarias. The NASA/ESA *Hubble* Space Telescope data was obtained from the data archive at the Space Telescope Science Institute, which is operated by AURA, the Association of Universities for Research in Astronomy, Inc., under NASA contract NAS-5-26555.

\*\* Light curves are only available at the CDS via anonymous ftp to [cdsarc.u-strasbg.fr](ftp://cdsarc.u-strasbg.fr) (130.79.128.5) or via <http://cdsarc.u-strasbg.fr/viz-bin/qcat?J/A+A/536/A53>

\*\*\* Research Fellow, Belgian National Fund for Scientific Research (FNRS).

\*\*\*\* Alexander von Humboldt fellow.



Strong gravitational lensing of quasars and the so-called “time delay method” in multiply imaged quasars is independent of the traditional standard candles (Refsdal 1964) and is based on well understood physics: general relativity. However, it requires to measure the time delays from long-term photometric monitoring of the many lensed quasars, which has long been a serious observational limitation. While the attempts to measure accurate time delays have been numerous, only few quasars have been measured with an accuracy close to the percent (e.g., Goicoechea 2002; Fassnacht et al. 2002; Vuissoz et al. 2008). In addition, the lens model necessary to convert time delays into  $H_0$  often remains poorly constrained and hampers a breaking of the degeneracies between the properties of the lensing galaxy and  $H_0$ . In recent years, successful attempts have been made to constrain the lens model as much as possible to break these degeneracies (Suyu et al. 2009, 2010).

COSMOGRAIL, the COSmological MONitoring of GRAVitational Lenses, aims both at measuring precise time delays for a large sample of strongly lensed quasars, and at obtaining and using all necessary observations to constrain the lens models. The present paper describes the COSMOGRAIL results for the quadruply imaged quasar HE 0435-1223, using deep VLT spectra and deconvolved HST images.

HE 0435-1223 ( $\alpha(2000)$ : 04h38min14.9s;  $\delta(2000)$  =  $-12^\circ 17' 14''.4$ ) was discovered by Wisotzki et al. (2000) during the Hamburg/ESO Survey (HES) for bright quasars in the Southern Hemisphere. It was identified two years later as a quadruply imaged quasar by Wisotzki et al. (2002). The redshift of the source is  $z_s = 1.689$  (Wisotzki et al. 2000) and that of the lens is  $z_l = 0.4546 \pm 0.0002$  (Morgan et al. 2005). The quasar shows evidence for intrinsic variability, which makes it a good candidate for determining the time delays between the different images. The local environment of the lensing galaxy has been studied in detail by Morgan et al. (2005) using the *Hubble* Space Telescope (HST) Advanced Camera for Surveys (ACS) and by Momcheva (2009), who has found that the lensing galaxy lies in a group of at least 11 members. The velocity dispersion of this group is  $\sigma \sim 496 \text{ km s}^{-1}$ .

Analytical lens models of HE 0435-1223 are given by Kochanek et al. (2006), who have also measured time delays from two years of optical monitoring:  $\Delta t_{AD} = -14.37^{+0.75}_{-0.85}$  days,  $\Delta t_{AB} = -8.00^{+0.73}_{-0.82}$  days, and  $\Delta t_{AC} = -2.10^{+0.78}_{-0.71}$  days. For a fixed  $H_0 = 72 \pm 7 \text{ km s}^{-1} \text{ Mpc}^{-1}$  they found that the lensing galaxy must have a rising rotation curve at the position of the lensed images and a non-constant mass-to-light ratio. Moreover, high dark matter surface densities are required in the lens halo. New monitoring data of Blackburne & Kochanek (2010) analysed using a physically motivated representation of microlensing give time delays compatible with those of Kochanek et al. (2006), although these authors do not provide their measured values.

## 2. Photometric monitoring

### 2.1. Optical imaging

HE 0435-1223 was monitored during more than six years, from January 2004 to March 2010, through the  $R$  filter, using three different telescopes: the Swiss 1.2 m Euler telescope located on the ESO La Silla site (Chile), the Belgian-Swiss 1.2 m Mercator telescope located at the Roque de Los Muchachos Observatory, La Palma, Canary Island (Spain), and the 1.5 m telescope located at the Maidanak Observatory (Uzbekistan). In addition we also use 136 epochs from the two-year long monitoring of Kochanek et al. (2006), from August 2003 to April 2005, obtained with the

ANDICAM camera mounted on the 1.3 m Small and Moderate Aperture Research Telescope System (SMARTS) located at the Cerro Tololo Inter-American Observatory (CTIO) in Chile. A summary of the observations is given in Table 1. Note that we used the published photometry for the SMARTS data, i.e., we did not reprocess the original data frames with our own photometric pipeline.

### 2.2. Image processing and deconvolution photometry

The data from the three telescopes used by the COSMOGRAIL collaboration are analysed with the semi-automated reduction pipeline described in Vuissoz et al. (2007). The main challenge was that we had to assemble data from different telescopes: each camera has a different size, resolution and orientation on the plane of sky.

The pre-reduction for each observing epoch consists of flat-fielding using master sky-flats. The Euler image with the best seeing was taken as the reference frame to register all other frames. This reference frame was taken on the night of November 11, 2005 and has a seeing of  $0''.82$ . Two reference stars were then chosen in the field of view (Fig. 1) to compute the geometrical transformations between the images. This transformation involves a spatial scaling and a rotation. The reference stars were also used to compute the relative photometric scaling between the frames taken at different epochs. Eventually, the L. A. Cosmic algorithm (van Dokkum 2001) was applied separately to every frame to remove cosmic rays. All images were checked visually to make sure that no pixel was removed inappropriately, especially in the frames with good seeing.

The photometric measurements were carried out using “deconvolution photometry” with the MCS deconvolution algorithm (Magain et al. 1998). This software has been successfully applied to a variety of astrophysical problems ranging from gravitationally lensed quasars (e.g., Burud et al. 2000, 2002) to the study of quasar host galaxies (e.g., Letawe et al. 2008), or to the search for extrasolar planets using the transit technique (e.g., Gillon et al. 2007a,b). Image deconvolution requires accurate knowledge of the instrumental and atmospheric point spread function (PSF). The latter was computed for each frame from the four stars labelled PSF 1-4 in Fig. 1. These stars are from 0 to 1 mag brighter than the quasar images in HE 0435-1223 and are located within  $2'$  from the centre of the field, which minimizes PSF distortions.

Because it does not attempt to achieve an infinitely high spatial resolution, the MCS algorithm produces deconvolved images that are always compatible with the sampling theorem. This avoids deconvolution artefacts and allowed us to carry out accurate photometry over the entire field of view. Moreover, the deconvolved image was computed as the sum of extended numerical structures and of analytical point sources whose shape is chosen to be symmetrical Gaussians. In the case of gravitationally lensed quasars, the numerical channel of this decomposition contains the lensing galaxy. The photometry and astrometry of the quasar images were returned as a list of intensities and positions of Gaussian deconvolved profiles. Finally, the deconvolved image can be computed on a grid of pixels of arbitrary size. In the present work, the pixel size in the deconvolved frames is half the pixel size of the Euler data, i.e.,  $0''.172$ . The spatial resolution in the deconvolved frames is two pixels full-width-at-half-maximum (FWHM), i.e.,  $0''.35$ .

With the MCS software, dithered images of a given target can be “simultaneously deconvolved” and combined into a single deep and sharp frame that matches the whole dataset at once,

**Table 1.** Summary of the optical monitoring data.

Telescope	Camera	FoV	Pixel	Period of observation	#obs.	Exp. time	Seeing	Sampling
Euler	C2	11' × 11'	0'344	Jan. 2004–Mar. 2010	301	5 × 360 s	1'37	6 days
Mercator	MEROPE	6.5' × 6.5'	0'190	Sep. 2004–Dec. 2008	104	5 × 360 s	1'59	11 days
Maidanak	SITE	8.9' × 3.5'	0'266	Oct. 2004–Jul. 2006	26	10 × 180 s	1'31	16 days
Maidanak	SI	18.1' × 18.1'	0'266	Aug. 2006–Jan. 2007	8	6 × 300 s	1'31	16 days
SMARTS	ANDICAM	10' × 10'	0'300	Aug. 2003–Apr. 2005	136	3 × 300 s	≤1'80	4 days
<b>TOTAL</b>	–	–	–	Aug. 2003–Mar. 2010	575	242.5 h	–	3.2 days

**Notes.** The temporal sampling is the mean number of days between two consecutive observations.

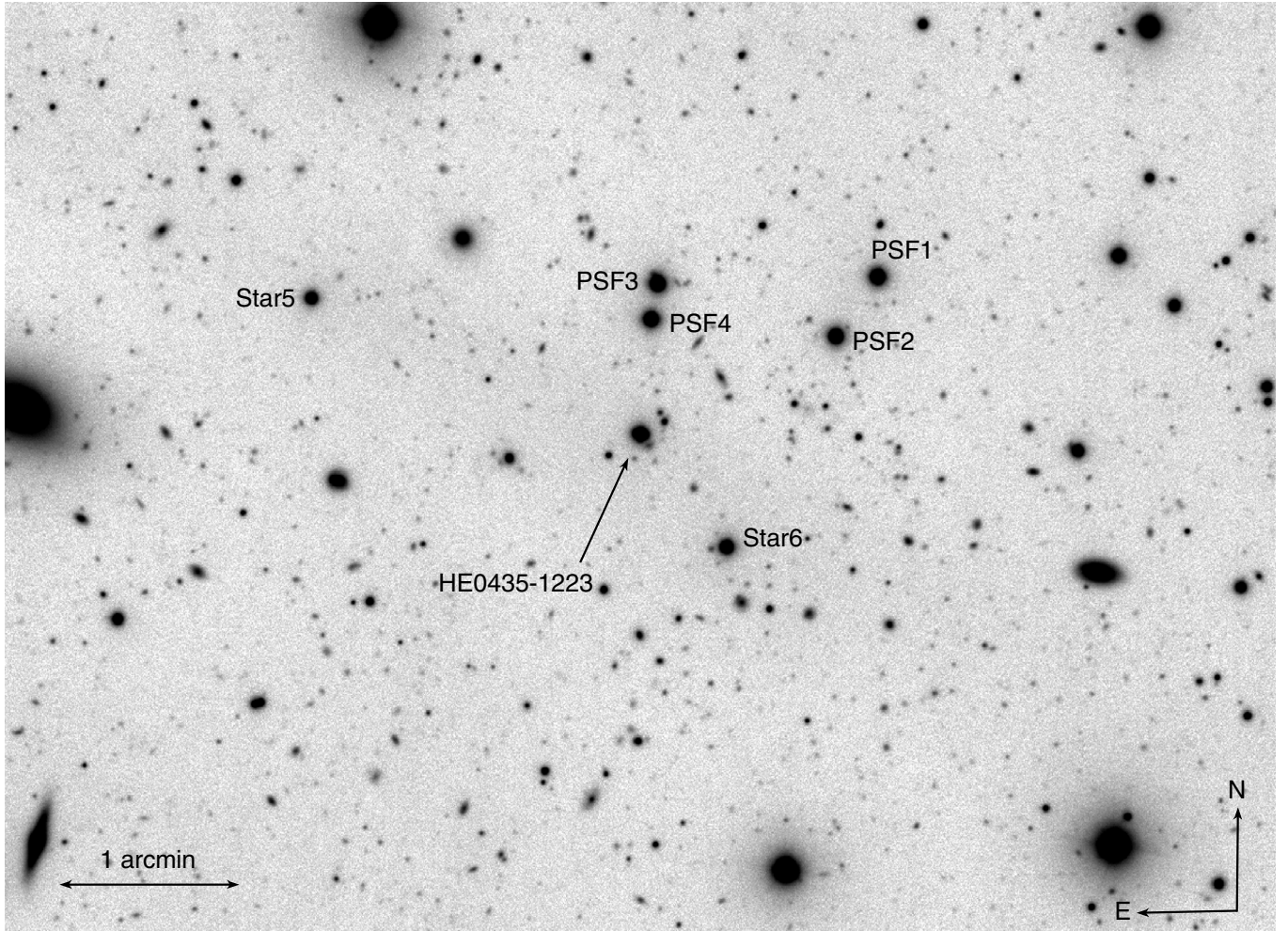


**Fig. 1.** Part of the field of view of the 1.2 m Swiss Euler telescope, with HE 0435-1223 visible in the centre. The four PSF stars used for deconvolution purposes and the two reference stars used to carry out the flux calibration are indicated.

given the PSFs and the noise maps of the individual frames. In doing this, the intensities of the point sources are allowed to vary from one frame to the next while the smooth background, which includes the lensing galaxy, is held constant in all frames. The result of the process is shown in Fig. 2, where the point sources are labelled as in Wisotzki et al. (2002). Prior information on the object to be deconvolved can be used to achieve the best possible results. In the case of HE 0435-1223 the relative positions of the point sources are fixed to the HST astrometry obtained in Sect. 3.

Figure 3 shows the deconvolution light curves obtained for each quasar image of HE 0435-1223, where the  $1\sigma$  error bars account both for the statistical and systematic errors. The statistical

part of the error was taken as the dispersion between the photometric points taken during each night. The systematic errors were estimated by carrying out the simultaneous deconvolution of reference stars in the vicinity of HE 0435-1223.

Finally, a small scaling factor was applied to the light curves of all telescopes, including the published light curves of Kochanek et al. (2006), to match the Euler photometry. These shifts are all smaller than 0.03 mag.

### 3. HST NICMOS2 imaging

We used deep near-IR HST images of HE 0435-1223 to derive the best possible relative astrometry between the quasar



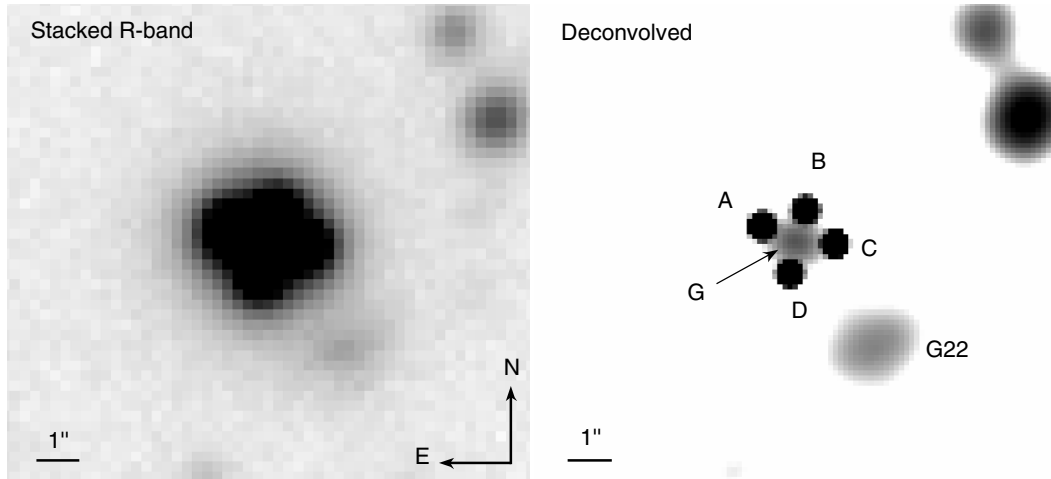


**Fig. 2.** Result from the simultaneous deconvolution of the ground-based frames. G is the lensing galaxy and G22 (Morgan et al. 2005) is its closest neighbour on the plane of the sky. The grey scale in the deconvolved image is set to display all light level above  $3 \times \sigma_{\text{sky}}$ . The FWHM resolution of the deconvolved image is  $0''.34$ .

images and the lensing galaxy and to constrain the light distribution in the lensing galaxy. The data are part of the CASTLES project (Cfa-Arizona Space Telescope LENS Survey) and were acquired in October 2004 (PI: C. S. Kochanek) with the camera 2 of NICMOS, the Near-Infrared Camera and Multi-Object Spectrometer. They consist of four dithered frames taken through the *F160W* filter (*H*-band) in the MULTIACCUM mode with 19 samples and calibrated by CALNICA, the HST image reduction pipeline. The total exposure time amounts to approximately 44 min and the pixel scale is  $0''.075652$ .

The MCS deconvolution algorithm was used to combine the four NIC2 frames into a deep sharp IR image. We followed the iterative technique described in Chantry et al. (2010) and Chantry & Magain (2007), which allowed us to build a PSF in the absence of a stellar image in the field of view. The method can be summarised as follows. First, we estimated the PSF using Tiny Tim software (Krist & Hook 2004) and carried out the simultaneous deconvolution of the four *F160W* frames using a modified version of the MCS software (Magain et al. 2007). This produces a first approximation of the extended channel of the deconvolved image, i.e., the lensing galaxy and the lensed quasar host galaxy. We reconvolved the latter by the PSF and subtracted it from the original data. A new estimate of the PSF was built on the new image that now contained only the quasar images. The process was repeated until the residual image was satisfactory (for more details see Chantry et al. 2010). Figure 4 shows the result. In this image the pixel size is half that of the original data and the resolution  $0''.075$  (FWHM), unveiling an almost full Einstein ring.

In the final deconvolved image, the lensing galaxy was modelled analytically rather than numerically to minimise the number of degrees of freedom. We found that the best-fit profile is an elliptical de Vaucouleurs with the parameters as given in Table 3. The astrometry of the quasar images relative to the lensing galaxy, corrected for the known distortions of the NIC2 camera and for the difference of pixel scale between the *x* and *y* directions is summarised in Table 2. Based on our previous work using deconvolution of NICMOS images (Chantry & Magain 2007), we estimate that the total error bars, accounting for residual correction of the distortions amounts to 2 mas. Our results agree well with previous measurements from HST/ACS

(Morgan et al. 2005) or HST/NIC2 imaging (Kochanek et al. 2006), also shown for comparison in Table 2.

## 4. Time delay measurement

### 4.1. Curve shifting method

Our method to measure the time delays is based on the dispersion technique of Pelt et al. (1996): the light curves are shifted in time and in magnitude to minimise a global dispersion function. In addition, the light curves are distorted on long time scales to account for slow microlensing variations. This was made by adding low-order polynomials to either the full curves or to specific observing seasons.

Pelt et al. (1996) has defined several dispersion statistics between pairs of light curves. We implemented a dispersion estimate similar to  $D_3^2$  (see Eq. (8) of Pelt et al. 1996), which performed a linear interpolation between points of one of the curves over a maximum range of 30 days. In the case of four light curves, we defined a total dispersion that is the sum of the dispersions computed using the 12 possible permutations of two curves among four. Each pair was considered twice so to avoid the arbitrary choice of a reference light curve. The photometric error bars were taken into account to weight the influence of the data points in the dispersion. We then minimised the total dispersion by modifying the time delays and the microlensing polynomials.

### 4.2. Microlensing and influence on the time delay

Simulated light curves that mimic the observed data were used to estimate the robustness of the method. The error bars on the time delays were calculated using Monte Carlo simulations, i.e., redistributing the magnitudes of the data points according to their photometric error bars. The width of the resulting time delay distributions gives us the  $1\sigma$  error bars.

Because of microlensing we do not have access to the intrinsic variations of the quasar. We represent microlensing in three of the light curves as a relative variation with respect to the fourth light curve, taken as a reference. We tested each of the four light curves in turn as a reference and kept the one that



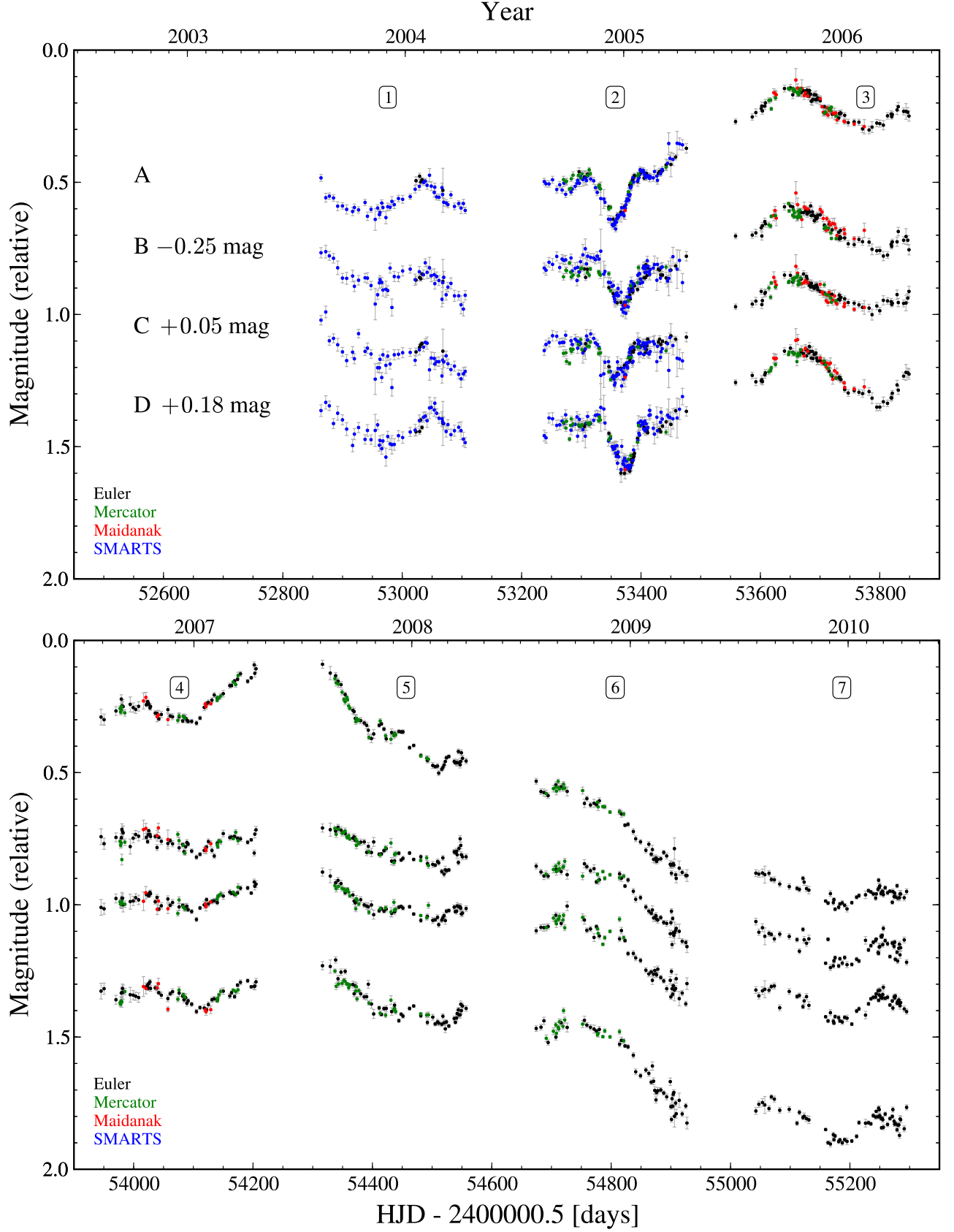


**Fig. 3.** *R*-band light curves of the four lensed images of HE 0435-1223 from December 2003 to April 2010. The magnitudes are given in relative units as a function of the Heliocentric Julian Day (HJD), along with their total  $1\sigma$  error bars. These light curves are available in tabular form at the CDS.

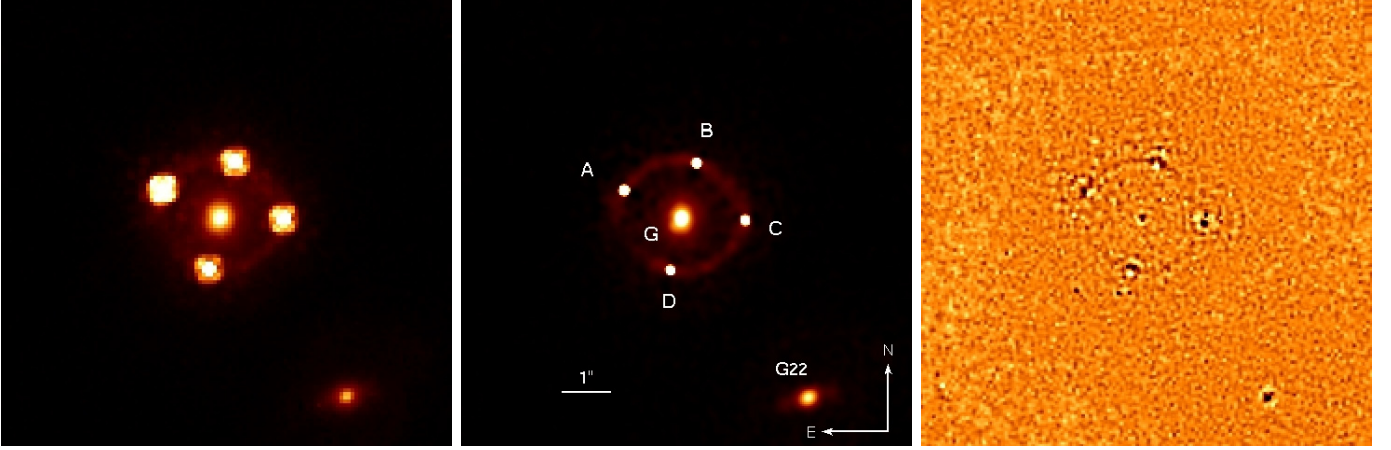


**Fig. 4.** *Left:* combination of the four original HST/NIC2 F160W frames of HE 0435-1223. The field of view is  $9 \times 9$  arcsec. *Middle:* deconvolved image, where the lensing galaxy is modelled as a de Vaucouleurs profile (see text). The nearest galaxy on the plane of the sky, G22, is also indicated. *Right:* residual map in units of the noise. The colour scale ranges from  $-4\sigma$  (white) to  $+4\sigma$  (black).

**Table 2.** Relative astrometry of HE 0435-1223 as derived from the simultaneous deconvolution of all NIC2 frames.

ID	This work		Mag (F160W)	Morgan et al. (2005)		Kochanek et al. (2006)	
	$\Delta\alpha$ (")	$\Delta\delta$ (")		$\Delta\alpha$ (")	$\Delta\delta$ (")	$\Delta\alpha$ (")	$\Delta\delta$ (")
A	0.	0.	$17.20 \pm 0.01$	0.	0.	0.	0.
B	$-1.4743 \pm 0.0004$	$+0.5518 \pm 0.0006$	$17.69 \pm 0.01$	$-1.477 \pm 0.002$	$+0.553 \pm 0.002$	$-1.476 \pm 0.003$	$+0.553 \pm 0.001$
C	$-2.4664 \pm 0.0003$	$-0.6022 \pm 0.0013$	$17.69 \pm 0.02$	$-2.469 \pm 0.002$	$-0.603 \pm 0.002$	$-2.467 \pm 0.002$	$-0.603 \pm 0.004$
D	$-0.9378 \pm 0.0005$	$-1.6160 \pm 0.0006$	$17.95 \pm 0.01$	$-0.938 \pm 0.002$	$-1.615 \pm 0.002$	$-0.939 \pm 0.002$	$-1.614 \pm 0.001$
G	$-1.1706 \pm 0.0030$	$-0.5665 \pm 0.0004$	$16.20 \pm 0.12$	$-1.169 \pm 0.002$	$-0.572 \pm 0.002$	$-1.165 \pm 0.002$	$-0.573 \pm 0.002$

**Notes.** The  $1\sigma$  error bars are the internal errors after deconvolution. Additional 2-mas systematic errors must be added to these (see text). The magnitudes are in the Vega system. For comparison we show the results from Morgan et al. (2005) using HST/ACS images and from Kochanek et al. (2006) using HST/NIC2 images.

**Table 3.** Shape parameters for the lensing galaxy in HE 0435-1223.

PA (°)	Ellipticity	$a_{\text{eff}}$ (")	$b_{\text{eff}}$ (")	$r_{\text{eff}}$ (")
174.8 (1.7)	0.09 (0.01)	1.57 (0.09)	1.43 (0.08)	1.50 (0.08)

**Notes.** The position angle (PA) is measured positive east of north. The  $1\sigma$  error bars (internal errors) are given in parenthesis.

minimised the residual microlensing variations to be modelled in the 3 others. This is best verified with component B as a reference.

With B as a reference light curve, we note that microlensing in C and D remains smooth and can therefore be modelled with a low-order polynomial drawn over the full length of the monitoring. However, A contains higher frequency variations that need to be accounted for in each season individually, as illustrated in Fig. 5. In doing this, we obtain fairly good fits to the light curves, as shown in the residual signal. To quantify the quality of these residuals, we applied the so-called *one-sample runs test of randomness*, a statistical test to estimate whether successive realizations of a random variable are independent or not. In practice the test was applied to a sequence of residuals to decide whether a model is a good representation of the data. For most seasons in our curves the number of runs was between  $1\sigma$  and  $3\sigma$  lower than the value expected for independent random residuals. Thus, although our microlensing model is not fully representative of the real signal, the deviations from the data points remain small.

We tested the robustness of our curve-shifting method in several ways. First, we modelled the microlensing variations using

polynomial fits of different orders. Second, we fitted these polynomials either across each individual season or across groups of seasons. Finally, we masked the seasons with the worst residual signal (Fig. 5). All these changes had only a negligible impact on the time delay measurements. We note that this is not the case when considering only two or three seasons of data, which shows the importance of a long-term monitoring with good temporal sampling.

#### 4.3. Final results

Our results are summarised in Table 4 and are compared with the previous measurements of Kochanek et al. (2006), who have used pure a polynomial fit to the light curves and two seasons of monitoring. Using the same data but with our modified dispersion technique, we obtained very similar time delays as Kochanek et al. (2006), but larger error bars. We prefer keeping a minimum possible number of degrees of freedom (e.g., in the polynomial order used to represent microlensing), in accordance with the Occam's razor principle, even to the cost of apparently larger formal error bars.

We also note that Kochanek et al. (2006) give their time delays with respect to A, which, with seven seasons of data, turns out to be the most affected by microlensing. As a consequence the error bars on these time delays are dominated by residual microlensing rather than by statistical errors. The time delays used in the rest of our analysis are therefore measured relative to B.

Finally, we used the mean values of our microlensing corrections to estimate the macrolensing R-band flux ratios between the four quasar images, assuming that no long-term microlensing

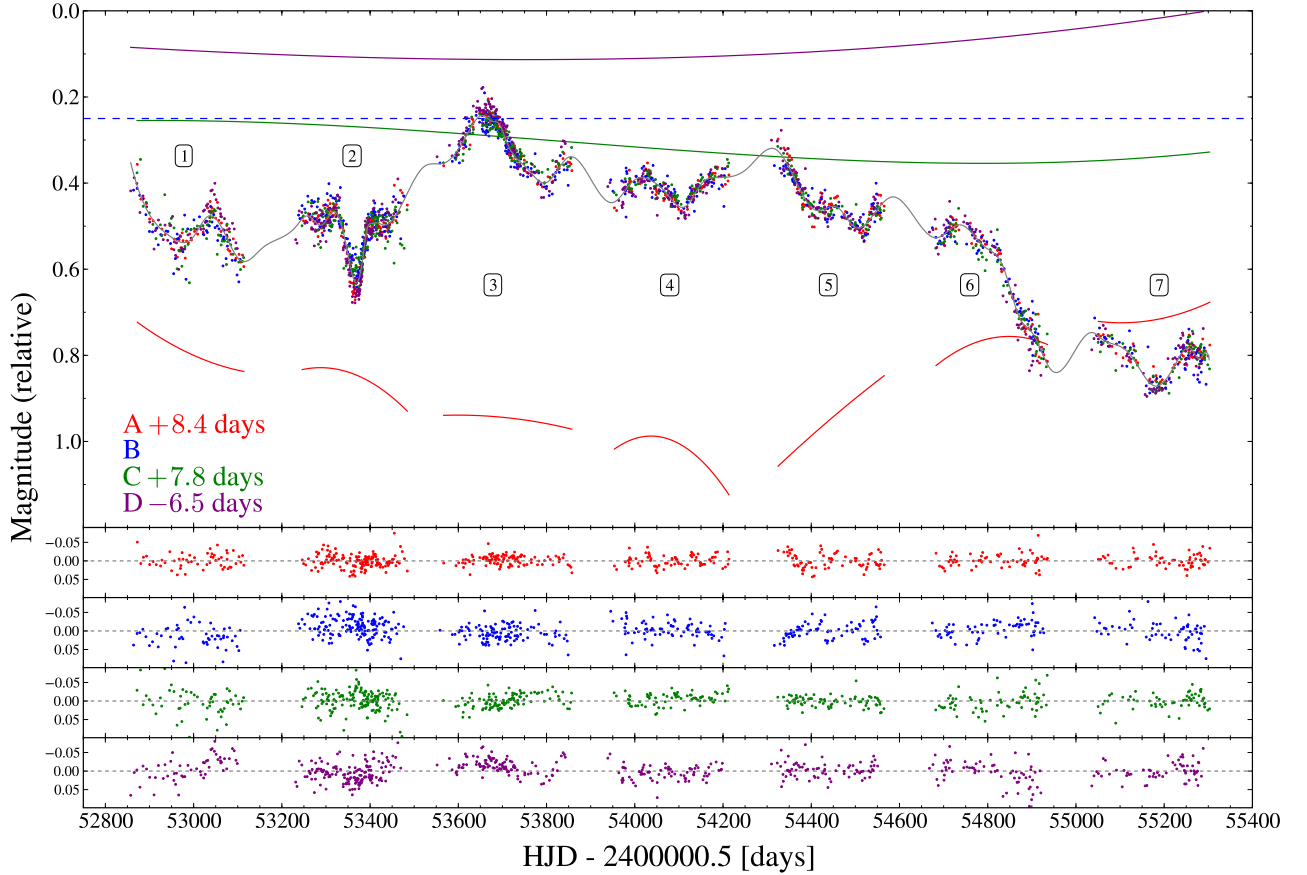


**Fig. 5.** Light curves obtained with all four telescopes and shifted by time delays of  $\Delta t_{BA} = 8.4$  days,  $\Delta t_{BC} = 7.8$  days and  $\Delta t_{BD} = -6.5$  days. The relative microlensing representations applied on curves A, C and D are shown as continuous curves with respect to the dashed blue line (see text). A fifth-order polynomial was used over the seven seasons to model microlensing on the quasar images C and D, while seven independent third-order polynomials were used for image A. The lower panels show residuals obtained by subtracting a simultaneous spline fit (grey) from the light curves.

affects the data. We found  $m_B - m_A = \Delta m_{BA} = 0.62 \pm 0.04$ ,  $\Delta m_{BC} = 0.05 \pm 0.01$ , and  $\Delta m_{BD} = -0.16 \pm 0.01$ , which is well compatible with the ratios measured at seven wavelengths by Mosquera et al. (2011). However, these authors report significant wavelength dependence of the image flux ratios, which led us not to use flux ratios as a constraint in the lens models.

## 5. Constraining the mass profile of the lensing galaxy

The goal of the present section is to constrain the radial mass profile of the lensing galaxy as much as possible, which is the main source of uncertainty on the determination of  $H_0$  with the time delay method. One way of doing this is to use the information contained in the Einstein ring that is formed by the host galaxy of the lensed quasar (Suyu et al. 2010, 2009; Warren & Dye 2003). This works well when a prominent Einstein ring is visible. Unfortunately, given the depth of the current HST images of HE 0435-1223, the radial extent of the ring is too small to efficiently apply this technique. We propose instead to use information on the dynamics and on the stellar mass of the lens, using deep optical spectroscopy.

### 5.1. Stellar population and velocity dispersion of the lensing galaxy

A deep VLT spectrum of the lensing galaxy is available from Eigenbrod et al. (2006). While the spectrum was originally used

to measure the redshift of the galaxy, it turns out to be deep enough ( $\langle S/N \rangle \sim 20$ ) to measure the stellar velocity dispersion and the mass-to-light ratio.

We analysed the data using full spectrum fitting with the ULYSS package (Koleva et al. 2009). The method consists in fitting spectra against a grid of stellar population models convolved by a line-of-sight velocity distribution. A single minimisation allowed us to determine the population parameters (age and metallicity) and the kinematics (redshift and velocity dispersion). The stellar mass-to-light ratio was derived from the age and metallicity for the considered model. The simultaneous fit of the kinematical and stellar population parameters reduced the degeneracies between age, metallicity and velocity dispersion (Koleva et al. 2008).

We performed the spectral fit using the PEGASE-HR single stellar population models (SSP, Le Borgne et al. 2004), where the observed flux,  $F_\lambda$ , is modelled as follows:

$$F_\lambda = P_n(\lambda) \times [L(v_{\text{sys}}, \sigma) \otimes S(t, [\text{Fe}/\text{H}], \lambda)] + Q_m(\lambda). \quad (1)$$

The models were built using the Elodie.3.1 (Prugniel & Soubiran 2001; Prugniel et al. 2007) spectral library and the Kroupa (Kroupa 2001) and Salpeter (Salpeter 1955) initial mass functions (IMF).  $L(v_{\text{sys}}, \sigma)$  is a Gaussian function of the systematic velocity,  $v_{\text{sys}}$ , and of the velocity dispersion,  $\sigma$ .  $S(t, [\text{Fe}/\text{H}], \lambda)$  is the model for the SSP and depends on age and metallicity.  $P_n$  is a polynomial of degree  $n$ , which models any residual uncertainty in the flux calibration and extinction correction. In addition,

**Table 4.** Time delays for HE 0435-1223, with the same arrival order convention as Kochanek et al. (2006), i.e., D arrives last.

Data	Method	$\Delta t_{AB}$	$\Delta t_{AC}$	$\Delta t_{AD}$	$\Delta t_{BC}$	$\Delta t_{BD}$	$\Delta t_{CD}$
SMARTS (seasons 1 and 2)	Kochanek (2006)	$-8.0 \pm 0.8$	$-2.1 \pm 0.8$	$-14.4 \pm 0.8$			
SMARTS (seasons 1 and 2)	dispersion	$-8.8 \pm 2.4$	$-2.0 \pm 2.7$	$-14.7 \pm 2.0$	$6.8 \pm 2.7$	$-5.9 \pm 1.7$	$-12.7 \pm 2.5$
COSMOGRAIL (all seasons)	dispersion	$-8.4 \pm 2.1$	$-0.6 \pm 2.3$	$-14.9 \pm 2.1$	$7.8 \pm 0.8$	$-6.5 \pm 0.7$	$-14.3 \pm 0.8$

**Table 5.** Model parameters of the lens potential well.

$R_{\text{eff}}$	8.44 kpc	radius containing 50% of the observed light
$R_E$	6.66 kpc	Einstein radius
$f_b$	parameter	baryonic fraction in the Einstein radius [0.05–0.5]
$r_*$	5.3 kpc	stellar component scaling radius
$M_*$	$M_h f_b / (1 - f_b)$	stellar total mass
$r_{*,\text{max}}$	$20 r_*$	stellar truncation radius
$\gamma_{\text{DM}}$	parameter	dark matter inner slope [0–2]
$r_s$	parameter	dark matter scaling radius [1, 2, 4, 8] $\times R_E$
$M_h$	parameter	dark matter total mass [ $4.8 \times 10^{11}$ – $9.1 \times 10^{12}$ ] $M_\odot$
$r_{s,\text{max}}$	$10 r_s$	dark matter truncation radius

**Notes.** For the variables used as parameters the ranges of values used are given between brackets.

the quasar spectrum might not be perfectly subtracted from the galaxy. To mimic this effect, we included an additive polynomial,  $Q_m$ . The order of the additive and multiplicative polynomials is the minimum required to provide an acceptable  $\chi^2$ , i.e., in our case ( $n = 10, p = 1$ ).

We obtained SSP-equivalent ages and metallicities of  $t \sim 3$  Gyr and  $[\text{Fe}/\text{H}] \sim 0.0$  dex respectively. The corresponding rest-frame  $B$ -band stellar mass-to-light ratio is  $M_*/L_B = 3.2^{+0.3}_{-0.5} M_\odot/L_{\odot,B}$  using a Kroupa IMF and  $M_*/L_B = 4.6^{+0.9}_{-0.7} M_\odot/L_{\odot,B}$  using a Salpeter IMF. The uncertainties in the age and metallicity were estimated via Monte Carlo simulations and propagated in the error in  $M_*/L_B$ .

To compute the physical velocity dispersion we subtracted quadratically the instrumental broadening from the measured profile, neglecting the dispersion of the models since they are based on high-resolution templates. The instrumental broadening was measured both from the PSF stars used to carry out the spatial deblending of the spectrum (Eigenbrod et al. 2006) and from the lamp spectra. We obtained the rest-frame physical stellar velocity dispersion of the lensing galaxy:  $\sigma_{\text{ap}} = 222 \pm 34 \text{ km s}^{-1}$  in an aperture of  $1''$ , i.e., 5.7 kpc.

## 5.2. Numerical integration of the Jeans equations

In this section we model the lensing galaxy using a 3D spherical potential well formed of two components, one for the stellar part of the mass and one for the dark matter halo. We then perform a numerical integration of the Jeans equations in 3D to predict a theoretical velocity dispersion and a total mass for the model. The assumption of spherical symmetry is sufficient for our purpose, as illustrated by the study of the lensed quasar MG 2016+112, where Koopmans & Treu (2002) introduced an anisotropy parameter and showed that it has almost no influence on the inferred mass slope.

The luminous component of the model is a Hernquist profile (Hernquist 1990):

$$\rho_*(r) = \frac{\rho_*(0)}{(r/r_*)(1 + r/r_*)^3}, \quad (2)$$

where  $\rho_*(0)$  is the central density and  $r_*$  is a scale radius chosen so that the integrated mass in a cylinder of radius  $R_{\text{eff}}$  (effective

radius) is equal to half the total stellar mass  $M_*$ . The profile has a maximum radius of  $r_{*,\text{max}} = 20 r_*$ .

The dark matter halo is modelled as a generalised Navarro, Frenk & White (NFW) profile (Navarro et al. 1996):

$$\rho_h(r) = \frac{\rho_h(0)}{(r/r_s)^{\gamma_{\text{DM}}} (1 + (r/r_s)^2)^{(3-\gamma_{\text{DM}})/2}}, \quad (3)$$

where  $\gamma_{\text{DM}}$  is the inner slope of the profile,  $r_s$  is the scaling radius and  $\rho_h(0)$  is the central mass density. For  $\gamma_{\text{DM}} = 1$  the model closely follows the standard NFW profile. Its total mass,  $M_h$ , is given in the truncation radius  $r_{h,\text{max}} = 10 r_s$ .

Following the usual convention, the integrated stellar and dark matter masses are related by the baryonic fraction  $f_b$ ,

$$f_b = \frac{M_*}{M_h + M_*}. \quad (4)$$

Because all integrations in this work were carried out numerically,  $f_b$  can easily be computed in any aperture. We chose to compute it in the Einstein radius, which is also where lensing gives the most accurate mass measurement. The velocity dispersion of the stellar component was computed by solving the second moment of the Jeans equation in spherical coordinates (Binney & Merrifield 1998). The velocity dispersion is then

$$\sigma_*^2(r) = \frac{1}{\rho_*(r)} \int_r^\infty dr' \rho_*(r') \partial_r \Phi(r'), \quad (5)$$

where  $\Phi(r)$  is the total gravitational potential. Equation (5) is solved numerically as follows. First, the density of each mass component (stars and dark halo) is sampled by  $N$  particles, using a Monte-Carlo method. Second, the potential is computed using a *treecode* method (Barnes & Hut 1986). For self-consistency, the density is computed by binning the particles in spherical shells. Then, a velocity is allocated to each particle at a distance  $r$  from the galaxy center, following a Gaussian distribution of variance  $\sigma_*(r)$ . Finally, the velocity dispersion of the model,  $\sigma_{\text{Jeans}}$ , is computed numerically, by integrating all the particle velocities in an aperture that matches exactly the slit used to carry out the observations.

The advantages of the numerical representation of the lens models are multiple. They allow us (i) to compute velocity



dispersions for any combination of density profiles, even non-parametric ones; (ii) to account for the truncation radius of the halo; (iii) to test the dynamical equilibrium of the system by evolving the model with time. Computing the velocity dispersion as well as the total mass in a cylinder along the line of sight of the observer is then straightforward.

In all calculations we fixed the effective radius to the one observed for the lensing galaxy, i.e.,  $R_{\text{eff}} = 8.44$  kpc. The remaining parameter space to explore is composed of the halo scale radius,  $r_s$ , the slope of the profile,  $\gamma_{\text{DM}}$ , and the baryonic fraction,  $f_b$ , within the Einstein radius.

### 5.3. Applying the dynamical and stellar population constraints

Using our HST photometry, we measured the total rest-frame *B*-band galaxy luminosity by converting its total *H*-band magnitude,  $m_{F160W} = 16.20$ . Using a *k*-correction of 1.148, and a galactic extinction<sup>1</sup> of  $E(B - V) = 0.059$  (Schlegel et al. 1998), we find  $L_B = 1.04 \times 10^{11} L_{B,\odot}$ . For a given galaxy model we can therefore compute the total stellar mass-to-light ratio,  $M_\star/L_B$ , as well as the baryonic fraction that we can compare with the observed ones. This requires a choice of IMF. For a Salpeter IMF we measured  $f_b = 0.65^{+0.04}_{-0.10}$ , while for a Kroupa IMF we measured  $f_b = 0.45^{+0.04}_{-0.07}$ . In our computation of the baryonic fraction, the total mass is the mass in the Einstein radius,  $M(<R_E)$ .

We compared the model properties to the data by computing a chi-square,  $\chi^2_{\text{Jeans}}$ . This  $\chi^2_{\text{Jeans}}$  includes the measured lens velocity dispersion and the total mass in the Einstein radius,  $M(<R_E) = (3.16 \pm 0.31) \times 10^{11} M_\odot$ . We allowed for a 10% error on the total mass in the Einstein radius to account for the weak dependence of this mass upon the choice of a lens model, which led to

$$\chi^2_{\text{Jeans}} = \left( \frac{\sigma_{\text{Jeans}} - 222}{34} \right)^2 + \left( \frac{M(<R_E) - 3.16 \times 10^{11}}{0.31} \right)^2. \quad (6)$$

We used our numerical integration of the Jeans equations to sample the  $\gamma_{\text{DM}} - f_b$  plane, for a given choice of the scale radius,  $r_s$ , of the dark matter halo. Figure 6 shows the value of  $\chi^2_{\text{Jeans}}$  for 960 000 galaxy models with  $r_s = 4 \times R_E = 25$  kpc. For a given choice of IMF a precise measurement of the baryonic fraction,  $f_b$ , can constrain the dark matter slope  $\gamma_{\text{DM}}$  well, at least in the case of a Kroupa IMF.

Figure 6 is drawn for  $r_s = 4 \times R_E = 25$  kpc, which gives the best  $\chi^2_{\text{Jeans}}$  values. However, models with  $\chi^2_{\text{Jeans}} < 1$  are also obtained with other values of  $r_s$ . We therefore test the influence of a change in  $r_s$  by building models for a range of scale radii,  $r_s = 5, 15, 30$  kpc (i.e.,  $r_s = 0.75\times, 2.25\times, 4.50 \times R_E$ ). Figure 7 summarises the results and shows no influence of  $r_s$  on the  $\gamma_{\text{DM}} - f_b$  relation unless  $r_s$  becomes unrealistically small.

The Hernquist profile in our model also has a scale parameter,  $r_\star$ , which is fixed to the observed value of the effective radius,  $R_{\text{eff}} = 8.44$  kpc. Although we have HST images that allow us to measure  $R_{\text{eff}}$  and although our error bars on this parameter are small, we note that studies of lensing galaxies by different authors often find different  $R_{\text{eff}}$  values from the same data. This is because different methods are used to subtract the quasar images and to mask (or not) the Einstein ring. We therefore computed models for a range of different  $R_{\text{eff}}$  and show the influence on the  $\gamma_{\text{DM}} - f_b$  plane in Fig. 8, for  $R_{\text{eff}} = 4.22, 8.44, 12.88$  kpc.

<sup>1</sup> A galactic extinction calculator is available at this address: <http://nedwww.ipac.caltech.edu/forms/calculator.html>

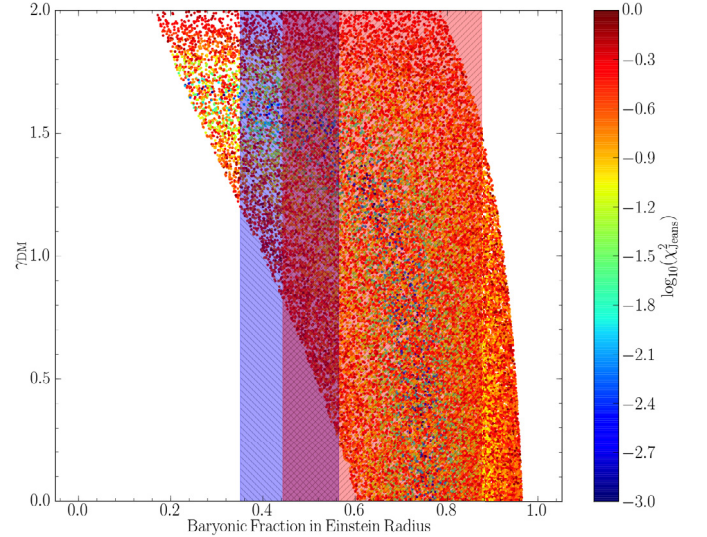


**Fig. 6.** Radial slope,  $\gamma_{\text{DM}}$ , of the dark matter halo as a function of the baryonic fraction in the Einstein radius,  $R_E$ . The colour code represents the value of  $\chi^2_{\text{Jeans}}$  for all acceptable models, i.e.,  $\chi^2_{\text{Jeans}} < 1$  (see text; Eq. (6)). The observational limits drawn on  $f_b$  using our spectrum of the lensing galaxy are indicated as shaded vertical regions. The blue region corresponds to a Kroupa IMF and the red regions corresponds to a Salpeter IMF. In this figure, all models have  $r_s = 4 \times R_E = 25$  kpc.

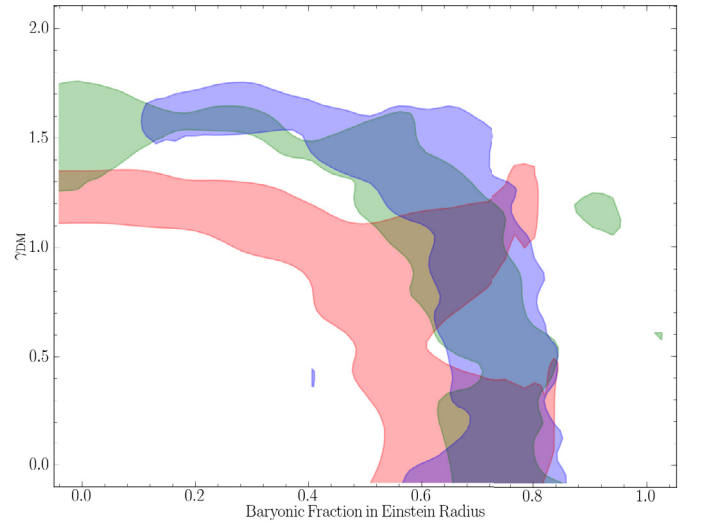


**Fig. 7.** Effect of change in  $r_s$ , the scale radius of the dark matter halo, on the  $\gamma_{\text{DM}} - f_b$  relation. The contours show the region containing 68% of the models. The blue area has  $r_s = 25$  kpc (our adopted choice for the final modelling), the green region has  $r_s = 15$  kpc, and the red region is for models with small scale radii,  $r_s = 5$  kpc.

This reflects an (unlikely high) 50% change in  $R_{\text{eff}}$  with respect to the actual measurement and translates into a 10–20% shift of the  $\gamma_{\text{DM}} - f_b$  relation. This is comparable to the width of the coloured areas in Fig. 8. Because our true measurement error on  $R_{\text{eff}}$  is certainly much better than 50%, we conclude that this parameter does not affect the models much, given the accuracy of the observations.

## 6. Towards $H_0$ with HE 0435-1223

The gravlens software (Keeton 2004) was used in combination with the dynamical and stellar population constraints to

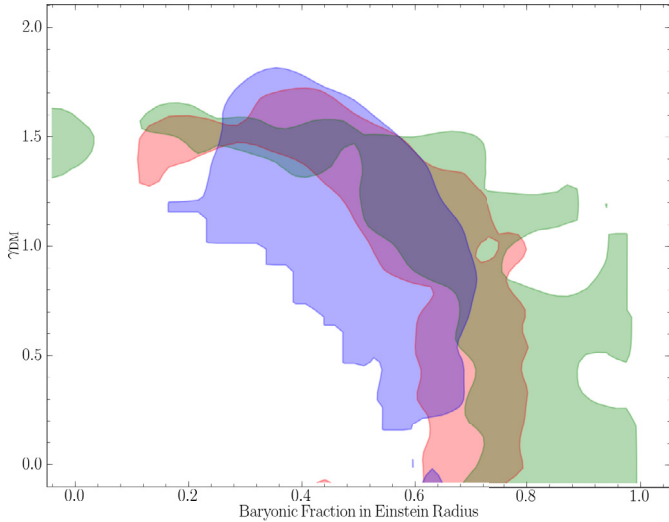


**Fig. 8.** Effect of a change in  $R_{\text{eff}}$  on the  $\gamma_{\text{DM}} - f_b$  relation. The contours show the region containing 68% of the models. The value adopted in this paper is  $R_{\text{eff}} = 8.44$  kpc, as measured from HST images. This corresponds to the area in red. The models in the blue region have  $R_{\text{eff}} = 4.22$  kpc, and the region in green has  $R_{\text{eff}} = 12.88$  kpc.

reproduce the lensing configuration of the quasar images and to attempt converting the time delays into  $H_0$ . We adopted a total potential well composed of the main lensing galaxy, the nearby galaxy G22 (see Morgan et al. 2005) plus an external shear.

The main galaxy is composed of a projected Hernquist + cuspy halo model identical to those in Eqs. (1) and (2).

For the Hernquist profile, we fixed the ellipticity and PA of the lensing galaxy to the observed ones.

We then estimated how well each of the models described in Sect. 5.2 reproduces the observed image configuration. In doing this, we allowed only the external shear ( $\gamma$ ,  $\theta_\gamma$ ), the Einstein radius of G22 and  $H_0$  to vary. The potential well of G22 was assumed to lie at its observed position and was modelled as a singular isothermal sphere (SIS). We assumed a conservative value of  $R_E(\text{G22}) < 0''.4$ , following the results of Morgan et al. (2005), who have found  $R_E(\text{G22}) = 0''.18$ .

We show in Fig. 9 the value of  $H_0$  for each lens model as a function of its dark matter slope,  $\gamma_{\text{DM}}$ . The colour code in the figure corresponds to the value of  $\chi^2_{\text{Tot}}$ , where the baryonic fraction,  $f_b \pm \sigma(f_b)$ , in the Einstein radius is now included in the calculation:

$$\chi^2_{\text{Tot}} = \chi^2_{\text{Jeans}} + \left( \frac{f_b(\text{model}) - f_b(\text{obs})}{\sigma(f_b)} \right)^2. \quad (7)$$

Including  $f_b$  is justified by Fig. 6, showing that different values of  $f_b$  select different lens models. We display our results for the two most common IMFs in use in stellar population modelling, the Salpeter and the Kroupa IMFs.

The points define a  $\chi^2_{\text{Tot}}$  surface with a clear valley which minimum indicates the best dark matter slopes for each IMF. These are  $\gamma_{\text{DM}}(\text{Sal}) \sim 1.15$  and  $\gamma_{\text{DM}}(\text{Kro}) \sim 1.54$  for the Salpeter and the Kroupa IMFs, respectively. Each model shown in Fig. 9 is also required to display a good lensing chi-square,  $\chi^2_L$ , after fitting of the quasar image positions with gravlens. The values of  $\chi^2_L$  are systematically lower for the lensing galaxies with Kroupa IMFs. The present lensing and dynamical work therefore favours a lensing galaxy with a Kroupa IMF, as also found by Cappellari et al. (2006) from 3D spectroscopy of early-type

galaxies and by Ferreras et al. (2008) using the SLACS sample of strong lenses (Bolton et al. 2008).

The points in Fig. 9 all have  $\chi^2_{\text{Jeans}} < 1$ , which prevents us, for now, from giving a value for  $H_0$  given the observational uncertainty on  $f_b$  and  $\sigma_{\text{ap}}$ . The measurement errors on both parameters will, however, easily improve with deeper and higher resolution spectroscopy of the lens.

With the current observational constraints we rely on previous work done on the total mass slope,  $\gamma'$ , of lensing galaxies. Koopmans et al. (2009) have measured the probability distribution function of  $\gamma'$  in the SLACS sample of strong lenses. They have found  $\langle \gamma' \rangle = 2.085^{+0.025}_{-0.018}$ , with an intrinsic spread of  $\sigma(\gamma') = 0.20$ , also confirmed in a more recent study by Auger et al. (2010). The models with the best  $\chi^2_{\text{Tot}}$  values in Fig. 9 correspond to a total slope of  $\gamma' = 2.1 \pm 0.1$  independent of the choice of an IMF. This is well within the rms limits of Koopmans et al. (2009) and leads to  $57 < H_0 < 71 \text{ km s}^{-1} \text{ Mpc}^{-1}$  with all models equiprobable within this range.

In our analysis we modelled the environment of the lensing galaxy as a SIS that represents galaxy G22, plus an external shear with a PA of the order of  $-15^\circ$ , and amplitudes in the range  $0.06 < \gamma < 0.08$ . However, we did not explicitly account for the fact that HE 0435-1223 lies within a group of galaxies (Momcheva 2009). The unknown convergence,  $\kappa$ , associated with the group leads to an overestimate of  $H_0$  by a factor  $(1 - \kappa)^{-1}$ , meaning that the range of acceptable  $H_0$  values would decrease further if we have underestimated the convergence caused by the group. Current imaging data suggest, however, that the line of sight is in fact slightly under-dense compared with other lensed systems (Fassnacht et al. 2011). However, the missing convergence is about  $\kappa \sim 0.01-0.02$ , leading to at most a 2% change (upwards) in  $H_0$ . The above statement should, however, be considered with care because the effect of a group is poorly approximated by a simple convergence term. Explicit modelling of the group halo is likely needed to properly account for the modifications induced on the main lens potential. Deep X-ray and/or optical integral field spectroscopy may turn out to be very useful as well in determining the centroid and mass of the group that contains the galaxy lensing HE 0435-1223.

## 7. Conclusion

We presented seven years of optical monitoring for the four lensed quasar images of HE 0435-1223. We found that the time delays are better expressed with respect to component B, which is the least affected by stellar microlensing in the lensing galaxy. The formal error bars on the time delays are between 5% and 10% depending on the component, which is remarkable given the very short time delays involved. In addition, the delays are robust against different tests performed on the data, including removal of subsets of data and monte carlo simulations. These tests are possible only with very long light curves, as provided by COSMOGRAIL. Most past lens monitorings have two to three seasons and much coarser temporal sampling. The delays are also independent of the way the microlensing variations are modelled. Given the short length of the delays, additionally improving the error bars will only be possible by increasing the temporal sampling of the curves, i.e., by merging all existing data on HE 0435-1223 taken by different groups over the years.

We introduced a method to convert the time delays into  $H_0$  purely based on external constraints on the radial mass slope of the lens. These constraints come from deep optical spectroscopy of the lens, which allowed us to measure its velocity dispersion and its stellar mass-to-light ratio. The present paper describes



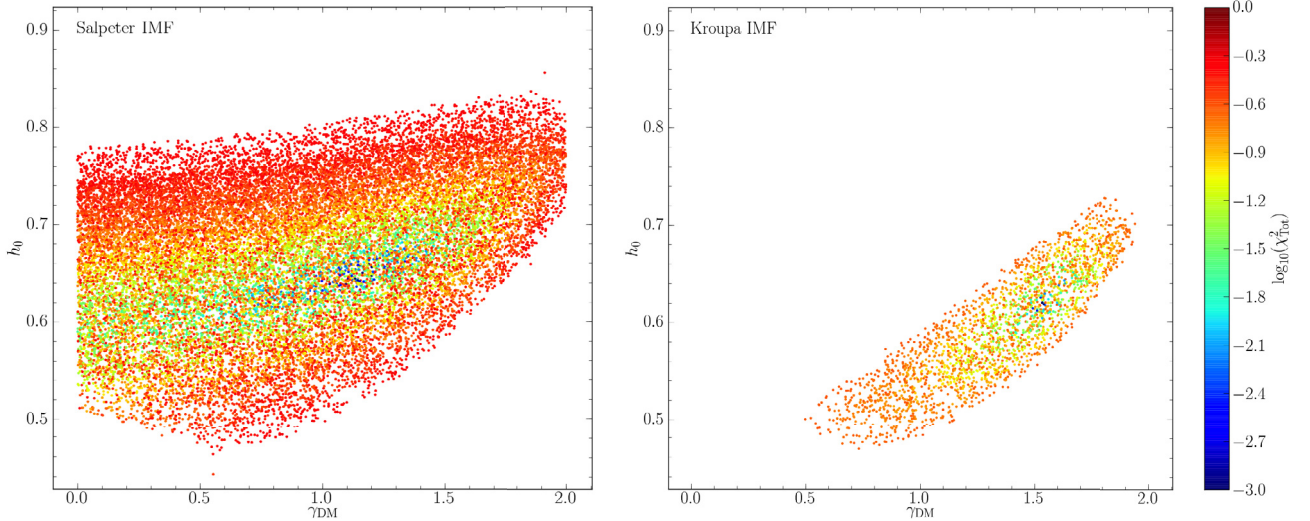


**Fig. 9.** Distribution of our lens models as a function of the dark matter slope and  $H_0$ . The colour code gives the value of  $\chi^2_{\text{Tot}}$  (see text; Eq. (7)). Only the models with  $\chi^2_{\text{Tot}} < 1$  are shown. The results in *the left panel* are for a Salpeter IMF, and for a Kroupa IMF in *the right panel*. The lensing  $\chi^2$  itself is not included in the figure. However, it is systematically lower for galaxies with Kroupa IMFs than for galaxies with Salpeter IMFs.

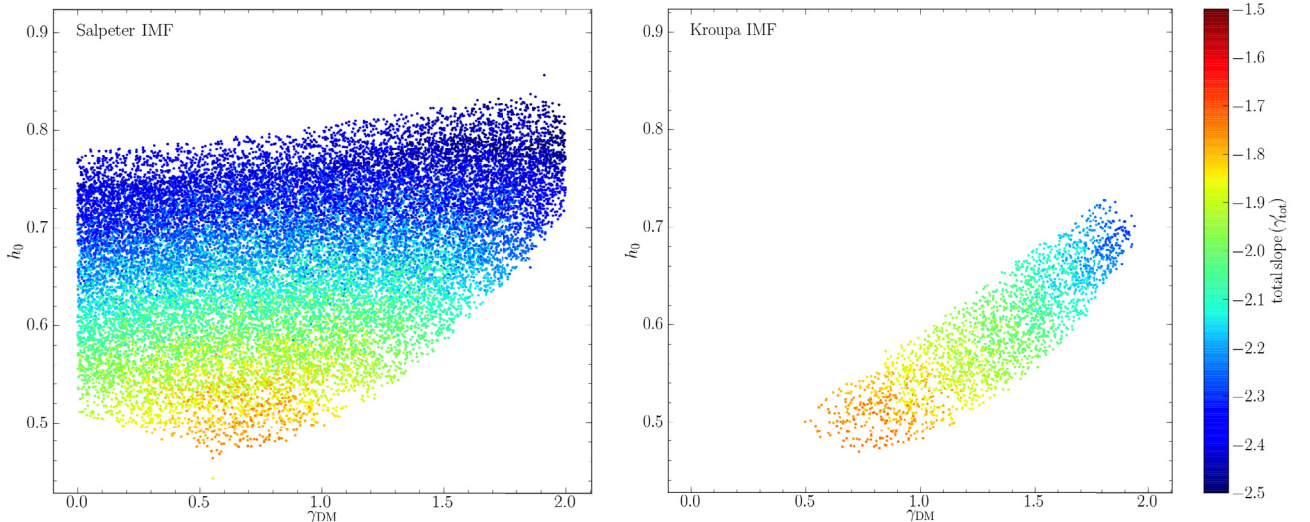


**Fig. 10.** Same as Fig. 9, but the colour code now gives the slope of the total (dark+luminous) mass profile,  $\gamma'$ . A logarithmic slope of  $\gamma' = 2$  corresponds to an isothermal profile, shown in green.

our approach, but the current observations of the lensing galaxy so far lead to a broad range of values for  $H_0$ .

Our methodology complement that presented by Suyu et al. (2009, 2010) well. Combining the two in the future will require follow-up observations such as (i) deep HST imaging to map the Einstein ring with high signal-to-noise; (ii) deep high resolution spectroscopy of the lens over a broad spectral range to narrow down the uncertainty on its velocity dispersion and stellar mass; (iii) integral field spectroscopy to measure all redshifts within 30–60'' around the lens; and (iv) X-ray imaging to pinpoint massive groups along the line of sight.

If all these observations are taken for HE 0435-1223 as well as for a few lenses with well measured time delays, the cost in terms of follow-up observations will still remain very modest compared with other existing methods to measure  $H_0$ , such as Cepheids and supernovae.

**Acknowledgements.** We are grateful to all the observers who contributed to the data acquisition at the Euler and Mercator telescopes as well as at Maidanak Observatory. COSMOGRAIL is financially supported by the Swiss National Science Foundation (SNSF). This work is also supported by the Belgian Federal

Science Policy (BELSPO) in the framework of the PRODEX Experiment Arrangement C-90312. V.C. thanks the Belgian National Fund for Scientific Research (FNRS). D.S. acknowledges a fellowship from the Alexander von Humboldt Foundation. M.K. has been supported by the Programa Nacional de Astronomía y Astrofísica of the Spanish Ministry of Science and Innovation under grant AYA2007-67752-C03-01 and DO02-85/2008 from Bulgarian Scientific Research Fund.

## References

- Auger, M. W., Treu, T., Bolton, A. S., et al. 2010, *ApJ*, 724, 511
- Barnes, J., & Hut, P. 1986, *Nature*, 324, 446
- Binney, J., & Merrifield, M. 1998, *Galactic astronomy* (Princeton University Press), Princeton Series in Astrophysics
- Blackburne, J. A., & Kochanek, C. S. 2010, *ApJ*, 718, 1079
- Bolton, A. S., Burles, S., Koopmans, L. V. E., et al. 2008, *ApJ*, 682, 964
- Burud, I., Hjorth, J., Jaunsen, A. O., et al. 2000, *ApJ*, 544, 117
- Burud, I., Courbin, F., Magain, P., et al. 2002, *A&A*, 383, 71
- Cappellari, M., Bacon, R., Bureau, M., et al. 2006, *MNRAS*, 366, 1126
- Chantry, V., & Magain, P. 2007, *A&A*, 470, 467
- Chantry, V., Sluse, D., & Magain, P. 2010, *A&A*, 522, A95
- Eigenbrod, A., Courbin, F., Meylan, G., Vuissoz, C., & Magain, P. 2006, *A&A*, 451, 759

- Fassnacht, C. D., Xanthopoulos, E., Koopmans, L. V. E., & Rusin, D. 2002, *ApJ*, 581, 823
- Fassnacht, C. D., Koopmans, L. V. E., & Wong, K. C. 2011, *MNRAS*, 410, 2167
- Ferreras, I., Saha, P., & Burles, S. 2008, *MNRAS*, 383, 857
- Freedman, W. L., & Madore, B. F. 2010, *ARA&A*, 48, 673
- Frieman, J. A., Turner, M. S., & Huterer, D. 2008, *ARA&A*, 46, 385
- Gillon, M., Magain, P., Chantry, V., et al. 2007a, in *Transiting Extrapolar Planets Workshop*, ed. C. Afonso, D. Wel Drake, & T. Henning, *ASP Conf. Ser.*, 366, 113
- Gillon, M., Pont, F., Moutou, C., et al. 2007b, *A&A*, 466, 743
- Goicoechea, L. J. 2002, *MNRAS*, 334, 905
- Hernquist, L. 1990, *ApJ*, 356, 359
- Hu, W. 2005, in *Observing Dark Energy*, ed. S. C. Wolff & T. R. Lauer, *ASP Conf. Ser.*, 339, 215
- Keeton, C. 2004, *Gravlens 1.06*, Software for Gravitational Lensing: Handbook Version 9
- Kochanek, C. S., Morgan, N. D., Falco, E. E., et al. 2006, *ApJ*, 640, 47
- Koleva, M., Prugniel, P., & De Rijcke, S. 2008, *Astron. Nachr.*, 329, 968
- Koleva, M., Prugniel, P., Bouchard, A., & Wu, Y. 2009, *A&A*, 501, 1269
- Koopmans, L. V. E., & Treu, T. 2002, *ApJ*, 568, L5
- Koopmans, L. V. E., Bolton, A., Treu, T., et al. 2009, *ApJ*, 703, L51
- Krist, J., & Hook, R. 2004, *The Tiny Tim User's Guide Version 6.3*
- Kroupa, P. 2001, *MNRAS*, 322, 231
- Le Borgne, D., Rocca-Volmerange, B., Prugniel, P., et al. 2004, *A&A*, 425, 881
- Letawe, Y., Magain, P., Letawe, G., Courbin, F., & Hutsemékers, D. 2008, *ApJ*, 679, 967
- Magain, P., Courbin, F., & Sohy, S. 1998, *ApJ*, 494, 472
- Magain, P., Courbin, F., Gillon, M., et al. 2007, *A&A*, 461, 373
- Momcheva, I. G. 2009, Ph.D. Thesis, The University of Arizona
- Morgan, N. D., Kochanek, C. S., Pevunova, O., & Schechter, P. L. 2005, *AJ*, 129, 2531
- Mosquera, A. M., Muñoz, J. A., Mediavilla, E., & Kochanek, C. S. 2011, *ApJ*, 728, 145
- Navarro, J. F., Frenk, C. S., & White, S. D. M. 1996, *ApJ*, 462, 563
- Pelt, J., Kayser, R., Refsdal, S., & Schramm, T. 1996, *A&A*, 305, 97
- Prugniel, P., & Soubiran, C. 2001, *A&A*, 369, 1048
- Prugniel, P., Soubiran, C., Koleva, M., & Le Borgne, D. 2007 [[arXiv:0703658](#)]
- Refsdal, S. 1964, *MNRAS*, 128, 307
- Riess, A. G., Macri, L., Casertano, S., et al. 2009, *ApJ*, 699, 539
- Riess, A. G., Macri, L., Casertano, S., et al. 2011, *ApJ*, 730, 119
- Salpeter, E. E. 1955, *ApJ*, 121, 161
- Schlegel, D. J., Finkbeiner, D. P., & Davis, M. 1998, *ApJ*, 500, 525
- Suyu, S. H., Marshall, P. J., Blandford, R. D., et al. 2009, *ApJ*, 691, 277
- Suyu, S. H., Marshall, P. J., Auger, M. W., et al. 2010, *ApJ*, 711, 201
- van Dokkum, P. G. 2001, *PASP*, 113, 1420
- Vuissoz, C., Courbin, F., Sluse, D., et al. 2007, *A&A*, 464, 845
- Vuissoz, C., Courbin, F., Sluse, D., et al. 2008, *A&A*, 488, 481
- Warren, S. J., & Dye, S. 2003, *ApJ*, 590, 673
- Wisotzki, L., Christlieb, N., Bade, N., et al. 2000, *A&A*, 358, 77
- Wisotzki, L., Schechter, P. L., Bradt, H. V., Heinmüller, J., & Reimers, D. 2002, *A&A*, 395, 17



### 3.2 Microlensing analysis of Q J0158–4325

The quasar Q J0158–4325 is lensed by a  $z = 0.317$  galaxy into two images, with an image separation of  $1''.22$ . A Hubble Space Telescope image is shown in Figure 3.9. Our light curves are displayed in Figure 3.10. Despite 8 years of monitoring, no correspondence of the variability patterns of the images A and B is seen. Yet, a simple lens model predicts a short delay, of only  $\Delta t_{AB} = -12.4$  day (Morgan et al. 2012). The variability in the light curves is apparently completely dominated by quasar microlensing, on both short and long time scales, and there is no hope to measure a delay from the present data.

However, this particularly strong and fast microlensing variability is interesting on its own. As illustrated in Section 1.2.3, microlensing is sensitive to the source size: the larger the source, the smoother the quasar microlensing variability. In Morgan et al. (2012), the microlensing variability of Q J0158–4325 is analyzed by the bayesian Monte Carlo technique of Kochanek (2004). This method is based on randomly simulating a large number of microlensing magnification curves, trying to reproduce the observed data. The parameter space is large, as the microlensing curves depend on perfectly unknown parameters such as the spatial configuration of lens stars, the effective velocity of their bulk motion, the stellar mass fraction of the lens galaxy (“how many microlenses”), the microlens mass, and of course the source size. Exploring this parameter space in order to fit our 8 year long curves is extremely CPU-costly: in total  $2.4 \cdot 10^{11}$  trial light curves were drawn by Morgan et al. (2012). The resulting inference on the source size is shown in Figure 3.11, in which the latter is parametrized by a scale radius  $r_s$  of an assumed surface brightness profile of the quasar. The size of the quasar, at optical wavelengths, is found to be of the order of  $5 \cdot 10^{15}$  cm  $\approx 2$  light days. Our optical light curves complement a 6-epoch monitoring with the Chandra X-ray Observatory. From the combined analysis, constraints on the size of the X-ray emitting region of the quasar could also be obtained.

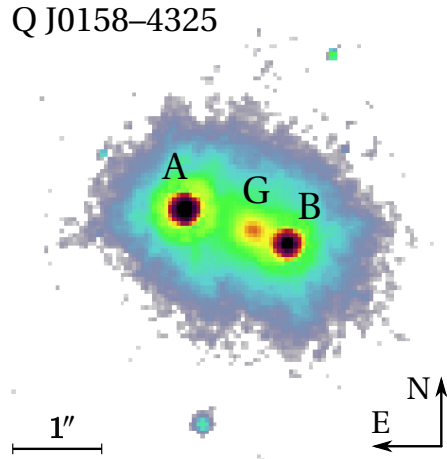


Figure 3.9: HST *I*-band Image of Q J0158–4325. Color encodes brightness (black is brightest). Image from the CASTLES survey, PI: C. S. Kochanek, <http://www.cfa.harvard.edu/castles/>

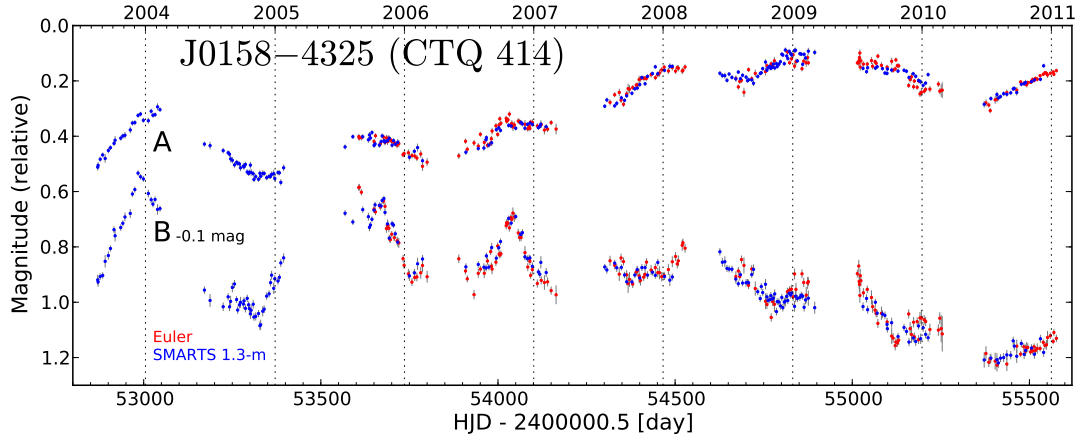


Figure 3.10: Light curves of the double J0158-4325 ( $z_{\text{lens}} = 0.317$ ,  $z_{\text{QSO}} = 1.26$ ), that we published in Morgan et al. (2012).

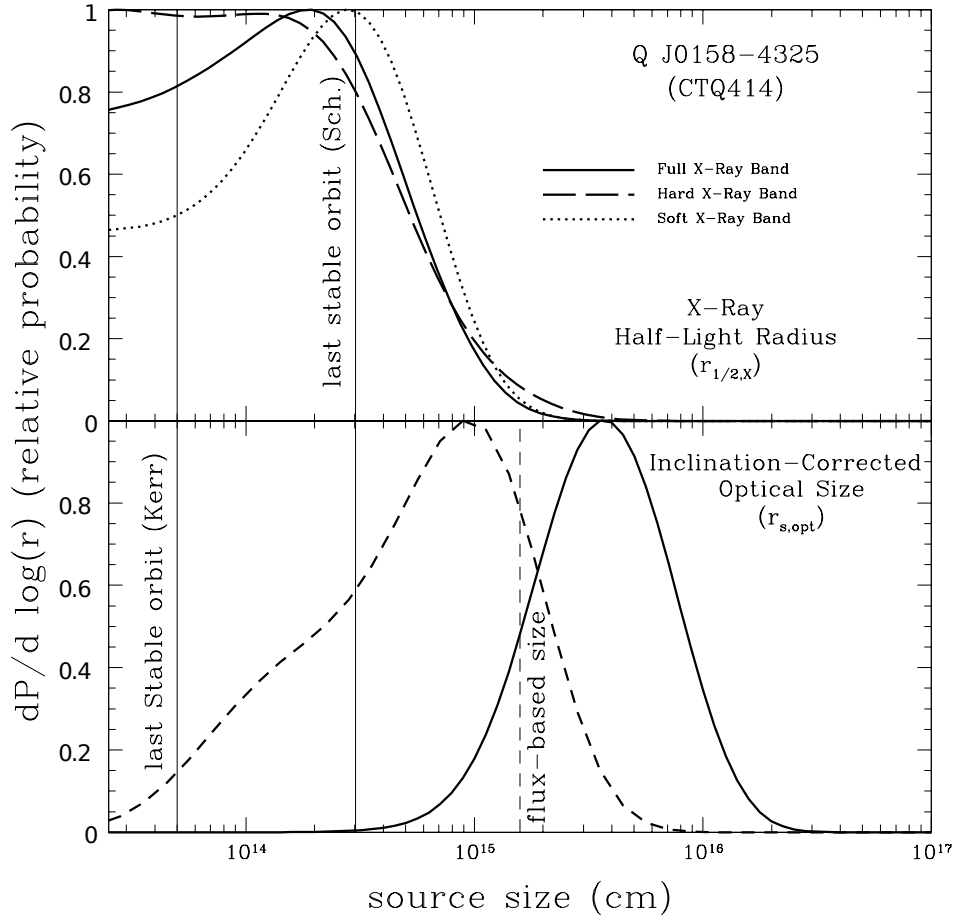


Figure 3.11: Probability distribution of the X-ray (top) and optical (bottom) size of the quasar J0158-4325, from Morgan et al. (2012). The solid curve in the bottom panel shows the estimate for the scale radius  $r_s$  in the optical ( $\lambda_{\text{rest}} \sim 3100 \text{ \AA}$ ) from the analysis of the light curves shown in Figure 3.10.

## 4 Cosmic shear measurement

### 4.1 Introduction

In this chapter we leave the subject of strong lensing and time delays, and focus on another way to constrain cosmology with gravitational lensing. *Cosmic shear* designates small apparent distortions of galaxies that are due to *weak* gravitational lensing (Figure 1.8 on page 19) by the largest structures in our Universe.

Independent observations such as galaxy redshift surveys have shown that the baryonic matter density of the Universe is not homogeneous on scales below a few hundred Mpc. Galaxies and galaxy clusters are distributed along filaments separated by voids, forming a foamy “cosmic web” (see Figure 1.1 on page 4 of this thesis). According to concordance cosmology, these structures should be largely dominated by dark matter; the observed galaxies reveal only a possibly biased part of the total picture. Weak gravitational lensing, which does not differentiate between baryonic and dark matter, is therefore a unique tool to map these structures at low redshift and learn about dark matter. It even allows us to probe the *evolution* of the statistical properties of these structures over cosmic time, thereby also constraining dark energy. For a review of this powerful cosmological probe see, e.g., Huterer (2010).

It remains to harness the observational effect. Weak lensing is literally too weak to be discernible on individual background sources. In the case of cosmic shear, that is shear measured on “random” areas of the sky and not only in proximity of galaxy clusters, the distortions are at best of the order of 1%. As every galaxy has an individual intrinsic shape and orientation, we cannot tell if and how a particular galaxy got sheared. An appealing way to reveal the shear induced by galaxy clusters is to locally average the apparent orientations of many background galaxies. Random intrinsic galaxy alignments will tend to cancel out, and the resulting average orientations will tangentially encircle mass over-densities. From such shear field measurements, the mass density can be partially reconstructed, as illustrated in Figure 4.1. Another approach, more suited to the delicate cosmic shear, is to analyze its imprint on *statistical* properties of the observed galaxy shapes, such as two-point correlation functions or power spectra. These functions quantify the size of the fluctuations in the shear field as a function of angular scale. Exploiting such statistics, the first detections of cosmic shear by several independent groups succeeded in 2000 (see Refregier 2003, for a review). Statistical shear measures can be related to the three dimensional power spectrum of matter density fluctuations,

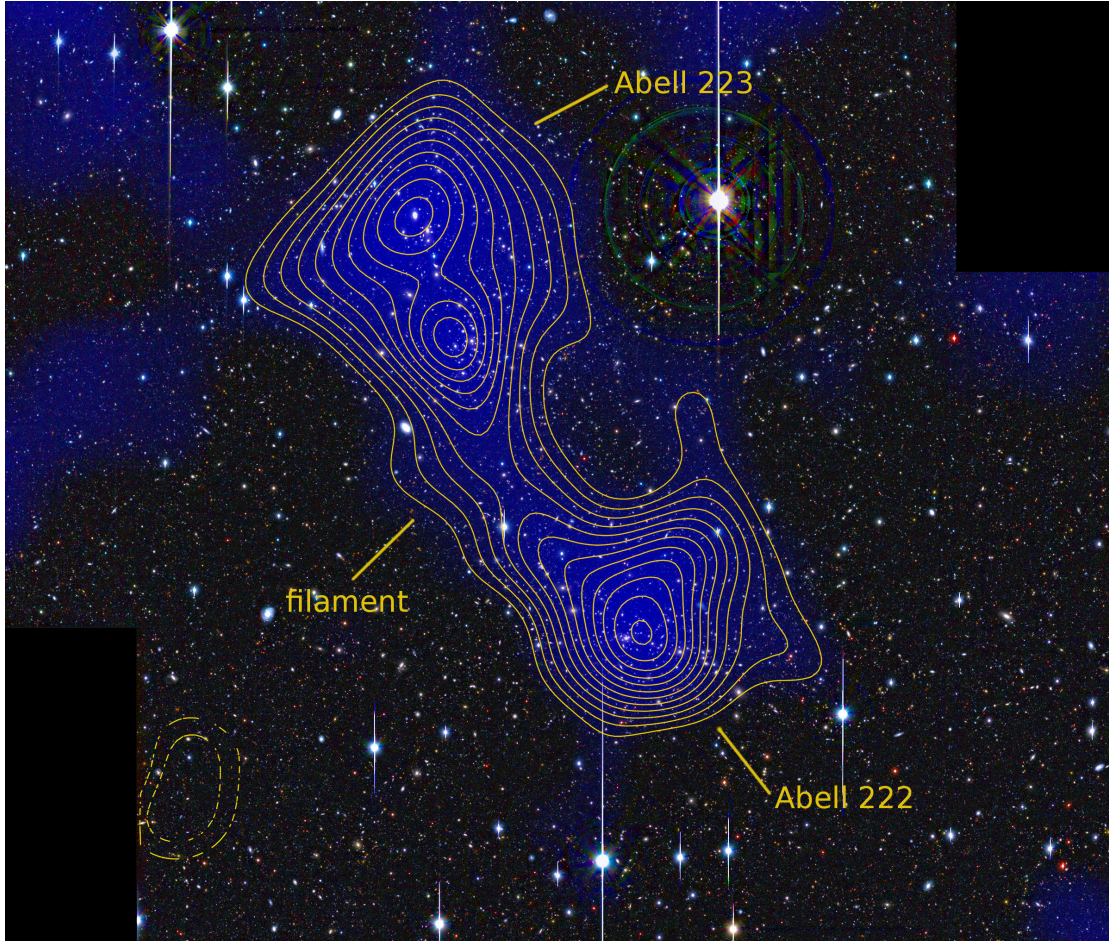


Figure 4.1: Detection of a dark-matter filament connecting two galaxy clusters, by Dietrich et al. (2012). Blue shades indicate the surface mass density as reconstructed from the weak lensing distortions of more than 40,000 background galaxies. The continuous (dashed) contours give the significance of the over-density (under-density) starting at  $2.5\sigma$  in steps of  $0.5\sigma$ . It is likely that this filament is rather perpendicular to the celestial sphere, and hence longer than it appears. By comparing these results with X-ray observations, the authors show that hot intergalactic plasma accounts for at most 10% of the mass of the filament; it is mainly made of dark matter. Image credit : Jörg Dietrich, University of Michigan / University Observatory Munich.

which in turn directly depends on cosmological parameters. They probe matter density and structure formation. Schneider et al. (2006) gives a thorough introduction to the observational techniques of weak lensing and to cosmic shear interpretation.

The first step of all these shear studies is to accurately measure the shapes of numerous – and thus faint – background galaxies, as distorted by weak lensing, over wide areas of the sky. The difficulty of this task is illustrated in Figure 4.2 : ground-based observations are degraded by atmospheric turbulence, diffraction of telescope optics, and noise. While space-based telescopes avoid the atmosphere, the complications remain very similar. First, the



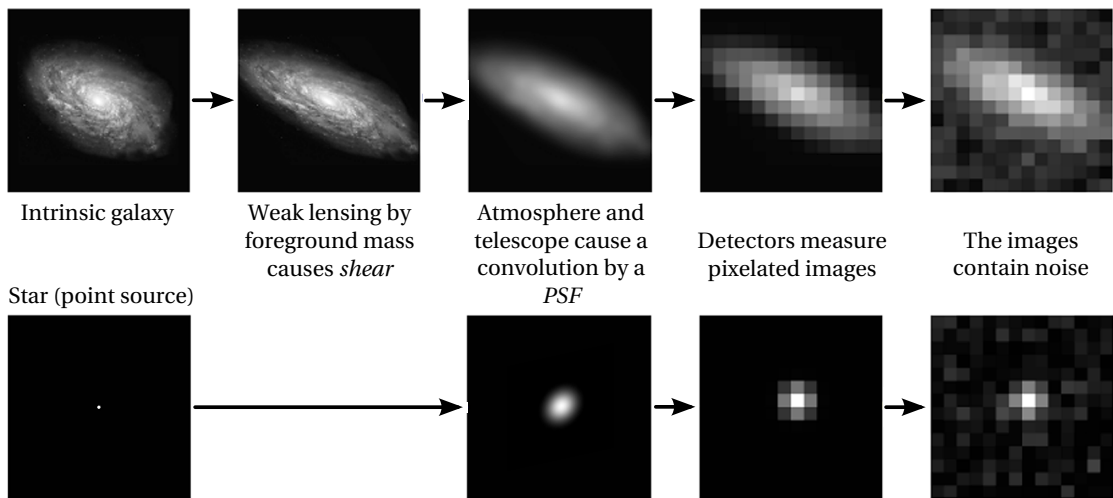


Figure 4.2: The “forward process” leading to the imaging data used in shear studies. This chapter describes a method to reconstruct shape properties of the *sheared* galaxies (second panel of the top row) from images of observed galaxies and stars (rightmost panels). In this visualization, the amplitude of the distortion by cosmic shear is exaggerated by a factor 10. Also note that for real ground-based data the size of the PSF is roughly comparable to the size of the observed galaxies. Illustration adapted from the GREAT08 handbook (Bridle et al. 2009).

Point Spread Function (PSF) that characterizes the smearing of the image (central panels of Figure 4.2) introduces anisotropies (e.g. ellipticity) that are typically several times larger than the distortions by cosmic shear. The PSF significantly varies across the field of view of telescopes. Even when using telescopes designed for optimal image quality, the PSF smearing has to be corrected for in order to reveal any shear signal. Second, the pixelation and *noise* of the images, as well as the simple isotropic component of the PSF, introduce both random scatter and bias in the measured shape properties of small and faint galaxies. Refregier et al. (2012) have recently illustrated the so-called *noise bias* using a didactic toy model. They draw simple 2D Gaussians on a pixel grid, add some noise, and fit those images with Gaussian profiles, leaving only the width of the profile as a free parameter. Despite this idealized situation in which the true “galaxy profile” is perfectly known, the resulting biases are comparable in magnitude to typical shear signals, and thus far too high to be neglected.

The paper at the end of this chapter (Tewes et al. 2012a) presents a novel technique, *MegaLUT*, to correct galaxy shape measurements for PSF smearing, pixelation, and noise in one single step. Our involvement in this subject was directly motivated by the GREAT10 galaxy challenge, a data analysis challenge organized in the form of a competition, and presented in the next section. To our knowledge, MegaLUT is the first technique that performs the shape measurement correction entirely using *supervised machine learning*. The idea is straightforward : by analyzing shape measurement biases on a large sample of simulated yet realistic galaxies with known “true” shape, one can learn how to empirically correct for these biases when facing real data. Machine learning has been applied so far only to correct for residual errors of techniques that try to analytically compensate for the smearing by the PSF. In contrast, our approach is to directly ask the “machine” to correct measured shape parameters of a galaxy, given observed images of the galaxy and a PSF-star. Our elementary implementation of such a machine –

namely a simple look-up table (LUT) – turns out to be competitive with the best alternative techniques applied to GREAT10, at a fraction of their computational cost.

### 4.2 The GREAT10 data analysis challenge

GRavitational lEnsing Accuracy Testing 2010 (GREAT10) (Kitching et al. 2011, 2012) is a data analysis challenge that was held for 9 months between December 2010 and September 2011. GREAT10 stands in a row with similar public weak lensing challenges<sup>1</sup>. Aside of comparing and improving existing shear measurement techniques, the aim of such well-defined and documented competitions is also to open up this problem to experts of image processing, computer science, and statistics not necessarily involved in astrophysical research. The simple formulation of the shear measurement problem makes it well suited for such blind analysis challenges based on simulated data.

The GREAT10 challenge consists of reconstructing at best different shear power spectra, “hidden” by the organizers in simulated images of 50 million PSF-convolved and noisy galaxies. The simulated PSF was a ground-based PSF, and it was given to the participants, for the position of each galaxy, both as a single noisy star and in exact analytic form. Figure 4.3 displays a few galaxies and associated PSF stars from different signal-to-noise ratio (S/N) categories of the challenge data.

The random intrinsic orientations of the galaxies were cleverly drawn<sup>2</sup> so that pure shear power spectra can be extracted directly from the estimated *sheared ellipticities* of the galaxies, i.e., the ellipticities that the galaxies had prior to their convolution by the PSF. Participants to the challenge could either submit a catalog of these sheared ellipticities (one for each galaxy), or directly submit shear power spectra. The latter case opened the possibility to empirically tweak the measured power spectra before submission. In this perspective, the true shear power spectrum was disclosed for a small training-subset of the full data. For the application of our MegaLUT technique to GREAT10, we decided to focus on the conditions of a real cosmic shear survey, and did not exploit any information of the analytic PSF or the shear power spectrum of this training set. MegaLUT processes each galaxy individually, disregarding its spatial location.

All submissions to GREAT10 are evaluated using 10 evaluation metrics, described in detail in the GREAT10 results paper (Kitching et al. 2012). The most important of these metrics are directly linked to the quality of a cosmological inference from cosmic shear. They quantify the comparison between the true and the reconstructed shear power spectra, as shown respectively in green and red in Fig. 6 of our paper at the end of this chapter. The simulated shear power spectra are roughly linear in the covered range of multipole moments ( $l = 10^2$  corresponds to angular scales of about  $1^\circ$ ,  $l = 10^3 \sim 10^4$ ). To probe the ability of the techniques to reconstruct these shear power spectra without any model assumptions, a random polynomial was added to the power spectrum of each data subset. These perturbations can be seen as

---

<sup>1</sup><http://www.greatchallenges.info>

<sup>2</sup>The intrinsic ellipticity correlation function contains *only* B-mode power. The analysis focused on the E-mode of the shear, as gravitational lensing does not produce B-mode patterns. This effectively decouples the shear signal from the intrinsic galaxy orientations.



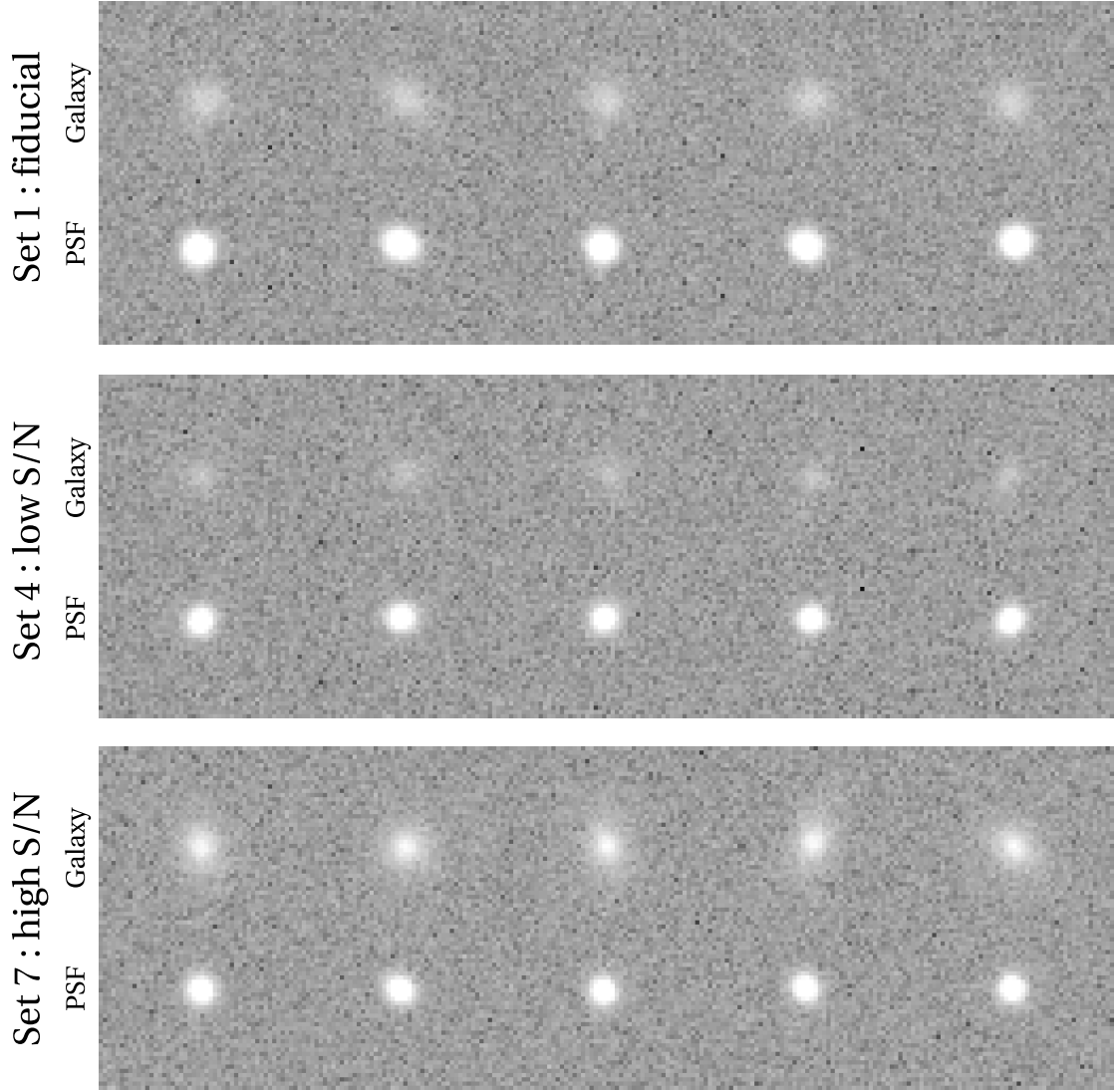


Figure 4.3: 15 out of 50 million GREAT10 galaxies (top) and corresponding PSF stars (bottom), from 3 different “sets” of the challenge data. All stamps are shown with the same logarithmic intensity scale.

kinks in the true power spectra shown in Fig. 6 of our paper. To reduce biases in cosmological inferences, shear measurement techniques should reconstruct these perturbations at best. Scalar metrics which measure the match of these power spectra are briefly introduced below.

- The “quality factor”  $Q$  is the most prominent GREAT10-metric; it tries to assess the overall performance of a method.  $Q$  is inversely proportional to the area between the true and measured shear power spectra: higher  $Q$ -values are better. This quality factor was used to compare the methods on the online leaderboard during the challenge.
- $\mathcal{M}$ ,  $\mathcal{A}$  designate respectively multiplicative and additive biases of the reconstructed power spectra. Values closest to zero are better.

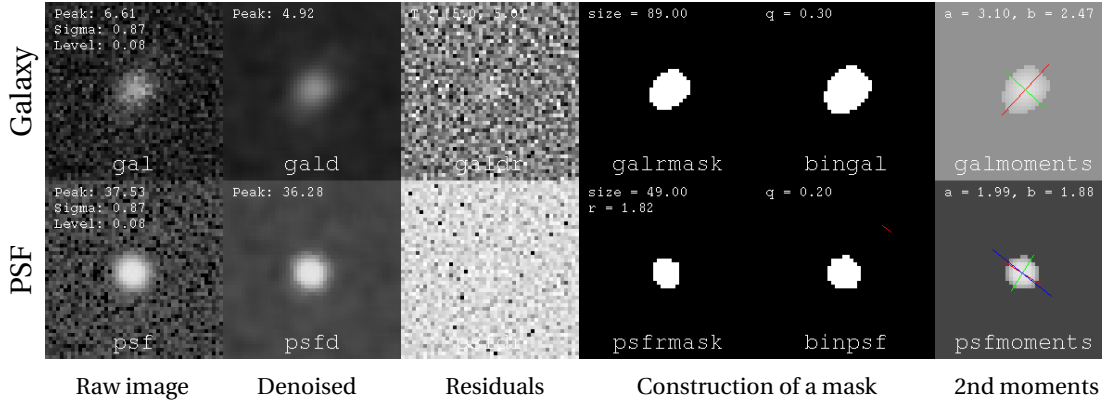


Figure 4.4: Control visualization of our first, modestly successful, attempt to implement a shape measurement for GREAT10 galaxies and PSF stars. The images are first strongly denoised, and the shapes are measured from the 2nd moments of denoised light distributions within masks. This shape measurement is referred to as “MMD”.

As illustrated in the inset of Fig. 6 of our paper, these metrics can also be evaluated individually for each of the 24 *sets* of the data, to study the behavior of a technique in different conditions covered by GREAT10. The spread of the  $\mathcal{M}$  and  $\mathcal{A}$  values evaluated per set is clearly also an indicator of the quality of a technique.

### 4.3 MegaLUT applied to GREAT10

The shape measurement part of MegaLUT can be seen as an interchangeable black box. We have considered two different choices in the scope of GREAT10.

In a first step, we experimented with our own simple shape measurement code, dubbed “MMD”. Its commonplace underlying principle is to measure the ellipticity and orientation of galaxies and stars by computing second moments of the light distributions. The key difficulty for any shape measurement algorithm is to minimize the sensitivity to image noise. To address this issue we made use of a wavelet-denoising method. The denoising can be rather strong, as MegaLUT will inherently correct for shape measurement biases. A summarizing screenshot of this MMD method is shown in Figure 4.4.

The second and much more successful variant completely outsources the shape measurement, by relying on the open *Source Extractor* package<sup>3</sup> (Bertin & Arnouts 1996). While Source Extractor is certainly one of the most widely used softwares in observational astrophysics, it is not renowned for shape measurement by the weak lensing community. Source Extractor focuses on efficient source detection and deblending, without any correction for PSF smearing or other biases. However, it *is* able to compute windowed second moments (“SEWIN”) that are rather robust against noise, even if these moments are highly biased – a perfect match for MegaLUT.

<sup>3</sup><http://www.astromatic.net/software/sextractor>

Table 4.1: Values of GREAT10 metrics achieved by the competing methods (based on Table 3 of Kitching et al. 2012).

Method	Approach	$Q$	$m$	$c/10^{-4}$	$\mathcal{M}/2$	$\sqrt{\mathcal{A}}/10^{-4}$
ARES 50/50	(DEIMOS + KSB)/2	105.80	-0.03	0.35	-0.0186	0.0728
cat7unfold2	“shapefit” & ML, PS	152.55	-	-	0.0214	0.0707
DEIMOS C6	Moments, analytic	56.69	0.01	0.08	0.0043	0.6329
fit2-unfold	“shapefit” & ML, PS	229.99	-	-	0.0408	0.0656
gfit	Model-fitting	50.11	0.01	0.29	0.0058	0.0573
im3shape	Model-fitting	82.33	-0.05	0.12	-0.0538	0.0945
KSB	Moments, analytic	97.22	-0.06	0.86	-0.0376	0.0872
KSB f90	Moments, analytic	49.12	-0.01	0.19	0.0208	0.0789
MegaLUT	MMD & ML	69.17	-0.27	-0.55	-0.1831	0.1311
MegaLUT	SEWIN & ML	104.14	-0.15	-0.06	0.0119	0.0819
method04	Moments, analytic	83.52	-0.17	-0.12	-0.0907	0.0969
NN23 func	Image deconvolution	83.16	-0.24	0.47	-0.0153	0.0982
shapefit	Model-fitting	39.09	0.11	0.17	0.0491	0.8686

The results achieved by those variants of MegaLUT and the other techniques competing in GREAT10 are presented in Table 4.1. The combination of MegaLUT and Source Extractor is shaded in gray. We developed this SEWIN variant only after the end of the GREAT10 competition, but its results were analyzed with the official analysis code by the principal investigator of GREAT10, Thomas Kitching. Our pure python implementation of MegaLUT is publicly available<sup>4</sup>, and our results are thus easily reproducible.

The second column of Table 4.1 gives reductive hints on how the different methods work. “ML” stands for Machine Learning, “analytic” designates an analytic correction for the anisotropy of the PSF, and “moments” identifies methods that use moments of the light distributions to measure the shapes, as do MMD and SEWIN. Importantly, “PS” indicates submissions of shear power spectra, instead of shape catalogs. The resulting possibility of additional empirical corrections to the power spectra was successfully exploited by the two methods that lead the competition in terms of the  $Q$  and won the challenge. More detailed descriptions of each method can be found in the GREAT10 results paper (Kitching et al. 2012).

Considering our conservative approach to not perform any corrections at the power spectrum level, the combination of MegaLUT with Source Extractor yields very competitive results. One highlight of our method is that it analyzed the entire GREAT10 data ( $\approx 1$  TB) in less than one day on a single desktop computer ( $< 3$  ms · CPU per galaxy). This is about 200 times faster than the winning entries fit2-unfold and cat7unfold2, which are limited in speed by their model-fitting algorithm.

<sup>4</sup><http://lastro.epfl.ch/megalut>, GPLv3 license

## 4.4 Outlook

In order to reduce statistical errors in the cosmological parameter inferences, large area shear surveys are required. Measuring shear statistics in only a small region of the sky yields biased results, due to *cosmic variance*: the large-scale structure is not isotropic, by definition. Figure 4.5 shows that, assuming perfectly unbiased shear measurements, it is truly the sky that limits the inference (see also Amara & Refregier 2007). A survey on the order of the full sky ( $41253 \text{ deg}^2$ ) is *needed* to reach an accuracy of 1% on the dark energy equation-of-state parameter. Keeping the systematic errors of measurement methods under control, so that they don't spoil this analysis, is the task of future GREAT-like challenges. On the observational front, planned weak lensing surveys will indeed cover a significant part of the entire sky.

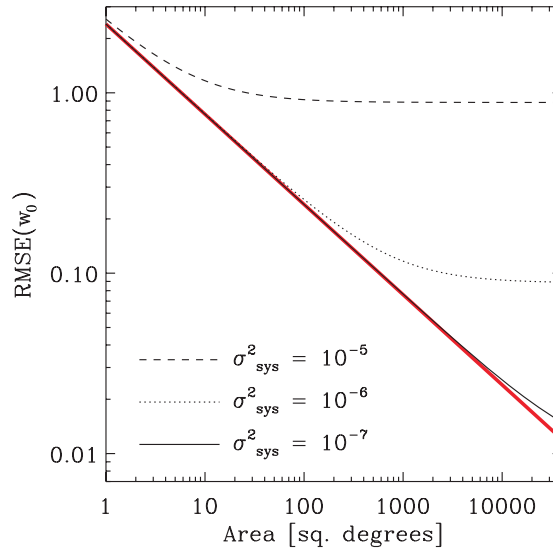


Figure 4.5: Accuracy on the dark energy equation of state parameter  $w_0$  as a function of area of a cosmic shear survey. The red line assumes no biases at all, while the black lines show different amplitudes of systematic errors in the shear power spectrum. Figure from Amara & Refregier (2008).

Cosmic shear is a main science goal for several future ground- and space-based surveys, such as the 8.4-m Large Synoptic Survey Telescope (LSST)<sup>5</sup> to be built in Chile, and ESA's *Euclid* space mission<sup>6</sup> scheduled for launch in 2020. *Euclid* will observe 1.5 *billion* ( $1.5 \cdot 10^9$ ) source galaxies, with typical redshifts around  $z = 1.0$ , by imaging roughly half the sky with a resolution below  $0''.2$  (*Euclid* Consortium 2011). These galaxies will be classified into several redshift bins to perform so-called weak lensing *tomography*, exploring the radial dimension of large scale structure. Considering this depth information, by means of photometric redshifts, further increases the cosmological constraining power of weak lensing.

This exciting perspective underlines the importance of not only accurate but also fast shear measurement techniques. Processing *Euclid*'s galaxies at a rate of one per second corresponds to 50 CPU years! MegaLUT's efficient combination of raw shape measurement and a pure

<sup>5</sup><http://www.lsst.org>

<sup>6</sup><http://www.euclid-ec.org>

machine learning correction for PSF and image noise certainly opens up an interesting path. Notably, a method like MegaLUT could also be used to quickly provide a set of initial conditions for further analyses. Especially the slow model-fitting techniques would benefit from good first-guess parameters. A meticulous source detection and measurement, as exploited by MegaLUT, will be done anyway on the imaging data of cosmic shear surveys.

The third GRavitational lEnsing Accuracy Testing challenge (GREAT3)<sup>7</sup>, supported by the European PASCAL2 Network of Excellence<sup>8</sup> and NASA/JPL<sup>9</sup>, will start in July 2013 for a period of 6 months. GREAT3 is a significant evolution of its predecessors. It makes use of a much more realistic image simulation software, notably involving real galaxy images, physically-motivated PSF models for ground- and space-based data, and multi-exposure imaging. We are looking forward to improving our empirical technique for this new edition. A simple 4-dimensional look-up table is obviously just a first step.

---

<sup>7</sup><http://www.great3challenge.info/>

<sup>8</sup><http://www.pascal-network.org/>

<sup>9</sup><http://www.jpl.nasa.gov/>





# A fast empirical method for galaxy shape measurements in weak lensing surveys

M. Tewes<sup>1</sup>, N. Cantale<sup>1</sup>, F. Courbin<sup>1</sup>, T. Kitching<sup>2</sup>, and G. Meylan<sup>1</sup>

<sup>1</sup> Laboratoire d'Astrophysique, École Polytechnique Fédérale de Lausanne (EPFL), Observatoire de Sauverny, 1290 Versoix, Switzerland  
e-mail: [malte.tewes@epfl.ch](mailto:malte.tewes@epfl.ch)

<sup>2</sup> SUPA, Institute for Astronomy, University of Edinburgh, Royal Observatory, Blackford Hill, Edinburgh, EH9 3HJ, UK

Received 26 March 2012 / Accepted 20 June 2012

## ABSTRACT

We describe a simple and fast method to correct ellipticity measurements of galaxies from the distortion by the instrumental and atmospheric point spread function (PSF), in view of weak lensing shear measurements. The method performs a classification of galaxies and associated PSFs according to measured shape parameters, and corrects the measured galaxy ellipticities by querying a large lookup table (LUT), built by supervised learning. We have applied this new method to the GREAT10 image analysis challenge, and present in this paper a refined solution that obtains the competitive quality factor of  $Q = 104$ , without any shear power spectrum denoising or training. Of particular interest is the efficiency of the method, with a processing time below 3 ms per galaxy on an ordinary CPU.

**Key words.** gravitational lensing: weak – methods: data analysis

## 1. Introduction

Gravitational lensing offers a means to map the distribution of matter over a broad range of spatial scales. In the strong regime, gravitational lensing gives rise to multiple images of distant sources. This allows both to study lensed sources in great details and to map the matter in the central parts of the lensing objects, either individual galaxies (e.g., Bolton et al. 2008; Faure et al. 2008; Courbin et al. 2012) or galaxy clusters (e.g., Coe et al. 2010; Shan et al. 2012). In the weak regime, only one image of the source galaxy is seen and its apparent distortion can only be measured statistically, by averaging the signal over many galaxies. This occurs either when the mass density in the lensing objects is too low, below the “critical density”, or when the sources are separated from the lenses in projection on the plane of the sky. Strong and weak lensing are sometimes combined e.g., to probe simultaneously the core and the large scale halo of galaxy clusters (e.g., Limousin et al. 2007).

On very large spatial scales, weak gravitational lensing is not caused anymore by mass along a specific line of sight, but rather by the combined gravitational fields of the large scale structures of the Universe. The signature of the lensing distortions, called *cosmic shear*, is best seen in this regime through its power spectrum or through its two-point correlation function across the whole sky. Since the first measurement of the effect (Maoli et al. 2001; Bacon et al. 2000; Kaiser et al. 2000; Van Waerbeke et al. 2000; Wittman et al. 2000), it was quickly realized that cosmic shear is a sensitive tool to measure indirectly some of the most important cosmological parameters, including the dark energy equation of state parameter and its evolution with redshift (Hu 1999). Several ground-based wide field surveys to measure cosmic shear with unprecedented accuracy are under way or

under study (e.g., Pan-STARRS<sup>1</sup>, DES<sup>2</sup>, Subaru HSC<sup>3</sup>, LSST<sup>4</sup>). Euclid<sup>5</sup>, a space mission currently being implemented by ESA, will image at least 15 000 square degrees of space with one of the main science objectives being the measurement of cosmic shear (see, e.g., Laureijs et al. 2011).

All the applications of gravitational shear, whether they be about galaxy and cluster halos or about dark energy, require the measurement of shapes of numerous and faint distant galaxies with optimal precision and without any significant systematic bias. Euclid will observe about 1.5 billion galaxies to achieve its scientific goal. However, any telescope produces images that are limited either by diffraction, by the Earth's atmosphere, or by both effects. The algorithms that will be used to measure galaxy shapes must correct for this smearing, characterized by the point spread function (PSF) of the entire image acquisition process. A considerable amount of work has been devoted so far to tackle this problem. Among the most popular approaches is the “KSB” family of methods (Kaiser et al. 1995), based on the measurement of the second order moments of the light distribution of galaxies. In these methods, the correction for the smearing by the PSF is done analytically. Many different implementations and improvements of KSB are currently in use. Other algorithms consider a fit of an analytical model to the galaxies (e.g., Miller et al. 2007; Kitching et al. 2008) or decompose them on an orthogonal basis of vectors called “shapelets” (Kuijken 2006; Refregier 2003; Refregier & Bacon 2003).

<sup>1</sup> <http://pan-starrs.ifa.hawaii.edu>

<sup>2</sup> <http://www.darkenergysurvey.org>

<sup>3</sup> <http://www.naoj.org/Projects/HSC/>

<sup>4</sup> <http://www.lsst.org>

<sup>5</sup> <http://www.euclid-ec.org>

Even if the PSF is properly accounted for, galaxy shape measurements, as well as the resulting shear measurements, are possibly biased by the presence of noise in the images (see e.g. Refregier et al. 2012; Melchior & Viola 2012). It is likely that, given the complexity of galaxy shapes, this “noise bias” will have to be addressed by an empirical calibration using synthetic data (Kacprzak et al. 2012). Such calibrations can be performed at the topmost level of the shear measurement (i.e., the recovered shear itself), or at the lower levels of the shape measurements (i.e., correcting every galaxy measurement). Recently, Gruen et al. (2010) introduced a promising method based on training a neural network to correct for the bias at the level of each individual galaxy. We propose in the present work an algorithm in line with the work of Gruen et al. (2010), but we apply a simple machine learning approach directly to the PSF removal problem instead of correcting for the residual bias of an existing PSF removal method. This potentially yields unbiased galaxy shapes, which is the primary goal of this work. However, as emphasized by Melchior & Viola (2012), also the *variance* of shape estimates leads to a bias on the shear measurement. We show in this paper that our method is competitive even without any specific calibration of this noise bias at the level of the shear power spectrum.

The article is structured as follows: the principles of our method are described in Sect. 2. Section 3 describes an application to the simulated data of the GRavitational Lensing Accuracy Testing 2010 (GREAT10) challenge (Kitching et al. 2011), illustrating how our method can be combined with existing shape measurement techniques. The results achieved on GREAT10 are presented in Sect. 4, while limitations and possible extensions to our method are discussed in Sect. 5. Lastly, Sect. 6 summarizes our conclusions.

## 2. Description of MegaLUT

This paper proposes a conceptually simple, empirical, and fast method to correct ellipticity measurements of galaxies for the distortion by the instrumental and atmospheric PSF. The central idea of the method is to perform a classification of galaxy-PSF pairs with respect to their measured shape parameters, i.e., the parameters characterizing both the galaxy and its PSF. For each of these classes, an ellipticity correction is estimated to remove the effect of PSF smearing. These corrections are obtained by supervised learning and written into a large but tractable lookup table (LUT), hence the name *MegaLUT*. With this approach, the problem of correcting galaxy shapes for the convolution by the PSF is reduced to a simple array indexing operation.

The goal of MegaLUT is to describe at best the ellipticities of individual galaxies prior to the convolution by the PSF. We do not consider here the additional problem of extracting the shear due to gravitational lensing. Depending on the applications, the gravitational shear signal may be derived either by computing the power spectrum of the measured galaxy shapes, or by averaging the latter locally over small regions of the sky. We stress that MegaLUT, implemented as described below, aims at recovering ellipticities only, neglecting any shape parameter not used for shear studies.

In the following, we will refer to *observed* galaxy shapes when dealing with the shape of galaxies convolved by their PSF, as recorded on a detector. Note that these observed galaxies can be either real or simulated. In addition, we refer to *sheared* galaxy shapes when dealing with the shape galaxies had prior to convolution by the atmospheric and instrumental PSF.

These *sheared* galaxy shapes, and in particular the sheared ellipticities are what we are after. To recover them from the observed galaxy shapes, the proposed method needs some knowledge of the PSF either as a parametric model (e.g., Moffat, Gaussian or other more sophisticated profiles), or as a decomposition on a basis of vectors (e.g., Shapelets, Zernike or Hermite polynomials), or simply as an array of pixels, i.e., a sampled image of a star or a stack of stars. We assume that the PSF has already been estimated at best at the position of each galaxy in the survey, i.e., PSF interpolation is considered as a separate/solved problem. The way galaxies and PSFs are represented need not be the same, as long as the same representations are adopted for the real and the synthetic learning data.

Through this paper, we will use the notion of *complex ellipticity*, common to shear studies, as defined in the GREAT10 challenge (Kitching et al. 2011). This complex ellipticity,  $e$ , is linked to the *elongation*  $\epsilon$  and position angle  $\theta$  of the objects, where  $\epsilon = a/b$ , and  $a$  and  $b$  are respectively the semi-major and semi-minor axis of the light distribution isophotes:

$$e = \frac{\epsilon - 1}{\epsilon + 1} e^{i2\theta} \quad (1)$$

$$= |\epsilon| [\cos(2\theta) + i \sin(2\theta)] \quad (2)$$

$$= e_1 + i e_2. \quad (3)$$

The factor 2 in the angular argument reflects shape invariance under rotation by  $180^\circ$ . Complex ellipticity does *not* encode the apparent size of an object.

Keeping the above in mind, MegaLUT consists of three steps: (1) generating a learning sample of simulated data; (2) building the lookup table (LUT) from this simulated data; (3) querying the LUT to recover the sheared galaxy shapes of the real data, i.e., the shapes of the (lensed) galaxies as they were before convolution by the PSF.

### 2.1. Step 1: generating the learning sample

The first step is to build a learning sample of observed galaxies with *known* sheared complex ellipticities  $e_{\text{Sheared}}$ , and randomly associating a PSF to each of these galaxies. Properties like pixel size, noise characteristics, galaxy morphology and PSF profiles of this learning sample should be as close as possible to the data to be analysed. To build such a learning sample, where observed galaxies and PSFs are in the form of pixelized images, we adopt the following procedure:

1. Draw artificial sheared (i.e., weakly lensed) galaxies, and associated PSFs, on a fine pixel grid. The adopted pixel sampling for the artificial images should simply be chosen fine enough so that it does not influence the results, given the required precision. For each galaxy, store the sheared ellipticity  $e_{\text{Sheared}}$ . For both the galaxies and the PSFs, randomly sample a broad range of radial profiles, apparent sizes, fluxes, ellipticities and orientations. This sampling can very well be uniform as long as it covers the full parameter space for real galaxies and PSFs.
2. Numerically convolve the galaxies with their associated PSFs.
3. Downsample the convolved galaxies and PSFs to match the pixel size of the real data.
4. Add realistic noise to the simulated images. The properties of the noise can easily be chosen to match that of the real data and may even include subtleties like cosmic rays and charge transfer inefficiency. In the present implementation the latter two effects are left out.

We now measure these simulated *observed* galaxies with any given shape measurement algorithm, leading to a set of parameters, such as size, ellipticity, position angle and flux. The shape measurement algorithm can be seen as a black box; it should be precise, but not necessarily accurate, i.e., it should be as insensitive as possible to noise, while systematic biases in the measurements are acceptable. Those biases will be inherently cancelled by the method. We do the same with the simulated PSFs, leading to a set of associated PSF shape parameters. Note that the shape measurement algorithms applied to the galaxies and to the PSF need not be the same.

At this point, the learning sample consists of an unordered collection of measured galaxy and PSF shape parameters, associated to the known underlying *sheared* galaxy ellipticities.

## 2.2. Step 2: building the LUT

Next, we classify the galaxies from the learning sample according to these measured shape parameters. A given galaxy can be seen as a point in a multidimensional space, each dimension corresponding to one parameter, e.g., size, ellipticity, position angle and flux of the galaxy, as well as size, ellipticity and position angle of the PSF. Some of these observed parameters are clearly degenerate with respect to the sheared ellipticities. For example, the absolute sizes of the galaxy and the PSF are not required to recover the sheared ellipticity. What matters is the relative size of the galaxy with respect to the PSF. Following a similar theoretical argumentation, the measured fluxes of the sources seem a priori irrelevant. Note that in practice, the flux – or signal-to-noise ratio S/N – of the galaxies and PSF stars could well be important, as it might bias the other measured shape parameters. For the specific application of MegaLUT described in this paper, we made use of a shape measurement whose biases do not significantly depend on the S/N within the considered range, as we will show in Sect. 3.2.3. Therefore, we do indeed disregard the fluxes in the following.

Similarly, the PSF smearing should be invariant with respect to rotation on the plane of the sky<sup>6</sup>. Hence, only the relative orientation between the PSF and the galaxy influences the correction for the PSF smearing.

Both to accommodate for the parameter degeneracies and to minimize the dimensionality of the LUT, we reduce the parameter space to the following set of four less degenerate continuous *coordinates*:

- $\epsilon_{\text{Gal}}$ : the elongation of the galaxy;
- $\epsilon_{\text{PSF}}$ : the elongation of the associated PSF;
- $r$ : the size ratio between the galaxy and its associated PSF;
- $\Delta\theta$ : the relative orientation of the PSF with respect to the galaxy.

Each galaxy can now be represented as a point in this four-dimensional space. The classification consists of dividing this space into numerous hyperrectangles (“4-orthotopes” in mathematical terms), that we call here *cells*. This is easily done by individually splitting the full range of observed values of each of the above coordinates into a finite number of bins. The coordinates of any galaxy can then be univocally associated to a corresponding cell.

Computationally, the four discretization functions that relate the continuous coordinate values to four indexes that identify a

cell can be kept short and very fast. They consist mainly of a rounding operation. We have explored the situation in which all the cells have the same size, i.e. the binning of the coordinates is regular. While this is the simplest choice, it is by no means a required condition.

Finally, to build the LUT, we distribute all galaxies of the learning sample among the corresponding cells. In each cell, the differences between the known *sheared* and the measured *observed* complex ellipticities  $e^{\text{Sheared}} - e_{\text{Obs}}$  give an estimation for a simple additive correction to undo the smearing by the PSF. But the galaxies in a cell, and hence also these differences, have random position angles on the sky. To obtain complex ellipticity corrections that are rotation invariant we express their orientations with respect to the measured orientation of the galaxy. In mathematical terms, this corresponds to computing:

$$\delta e := \frac{e^{\text{Sheared}} - e_{\text{Obs}}}{e_{\text{Obs}}/|e_{\text{Obs}}|} \quad \text{with } \delta e, e^{\text{Sheared}}, e_{\text{Obs}} \in \mathbb{C} \quad (4)$$

for each simulated galaxy. These  $\delta e$  can now be averaged within each cell. The LUT, as it will be used in the next step, thus consists of a multidimensional array of complex ellipticity corrections  $\langle \delta e \rangle$ . The standard deviation of the  $\delta e$  within each cell can be used to express the uncertainty of these corrections.

## 2.3. Step 3: querying the LUT for real galaxies

For each galaxy and PSF pair *in the real data*, we measure the observed shape parameters using the exact same black box as applied on the learning sample. Hence any systematic errors inherent to the shape measurement are cancelled. The measured parameters are transformed into coordinates, and the coordinates are discretized into integer indexes of the LUT, again by the exact same simple functions that were used to build the LUT. Through a simple array indexing operation, the complex ellipticity correction  $\langle \delta e \rangle$  can thus be directly read from the LUT. Finally, we obtain the estimation of the sheared ellipticity by applying the correction to the observed galaxy shape:

$$\hat{e}^{\text{Sheared}} = e_{\text{Obs}} + \langle \delta e \rangle \cdot \frac{e_{\text{Obs}}}{|e_{\text{Obs}}|}, \quad (5)$$

where the multiplication by  $e_{\text{Obs}}/|e_{\text{Obs}}|$  corresponds to a rotation of the correction by the measured orientation of the galaxy.

In the scope of cosmic shear surveys, the recovery of the sheared ellipticity has to be done for billions of galaxies, hence the simplicity and computational speed of this LUT query are crucial. Figure 1 summarizes the procedure.

## 3. Implementation for the GREAT10 challenge data

We applied MegaLUT to the GREAT10 Galaxy Challenge, described in detail in the handbook and results papers (Kitching et al. 2011, 2012). The challenge consists of recovering the shear power spectrum by measuring the sheared ellipticities of 50 million simulated noisy galaxies placed on a rectangular grid. The shape of the PSF is variable across the field of view, but it is provided, at the position of each galaxy, both as a noisy pixelized stamp and under exact analytical form. For our implementation of MegaLUT, we have exclusively used the noisy PSF images.

In this section, we describe how we generated the learning sample for MegaLUT, and how we improved on the shape measurement since the end of the GREAT10 challenge.

<sup>6</sup> We neglect in this first approach possible rotation-dependent effects due to finite and square stamp size, pixel sampling, or charge transfer inefficiency.



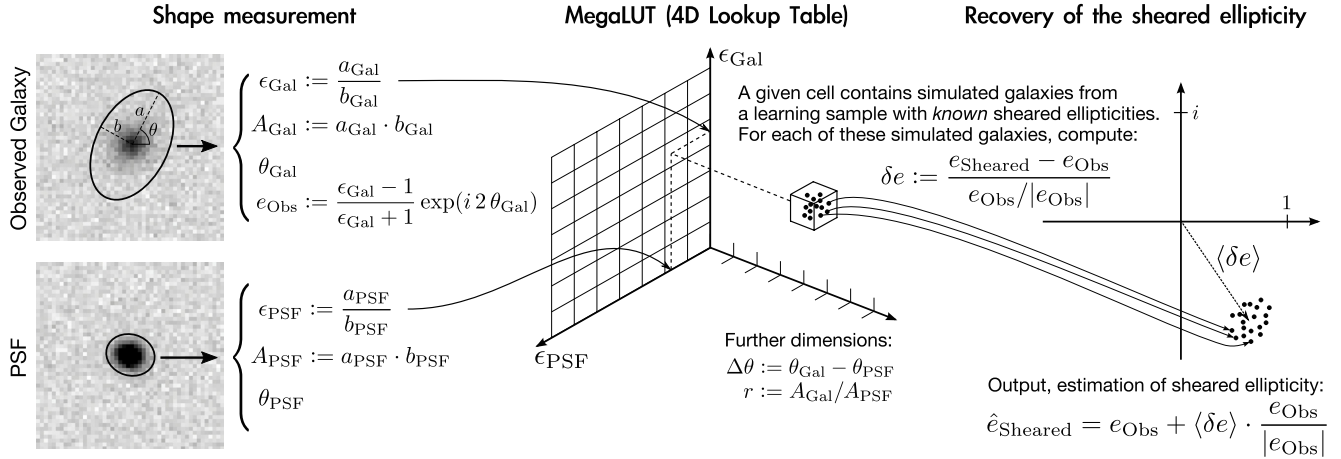


**Fig. 1.** Structure of a MegaLUT query to recover the *sheared* ellipticity, that is the ellipticity the galaxy had prior to the PSF convolution, from the observed shapes of the galaxy and the PSF. The shape measurement requires most of the computational time; it should be as precise as possible, but does not need to be *accurate*, as MegaLUT cancels any biases in the coordinates.

### 3.1. Generation of the learning sample

The GREAT10 Coordination Team has simulated the galaxy images to be analysed by superposing two exponential profiles of the form  $\exp(-kR^{1/n})$ , namely a disk ( $n = 4$ ) and a bulge ( $n = 1$ ), that may be misaligned with respect to each other. Then, before convolving them by the PSF, the shear signal was introduced by explicitly applying a distortion to the galaxy images (Kitching et al. 2011).

To build our learning sample, we have chosen to *directly* draw sheared galaxies using a single elliptical exponential profile with  $n = 1.5$ . Doing so we keep the generation of our learning sample as simple as possible, and show that a detailed knowledge of the GREAT10 simulation details is not required by our method. Furthermore, this simplification unambiguously links the true sheared ellipticities of our learning sample galaxies to their analytical form.

For the PSF, we use Moffat profiles with  $\beta = 3$ , i.e., the same profile that was used to generate the PSFs of GREAT10.

Before drawing the stamps for the learning set, we need to determine the ranges of sheared galaxy and PSF sizes and ellipticities so that the resulting measured shape parameters, and thus the 4 coordinates of MegaLUT as described in Sect. 2.2, cover the values required to process the GREAT10 data. In practice, we therefore first run a shape measurement algorithm on the GREAT10 data, and then empirically adjust the input parameter ranges of the learning simulations so that the observed characteristics ( $a_{\text{Gal}}$ ,  $a_{\text{PSF}}$ ,  $\epsilon_{\text{Gal}}$ ,  $\epsilon_{\text{PSF}}$ ) match those of the GREAT10 stamps. Position angles of the galaxies and PSFs follow a uniform distribution across all possible orientations. The signal-to-noise ratio (S/N) is simply kept constant, for both the galaxies and the PSFs, to the fiducial S/N of the GREAT10 data. The centroid positions of the galaxy and PSF profiles within the stamps are randomized by a uniformly distributed scatter of  $\pm 1$  large pixel in each direction.

We now draw, and then convolve, these galaxy and PSF profiles on fine pixels, 4 times smaller than the GREAT10 pixels (i.e., 16 times in area). We bin the pixels  $4 \times 4$  to match the GREAT10 sampling and we add a simple Gaussian noise with  $\sigma = 1$  ADU (in the same flux scale as GREAT10) to the convolved galaxy and to the PSF images. This is well representative of the “sky-limited” acquisition regime. Taken individually, the resulting stamps are indistinguishable from the

GREAT10 data in terms of the proposed shape measurement and visual inspection.

### 3.2. Shape measurement methods

In the scope of the GREAT10 challenge, we have compared two fast shape measurement methods, both based on the computation of the 2nd order moments of the light distribution. Here we briefly describe them and assess their precision.

#### 3.2.1. Masked 2nd moments + denoising (hereafter MMD)

To optimally include the shape measurement in our workflow and test the feasibility of the proposed method, we have, in a first step, implemented our own shape measurement. It sequentially processes the pairs of galaxies and PSFs, stamp by stamp, and can be summarized as follows:

1. Denoise the stamp, using hard thresholding of the first and second level of its Haar wavelet coefficients.
2. Build a boolean isophotal mask for the denoised stamp, selecting only those pixels whose values are above a certain fraction of the maximum value.
3. Compute the barycenter, and the centered 2nd order moments of the resulting (i.e. masked and denoised) stamps.
4. Transform the 2nd order moments into an orientation  $\theta$  and a semi-major and semi-minor axes  $a$  and  $b$ . In doing this, we use the same formalism as in the SExtractor package (Bertin & Arnouts 1996b).

The denoising step is important to increase the precision of the measured parameters and also because it smoothes the contour of the isophotal mask. As MegaLUT cancels biases of the shape measurement step, we can make use of a rather strong denoising, even if the latter does not completely preserve object shapes.

We have submitted MegaLUT only in combination with this first MMD shape measurement method to the GREAT10 challenge leaderboard.

#### 3.2.2. SExtractor windowed 2nd moments (SEWIN)

The widely used SExtractor software (Bertin & Arnouts 1996a) implements “windowed” measurements of the centroids and

2nd order moments. The computation of the latter are similar to the basic 2nd order moments, except that the pixel values are weighted, in a similar way to which it is done in KSB, by an adaptive circular Gaussian window<sup>7</sup>. While these windowed parameters can be significantly biased with respect to the basic ones, they are far less sensitive to noise in the input images.

As an alternative to the simple MMD shape measurement, we thus include a second shape measurement based solely on the latest SExtractor (version 2.8.6) in our analysis. To retain its advantage in computational speed, simplicity, and reproducibility, we do not combine it with prior denoising of the images.

We have considered this second shape measurement method only after the GREAT10 challenge deadline. Thus its results are not included in Kitching et al. (2012).

### 3.2.3. Analysis of the shape measurement precision

For MegaLUT to deliver precise results, the scatter of ellipticity corrections within each cell should be as small as possible (e.g., see Fig. 1). This scatter has three sources:

1. The precision of the shape measurement, i.e., the sensitivity of the coordinates to noise in the images. An imprecise shape measurement will randomly allocate the learning sample galaxies to the wrong cells. Additionally, these random errors will also influence the querying the LUT. Note that in practice, galaxies and PSF images are sampled on a discrete pixel grid, resulting in an inherent limit in precision for any shape measurement.
2. The reduction of the multidimensional parameter space to a limited number of coordinates. A given choice of coordinates effectively marginalizes over all parameter dependencies not explicitly included in the chosen coordinates. If for instance the measurement of an elongation depends on the signal to noise ratio (S/N) of a source, and the LUT does not discriminate according to S/N, stamps differing only by their S/N may be allocated to different cells.
3. The actual variation of the ellipticity correction within the finite size of the cells, due to the continuous evolution of the ellipticity corrections,  $\delta e$ , in the parameter space. This effect is inherent to the method, but can be easily addressed by choosing a sufficiently fine sampling of the parameter space. For the sampling used in our implementation, this source of scatter is insignificant compared to the first two points.

We evaluate the precision of the two shape measurement methods presented in the previous sections by running them on 400 realizations of a single simulated galaxy and an associated PSF. The corresponding stamps are drawn using the same light profiles as for the learning sample, but we keep all parameters of the profiles constant, by setting them to typical values representative of the GREAT10 data. Only the noise realization and the scatter in centroid positions differ between these simulated stamps.

The histograms for the four coordinates obtained through the two methods are shown in Fig. 2. In this plot, each coordinate  $c$  obtained from MMD has been linearly rescaled ( $c' = m \cdot c$ ) so that its variance can be equitably compared to the variance of the SEWIN coordinate. Indeed, the different ways of masking and weighting the second order moments yield significantly different raw shape parameters; for instance, the elongations measured by

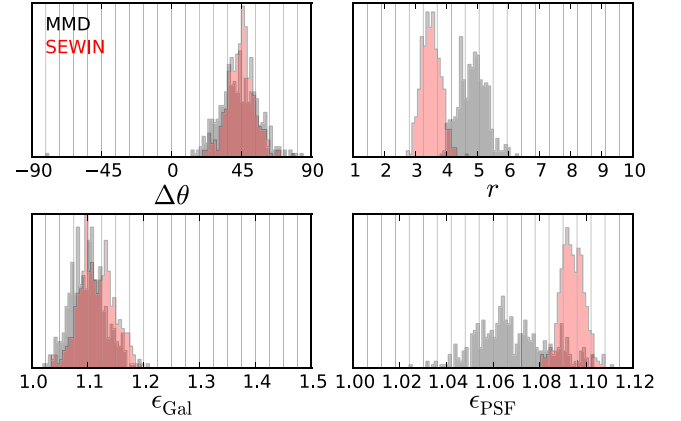


**Fig. 2.** Comparison of the precision of the shape measurements methods used in this work, obtained by running them on 400 noisy realizations of always the same galaxy and PSF pair. MMD results are shown in grey, SEWIN in red. The shape parameters measured by MMD are rescaled so that their variance can be equitably compared to the variance of the SEWIN ones (see text). The vertical lines indicate the 20 bins in each coordinate, as used for all applications to GREAT10 described in this paper. See Fig. 1 for a description of the coordinates.

SEWIN are systematically about half of the elongations from MMD. For each coordinate, the scaling factor  $m$  is chosen so that the range of coordinates computed for the full learning sample by the two techniques robustly overlaps. Note that this rescaling is only required for the comparative study of Fig. 2.

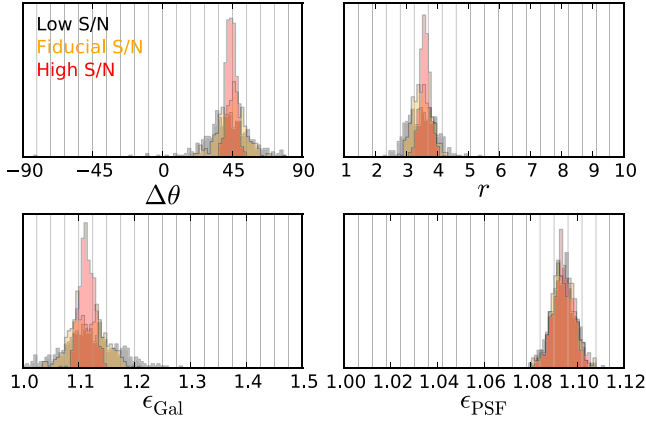
Discrepancies in accuracy (i.e. positions of the peaks) of the techniques is not a concern, as MegaLUT corrects for bias using the learning sample; the peaks should simply be as narrow as possible. The SEWIN method clearly evinces a higher precision than the simple MMD that was submitted to the GREAT10 challenge. This is especially true for the measurement of the elongation of the PSF.

The width of the histograms in Fig. 2 gives the *resolution* of the shape measurement for data very similar to GREAT10. The bin size used to discretize the coordinates of the LUT cells can now be chosen fine enough to avoid any significant degradation of this resolution.

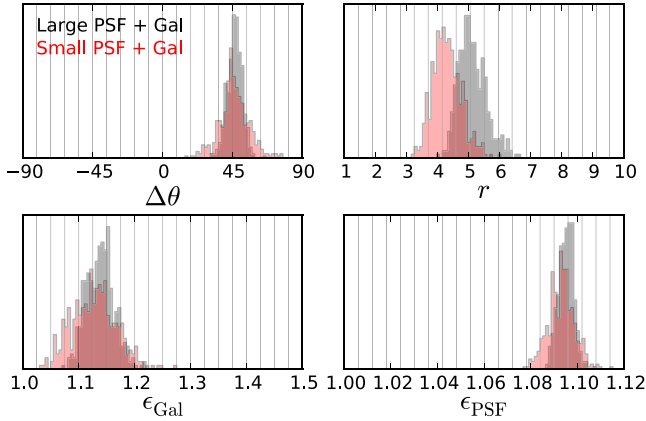
To evaluate the importance of the second source of scatter, that is the marginalization over potentially discriminating parameters, we process in a similar way. In Fig. 3, we compare the SEWIN measurements for the 3 different signal-to-noise ratios encountered in the GREAT10 data. We observe that the centroids of all 4 coordinates, as obtained from SExtractor, are not significantly affected by the S/N, at least within the range of S/N explored in GREAT10. This is a remarkable property of SExtractor’s windowed moments, hence it is justified not to include the S/N as a coordinate in the LUT. Naturally, we do observe an increase in the *variance* of the coordinates with decreasing S/N; such a lack of precision inevitably degrades the shear signal, whatever be the accuracy of the correction.

Figure 4 illustrates a similar analysis, but varying the size of the galaxy and PSF, instead of the S/N. The coordinate  $r$  discriminates stamps by their galaxy-to-PSF area *ratio*. For an analytical convolution, this ratio would not be affected by rescaling both the galaxy and the PSF by the same factor. However, as a consequence of the pixelization, the histogram for the values of  $r$  slightly depends on the galaxy and PSF scale. At the cost of adding one more dimension to the LUT, this limitation may be addressed by including both the galaxy and the PSF size as coordinates to the LUT, instead of their ratio.

<sup>7</sup> The windowed parameters are described in the SExtractor manual by E. Bertin, available at <http://www.astromatic.net/software/sextractor>



**Fig. 3.** Sensitivity of SEWIN coordinates to the 3 different signal-to-noise ratios of GREAT10, for a typical galaxy and PSF. There is no observable bias of the shape measurements with changing S/N. Therefore we do not include the S/N as a dimension of the LUT.



**Fig. 4.** Sensitivity of SEWIN coordinates to the size of the PSF and galaxy pair. The distinction between the small (red) and large (blue) couples is a factor 1.8 in full width at half maximum of both the PSF and the galaxy, covering the range from the smallest to the widest PSFs in GREAT10. For the present MegaLUT implementation, the measurement of the size ratio  $r$  should ideally *not* depend on this rescaling.

Aside from the mentioned sources of scatter within the cells, the ellipticity corrections can also be *biased*, if the learning sample is not representative enough of the galaxies and PSFs to be analyzed. Our method is indeed a machine learning method. As such, the quality of the training set is important. We discuss this source of error in Sect. 5.

### 3.3. Building the LUT

Given the resolution of the two considered shape measurement methods (see Fig. 2), we have chosen, for all our applications to GREAT10, to use a regular sampling of 20 bins in each of the 4 coordinates, yielding  $20^4 = 160\,000$  cells. As expected, further increasing this sampling did not improve the performance of the algorithm.

For our submission of MegaLUT using the MMD shape measurement to the GREAT10 challenge, we built a learning sample of 2.1 million galaxies. Since then, we increased this number to 9 millions, without changing neither the profiles nor the parameter distributions. As illustrated in Fig. 5, this number is large enough to sufficiently fill the required cells of the LUT. But in fact, we observe that the GREAT10 scores achieved do

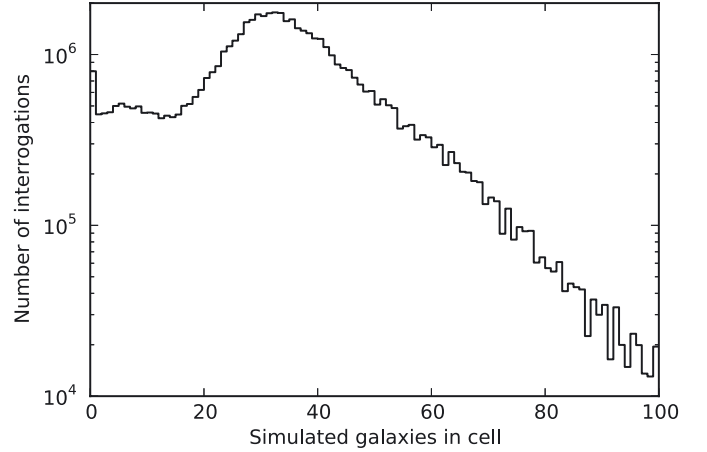


**Fig. 5.** Histogram of the number of learning sample galaxies in the cells as encountered by the 50 million queries to the LUT. The cells of the LUT that are most queried by the GREAT10 data are sufficiently filled by the learning sample. Using a learning sample of 9 million galaxies, we find that only 5% of the queries found less than 5 learning galaxies in their cells. Note that for those queries falling on an empty cell, our implementation returns the mean correction from the cells neighbors.

**Table 1.** Quality factors  $Q$  and further GREAT10 metrics obtained by MegaLUT in combination with the two discussed shape measurement methods MMD and SEWIN.

Method	$Q$	$m$	$c/10^{-4}$	$M/2$	$\sqrt{\mathcal{A}}/10^{-4}$
MegaLUT + MMD	69.17	-0.27	-0.550	-0.1831	0.1311
MegaLUT + SEWIN	104.14	-0.15	-0.057	0.0119	0.0819

**Notes.** All values are computed using the same analysis code as for the GREAT10 results paper. The description of these metrics can be found in Kitching et al. (2012). The entry MegaLUT + MMD refers to the submission “MegaLUTsim2.1 b20” in Kitching et al. (2012).

not significantly decrease when using only our initial learning sample of 2.1 million galaxies.

## 4. Results on the GREAT10 challenge data

We participated in the GREAT10 challenge by combining MegaLUT with the MMD shape measurement (Sect. 3.2.1), reaching an encouraging quality factor  $Q$  of 69.2 (Kitching et al. 2012).

With the SExtractor-based SEWIN shape measurement (Sect. 3.2.2) – implemented after the challenge deadline, and thus not in the official leaderboard – MegaLUT reaches a  $Q$  factor of 104, without power spectrum denoising or training. This score is competitive with the results achieved by the best ellipticity catalog submission to GREAT10.

The achieved values of all GREAT10 metrics obtained using the two shape measurements are presented in Table 1. We observe that the SEWIN shape measurement substantially improves (i.e., reduces) both the one-point ( $m$ ,  $c$ ) and power spectrum ( $M/2$ ,  $\sqrt{\mathcal{A}}$ ) bias estimates. Performance details of MegaLUT + SEWIN, for each set of the GREAT10 data, are displayed in Fig. 6.

We implemented MegaLUT in pure PYTHON in a few hundred lines of code<sup>8</sup>. Using the SExtractor shape

<sup>8</sup> The code is available at <http://lastro.epfl.ch/megalut>



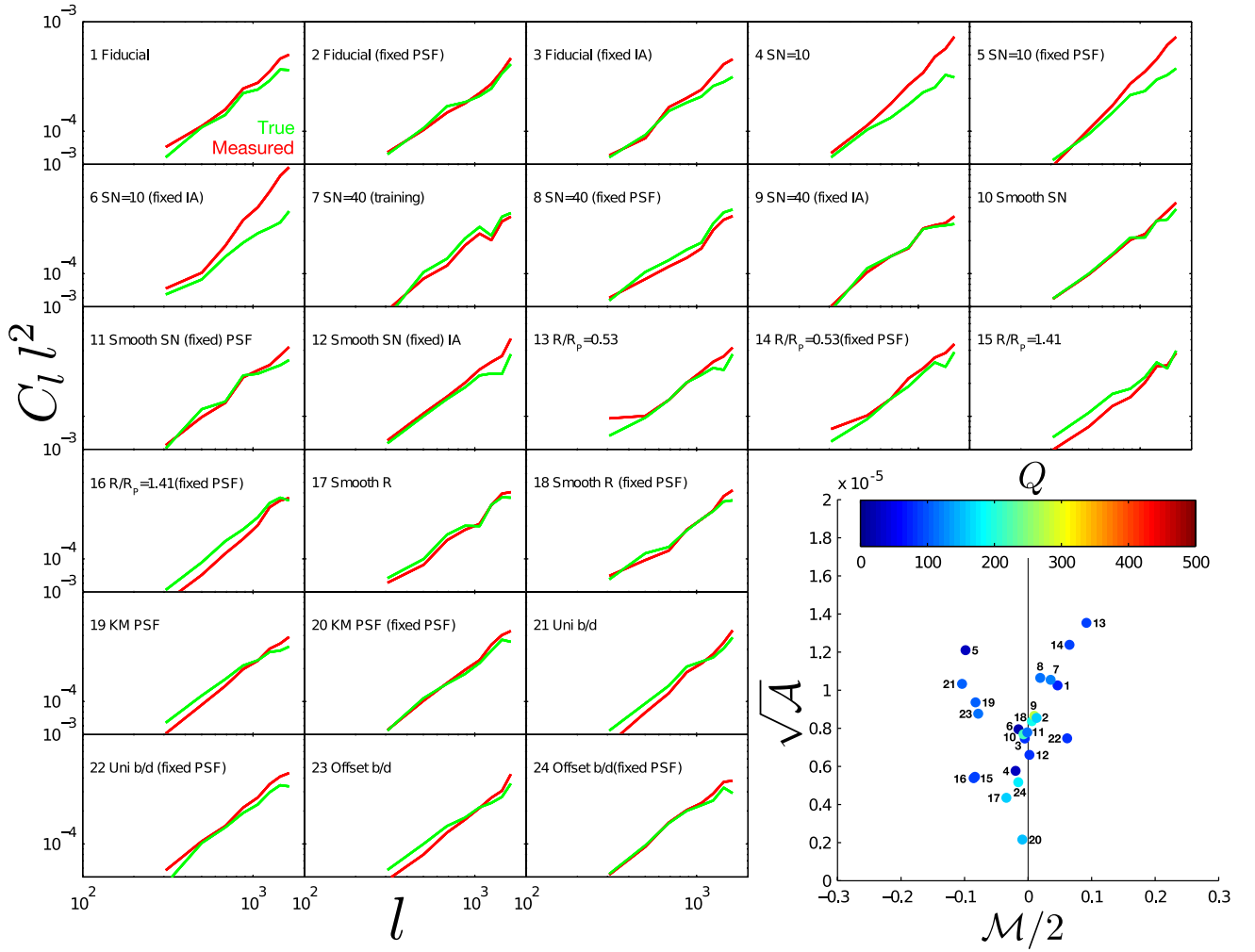


**Fig. 6.** Power spectra of the sheared ellipticities as obtained by MegaLUT + SEWIN for each set of the challenge. This figure can be directly compared with those from all GREAT10 submissions described in [Kitching et al. \(2012\)](#). The red lines represent the *measured* shear power, obtained without the denoising term, while the green lines represent the *true* shear power. The inset gives the metrics  $\mathcal{M}/2$ ,  $\sqrt{\mathcal{A}}$  and  $\mathcal{Q}$  (without denoising or training) for each set.

measurement, the whole process of detecting, characterizing the galaxy/PSF pairs, and querying the LUT takes less than 3 milliseconds per galaxy on an AMD Opteron 2216 2.4 GHz CPU. Given the competitive quality metrics, this makes MegaLUT a very efficient solution to the PSF correction problem.

## 5. Discussion

MegaLUT splits the measurement process of sheared ellipticities into two distinct parts: the shape measurement itself, and the subsequent ellipticity correction by a simple form of supervised learning. Limitations of the shape measurement algorithms in the presence of noise as well as the finite sampling and dimensionality of the LUT are practical error sources. They are discussed in Sect. 3.2.3. We recall that even if our empirical method corrects for biases on the estimated sheared ellipticities, the remaining variance in this output will degrade the weak lensing signal, and in particular bias the shear power spectrum.

The remaining and more fundamental sources of error concern the discrepancies between the learning sample and the data to be analyzed. In this paper, we have kept the learning sample

as elementary as possible, using a single simply parametrized profile for the galaxies. All the free parameters describing the generation of these learning galaxies and the associated PSFs, such as size and ellipticity, directly relate to coordinates of the LUT. Assuming a perfect shape measurement and noiseless data, two galaxy-PSF pairs from the learning sample would get attributed the same coordinates only if the pairs are virtually identical, except for their absolute orientation and size. As a consequence, for such a simple parametrization of the learning sample, the actual distributions of parameters used to generate the learning sample do not act as priors of the method. Indeed, the queried ellipticity corrections don't depend on these distributions, as long as the LUT gets sufficiently filled with learning data in all required cells.

But clearly, real galaxies do not follow smooth exponential light profiles. Instead, their possibly multiple components follow a variety of slopes, contain asymmetries, and may well not come isolated. Any employed shape measurement is sensitive to these substructures. Therefore, a machine learning approach like MegaLUT will yield biased results if it is not trained on realistic galaxies. How can we deal with this necessity for a realistic learning sample?

Let us note that for a real galaxy there is no longer a natural and unambiguous definition of ellipticity as we have for the simple smooth profiles with perfectly elliptical isophotes. The ellipticity of a real galaxy must be defined through a measurement on the image. Hence, to combine MegaLUT with a more detailed and realistic learning sample, one can easily *measure* the sheared ellipticities of the simulated galaxies before the convolution by the PSF and the addition of noise. This procedure allows to use simulated learning galaxies with arbitrary substructure, and also to shear them in a well controlled way once they have been drawn on a pixel grid. When such a detailed learning sample is built, the distribution of parameters describing the generation of galaxy substructure (e.g. light profiles, clumps, companions) would influence the distribution of ellipticity corrections inside the LUT cells. They would thus effectively act as priors on the method, to be chosen according to the population of galaxies to be analyzed. Ideally such simulated data should be cosmology-independent and blind, to avoid confirmation bias effects.

Furthermore, such an increase in details of the learning sample represents an opportunity for more sophisticated shape measurement methods to test the benefits of additional characterizations of the galaxies and PSF, as for example an estimation of the radial slope of the light distributions. If consequently the desired number of coordinates or cells of the LUT increases significantly, the memory requirements and CPU time for the generation of enough learning data might become a limitation. In any case, the brute-force LUT with manually chosen coordinates could be replaced by a fast interpolation across sparse data in a large parameter space, for instance by using an artificial neural network like those employed by Gruen et al. (2010).

## 6. Conclusion

In this paper we have presented MegaLUT, a new method to correct galaxy shape measurements from smearing by the instrumental and atmospheric PSF. We list below a summary of the advantages of our method.

1. MegaLUT is empirical. It does not need to rely on a specific shape measurement method or shape definition, and does not require the shape measurement to be accurate (bias is tolerated) as long as it is precise (low variance). The shape measurement itself can be considered as an interchangeable black box.
2. As a consequence, MegaLUT can well be combined with existing shape measurements techniques, in particular it can make use of strong image denoising to increase the shape precision, even if the denoising itself introduces biases in the measured parameters.
3. Each galaxy is processed individually, hence MegaLUT is independent from the spatial power spectrum of the shear field or the PSF variations.
4. The total computational cost of the analysis of a galaxy and its corresponding PSF is dominated by the shape measurement process, as the shape *correction* essentially reduces to a simple array indexing operation. When combined with

an efficient shape measurement, MegaLUT is fast, with a total processing time of a few milliseconds per galaxy, on an ordinary CPU.

By applying this method to the GREAT10 challenge (Kitching et al. 2011, 2012), we have shown that its results are well competitive ( $Q = 104$ ) with the best submitted methods, despite a truly simplistic learning sample and the lack of additional corrections for bias at the level of the shear power spectra. Like for any machine learning technique, once the technical aspects are well controlled, it's ultimately the quality of this learning sample that limits the performance of the shape measurement itself. To obtain the best possible shape estimates for real weak lensing observations, a more representative learning sample might be required. We have discussed in Section 5 how a learning sample containing arbitrarily realistic galaxies and PSFs could easily be used. In particular, such a learning sample can be build directly using high-resolution observations, like Hubble Space Telescope images.

*Acknowledgements.* This work is supported by the Swiss National Science Foundation (SNSF). We thank the GREAT10 Coordination Team for organizing the stimulating challenge and sharing the quality factor calculation codes. GREAT10 was sponsored by a EU FP7 PASCAL 2 challenge grant. TDK was supported by a Royal Society University Research Fellowship. We would also like to thank the anonymous referee for her/his beneficial comments.

## References

- Bacon, D. J., Refregier, A. R., & Ellis, R. S. 2000, MNRAS, 318, 625  
 Bertin, E., & Arnouts, S. 1996a, A&AS, 117, 393  
 Bertin, E., & Arnouts, S. 1996b, in Astrophysics Source Code Library, record ascl:1010.064  
 Bolton, A. S., Burles, S., Koopmans, L. V. E., et al. 2008, ApJ, 682, 964  
 Coe, D., Benítez, N., Broadhurst, T., & Moustakas, L. A. 2010, ApJ, 723, 1678  
 Courbin, F., Faure, C., Djorgovski, S. G., et al. 2012, A&A, 540, A36  
 Faure, C., Kneib, J.-P., Covone, G., et al. 2008, ApJS, 176, 19  
 Gruen, D., Seitz, S., Koppenhoefer, J., & Riffeser, A. 2010, ApJ, 720, 639  
 Hu, W. 1999, ApJ, 522, L21  
 Kacprzak, T., Zuntz, J., Rowe, B., et al. 2012, MNRAS, submitted [arXiv:1203.5049]  
 Kaiser, N., Squires, G., & Broadhurst, T. 1995, ApJ, 449, 460  
 Kaiser, N., Wilson, G., & Luppino, G. A. 2000 [arXiv:astro-ph/0003338]  
 Kitching, T. D., Miller, L., Heymans, C. E., van Waerbeke, L., & Heavens, A. F. 2008, MNRAS, 390, 149  
 Kitching, T., Amara, A., Gill, M., et al. 2011, Ann. Appl. Stat., 5, 2231  
 Kitching, T. D., Balan, S. T., Bridle, S., et al. 2012, MNRAS, 423, 3163  
 Kuijken, K. 2006, A&A, 456, 827  
 Laureijs, R., Amiaux, J., Arduini, S., et al. 2011 [arXiv:1110.3193]  
 Limousin, M., Richard, J., Jullo, E., et al. 2007, ApJ, 668, 643  
 Maoli, R., Van Waerbeke, L., Mellier, Y., et al. 2001, A&A, 368, 766  
 Melchior, P., & Viola, M. 2012, MNRAS, accepted [arXiv:1204.5147]  
 Miller, L., Kitching, T. D., Heymans, C., Heavens, A. F., & van Waerbeke, L. 2007, MNRAS, 382, 315  
 Refregier, A. 2003, MNRAS, 338, 35  
 Refregier, A., & Bacon, D. 2003, MNRAS, 338, 48  
 Refregier, A., Kacprzak, T., Amara, A., Bridle, S., & Rowe, B. 2012 [arXiv:1203.5050]  
 Shan, H., Kneib, J.-P., Tao, C., et al. 2012, ApJ, 748, 56  
 Van Waerbeke, L., Mellier, Y., Erben, T., et al. 2000, A&A, 358, 30  
 Wittman, D. M., Tyson, J. A., Kirkman, D., Dell'Antonio, I., & Bernstein, G. 2000, Nature, 405, 143

## 5 Strong lensing by QSO host galaxies

### 5.1 Introduction

This last chapter deals again with strong gravitational lensing. It presents results from a spectroscopic search of literal “QSO-lenses”, that is QSO<sup>1</sup> host galaxies acting as lenses. This configuration is uncommon : the term QSO-lens is usually used to designate systems in which a quasar is seen as multiply-imaged point source, lensed by a foreground galaxy.

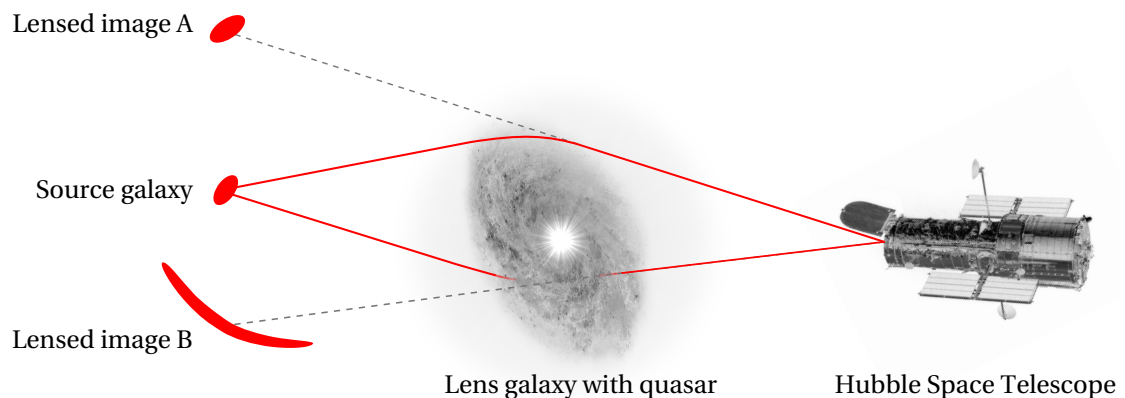


Figure 5.1: Strong lensing by QSO host galaxies. The bright quasar sits in the lens galaxy, while the distant source galaxy is much fainter. Sharp imaging such as from the Hubble Space Telescope is required to spatially resolve the lensed images, as they would otherwise remain hidden in the bright glare of the foreground quasar.

Why search for new galaxy-scale strong gravitational lens systems ? The results presented in Chapter 3 of this thesis give a compelling case for searching for new gravitationally lensed quasars. For these lenses, it's the variable nature of the source that enables us to measure the time delays so useful to constrain cosmological parameters. In this context, the lens itself may seem secondary. But importantly, strong lensing also allows us to probe the mass density distribution of the lenses, especially if the observations feature *extended* lensed images such as wide arcs, and not only unresolved quasar images. A recent highlight in the field

<sup>1</sup>QSO stands for Quasi-Stellar Object, a synonym of quasar. Quasars are briefly introduced in Section 1.2.1 on page 11 of this thesis.

of galaxy lenses is the gravitational detection of a low-mass ( $2 \cdot 10^8 M_\odot$ ) dark satellite galaxy at a distance of  $z = 0.881$ , by accurate modeling an Einstein ring (Vegetti et al. 2012). Such observations of galaxy substructure, predicted by numerical simulations but rarely “seen”, are absolutely crucial to test our current cold dark matter cosmological model. Another motivation for searching new galaxy lenses is to obtain large samples of cases for different lens galaxy categories. Properties such as the mass profile, and its evolution with redshift, can then be statistically studied within each category. If these samples are well defined, they allow for robust generalization of the results to similar galaxies not acting as strong lenses. Two surveys fit exactly in this picture : SLACS<sup>2</sup> builds and analyses a sample of lenses formed by early-type (i.e., elliptical to lenticular) galaxies (Bolton et al. 2006), and SWELLS successfully focused its search and follow-up observations on edge-on late-type (lenticular to spiral) lenses (Treu et al. 2011).

For a review on how strong lensing allows us to explore the spatial mass distribution in galaxies, see Treu (2010). The foremost goal of our search for QSO host galaxies acting as lenses is to weigh galaxies of this particular class, and compare their dynamical and lensing masses.

### 5.2 The SDSS spectroscopic survey

The next question to answer is how to perform a systematic search for such relatively small strong galaxy lenses. Identifying these systems from ground-based survey *images* is close to impossible if the Einstein radii, that is approximatively the angular separation between the lens and the lensed images, approaches the spatial resolution of the data. And indeed, as illustrated in this thesis by the COSMOGRAIL sample, Einstein radii as small as  $1''$  are common for lens galaxies.

Both SLACS and SWELLS select their lens candidates from the ground-based Sloan Digital Sky Survey (SDSS), and our search for “QSO-lenses” is also done in the same way and using this same survey. The trick is to perform a *spectroscopic* search.

SDSS is a survey of about a quarter of the sky, using a dedicated 2.5-m telescope in New Mexico (USA). The particularity making SDSS truly “one of the most ambitious and influential surveys in the history of astronomy”<sup>3</sup> is that it performs spectroscopy of selected targets of its multi-filter imaging data. The SDSS has so far obtained spectra of about 1.5 million galaxies, 230000 quasars, and 670000 stars<sup>4</sup>, in a spectral range from 3900 to 9100 Å and with a resolution  $\lambda/\Delta\lambda$  of 1800. This is accomplished by using a fiber-fed spectrograph capable of simultaneously recording more than 600 spectra of different targets in the field of view. In such a design, optical fibers bring the light from the focal plane of the telescope to the spectrograph. The heads of these fibers must be individually placed at the position of each target in the focal plane. In the case of SDSS, robots drill aluminum “plug-plates” to hold the fibers in place, and plug in the fiber heads, for *each* observing field. A detail of such a plug-plate is shown in Figure 5.2. The small black dot in the center of each fiber head is the opening that accepts the light to be analyzed. These holes have a diameter of  $180 \mu\text{m}$ , corresponding to  $3''$  on the sky.

---

<sup>2</sup>See <http://www.slacs.org> for an image gallery, a summary of major results, and a publication list.

<sup>3</sup><http://www.sdss.org/>

<sup>4</sup><http://www.sdss3.org/dr9/> (August 2012)



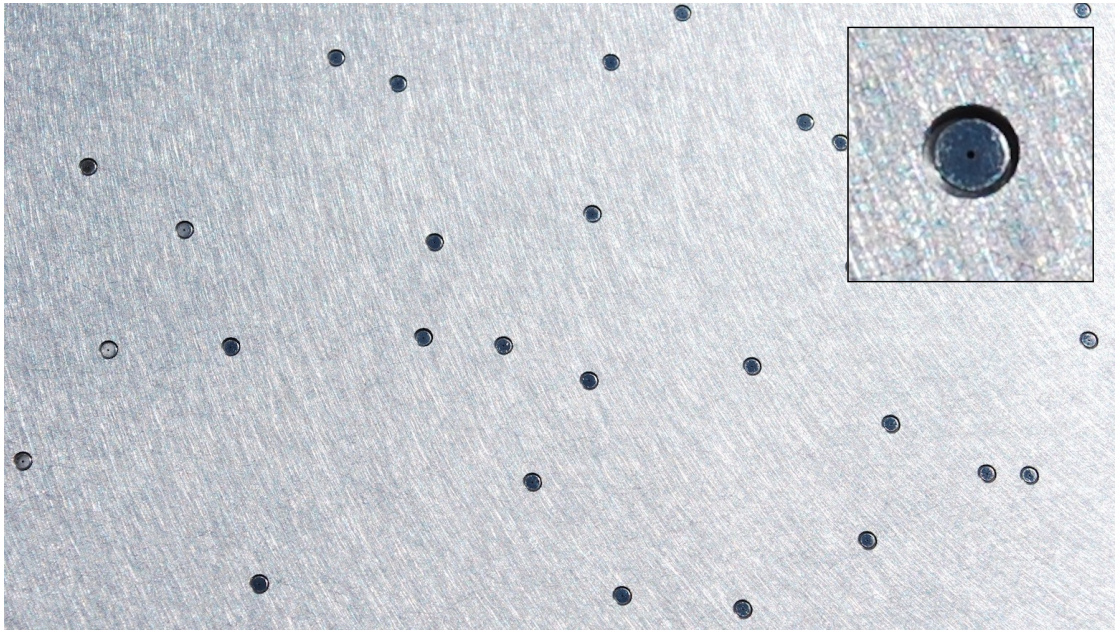


Figure 5.2: Close-up of a plug-plate that holds the optical fibers in the focal plane of the SDSS telescope. The inset zooms on one of the installed fiber heads. Original photograph by User:EdPost / Wikimedia Commons / CC-BY-SA-3.0

How to find strong lenses in these spectra? The idea is to look for emission lines superposed to the spectrum of a given galaxy, but at a higher redshift. The spectrograph fibers mix up all the light received within  $1''.5$  from the center of their targets, and even a bit more, as the image is blurred by the PSF. If light from a background object at a *significantly different redshift* from the foreground galaxy is recorded within this aperture, it is likely that the background object is somehow gravitationally lensed. A dedicated follow-up observation by deep and sharp imaging can then be afforded to confirm the candidate and reveal the magnified and distorted images. A striking advantage of the spectroscopic selection technique is that the source and lens redshifts are directly known already from the survey data.

Figure 5.3 shows such a continuum-subtracted SDSS spectrum of a target classified as QSO. Strong typical emission lines of the quasar, indicated by black dotted lines, are clearly observed at a redshift of 0.209. In addition, several other emission lines can be discerned. Taken individually, the latter would be hard to interpret. But altogether, they can be matched to hydrogen and oxygen lines at a much higher redshift of 0.558, as identified by the red dashed lines. Figure 5.4 shows the corresponding imaging data. The SDSS image does not give any hint about the origin of these emission lines at two different redshifts. In contrast, the sharp HST image not only clearly reveals two wide arcs, but also the interesting and apparently double structure of this particular lens.

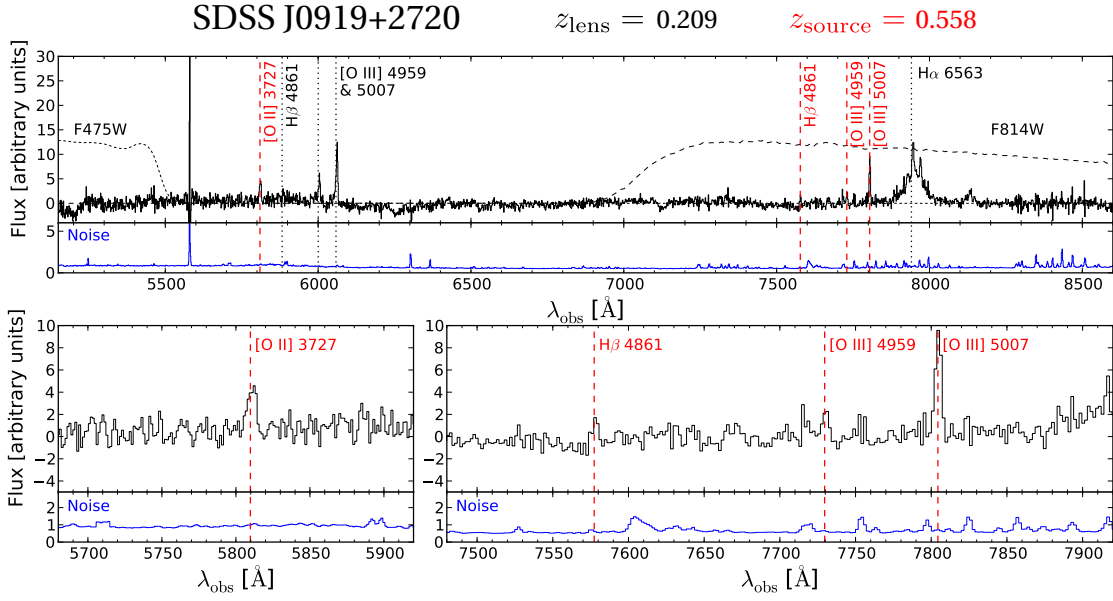


Figure 5.3: Continuum-subtracted SDSS spectrum of the QSO-lens J0919+2720. The top panel gives an overview of the spectrum, while the bottom panels show cutouts around the detected background emission lines. The dashed curves give the relative transmissions of the two filters used for HST imaging, in arbitrary units.

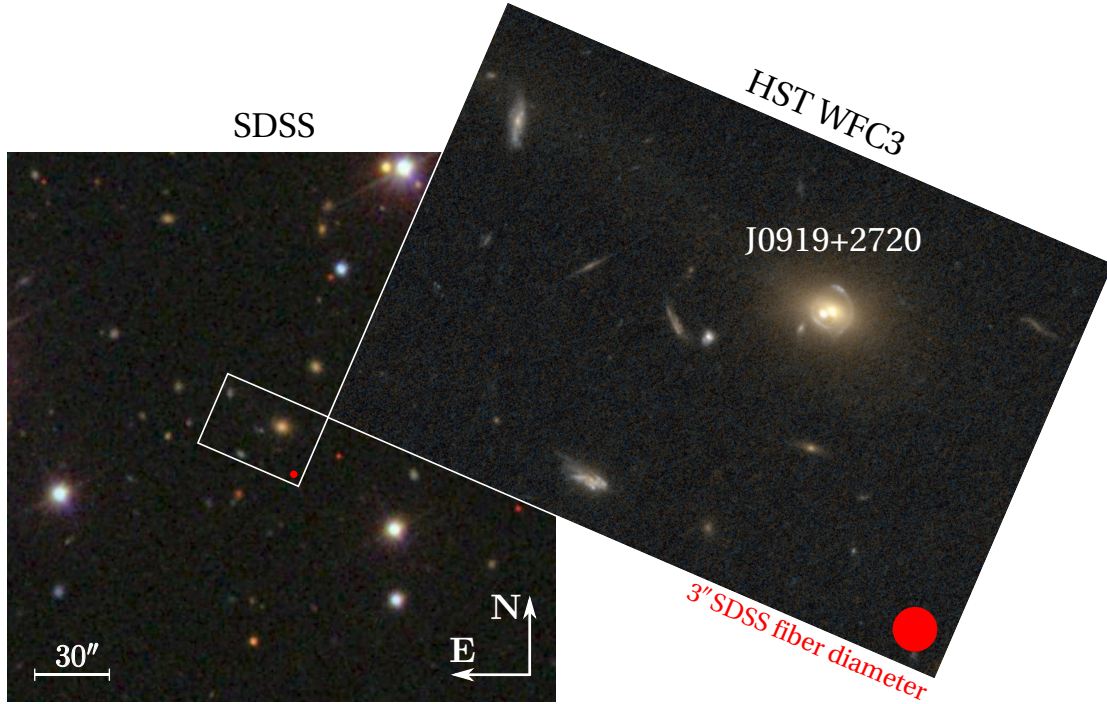


Figure 5.4: SDSS and Hubble Space Telescope (HST) images of J0919+2720. The red disk on the bottom right of both insets shows the size of fiber feeding the SDSS spectrograph. The corresponding spectrum, that lead to our selection of this lens for follow-up imaging by the HST, is shown in Figure 5.3.



## 5.3 Results

The paper inserted at the end of this chapter (Courbin et al. 2010) summarizes the simple algorithm that we have implemented to search for lens candidates, trawling through the SDSS database of quasar spectra. It essentially corresponds to a cross-correlation between the observed spectra and redshifted emission line templates.

In our initial search run, realized in the scope of excellent LASTRO summer projects of François R  rat and Dheeraj Reddy, we identified four highly convincing lens candidates: SDSS J0013+1523 (Figure 1 of Courbin et al. 2010), J0919+2720 (Figure 5.3), J0827+5224, and J1005+4016 (Figure 5.5). They all feature 4 consistently redshifted “background” emission lines. Follow-up observations in May 2010 with the 10-m Keck I telescope on Mauna Kea (Hawaii) and in February and March 2011 with the Hubble Space Telescope (HST) have led to two publications.

**Courbin et al. (2010)** This first letter announces the likely confirmation of a first candidate, SDSS J0013+1523, based on spectroscopy and adaptive optics *K*-band imaging from the Keck telescope. It is included at the end of this chapter.

**Courbin et al. (2012)** This second article presents Keck but also the HST follow-up observations for all four candidates. Color combined HST images of the 3 new candidates, which led to the press release STSci-2012-14 of the Space Telescope Science Institute are shown in Figure 5.6.

Two of the four candidates, namely J0919+2720 and J1005+4016, display prominent gravitational arcs. In J0919+2720, the bright point-like quasar is displaced with respect to an early-type main lens galaxy. A first rough estimate of the total mass within the rings yields  $21 \pm 6 \cdot 10^{10}$  solar masses ( $M_{\odot}$ ) for this exotic combination, which might be an ongoing merger. For J1005+4016, the arc surrounds a QSO in a face-on spiral galaxy. For this system the mass within the Einstein radius is estimated to be  $7.5 \pm 1 \cdot 10^{10} M_{\odot}$ . For all cases, a detailed lensing analysis is still pending. Unfortunately, the HST observations could not confirm the potential counter-image “B” identified in the Keck imaging of J0013+1523. It might be obscured by dust, and thus too faint in the optical, or it might have been an artifact of the adaptive optics images (Courbin et al. 2012). The present HST images are not conclusive on the strong lens nature of this candidate.

Since the initial selection of these candidates, the spectroscopic search for QSO-lenses has been carried on at LASTRO in the scope of student projects and master theses. Future high resolution *imaging* surveys such as Euclid (Section 4.4) will also boost the potential for discoveries of new strong lenses. To search for lenses in the roughly  $10^{13}$  pixels of Euclid’s sky map, efficient algorithms are required. Spectroscopically selected lenses like those presented in this chapter constitute a precious sample for the training and evaluation of such robots.

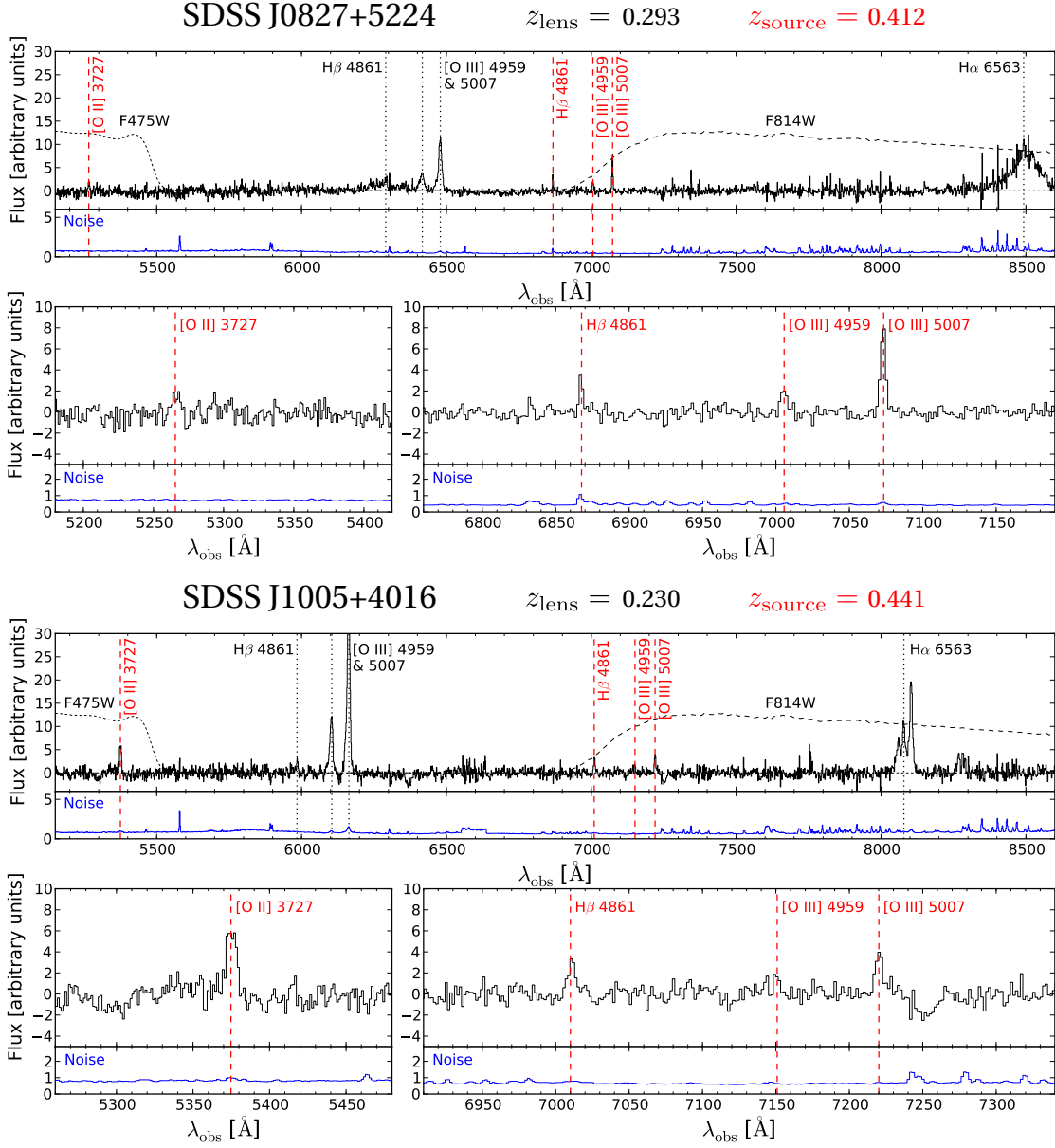


Figure 5.5: SDSS spectra of J0827+5224 and J1005+4016, displayed in the same way as J0919+2720 (Figure 5.3) as and as J0013+1523 (Figure 1 of Courbin et al. 2010).

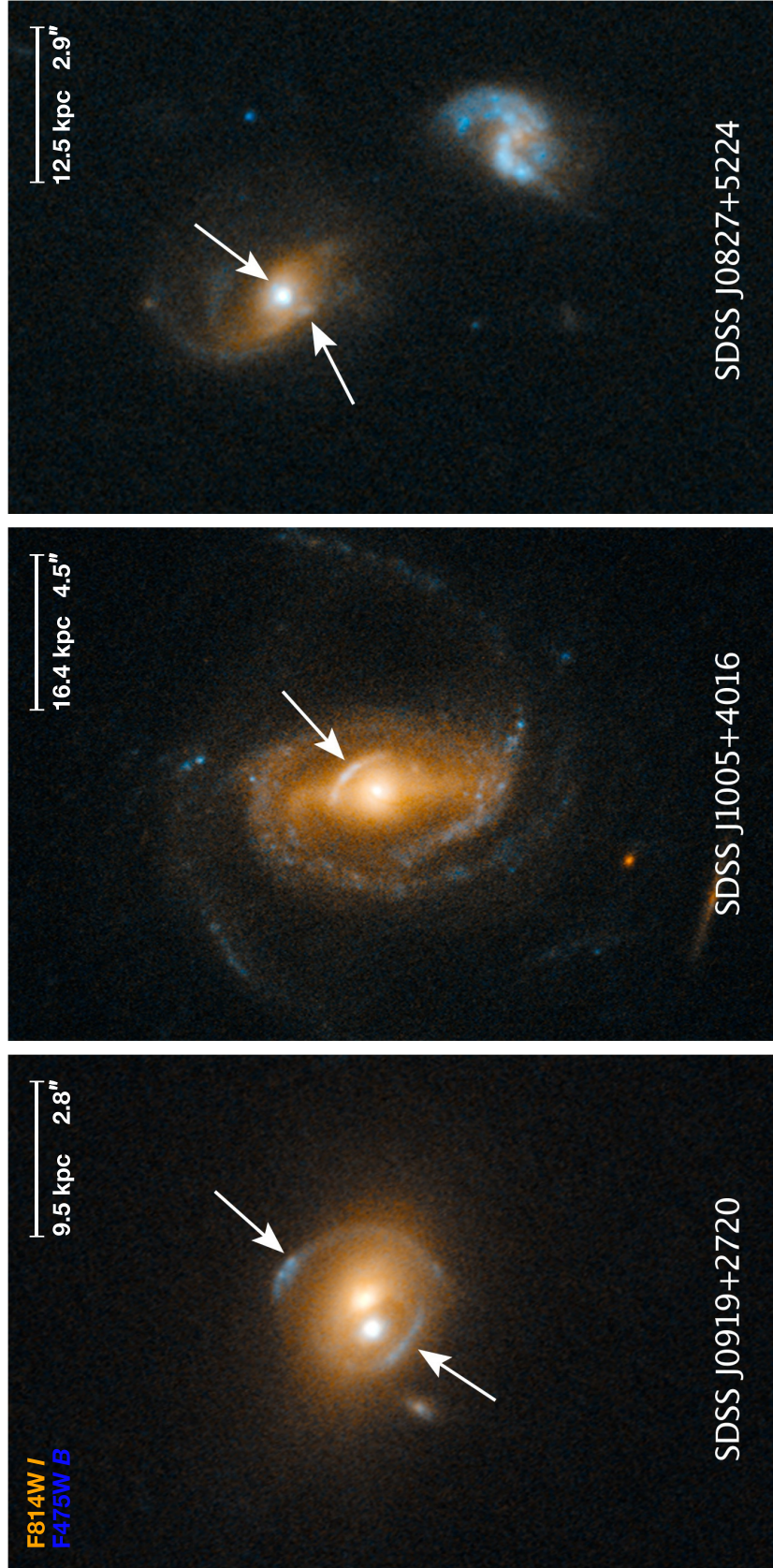


Figure 5.6: HST press release image of the 3 QSO lenses announced in Courbin et al. (2012). The panels show color composites of HST/WFC3 images taken in February and March 2011. The scales in kilo-parsec (kpc) are computed for the distance of the foreground lens galaxy. Image credit : NASA, ESA, and F. Courbin (EPFL, Switzerland), PR STScI-2012-14.



LETTER TO THE EDITOR

# First case of strong gravitational lensing by a QSO: SDSS J0013+1523 at $z = 0.120$ \*

F. Courbin<sup>1</sup>, M. Tewes<sup>1</sup>, S. G. Djorgovski<sup>2</sup>, D. Sluse<sup>3, \*\*</sup>, A. Mahabal<sup>2</sup>, F. R  rat<sup>1</sup>, and G. Meylan<sup>1</sup>

<sup>1</sup> Laboratoire d'astrophysique,   cole Polytechnique F  d  rale de Lausanne (EPFL), Observatoire de Sauverny, 1290 Versoix, Switzerland

e-mail: [malte.tewes@epfl.ch](mailto:malte.tewes@epfl.ch)

<sup>2</sup> Division of Physics, Mathematics, and Astronomy, California Institute of Technology, Pasadena, CA 91125, USA

<sup>3</sup> Astronomisches Rechen-Institut am Zentrum f  r Astronomie der Universit  t Heidelberg, M  nchhofstrasse 12-14, 69120 Heidelberg, Germany

Received 8 March 2010 / Accepted 7 June 2010

## ABSTRACT

We present the first case of strong gravitational lensing by a QSO: SDSS J0013+1523 at  $z = 0.120$ . The discovery is the result of a systematic search for emission lines redshifted behind QSOs, among 22 298 spectra of the SDSS data release 7. Apart from the  $z = 0.120$  spectral features of the foreground QSO, the spectrum of SDSS J0013+1523 also displays the [O II] and H $\beta$  emission lines and the [O III] doublet, all at the same redshift,  $z = 0.640$ . Using sharp Keck adaptive optics  $K$ -band images obtained using laser guide stars, we unveil two objects within a radius of  $2''$  from the QSO. Deep Keck optical spectroscopy clearly confirms one of these objects at  $z = 0.640$  and shows traces of the [O III] emission line of the second object, also at  $z = 0.640$ . Lens modeling suggests that they represent two images of the same  $z = 0.640$  emission-line galaxy. Our Keck spectra also allow us to measure the redshift of an intervening galaxy at  $z = 0.394$ , located  $3.2''$  away from the line of sight to the QSO. If the  $z = 0.120$  QSO host galaxy is modeled as a singular isothermal sphere, its mass within the Einstein radius is  $M_E(r < 1 h^{-1} \text{ kpc}) = 2.16 \times 10^{10} h^{-1} M_\odot$  and its velocity dispersion is  $\sigma_{\text{SIS}} = 169 \text{ km s}^{-1}$ . This is about  $1\text{-}\sigma$  away from the velocity dispersion estimated from the width of the QSO H $\beta$  emission line,  $\sigma_*(M_{\text{BH}}) = 124 \pm 47 \text{ km s}^{-1}$ . Deep optical HST imaging will be necessary to constrain the total radial mass profile of the QSO host galaxy using the detailed shape of the lensed source. This first case of a QSO acting as a strong lens on a more distant object opens new directions in the study of QSO host galaxies.

**Key words.** gravitational lensing: strong – quasars: individual: SDSS J0013+1523 – dark matter

## 1. Introduction

With the growing number of ongoing and future wide-field surveys, strong gravitational lensing is becoming a powerful tool to weigh individual galaxies and study their total radial mass profiles. Historically, strong lenses have long been source-selected, i.e., they were found by identifying gravitationally lensed multiple images of distant sources such as QSOs, either in the optical (e.g., SDSS, Oguri et al. 2006) or in the radio (e.g., the CLASS survey, e.g., Browne et al. 2003; Myers et al. 2003). The discoveries of multiply imaged QSOs, by numerous independent teams over two decades, have led to a sample of about 100 strongly lensed QSOs. Detailed HST imaging is now available for most of these objects mainly thanks to the CfA-Arizona Space Telescope LEns Survey (CASTLES, Mu  oz et al. 1998; Impey et al. 1998). The second largest sample of source-selected systems is the one obtained in the COSMOS

field (Faure et al. 2008), where the sources are almost always emission-line galaxies.

Source-selected samples tend to yield lensing galaxies spanning a broad range of physical properties, i.e., effective radii, Einstein radii, dark matter profiles, total masses, and environments. With current wide-field surveys such as the SDSS, it is now also possible to build lens-selected samples, where the lenses can be chosen with well-defined photometric properties. The largest sample of these lens-selected systems to date is the SLACS sample (e.g., Bolton et al. 2008), where the lenses are color-selected early-type galaxies with  $0.1 < z < 0.6$  and where the sources are emission line galaxies with  $z > 0.5$ . While source-selected samples use optical or radio data to look for multiple images, SLACS uses SDSS optical spectra to look for emission lines redshifted behind the selected lensing galaxies, following the technique of Warren et al. (1996).

Following the same approach, we started to compile a lens-selected sample where the foreground lenses are QSOs in place of early-type galaxies. Our long-term goal is to provide a direct measure of the total mass of QSO host galaxies and to use SLACS as a non-QSO ‘‘control’’ sample. Because the lensing QSOs are at low redshift ( $z < 0.4$ ), the range of follow-up applications is very rich, as their H $\beta$ , H $\alpha$ , [O III] emission lines are clearly measurable in the SDSS spectra. In addition, the angular size and luminosity of their host galaxies make it possible to carry out direct spectroscopy of the host (e.g., Lewate et al. 2007;

\* Some of the data presented herein were obtained at the W. M. Keck Observatory, which is operated as a scientific partnership among the California Institute of Technology, the University of California and the National Aeronautics and Space Administration. The Observatory was made possible by the generous financial support of the W. M. Keck Foundation. This program also makes use of the data collected by the SDSS collaboration and released in DR7.

\*\* Alexander Von Humboldt fellow.



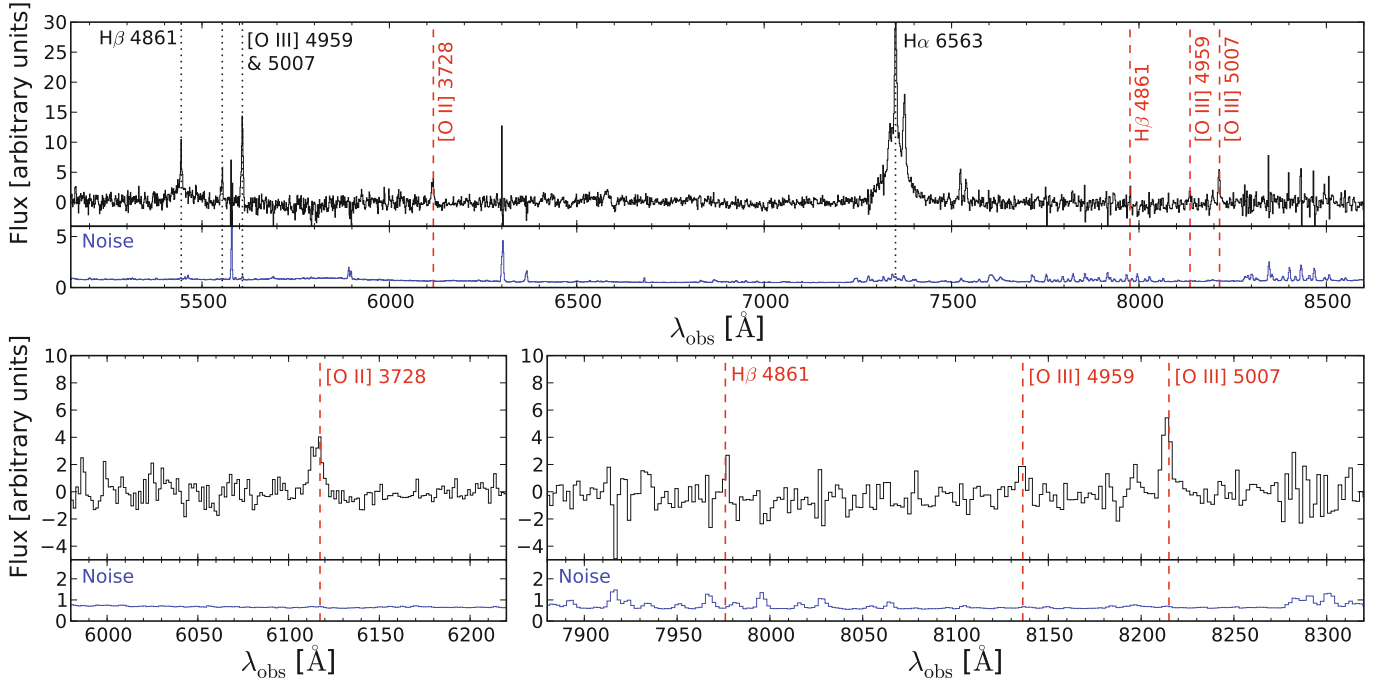


**Fig. 1.** *Top:* SDSS spectrum of SDSS J0013+1523, after subtraction of the continuum, as provided by the SDSS pipeline. The emission lines associated with the foreground  $z = 0.120$  QSO are shown with vertical dotted lines (black) and the emission lines associated with the  $z = 0.640$  background object are shown with dashed lines (red). The noise spectrum is also displayed indicating the position of the strongest sky lines. *Bottom:* from left to right zooms on the  $z = 0.640$  [O II], H $\beta$  and on the [O III] doublet. The noise spectrum does not show any strong feature at the position of the background emission lines. Note as well that the [O II] doublet is spectrally resolved. No smoothing has been applied.

Letawe et al. 2004; Courbin et al. 2002). Our sample will therefore allow us to test directly the scaling laws established between the properties of QSO emission lines, the mass of the central black hole, and the total mass of the host galaxies (e.g., Kaspi et al. 2005; Bonning et al. 2005; Shen et al. 2008).

In this paper, we focus on the discovery of the first case of a QSO, SDSS J0013+1523 (RA(2000): 00<sup>h</sup>13<sup>m</sup>40.21<sup>s</sup>; Dec(2000): +15°23′12.1″;  $z = 0.120$ ;  $r = 18.04$ ), producing two images of a background galaxy ( $z = 0.640$ ) due to strong gravitational lensing.

## 2. Spectroscopic search in SDSS

We used the SDSS DR7 catalogue (Abazajian et al. 2009) of spectroscopically confirmed QSOs to build a sample of potential lenses, without applying any magnitude cut. We considered all QSOs in the catalogue with  $0 < z_1 < 0.7$ , providing a sample of 22 298 potential lenses with SDSS spectra. In these spectra, we look for emission lines redshifted beyond the redshift of the QSO. Since the SDSS fiber is comparable in size (3″ in diameter) to the typical Einstein radius of our QSOs, the object responsible for the background emission lines is very likely to be strongly lensed (e.g., Bolton et al. 2008).

Looking for emission lines in the background of QSOs is far more difficult than behind galaxies, for three reasons: (i) the QSO outshines the lensed background images, making follow-up imaging very challenging and (ii) in contrast to early-type galaxies, QSO spectra span a huge range of properties, both in the continuum and emission lines. It is therefore impossible to subtract a QSO template from the SDSS spectra and to search for emission lines in the residual spectrum. Finally, (iii), QSO spectra have many weak iron features that can mimic faint background emission lines. These lines lead to false positives that

can be removed statistically thanks to the huge number of QSO spectra available in SDSS.

Although our search technique will be the topic of a future paper, the main components of our strategy are the following. First we subtract the continuum of the QSO spectra using a spline fit. Then, we cross-correlate the continuum-subtracted spectra with several analytical templates of emission lines. We typically use 3 templates, one with only the optical H $\beta$  and [O III] doublet, a second to which we add the [O II] doublet, and a third that also contains H $\alpha$ . The cross-correlation provides us with a catalogue of candidates, a candidate being defined as a significant peak in the cross-correlation function of redshift higher than the foreground QSO. Each QSO spectrum has many possible candidates, of which we retain the 5 most significant. For those, we fit Gaussian profiles to each of the candidate emission lines and compute a quality factor, based on the total signal-to-noise ratio (S/N) in the spectroscopic lines.

The quality factor is used to select the most likely candidates in terms of S/N. However, at this point, the catalogue of candidates still needs to be cleaned from false positives produced by residuals caused by either sky subtraction or faint features in the spectrum of the foreground QSO. Thanks to the large number of QSOs in the SDSS sample, these can be identified statistically and rejected efficiently. As a final step, we carry out a visual inspection of the most probable candidates. This process leaves us with about 10 candidates that have at least 3 significant emission lines and an additional 4 candidates with 4 emission lines. SDSS J0013+1523 is one of the latter. Its SDSS spectrum and the background emission lines at  $z_s = 0.640$  are shown in Fig. 1.

If all 14 objects are actually lensed, the probability of finding these objects is  $14/22,298 = 6.2 \times 10^{-4}$ . This is about 8 times less than in SLACS, where the discovery rate is 0.005 (e.g., Auger et al. 2009). However, our selection function is very different from SLACS, because of (i) the contrast between the QSO



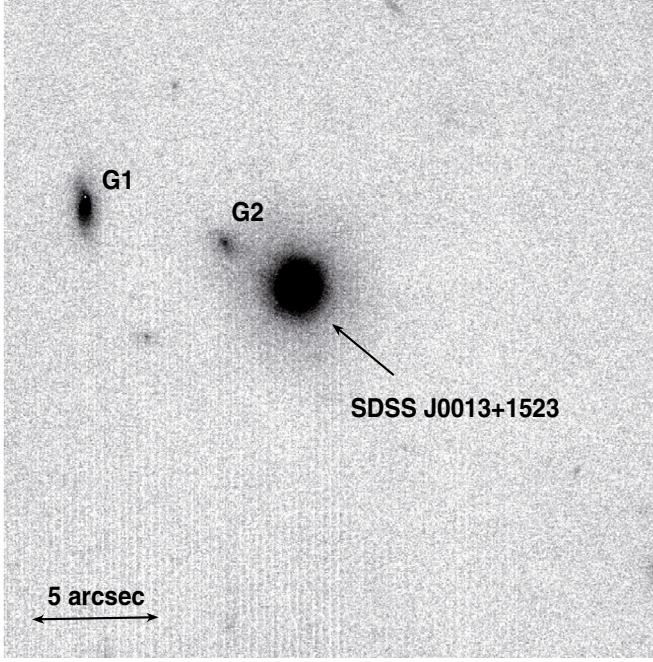


**Fig. 2.** Full field of view of the Keck NIRC2+AO observations. No star is available to construct the PSF. Also indicated are galaxies G1 and G2, which may contribute to the external shear of the lens models. From our Keck spectra, galaxy G2 is at  $z = 0.394$ . North is to the top, east left.

and the background emission lines; (ii) the regions of the QSO spectra that must be masked due to strong QSO spectral features; (iii) the requirement to see multiple background emission lines simultaneously outside the masked regions; (iv) differences between the redshift distributions of QSOs in our sample and the galaxies in SLACS. A detailed study of the selection function (e.g., Dobler et al. 2008) beyond the scope of the present discovery paper. However, if real, the difference between the SLACS discovery rate and ours may reflect a genuine difference between the lensing cross-sections of the two samples, i.e., between the physical properties of QSO and non-QSO galaxies.

### 3. Keck adaptive optics imaging

The imaging observations were obtained on the night of 11 September 2009 UT, using the NIRC2 instrument<sup>1</sup> in the laser guide star adaptive optics mode (LGS AO, Wizinowitch et al. 2006) at the 10-m Keck-2 telescope on Mauna Kea, Hawaii, in variable conditions. Images were obtained in the  $K'$  band, using the “wide field” NIRC2 camera with the FOV  $\approx 40$  arcsec, and the pixel scale of  $0.0397''$ . The observations consist of 42 dithered exposures of 40 s each. The data were reduced using standard procedures, leading to the combined image shown in Fig. 2.

Owing to the small field of view of the NIRC2+AO imager, no star is available to construct a numerical point spread function (PSF), hence making image deconvolution impossible. We nevertheless subtracted the low spatial frequencies of the PSF in two different ways.

First, we used the GALFIT package (Peng 2002) to fit analytical profiles to the data. We tried a number of different models where the QSO is represented with either a Gaussian or a Moffat profile and where the host galaxy is represented by an elliptical Sersic, a de Vaucouleurs, or an exponential disk profile. We

**Table 1.** Summary of the Keck astrometry.

Object	$x''$	$y''$	Flux
QSO	+0.000	+0.000	–
A	+0.731	+0.027	1.00
B	–0.539	+0.132	0.72
G1	–8.318	+2.873	–
G2	–2.842	+1.610	–

**Notes.** The error bars in the positions are about 20 mas, i.e., about half a pixel.

found that the best fits were those with a Moffat for the QSO and an exponential disk for the host. This model was subtracted from the 42 individual images and the difference images were then stacked and cleaned for cosmic-rays using sigma-clipping.

As a second method, we computed an estimate of the PSF directly from the QSO itself. The goal here was to remove the low frequency signal of the PSF (plus QSO host galaxy), by symmetrizing the image of the QSO. For each of the 42 frames, we produced 10 different duplicates rotated by 36 degrees about the QSO centroid. We then took the median of these 10 rotated frames, hence producing a circularly symmetric PSF. Thanks to the median average, all small details in the PSF were removed, i.e., the spikes, any blob in the PSF, and the putative lensed images of a background object. The 42 PSFs were then subtracted from the data and the residual images were stacked together.

The results of these two ways of subtracting the QSO are shown in Fig. 3. The subtraction is found satisfactory for distances larger than  $0.25''$  away from the QSO. In this area, the structures in the PSF-subtracted data change depending on the model we adopt in GALFIT. This is because the first diffraction ring of the PSF that cannot be modeled analytically. This ring is more accurately modeled by our second subtraction method, where we symmetrized the PSF.

Two obvious objects are found to the east and west of the QSO, labelled A and B in Fig. 3. These are outside the area where the PSF subtraction is uncertain and they are not located on the PSF spikes indicated by dashed lines in the middle panel of Fig. 3. We consider them as the best candidates for lensed images of a source at  $z_s = 0.640$ . All other faint structures are either superimposed with PSF features or are not fitted by lens models (Sect. 5). A summary of the relative astrometry and the flux ratio of objects A to B is given in Table 1.

### 4. Keck optical spectroscopy

Deep Keck optical spectra were obtained on the night of 20 December 2009, using the LRIS<sup>2</sup> instrument (Oke et al. 1995). The weather conditions were variable, with patchy clouds. The seeing at the moment of the observations was  $1.5''$ .

A long slit was used ( $1.5''$  wide), with a position angle (PA) of  $70^\circ$ , ensuring that we could observe simultaneously the QSO as well as object A and galaxy G2. Object B also enters partly in the slit. The data consist of 3 exposures of 600 s each, with nodding along the slit to minimize the effect of CCD traps. The wavelength range from  $3500 \text{ \AA}$  to  $8500 \text{ \AA}$  is covered using the dichroic #560 that splits the beam into a blue and a red channels. The spectrum in the blue channel is obtained using a 400 lines/millimeter grism and the spectrum in the red channel is obtained with a 600 lines/millimeter grism.

<sup>1</sup> <http://www2.keck.hawaii.edu/inst/nirc2/>

<sup>2</sup> <http://www2.keck.hawaii.edu/inst/lris/>

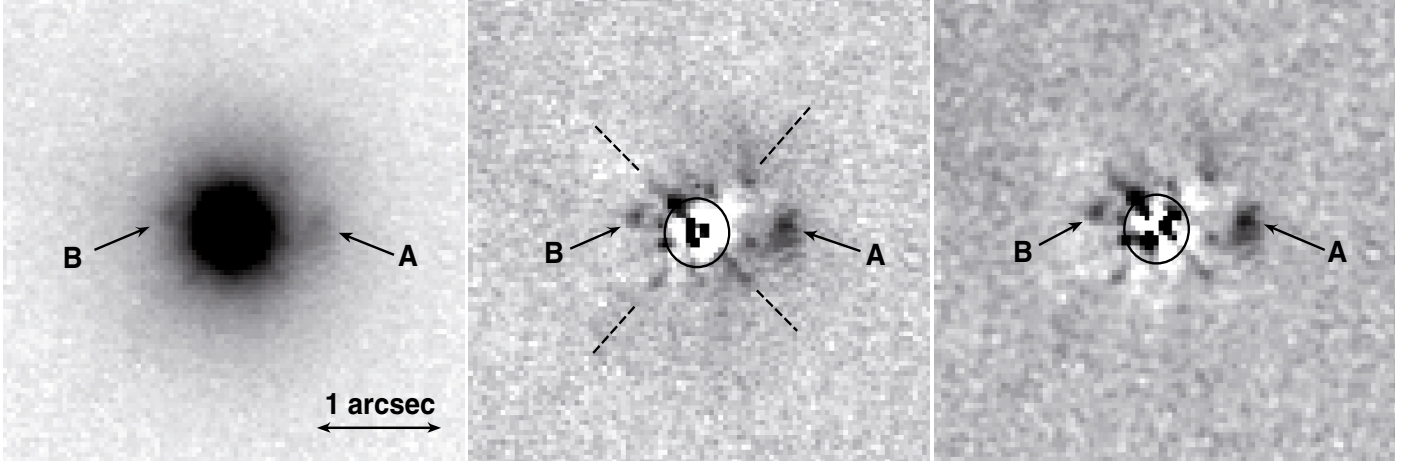


**Fig. 3.** *Left:* zoom on the central part of Fig. 2. The resolution is  $0.1''$  FWHM and the pixel scale is  $0.0397''$ . Two objects, labelled A and B, appear in the vicinity of the QSO. *Middle:* residual after subtraction of the GALFIT model (Moffat+exponential disk), where objects A and B are now well visible. The circle indicates the position of the QSO. Its size,  $0.5''$  in diameter, corresponds to the region where the subtraction may not be reliable, mainly due to the presence of the complex first Airy ring of the PSF. Spike-like features in the PSF are indicated by the dashed lines. *Right:* as in the middle panel, but a symmetrized PSF has been subtracted. This removes more effectively the Airy ring than an analytical model of the PSF.

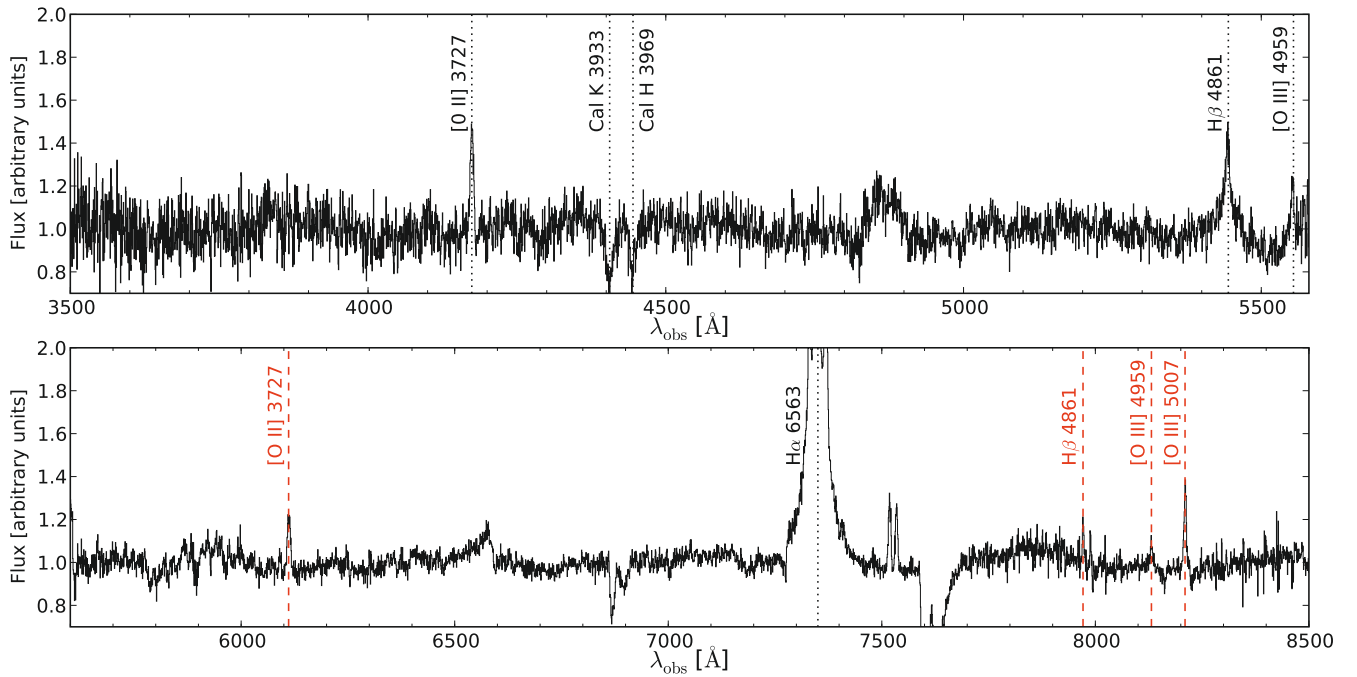


**Fig. 4.** Keck/LRIS spectrum of SDSS J0013+1523, normalized to the continuum. As in Fig. 1, the labels in black show the spectral features associated with the foreground  $z = 0.120$  QSO and the labels in red show the emission lines of the  $z = 0.640$  background galaxy. No smoothing has been applied.

The data were reduced using the IRAF<sup>3</sup> package, to perform the wavelength calibration, the sky subtraction, and the spectra combination in two dimensions. The pixel size in the blue channel is  $0.6 \text{ \AA}$  in the spectral direction and  $0.135''$  in the spatial direction. In the red channel the spectral scale is  $0.8 \text{ \AA}$  per pixel and the spatial scale is  $0.210''$  per pixel. The final 1D spectrum was extracted, confirming all of the  $z = 0.640$  emission lines seen in the SDSS spectrum (Fig. 4). In addition to the QSO spectrum we also obtained the spectrum of galaxy G2, allowing us

to measure its redshift from the [O II], H $\beta$ , and [O III] emission lines,  $z = 0.394$ . This rules out the possibility that G2 is a counter image of object A. We do not detect the continuum of G2.

The seeing for the 2D spectra was poor, but sufficient to separate spatially the spectrum of the QSO from that of object A. This was achieved by subtracting a two-dimensional Moffat profile from the data, clearly unveiling the four  $z = 0.640$  emission lines seen in the 1D spectrum, off-centered by  $0.8''$  from the centroid of the QSO. This is almost exactly the separation between the QSO and object A. We show in Fig. 5 the result of the QSO subtraction for the two brightest emission lines. Although

<sup>3</sup> <http://iraf.noao.edu/>

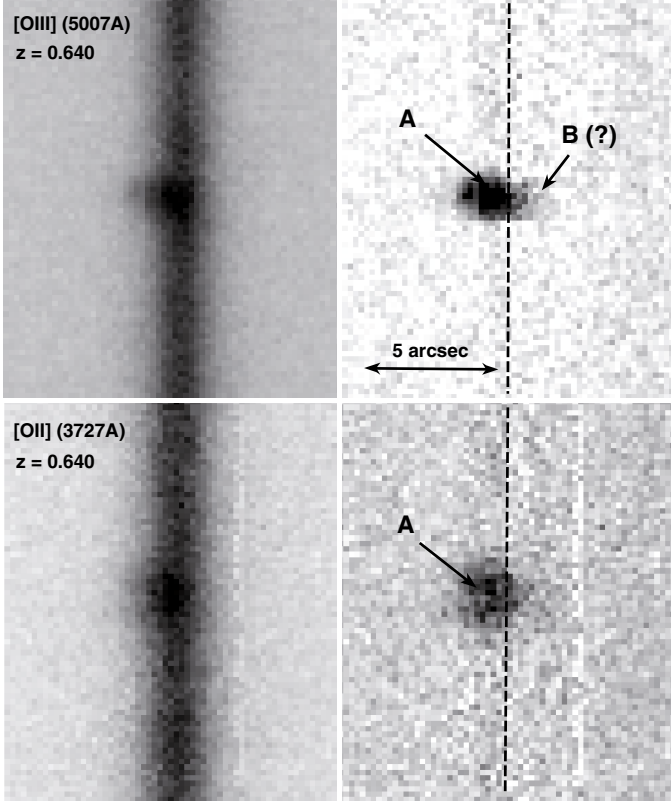


**Fig. 5.** Two-dimensional spectrum of SDSS J0013+1523 obtained with the Keck and LRIS. The spatial direction runs along the  $x$ -axis and the spectral direction along the  $y$ -axis (red to the top). *Top:* zoom on the [O III] (5007 Å) emission line, redshifted to  $z = 0.640$ . The left panel shows the original spectrum, while the right panel shows the data after subtraction of the QSO spatial profile, centered on the dashed line. Object A is clearly detected, off-center with respect to the QSO, and traces of B may be present at the position expected from the AO images. *Bottom:* same as above but for the [O II] (3727 Å) doublet.

the signal is very weak, we can also detect a weak [O III] emission line at the position expected for object B. Deeper observations with better seeing would be needed to provide firm conclusions.

## 5. Lens modeling

We show that the observed image configuration is consistent with the gravitational lens hypothesis. We model the mass distribution of the lens with a singular isothermal sphere (SIS) and include the effect of the environment as an external shear. This simple model has three parameters: the angular Einstein radius  $\theta_E$  of the SIS, the amplitude  $\gamma$ , and the position angle  $\theta_\gamma$  of the shear. The observational quantities used to constrain the model are the relative positions of the lensed images A and B and the flux ratio of these images. Since the flux ratio can be affected by differential extinction, PSF uncertainties, or microlensing, we assume an error of up to 20% in the flux ratio reported in Table 1. The center of the SIS is assumed to be coincident with the position of the lensing QSO. Using the `lensmodel` lensing code developed by Keeton (2001), we find that the observed system can be perfectly reproduced ( $\chi^2 \sim 0$ ) with the following model parameters  $(\theta_E, \gamma, \theta_\gamma) = (0.64 \pm 0.06'', 0.019 \pm 0.02, 43_{-4}^{+6})$ .

The angular Einstein radius  $\theta_E$  of the SIS model is directly related to the central velocity dispersion  $\sigma_{\text{SIS}}$  of the stars in the galaxy by the equation

$$\theta_E = \frac{4\pi\sigma_{\text{SIS}}^2}{c^2} \frac{D_{\text{ls}}}{D_{\text{os}}}, \quad (1)$$

where  $D_{\text{ls}}$  (respectively  $D_{\text{os}}$ ) is the angular cosmological distance between the lens and the source (resp. observer and source). Using this formula, we find  $\sigma_{\text{SIS}} \sim 169 \text{ km s}^{-1}$  for our best model. Because multiple images are observed, the surface mass density  $\Sigma$  inside the Einstein radius equals the critical surface mass density  $\Sigma_c$ . This allows us to calculate the amount of mass  $M_E$  inside the Einstein radius  $R_E = 1 h^{-1} \text{ kpc}$ . We find  $M_E = 2.16 \times 10^{10} h^{-1} M_\odot$ . This mass might be overestimated as the intervening galaxies G1 and G2 are not included in the lens modeling, due to the lack of sufficient observational constraints (such as the masses of G1 and G2). However, Keeton & Zabludoff (2004) show that this overestimate is unlikely to be larger than 6%. This would result in an overestimate of 3% in the velocity dispersion, i.e., only  $5 \text{ km s}^{-1}$ .

We can compare  $\sigma_{\text{SIS}}$  to two estimates of the velocity dispersion based on the SDSS spectrum of SDSS J0013+1523. Shen et al. (2008) measure the stellar velocity dispersion of the host galaxy, based on the broadening of absorption features observed in its spectrum. They derive a surprisingly small value,  $\sigma_* = 96.4 \pm 13.8 \text{ km s}^{-1}$ . We note, however, that this value is based on a low S/N spectrum of the host galaxy, following a principle component analysis decomposition of the SDSS spectrum. While this is certainly sufficient to measure, statistically, velocity dispersions for a large sample of objects, the accuracy reached for individual objects remains limited.

An indirect but more robust estimate of  $\sigma_*$  can be found using the relation between the black hole mass and the galaxy velocity dispersion derived by Gültekin et al. (2009) for all type of host galaxies. Using the black hole mass estimate  $\log(M_{\text{BH}}) = 7.24 \pm 0.27 M_\odot$  derived by Shen et al. (2008) from the width of the H $\beta$  emission line of the QSO, we obtain  $\sigma_*(M_{\text{BH}}) = 124 \pm 47 \text{ km s}^{-1}$ . We note that the width of the QSO H $\beta$  measured by Shen et al. (2008),  $\text{FWHM}(\text{H}\beta) \sim 2920 \pm 390 \text{ km s}^{-1}$ , compares well with our measurement from the Keck spectra:  $\text{FWHM}(\text{H}\beta) \sim 3090 \text{ km s}^{-1}$ . The error associated with the former estimate is derived by adding quadratically the intrinsic scatter in the error in the black hole mass and by propagating the various errors in the formula of Gültekin et al. (2009). The latter estimate is, within  $1\sigma$ , compatible with the lensing velocity dispersion.

## 6. Conclusions

We have conducted a systematic spectroscopic search for QSOs acting as strong gravitational lenses on background emission-line galaxies. This has produced a sample of about 14 potential lenses.

We have presented Keck-AO imaging of one of the most likely candidates, SDSS J0013+1523, a QSO at  $z = 0.120$  whose spectrum additionally displays four emission lines at the same redshift,  $z = 0.640$ . After PSF subtraction, we found two faint objects, A and B, within a radius of  $2''$  from the QSO.

Keck LRIS spectroscopy of SDSS J0013+1523 spatially resolves object A and confirms that it is at  $z = 0.640$ . Traces of object B may be seen at the expected position, also at  $z = 0.640$ . We measured the redshift of one of the two galaxies seen in the vicinity of the QSO, galaxy G2 at  $z = 0.394$ .



The position, flux ratio, and shape of objects A and B are fully compatible with simple lens models involving a singular isothermal sphere plus external shear. Although lower than in most galaxies in SLACS, the velocity dispersion found from the lens models is within  $1\sigma$  compatible with that estimated from the empirical scaling laws established between the mass of the central black-hole and that of the QSO host galaxy.

Given the available observations, SDSS J0013+1523 is the first example of strong gravitational lensing by a QSO. Full confirmation will require deep HST observations in the optical, where the emission lines of the background object are prominent.

Apart from the exotic nature of SDSS J0013+1523, the discovery may open a new direction in the study of QSOs, providing a powerful test of existing empirical scaling laws in QSOs and allowing us to measure the total radial mass profile of QSO host galaxies with unprecedented accuracy.

*Acknowledgements.* The authors would like to thank T. Treu, R. Gavazzi, A. Bolton and T. Boroson for helpful discussions. This work is partly supported by the Swiss National Science Foundation (SNSF). S.G.D. and A.A.M. acknowledge a partial support from the US NSF grants AST-0407448 and AST-0909182, and the Ajax Foundation. We thank the staff of the Keck Observatory for their expert help during the AO and LRIS observations. D.S. acknowledges a fellowship from the Alexander von Humboldt Foundation.

## References

- Abazajian, K. N., Adelman-McCarthy, J. K., Agüeros, M. A., et al. 2009, *ApJS*, 182, 543
- Auger, M. W., Treu, T., Bolton, A. S., et al. 2009, *ApJ*, 705, 1099
- Bolton, A. S., Burles, S., Koopmans, L. V. E., et al. 2008, *ApJ*, 682, 964
- Bonning, E. W., Shields, G. A., Salviander, S., & McLure, R. J. 2005, *ApJ*, 626, 89
- Browne, I. W. A., Wilkinson, P. N., Jackson, N. J. F., et al. 2003, *MNRAS*, 341, 13
- Courbin, F., Letawe, G., Magain, P., et al. 2002, *A&A*, 394, 863
- Dobler, G., Keeton, C. R., Bolton, A. S., & Burles, S. 2008, *ApJ*, 685, 57
- Faure, C., Kneib, J.-P., Covone, G., et al. 2008, *ApJS*, 176, 19
- Gültekin, K., Richstone, D. O., Gebhardt, K., et al. 2009, *ApJ*, 698, 198
- Impey, C. D., Falco, E. E., Kochanek, C. S., et al. 1998, *ApJ*, 509, 551
- Kaspi, S., Maoz, D., & Netzer, H. 2005, *ApJ*, 629, 61
- Keeton, C. R. 2001, unpublished [arXiv:astro-ph/0102341]
- Keeton, C. S., & Zabludoff, A. I., 2004, *ApJ*, 612, 660
- Letawe, G., Courbin, F., Magain, P., et al. 2004, *A&A*, 424, 455
- Letawe, G., Courbin, F., Magain, P., et al. 2007, *MNRAS*, 378, 83
- Muñoz, J. A., Falco, E. E., Kochanek, C. S., et al. 1998, *Ap&SS*, 263, 51
- Myers, S. T., Jackson, N. J., Browne, I. W. A., et al. 2003, *MNRAS*, 341, 1
- Oke, J. B., Cohen, J. G., Carr, M., et al. 1995, *PASP*, 107, 375
- Oguri, M., Inada, N., Pindor, B., et al. 2006, *AJ*, 132, 999
- Peng, C. Y., Ho, L. C., Impey, C. D., & Rix, H.-W. 2002, *AJ*, 124, 266
- Shen, J., Vanden Berk, D. E., Schneider, D. P., & Hall, P. B. 2008, *ApJ*, 135, 928
- Treu, T., & Koopmans, L. V. 2004, *ApJ*, 611, 739
- Treu, T., Koopmans, L. V., Bolton, A. S., Burles, S., & Moustakas, L. A. 2006, *ApJ*, 640, 662
- Warren, S. J., Hewett, P. C., Lewis, G. F., et al. 1996, *MNRAS*, 278, 139
- Wizinowich, P., Le Mignant, D., Bouchez, A. H., et al. 2006, *PASP*, 118, 297

## A QCgravlens: a didactic simulation

QCgravlens is an application for Mac OS X that “gravitationally lenses” the video flux from a webcam in real time, simulating the deflection by the lens galaxy of RX J1131–1231. Technically, the program remaps the pixels according to precalculated deflections, which were obtained using a simple Singular Isothermal Ellipsoid (SIE) lens model. The live display can be switched between the source- and image plane. Caustics and critical curves are superposed to the respective views. By displacing bright or colorful source objects in front of the camera, all common strong lensing configurations due to simple galaxies can be explored.

The application is available at <http://obswww.unige.ch/~tewes/QCgravlens>.



Figure A.1: Screenshots of QCgravlens. The left panel shows the source plane as recorded by the webcam, and the right panel simulates a view as it would be seen through the potential well of the lens galaxy. The small red circles depict the model source position and the observed astrometry of the quasar images of RX J1131–1231.





# Bibliography

- Amara, A. & Refregier, A. 2007, MNRAS, 381, 1018
- Amara, A. & Refregier, A. 2008, MNRAS, 391, 228
- Barger, V., Guarnaccia, E., & Marfatia, D. 2006, Physics Letters B, 635, 61
- Bertin, E. & Arnouts, S. 1996, Astronomy and Astrophysics Supplement, 117, 393
- Bolton, A. S., Burles, S., Koopmans, L. V. E., Treu, T., & Moustakas, L. A. 2006, ApJ, 638, 703
- Bridle, S., Shawe-Taylor, J., Amara, A., et al. 2009, Annals of Applied Statistics, 3, 6
- Chantry, V., Sluse, D., & Magain, P. 2010, A&A, 522, 95
- Claeskens, J.-F., Sluse, D., Riaud, P., & Surdej, J. 2006, A&A, 451, 865
- Courbin, F., Chantry, V., Revaz, Y., et al. 2011, A&A, 536, A53 (Chapter 3, p. 83 of this thesis)
- Courbin, F., Faure, C., Djorgovski, S., et al. 2012, A&A, 540, 36
- Courbin, F., Tewes, M., Djorgovski, S. G., et al. 2010, A&A, 516, L12 (Chapter 5, p. 123 of this thesis)
- Dietrich, J. P., Werner, N., Clowe, D., et al. 2012, Nature, 487, 202
- Dobke, B. M., King, L. J., Fassnacht, C. D., & Auger, M. W. 2009, MNRAS, 397, 311
- Dyson, F. W., Eddington, A. S., & Davidson, C. 1920, Philosophical Transactions of the Royal Society of London. Series A, 220, 291
- Eigenbrod, A., Courbin, F., Meylan, G., et al. 2008a, A&A, 490, 933
- Eigenbrod, A., Courbin, F., Sluse, D., Meylan, G., & Agol, E. 2008b, A&A, 480, 647
- Euclid Consortium. 2011, arXiv, 1110.3193
- Eulaers, E. & Magain, P. 2011, A&A, 536, A44
- Freedman, W. L. & Madore, B. F. 2010, Annual Review of Astronomy and Astrophysics, 48, 673
- Friedmann, A. 1922, Zeitschrift für Physik, 10, 377
- Friedmann, A. 1924, Zeitschrift für Physik, 21, 326

## Bibliography

---

- Hanson, D., Challinor, A., & Lewis, A. 2010, *General Relativity and Gravitation*, 42, 2197
- Hogg, D. W. 1999, arXiv, astro-ph/9905116
- Hubble, E. 1925, *Contributions from the Mount Wilson Observatory*, 304, 1
- Hubble, E. 1929, in *Proceedings of the National Academy of Sciences of the United States of America*, 168–173
- Huterer, D. 2010, *General Relativity and Gravitation*, 42, 2177
- Keeton, C. R. & Moustakas, L. A. 2009, *ApJ*, 699, 1720
- Kitching, T., Amara, A., Gill, M., et al. 2011, *Ann. Appl. Stat.*, 5, 2231
- Kitching, T. D., Balan, S. T., Bridle, S., et al. 2012, *MNRAS*, 423, 3163
- Kochanek, C. S. 2004, *ApJ*, 605, 58
- Kochanek, C. S., Dai, X., Morgan, C., Morgan, N., & Poindexter, S. C. G. 2007, in *Statistical Challenges in Modern Astronomy IV*, ASP Conference Series, 371
- Kochanek, C. S., Morgan, N. D., Falco, E. E., et al. 2006, *ApJ*, 640, 47
- Kochanek, C. S. & Schechter, P. L. 2004, *Measuring and Modeling the Universe*, 117
- Komatsu, E., Smith, K. M., Dunkley, J., et al. 2011, *The Astrophysical Journal Supplement*, 192, 18
- Larson, D., Dunkley, J., Hinshaw, G., et al. 2011, *The Astrophysical Journal Supplement*, 192, 16
- Leavitt, H. S. & Pickering, E. C. 1912, *Harvard College Observatory Circular*, 173, 1
- Lemaître, G. 1927, *Annales de la Societe Scientifique de Bruxelles*, A47, p. 49-59
- Linder, E. V. 2004, *Physical Review D*, 70, 43534
- Linder, E. V. 2011, *Physical Review D*, 84, 123529
- Longair, M. S. 2008, *Galaxy Formation* (Springer)
- MacLeod, C. L., Ivezić, Z., Kochanek, C. S., et al. 2010, *ApJ*, 721, 1014
- Magain, P., Courbin, F., & Sohy, S. 1998, *ApJ*, 494, 472
- Morgan, C. W., Hainline, L. J., Chen, B., et al. 2012, *ApJ*, 756, 52
- Narayan, R. & Bartelmann, M. 1996, arXiv, astro-ph/9606001
- Oguri, M. & Marshall, P. J. 2010, *MNRAS*, 405, 2579
- Paraficz, D. & Hjorth, J. 2010, *ApJ*, 712, 1378
- Perlmutter, S., Aldering, G., Goldhaber, G., et al. 1999, *ApJ*, 517, 565
- Refregier, A. 2003, *Annual Review of Astronomy and Astrophysics*, 41, 645

- Refregier, A., Kacprzak, T., Amara, A., Bridle, S., & Rowe, B. 2012, arXiv, 1203.5050
- Refsdal, S. 1964, MNRAS, 128, 307
- Riess, A. G., Filippenko, A. V., Challis, P., et al. 1998, Astronomical Journal, 116, 1009
- Riess, A. G., Macri, L., Casertano, S., et al. 2011, ApJ, 730, 119
- Saha, P. 2000, Astrophysics Source Code Library, record ascl:1010.064, 120, 1654
- Saha, P. 2004, A&A, 414, 425
- Schmidt, R. W. & Wambsganss, J. 2010, General Relativity and Gravitation, 42, 2127
- Schneider, P., Kochanek, C. S., & Wambsganss, J. 2006, Saas-Fee Advanced Course, Vol. 33, Gravitational Lensing: Strong, Weak and Micro, ed. G. Meylan, P. Jetzer, & P. North (Springer Verlag)
- Shapley, H. 1918, PASP, 30, 42
- Slipher, V. M. 1913, Lowell Observatory Bulletin, 2, 56
- Slipher, V. M. 1915, Popular Astronomy, 23, 21
- Sluse, D., Chantry, V., Magain, P., Courbin, F., & Meylan, G. 2012, A&A, 538, A99
- Stalin, C. S., Gupta, A. C., Gopal-Krishna, Wiita, P. J., & Sagar, R. 2005, MNRAS, 356, 607
- Suyu, S. H. 2012, arXiv, 1202.0287
- Suyu, S. H., Auger, M. W., Hilbert, S., et al. 2012a, arXiv, 1208.6010 (Chapter 3, p. 61 of this thesis)
- Suyu, S. H., Marshall, P. J., Auger, M. W., et al. 2010, ApJ, 711, 201
- Suyu, S. H., Treu, T., Blandford, R. D., et al. 2012b, arXiv, 1202.4459
- Tewes, M., Cantale, N., Courbin, F., Kitching, T., & Meylan, G. 2012a, A&A, 544, A8 (Chapter 4, p. 107 of this thesis)
- Tewes, M., Courbin, F., & Meylan, G. 2012b, arXiv, 1208.5598 (Chapter 2, p. 29 of this thesis)
- Tewes, M., Courbin, F., Meylan, G., et al. 2012c, arXiv, 1208.6009 (Chapter 3, p. 49 of this thesis)
- Thomas, S., Abdalla, F., & Lahav, O. 2010, Phys. Rev. Lett., 105, 031301
- Treu, T. 2010, Annual Review of Astronomy and Astrophysics, 48, 87
- Treu, T., Dutton, A. A., Auger, M. W., et al. 2011, MNRAS, 417, 1601
- Tsupko, O. Y. & Bisnovatyi-Kogan, G. S. 2012, Gravitation and Cosmology, 18, 117
- Vegetti, S., Lagattuta, D. J., McKean, J. P., et al. 2012, Nature, 481, 341
- Vuissoz, C., Courbin, F., Sluse, D., et al. 2008, A&A, 488, 481

## Bibliography

---

Walsh, D., Carswell, R. F., & Weymann, R. J. 1979, *Nature*, 279, 381

Weinberg, D. H., Mortonson, M. J., Eisenstein, D. J., et al. 2012, arXiv, 1201.2434

Zehavi, I., Zheng, Z., Weinberg, D. H., et al. 2011, *ApJ*, 736, 59

# Malte Tewes



Laboratoire d'astrophysique, Ecole Polytechnique Fédérale de Lausanne (EPFL)  
Observatoire de Sauverny, CH – 1290 Versoix, Switzerland  
<http://obswww.unige.ch/~tewes/>  
[malte.tewes@a3.epfl.ch](mailto:malte.tewes@a3.epfl.ch)

Born on 9 January 1984 in Stuttgart, German citizen, single  
Languages: German (native), French (native), English (fluent)

## Education

Since 2008     PhD student in the Laboratory of Astrophysics (LASTRO) at EPFL  
                    Thesis advisors: Prof. Georges Meylan and Dr. Frédéric Courbin

2002 - 2008     Physics studies at EPFL: Bachelor in 2006, Master & Dipl.-Ing. in 2008

## Refereed publications

*Two accurate time-delay distances from strong lensing: Implications for cosmology*

S. H. Suyu, M. W. Auger, S. Hilbert, P. J. Marshall, **M. Tewes**, T. Treu, C. D. Fassnacht, L. V. E. Koopmans, D. Sluse, R. D. Blandford, F. Courbin and G. Meylan 2012, submitted to ApJ, arXiv:1208.6010

*COSMOGRAIL XII: Time delays and 9-yr optical monitoring of the lensed quasar RX J1131-1231*

**M. Tewes**, F. Courbin, G. Meylan, C. S. Kochanek, E. Eulaers, N. Cantale, A. M. Mosquera, P. Magain, H. Van Winckel, D. Sluse, G. Cataldi, D. Vörös and S. Dye 2012, submitted to A&A, arXiv:1208.6009

*COSMOGRAIL XI: Techniques for time delay measurement in presence of microlensing*

**M. Tewes**, F. Courbin and G. Meylan 2012, submitted to A&A, arXiv:1208.5598

*Further Evidence that Quasar X-Ray Emitting Regions are Compact: X-Ray and Optical Microlensing in the Lensed Quasar Q J0158-4325*

C. W. Morgan, L. J. Hainline, B. Chen, **M. Tewes**, C. S. Kochanek, X. Dai, S. Kozłowski, J. A. Blackburne, A. M. Mosquera, G. Chartas, F. Courbin and G. Meylan 2012, ApJ 756 52

*Image analysis for cosmology: results from the GREAT10 Galaxy Challenge*

T. D. Kitching, [...], **M. Tewes** et al. 2012, MNRAS 423 3163

*A fast empirical method for galaxy shape measurements in weak lensing surveys*

**M. Tewes**, N. Cantale, F. Courbin, T. D. Kitching and G. Meylan 2012, A&A 544 A8

*Three quasi-stellar objects acting as strong gravitational lenses*

F. Courbin, C. Faure, S. G. Djorgovski, F. R  rat, **M. Tewes**, G. Meylan, D. Stern, A. Mahabal, T. Boroson, R. Dheeraj and D. Sluse 2012, A&A 540 A36, press release STScI-2012-14

*COSMOGRAIL IX: Time delays, lens dynamics and baryonic fraction in HE 0435-1223*

F. Courbin, V. Chantry, Y. Revaz, D. Sluse, C. Faure, **M. Tewes**, E. Eulaers, M. Koleva, I. Asfandiyarov, S. Dye, P. Magain, H. van Winckel, J. Coles, P. Saha, M. Ibrahimov and G. Meylan 2011, A&A 536 A53

*VLT adaptive optics search for luminous substructures in the lens galaxy towards SDSS J0924+0219*

C. Faure, D. Sluse, N. Cantale, **M. Tewes**, F. Courbin, P. Durrer and G. Meylan 2011, A&A 536 A29

*First case of strong gravitational lensing by a QSO: SDSS J0013+1523 at  $z = 0.12$*

F. Courbin, **M. Tewes**, S. G. Djorgovski, D. Sluse, A. Mahabal, F. R  rat and G. Meylan 2010, A&A 516 L12, press releases by Caltech & EPFL, Nature Research Highlight (Nature 466 668)

## Conference Talks

*COSMOGRAIL: Mass production of QSO lens time delays*

SnowPAC conference (Utah, USA), March 2012

*Time delay measurements in presence of microlensing, and analysis of HE0435-1223*

Strong lensing workshop in Courmayeur (Italy), June 2011

## Teaching experience

- Teaching Assistant at EPFL for *Observational Cosmology* (master course, 2009 - 2011), *Introduction to Astrophysics* (bachelor course, 2009), *Practical Work in Astrophysics* (master lab, 2008 - 2010)
- Co-supervised 4 master and 5 summer project students
- Initiated and heavily contributed to a series of bimonthly informal meetings at the Observatory of Sauverny about practical computing-related topics for astronomers (e.g., SVN, Sphinx, python modules `multiprocessing`, `pickle`, `emcee`).

## Observing experience

- 96 nights on the Swiss Euler telescope (ESO La Silla, Chile), observing mostly for the exoplanet group of the University of Geneva, with the high-resolution echelle spectrograph *Coralie*
- 14 nights on the Belgian Mercator Telescope (La Palma, Canary Islands, Spain)
- 6 nights on the NTT (ESO La Silla, Chile)